MAGNETISM AND MAGNETOTRANSPORT IN COMPLEX OXIDE THIN FILM HETEROSTRUCTURES

A Dissertation
Presented to the Faculty of the Graduate School
of Cornell University
In Partial Fulfillment of the Requirements for the Degree of
Doctor of Philosophy

by
Rajesh Vilas Chopdekar
January 2009

MAGNETISM AND MAGNETOTRANSPORT IN COMPLEX OXIDE THIN FILM HETEROSTRUCTURES

Rajesh Vilas Chopdekar, Ph. D.

Cornell University 2009

The nature of magnetism at thin film surfaces and interfaces is not yet fully understood, yet it is quite important for both fundamental studies and technological applications. In this dissertation, I present a study of the magnetism and magnetotransport in single thin film layers as well as at interfaces of Fe_3O_4/spinel chromite/LSMO and Fe_3O_4/spinel chromite/Fe_3O_4 heterostructures. To begin with, investigations of single layer thin films on metallic oxides such as perovskite structure $SrRuO_3$ and spinel structure $LiTi_2O_4$ elucidate the dependence of transport properties on parameters such as thickness, film strain state, and crystal orientation. In addition, the magnetism of $CoFe_2O_4$ thin films is examined while dynamically altering the strain state via the temperature-dependent lattice parameter of piezoelectric $BaTiO_3$ substrates.

Detailed spectroscopy experiments indicate that magnetism at the (110) LSMO and (111) LSMO surfaces are not suppressed compared to (001) LSMO interfaces. In addition, no magnetic coupling was observed between LSMO and spinel chromite layers above 100K. In contrast, the (110) Fe_3O_4 surface exhibited a significant change in anisotropy accompanied by an enhanced magnetization in the spinel chromite layer to beyond room temperature. At the isostructural interface, there is strong ferromagnetic coupling between Fe and Cr ions in bilayers. Our results on Fe_3O_4 and LSMO surfaces, combined with measurements on the angular, field and temperature

dependence of junctions with LSMO and Fe_3O_4 electrodes, indicate that spin polarization is not intrinsically suppressed at a surface or interface but that magnetization and spin polarization depends on the crystal surface orientation, strain state and surface or interface reconstruction.

BIOGRAPHICAL SKETCH

Rajesh Vilas Chopdekar was born to Pratibha and Vilas Chopdekar in New Jersey on October 7, 1979. At a young age he was interested in both mathematics and science, which was actively encouraged by both parents. His older brother Neel helped to instill in him a love of reading which persists to this day. His father Vilas, an analytical chemist, would often take him to work on Saturday mornings where he would assist his father in computer work as well as in simple experiments. This led him to take apart and examine old and broken electronics, though more often than not they remained broken.

In high school, while Rajesh did well in classes he also enjoyed hobbies such as writing or participating in the school-sponsored music programs as a saxophone player. He had briefly considered attending college to pursue a degree in the humanities, but after his brother began attending Cornell University in 1991 in the College of Engineering, Rajesh fell in love with the campus as he spent time visiting his brother. Upon being admitted to Cornell, he decided on either Chemical Engineering or Engineering Physics as candidate majors. However, he was impressed by the challenging EP curriculum and eventually received his Bachelor's degree in May 2001.

After a year in a professional degree program (the Masters of Engineering program), he applied to the Ph.D. program in Applied Physics. His advisor, Prof. Yuri Suzuki, planned on moving to the University of California in 2003, and instead of switching to another research group, Rajesh chose to enroll in the Cornell-Berkeley Exchange Scholar program and complete his degree work in California. He has lived, worked, and enjoyed the sunny weather in California for the past five years, though he misses the snowy winters of NJ and NY of his youth.

For my parents and my brother

ACKNOWLEDGMENTS

The beginnings of my career as a graduate student began in the summer of 2000 when I completed my Junior year as an undergraduate in Cornell's Engineering Physics program. I applied to the Research Experience for Undergraduates program of the Cornell Center for Materials Research, and was paired with Professor Yuri Suzuki as my research advisor. My work on patterning thin films of $YBa_2Cu_3O_7$ led into a research position during my Senior year as well as my Masters of Engineering year. She inspired both a dedication to thoroughness as well as providing a comfortable environment for discussion of both academic concerns as well as personal ones. I'm thankful that her office door in Bard 128 was always open to me and I felt quite enthusiastic about pursuing research in her lab. This has not changed since her move to Berkeley, and she gave me the somewhat daunting freedom to independently pursue many avenues of research, learn how to manage a lab environment, and how to pursue collaborations while giving critical analysis of my results. Thanks for everything, Yuri.

During my time at Cornell I was mentored by two graduate students: Darren Dale and Guohan Hu. Darren had built a pulsed laser deposition chamber in Prof. Suzuki's lab, and I thank him for showing me the intricacies of the PLD process as well as instilling in me the values of being methodical and thorough in whatever matter I was investigating. Guohan taught me a lot about nanofabrication and introduced me to the Quantum Design PPMS transport characterization tool which would become instrumental in this dissertation work (after significant modification). Yan Wu and Lu Chen also taught me about the deposition and characterization tools available at Cornell and in Yuri's lab during my undergraduate years. Also, I would like to thank John Hunt, John Sinnott, and Maura Weathers for graciously instructing me in the use of the CCMR characterization facilities.

While I had planned to leave academia temporarily after obtaining my professional degree, the dot-com bubble burst and I reconsidered my decision. Instead of applying to other universities exclusively, Professor Alexander Gaeta encouraged me to apply to the Applied Physics program at Cornell as well, and I thank him for doing so.

I was accepted into the Ph.D. program at Cornell in the summer of 2002, and was surprised to hear Prof. Suzuki announce that she was offered and accepted a faculty position at the University of California at Berkeley Materials Science and Engineering Department. However, I felt that the beginnings of my research project were quite interesting, and decided to move with her group to California. Though there has been a lot of red tape and petitions that I've had to go through in order to submit this dissertation and finish my degree, I don't regret my decision to move to California to finish the projects that I started in Ithaca. In addition, Yuri was able to excel in her career during her time here, as she is now a full professor, but also was able to start a family and now has two children with her husband Prof. Ian Fisher.

A special thanks to Prof. Bob Buhrman, Prof. David Hammer, and Prof. Sandip Tiwari for agreeing to join my special committee and being patient with me as I navigated the somewhat problematic situation of being an Exchange Scholar between Cornell and Berkeley while trying to complete the Cornell degree requirements. I thank you for your efforts!

I also thank Lena Fitting Kourkoutis from Prof. David A. Muller's group at Cornell Applied Physics for performing STEM analysis of spinel chromite-Fe_3O_4 multilayers as well as EELS linescans across the interfaces to determine the elemental concentrations and how they changed from the expected abrupt interface. TEM analysis was performed by Alexandra Ford and Franklin Wong at the National Center for Electron Microscopy at Lawrence Berkeley National Laboratory.

Much of this work was performed at the University of California, Berkeley, and I would be remiss if I did not acknowledge the assistance received in helping to set up the Suzuki lab in Berkeley. Fellow Cornell graduate students Trevor Olson and Lisa Alldredge made the trip from Ithaca to Berkeley with me, and I thank them and their spouses for their companionship and their assistance during my first two years after the move. Berkeley MSE staff members Chris Kumai, Steve Montalvo, Ken Yee, and Pete Sobingsobing were instrumental in getting the lab equipment hooked up in working order as well as ensuring that we were working in a safe environment. While Dr. Peter Revesz instructed me on how to use the Cornell RBS tandetron to take my own data, Dr. Kin Man Yu of Lawrence Berkeley Lab Materials Science Division provided many RBS measurements of both bulk and thin film samples for the Suzuki lab from 2003 to the present.

Dr. Yayoi Takamura joined the group as Prof. Suzuki's first postdoc in Berkeley. The old adage about teaching being the best way to learn is true – as I trained her on the fabrication and characterization tools that we use, I ended up learning tool operations much more thoroughly. She has also critically read many of my manuscripts and has given quite useful advice. I thank her for her advice and for her friendship, and am proud of her current status as an Assistant Professor at University of California, Davis. Hopefully I had some small contribution to her success.

Much of my efforts in exploring complex oxide properties have been spent at synchrotrons since the spring of 2005, and many people contributed to the shift in my research towards synchrotron-based characterization techniques. Early experiments of my samples were performed by Hendrik Ohldag and John Freeland, and I thank them for their time and insights. Elke Arenholz, Andreas Scholl, and Andrew Doran provided their expertise as I learned beamline and endstation operations, and I would not have been able to construct my experiments without their advice. I would like to especially thank Dr. Marco Liberati for his patience as I learned the software and quite complex hardware of both beamlines 4.0.2 and 7.3.1.1 at the Advanced Light Source. As he interacted with and eventually joined Prof. Suzuki's research group as a postdoc, I grew to value the friendship of Marco, his wife, and his now four children.

Prof. Suzuki's lab is often a learning environment, and the students that have passed through her lab as guests or members have affected my life in many ways. I value and thank discussions with Janell Neulinger and Mike Scarpulla, and have had a strong collaboration with Rouin Farshchi and Prof. Oscar Dubon in studying the transport properties of nanoscale-fabricated (Ga,Mn)As structures.

As the senior student in Prof. Suzuki's lab for the past few years, I have had the privilege of working with many talented graduate students as they began their own research. Lexi Ford provided some nice initial TEM analysis of my complex oxide heterostructures, and Franklin Wong continued the TEM analysis while providing extensive discussion of the underlying physics behind many complex oxide properties. Joanna Bettinger has become a close friend and was always a welcome companion during the long stretches of beamtime at the Advanced Light Source, as well as encouraging me to step outside the lab once in a while to experience life in California. Brittany Nelson-Cheeseman brought a positive attitude to work in the Berkeley Microfabrication Laboratory and at the Cornell High Energy Synchrotron Source, and always made me smile with her infectious optimism. It's been a pleasure to teach Virat Mehta, Jodi Iwata, and Alexander Grutter about the various cryostats and vacuum chambers that the Suzuki group owns, and I believe the tools are in good hands after I leave.

A personal thanks to Allen Wang, my undergraduate roommate from Cornell, and his sister Connie Wang for their constant friendship through both highs and lows in both my life as well as their lives. It was an honor to be Allen's best man at his wedding on 8/8/08, and I thank both Allen and Connie for acting as relief valves whenever research frustrations would discourage me.

Finally I would like to thank my brother Neel and my parents Vilas and Pratibha for always supporting me in whatever path I chose. Though I ended up moving across the country from them to complete my Ph.D., their love and encouragement have made this journey much easier. This work is dedicated to them.

This research was supported by the Office of Naval Research (N00014-97-1-0564) and the Office of Basic Energy Sciences, Division of Materials Sciences and Engineering, of the U.S. Department of Energy under Contract No. DE-AC02-05CH11231.

TABLE OF CONTENTS

LIST OF FIGURES

LIST OF TABLES

LIST OF ABBREVIATIONS

AFM	Atomic Force Microscopy
APB	Anti-phase boundary
BTO	$BaTiO_3$
CCO	$CoCr_2O_4$
CFO	$CoFe_2O_4$
DSO	$DyScO_3$
EELS	Electron energy loss spectroscopy
ETO	$EuTiO_3$
FFT	Fast Fourier transform
GSO	$GdScO_3$
H	Applied Magnetic Field
H_c	Thermodynamic Critical Field
H_{c1}	Lower Critical Field
H_{c2}	Upper Critical Field
HRTEM	High Resolution Transmission Electron Microscopy
JMR	Junction Magnetoresistance Ratio
LAO	$LaAlO_3$
LSAT	$(LaAlO_3)_{0.3} (Sr_2AlTaO_6)_{0.7}$
LCMO	$La_{0.7}Ca_{0.3}MnO_3$
LSMO	$La_{0.7}Sr_{0.3}MnO_3$
LTO	$LiTi_2O_4$
μ_B	Bohr magneton
m	magnetic moment
M	magnetization
MAO	$MgAl_2O_4$
MCO	$MnCr_2O_4$
MFM	Magnetic Force Microscopy
MR	Magnetoresistance
NGO	$NdGaO_3$
O_h	Octahedral site
PEEM	Photoemission Electron Microscopy
PPMS	Physical Property Measurement System
RBS	Rutherford Backscattering Spectrometry
SQUID	Superconducting Quantum Interference Device
SRO	$SrRuO_3$
STEM	Scanning Transmission Electron Microscopy
STO	$SrTiO_3$
ρ	resistivity
R	resistance
R_{Hall}	Hall Coefficient
R_{RMS}	root mean square surface roughness
R_s	Sheet resistance

T	temperature
t	thickness
T_c	Curie Temperature
T_{crit}	Critical Temperature
T_d	Tetrahedral site
T_N	Neel Temperature
TEM	Transmission Electron Microscopy
VDP	van der Pauw
VSM	Vibrating Sample Magnetometry
WHH	Werthamer, Helfand and Hohemberg
XAS	X-ray absorption spectroscopy
XEDS	X-ray Energy Dispersive Spectrometry
XMCD	X-ray magnetic circular dichroism
XMLD	X-ray magnetic linear dichroism
XRD	X-ray diffraction

CHAPTER 1

INTRODUCTION TO COMPLEX OXIDE HETEROEPITAXY

There has been much interest in the investigation of transport, magnetism, and spin polarization in epitaxial oxide thin films and heterostructures in recent years. Many of these studies have utilized transition metal oxides which offer a variety of magnetic and electronic ground states. For example, high spin polarization has been theoretically proposed and experimentally verified in materials such as $La_{0.7}Sr_{0.3}MnO_3$ and Fe_3O_4, and devices using such materials should offer good spin injection efficiency with highly tunable properties. In order to make such devices, these highly-spin polarized materials have been incorporated into heterostructures in which the heterointerface may have unexpected properties. Recent studies have also examined emergent behavior at heterointerfaces not present in either component phase, such a high mobility metallic layer at the interface of the two band insulators $LaAlO_3$ and $SrTiO_3$.[1] Also, thin films may exhibit properties not present in bulk due to lattice distortions induced by epitaxial strain. An example of this is the room-temperature thin film ferroelectricity in the nominally quantum paraelectric $SrTiO_3$.[2]

Epitaxial oxide thin films provide model systems where epitaxial strain and heterointerfaces can be used to generate novel functionality that can be in turn incorporated into devices. Thus when evaluating the magnetic and transport properties of complex oxide thin film devices, it is crucial to determine the effect of epitaxial strain as well as interface effects on sample properties. This chapter will begin by describing some prototypical materials in the complex oxide family that are studied in this dissertation, and will be followed by a discussion of previous work in exploring magnetism and spin polarization in oxide thin film structures.

1.1 Perovskite Oxides

The perovskite structure with molecular formula ABO_3 may be visualized as a simple cubic lattice of an alkaline earth or lanthanide (A), with a transition metal (B) at the center of the unit cell surrounded by anions at the face centers (Figure 1.1). Thus the transition metal and oxygen form a BO_6 octahedron, and the crystal field from the oxygen ligand field breaks the transition metal fivefold d-level degeneracy into t_{2g} and e_g sublevels (Figure 1.2) separated by an energy *10dq* of order 1 eV for *3d* transition metal oxides. Magnetic and transport properties are extremely sensitive to the B-O-B bond angle as well as the valence of the transition metal, thus by hydrostatic pressure, epitaxial strain, or chemical doping on the A site one may drastically alter material properties.

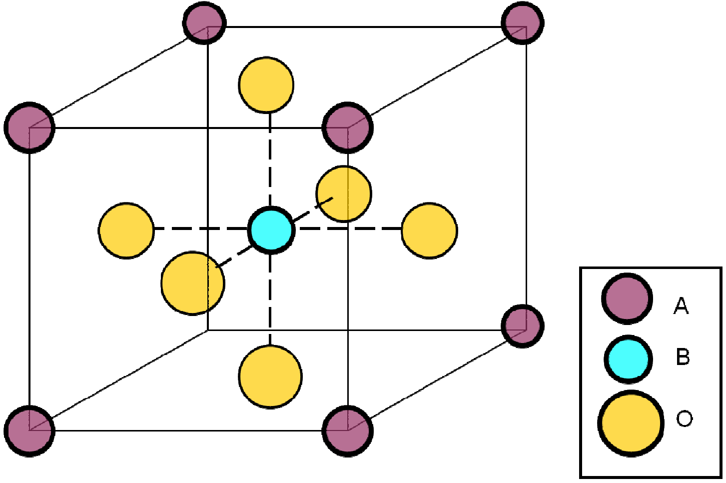

Figure 1.1– Diagram of perovskite ABO_3 crystal structure.

For instance, a parent composition of the colossal magnetoresistive manganites is the antiferromagnetic insulator $LaMnO_3$ composed of Mn^{3+} only ions. Similarly, $SrMnO_3$ is an antiferromagnetic insulator but contains only Mn^{4+} in the octahedral sites. However, an alloy of the two antiferromagnetic materials such as $La_{0.7}Sr_{0.3}MnO_3$ yields a ferromagnetic metallic ground state due to the presence of both Mn^{3+} and Mn^{4+} mediating ferromagnetism and metallic transport via the double-exchange mechanism.[3]

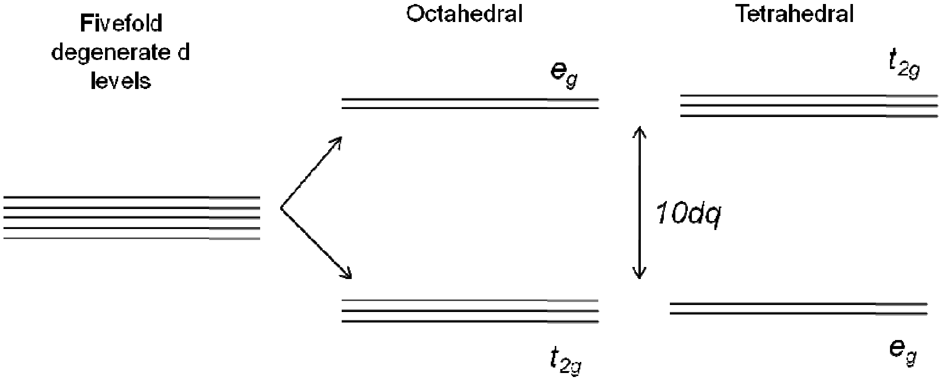

Figure 1.2– Schematic of how octahedral or tetrahedral crystal fields split the degeneracy of the d levels.

However, cation doping to vary the Mn^{3+}/Mn^{4+} ratio is not the only method to modify magnetic properties in the manganites. Hwang *et al.* show that the Curie temperature of bulk samples can be greatly affected either by external hydrostatic pressure or by internal chemical pressure via substitution of La by Pr, and both types of pressure affect the magnetic properties by varying the bonding relationship between Mn and O ions.[4] In an analogous manner, thin film epitaxial strain can also affect magnetic and transport properties due to change in Mn-O bond angle or distance.

For comparison, the itinerant ferromagnet $SrRuO_3$ may also be considered. Cation doping is not necessary to make this material ferromagnetic, and it is metallic both above and below its ferromagnetic ordering temperature in contrast to the manganites.[5] However, using epitaxial strain one may suppress magnetization,[6] increase resistivity,[7] or alter magnetic anisotropy[8] of $SrRuO_3$ films without varying film stoichiometry.

1.2 Spinel Oxides

The spinel structure with molecular formula AB_2O_4 is a face-centered cubic lattice of anions with partial occupation of interstitial tetrahedral and octahedral sites

(Figure 1.3). Many divalent or trivalent elements from the s, p, and d-blocks can be found in spinel solid solutions, but monovalent and tetravalent ions may also be found in spinels. Table 1.1 illustrates the variety of properties found in spinels with *3d* transition metal cations as collated from literature.[9, 10]

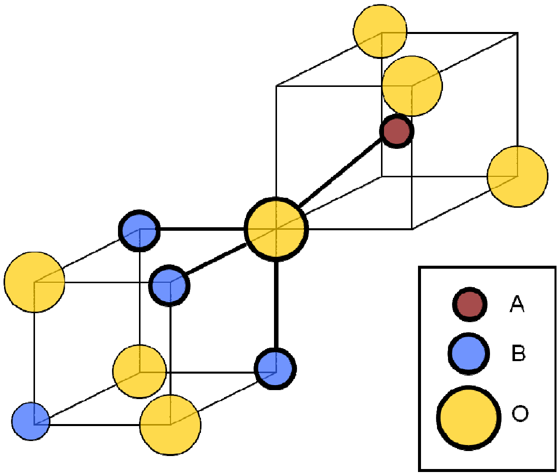

Figure1.3– Diagram of spinel AB_2O_4 crystal structure.

Room temperature magnetism occurs with high iron-content in spinel oxides, and these compositions are termed 'ferrites'. Ferrites have found much use in bulk for high-frequency applications, but in thin film form their high Curie temperature (150-500 °C) has made them desirable for integration in spin-dependent heterostructures. One interesting feature of spinel structure oxides is that the competition between exchange interactions of the A and B sites (J_{AA}, J_{BB}, and J_{AB}) can result in magnetic behavior not seen in simple ferromagnets such as elemental Co, Ni, or Fe. Such interactions are dictated by the magnetic species on the site as well as the bond angle between the cation and bonding oxygen. For instance, the chromite spinel $CoCr_2O_4$ becomes ferrimagnetic at 95K, but the moments have a short-range helical modulation of the normally collinear moment alignment.[11] Below 25K, this modulation 'locks in' and becomes a long-range spiral order with coincident weak ferroelectricity due to the non-reciprocal nature of the spiral order.[12]

Another example of a spinel oxide is the first-known magnetic material: Fe_3O_4.

The site-specific stoichiometry of Fe_3O_4 is $[Fe^{3+}]^A(Fe^{2+}Fe^{3+})^BO_4$, but the exchange interaction strengths dictate that while all A site cation moments are parallel and all B site cation moment s are parallel, the A and B site moments are antiparallel to each other and the result is a ferrimagnetic moment configuration. Even though the magnitude of the total ferromagnetic moment in Fe_3O_4 is 14 μ_B, the antiparallel nature of the A and B sites results in a net moment of only 4 μ_B.

Substituting Co into Fe_3O_4 results in the highly magnetostrictive and insulating material $CoFe_2O_4$. Even a small amount of addition of Co to ferrites can significantly change both the sign and the magnitude of the crystal anisotropy constants.[13] Thus in a spinel multilayer one may use a $CoFe_2O_4$ layer to strongly exchange couple to a softer magnetic layer.[14] However, any interdiffusion between layers such as in annealed multilayers can result in modification of the sample magnetic anisotropy.[15]

Table 1.1– Example spinel properties as a function of cation type or valence.

Spinel	**Avg. d^n on B site**	**Properties**
$LiTi_2O_4$	0.5	Metallic, Superconductor, T_{crit} ~13K
$MgTi_2O_4$	1	Metallic / spin singlet insulator, T_{order}~250K
LiV_2O_4	1.5	Heavy fermion metal
ZnV_2O_4, $ZnCr_2O_4$	2, 3	Insulator / AFM
AlV_2O_4, $LiMn_2O_4$	2.5, 3.5	Charge-ordered insulator
Fe_3O_4	4.5	Metallic, FM, T_{Verwey} ~125K, T_c ~ 858K
$CoFe_2O_4$	4	Insulator, FM, T_c ~ 793K
$MnCr_2O_4$	3	Insulator, FM, T_c ~50K, T_{SR}~17K
$CoCr_2O_4$	3	Insulator, FM, T_c ~95K, T_{SR}~25K

The spinel oxide family also has members with more exotic properties. For instance, $LiTi_2O_4$ is the only know superconducting spinel oxide material, and had one of the highest critical temperatures (13K) before the discovery of high-temperature superconductivity.[16] Superconductivity is mediated by the equal amounts of Ti^{3+} and Ti^{4+} on octahedral interstitial sites in the spinel lattice, and disruption of the octahedral sublattice can suppress or eliminate the superconducting phase. Such substitution with elements such as Mg or Mn has been used to explore the source of compositionally induce metal-nonmetal and magnetic transitions.[17]

1.3 Spin-polarized oxides

The nature of magnetism at surfaces and interfaces has been a fundamental issue that has yet to be completely understood, and experimental data can often be at odds with theoretical predictions. In particular, experiments probing the magnetization at the surface and interfaces of highly spin-polarized materials suggest that surface magnetization is suppressed compared to the bulk. These highly spin-polarized materials include complex transition metal oxides such as Fe_3O_4 and $La_{0.7}Sr_{0.3}MnO_3$ (LSMO).

For example, Park *et al.* showed that in (001) LSMO thin films, surface magnetization, as measured by spin-polarized photoemission, falls much more rapidly compared to bulk as a function of temperature.[18] More recently, Infante *et al.* have found that (110) $La_{0.7}Ca_{0.3}MnO_3$ (LCMO) thin films exhibit a slower decay of magnetization as a function of increasing temperature compared to (001) LCMO films.[19] And insertion of 2 $LaMnO_3$ monolayers at the interface of a $La_{0.6}Sr_{0.4}MnO_3$/ $SrTiO_3$ bilayer shows a marked improvement in temperature dependent magnetization over a bilayer without the $LaMnO_3$ monolayers, showing that a composition modulation can have a drastic impact on an electrode-barrier interface. Finally, spin polarized photoemission studies of Fe_3O_4 have reported spin polarization values of -40 to -80% depending on the crystal surface being probed.[20-24] To date, the applicability of bulk spin polarization values at surfaces of Fe_3O_4 or LSMO and the dependence of spin polarization values on crystal surface orientation has yet to be fully understood.

While high spin polarization at Fe_3O_4 surfaces might be theoretically predicted,[25] Fe_3O_4 thin films in magnetic tunnel junctions with MgO barrier layers have met with limited success.[26, 27] Junction magnetoresistance (JMR) values in Fe_3O_4/MgO/Fe_3O_4 junctions of no more than 1% were observed even at cryogenic temperatures, whereas highly spin-polarized materials should yield JMR values close to 100%.

Significant JMR values in Fe_3O_4 and LSMO based magnetic tunnel junctions have prompted a reinvestigation of the nature of magnetism in highly spin polarized materials and the role of the interface with the barrier layer. [28-30] The use of an isostructural spinel barrier layer in Fe_3O_4/barrier/LSMO junctions has provided an order of magnitude increase in low-field junction magnetoresistance over similar structures with a rocksalt structure barrier layer.[28] The use of $SrTiO_3$ as a barrier layer has also been attempted, with similar JMR as the rocksalt MgO case.[31] Finally, a spacerless LSMO/Fe_3O_4 shows hysteretic resistance behavior with a maximum MR of -5% at 55K.[32] In contrast, a spin filter type device with LSMO/$NiFe_2O_4$/Au structure showed up to +50% MR at low temperatures, and reinforces the idea that spin-dependent transport can occur in perovskite-spinel complex oxide heterostructures with high spin injection efficiency.[33]

In the context of such varied properties for heterostructures with perovskite and spinel interfaces, it is important to understand the nature of magnetism at the interface between these isostructural and non-isostructural magnetic complex oxides.

1.4 Synopsis of following chapters

Correlating the structure and the origin of the magnetism from multiple magnetic species at the oxide interfaces is crucial in explaining the magnetic and electronic behavior of complex oxide heterostructures. LSMO has a perovskite structure where the magnetism is found in octahedrally coordinated Mn^{3+} and Mn^{4+} sites. On the other hand, spinel structure oxides such as Fe_3O_4 and the barrier layer in the Fe_3O_4/LSMO based junctions are both composed of tetrahedral and octahedral interstitial sites amongst a face-centered cubic oxygen lattice. The interaction among magnetic ions on each sublattice and between tetrahedral and octahedral sublattices can give rise to complex magnetic behavior. In addition, the site preferences of transition metal cations, as well as the ease of cation migration in the open spinel structure,[34] also complicate the magnetism at the interface of heterostructures synthesized via non-equilibrium routes. Therefore, in order to determine the details of the interface magnetism, element specific and interface sensitive probes such as X-ray absorption spectroscopy (XAS) and X-ray magnetic circular dichroism (XMCD) must be used. Spectroscopy and spectro-microscopy both allow for the determination of interface cation magnetization, valence, and site symmetry, while element-specific hysteresis loops elucidate the anisotropy of the interface moments with respect to bulk film properties. Combined with local structural probes such as scanning transmission electron microscopy (STEM), in this work these techniques have shed light on the origin of the large JMR and strong exchange coupling observed in LSMO and Fe_3O_4-based heterostructures.

Chapter Two discusses pulsed laser deposition as the primary tool for sample growth in this work, as well as elaborating on various characterization techniques for both single layer films as well as multilayers.

Chapters Three and Four explore film properties such as magnetotransport in single films of the metallic perovskite $SrRuO_3$ and the superconducting spinel $LiTi_2O_4$. While $SrRuO_3$ is a common choice for all-perovskite oxide ferroelectric structures, ultrathin films show markedly different properties than bulk and it is important to consider such properties at heterostructure interfaces.

Chapter Five examines the influence that epitaxial strain may have on non-isostructural interfaces by examining film properties of magnetostrictive spinel

$CoFe_2O_4$ as deposited on substrates such as isostructural $MgAl_2O_4$ and non-isostructural but piezoelectric $BaTiO_3$. The latter combination serves as a model system of an epitaxial multiferroic (both ferromagnetic and ferroelectric) thin film composite.

Chapter Six details the investigation of 'bulk' magnetism in ferromagnetic perovskite $(La,Sr)MnO_3$ films and the corresponding investigation of surface magnetization using soft X-ray magnetic circular dichroism spectroscopy. Both surface and whole film magnetic properties are compared to transport and structural properties as a function of crystallographic orientation.

Chapter Seven discusses isostructural multilayers composed of the proposed half-metal Fe_3O_4 and ferrimagnetic insulators such as $CoCr_2O_4$ and $MnCr_2O_4$. Structural characterization shows that individual layers interact at spinel-spinel interfaces through a nano-scale interdiffused area, and the high temperature ferrimagnetism of the Fe_3O_4 polarizes the nominally paramagnetic chromite interface moments through a proximity effect that persists up to 500K and at least 5 nm away from the interface.

Chapter Eight expands on the previous chapter's use of isostructural materials to construct an all-spinel metal/insulator/metal device. From bulk properties, one would believe that the paramagnetic insulator would serve to decouple the magnetization of the electrodes, but the proximity effect at both chromite/Fe_3O_4 interface effectively couples both electrodes together and transport through the trilayer stack is equivalent to that of a single ferrimagnet.

Chapter Nine brings the previous investigations together to examine magnetotransport with Fe_3O_4 as one electrode material and LSMO as the other electrode material in a trilayer structure. The choice of substrate orientation and film thickness serve to maximize the LSMO interface magnetization, and the non-isostructural interface between chromite and LSMO serve to decouple the switching characteristics of each electrode. However, the barrier material does affect the Fe_3O_4 interface anisotropy, and angular dependence of the junction magnetoresistance ratio sheds light on how this interface anisotropy affects the orientation of the electrode moments and thus the effective spin polarization.

CHAPTER 2

GROWTH AND CHARACTERIZATION

2.1 Abstract

In this chapter, the technique of pulsed laser deposition (PLD) is described in terms of fabrication of epitaxial transition metal oxide thin films. The non-equilibrium nature of PLD results in periodic mass transport at hyperthermal velocities and the resultant crystallization of complex crystal structures in single crystalline form. Furthermore, an introduction to both structural and magnetic characterization techniques such as X-ray diffraction and X-ray magnetic circular dichroism are presented. Since the volume of material in thin film form is much less than the accompanying substrate, sensitive tools such as SQUID magnetometry or element-specific probes such as soft X-ray absorption are necessary to evaluate the properties of the thin film in detail.

2.2 Pulsed laser deposition

While thin film fabrication of metals and simple oxides can be performed by a variety of equilibrium techniques such as thermal evaporation, complex oxides pose a more difficult issue. In order to successfully stabilize such materials from a single target, one must establish congruent transfer of the target material to the substrate. In addition, due to relative differences in constituent vapor pressure, it is often difficult to maintain single phase or even proper stoichiometry of the film as compared to the initial target. While one route to combat this issue is to use multiple simple sources with carefully tuned deposition rates such as in molecular beam epitaxy, a more straightforward route is to use a highly non-equilibrium process such as pulsed laser deposition for mass transport.[35]

The roots of PLD originate in the study of the interaction between intense laser light and solid matter. The advent of excimer laser technology, which provides up to gigawatt laser power with pulse widths of tens of nanoseconds, allows for reproducible delivery of large amounts of energy confined to a small area. Energy densities of order 1 J/cm^2 achieve superheating of the illuminated area with timescales much faster than equilibrium thermal diffusion times. Areas outside of the laser-irradiated area remain in thermal equilibrium while the laser-irradiated areas change phase from a solid to a weakly ionized plasma due to laser-plume interactions and inverse bremsstrahlung heating. Due to the short interaction depth (on the order of microns) into the target, a highly directional plume of material escapes the surface of the target. The geometry of a typical PLD chamber is shown in Figure 2.1. Although the plume expands and thermalizes in ambient background gas, the transit time between the target and a substrate holder 5 cm away from the target is of order milliseconds. A luminous plume is visible to the naked eye when depositing in an ambient O_2 atmosphere as seen in Figure 2.2, but some scattering and conversion from kinetic energy to photons is observable even in depositions in high vacuum. Such optical emission spectra can be probed to identify excited species in the plume.[36, 37] The volume of material ejected in a single pulse results in deposition of a partial monolayer of material on the substrate holder. If the substrate holder is kept at an elevated temperature to facilitate surface diffusion while at a low enough temperature to prevent equilibrium re-evaporation of the material, a crystalline film of the target material will template on the substrate and grow in thickness.

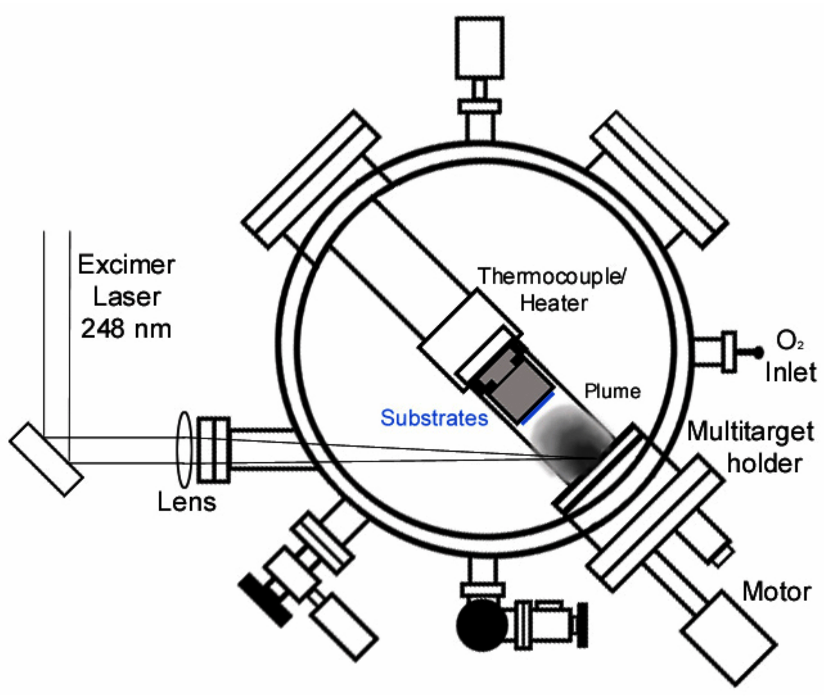

Figure 2.1 – Schematic of a typical pulsed laser deposition vacuum chamber.

Figure 2.3 illustrates the timescales involved in PLD. While a discussion of X-ray scattering as an *in-situ* monitor of film growth is beyond the scope of this work,[38, 39] we may simply say that the anti-Bragg intensity modulation at the (0 0 0.5) position is a sensitive probe of material coverage and crystallinity of a film surface. In Figure 2.3, approximately 400 pulses are averaged over a 1 second interval with the laser pulse trigger set at t_0=500 ms. The sharp drop in intensity at t_0 + 20 ms is the arrival of plume species on the substrate surface, and the resulting disorder of the plume species results in a drop in anti-Bragg intensity. The slow increase in intensity over 500 ms is due to surface diffusion of plume species to low-energy positions that template on the previous layer's crystal structure.

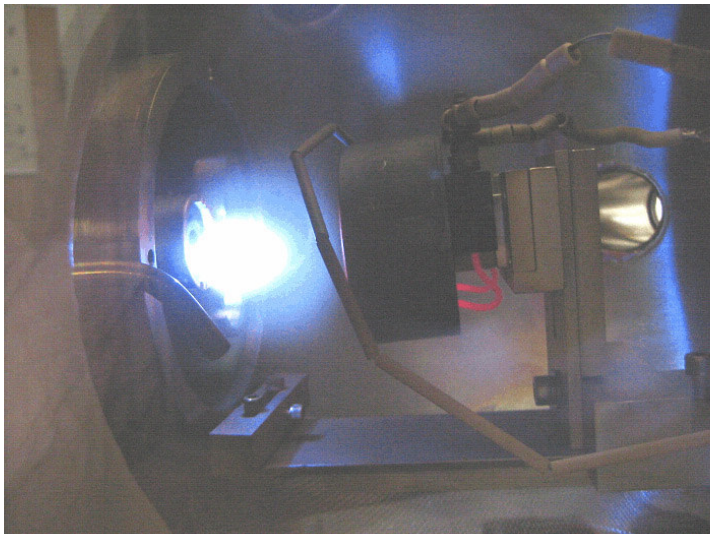

Figure 2.2 – Photograph of plume from a $La_{0.7}Sr_{0.3}MnO_3$ *target in 300 mTorr of* O_2 *after arrival of a 150 mJ laser pulse focused to an areal density of* $2J/cm^2$.

The pulsed nature of the plume arrival is in sharp contrast to the much slower but constant mass transport rates of thermal evaporation, and results in the possible stabilization of phases not allowed or thermodynamically unfavored in standard phase equilibrium diagrams. For instance, while $LaTiO_3$ is difficult to grow in bulk, ablation from a stable $La_2Ti_2O_7$ target in high vacuum onto a lattice-matched substrate consistently produces crystalline films of $LaTiO_3$ for a variety of film thicknesses.[40]

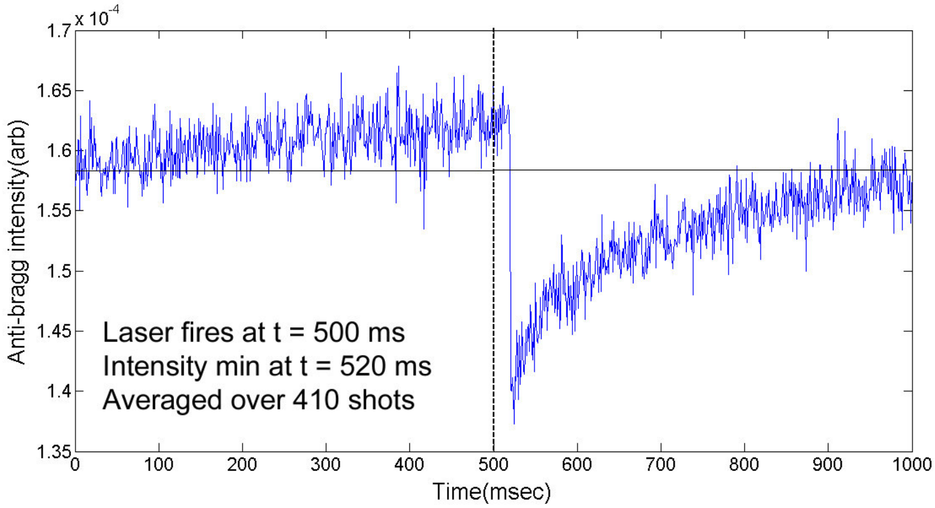

Figure 2.3 – Anti-Bragg intensity as a function of time for a film of $SrTiO_3$ *grown on a (001)* $SrTiO_3$ *substrate.*

2.3 Atomic force microscopy

Microstructural analysis of thin film samples is an essential component to correlating magnetic and electronic properties with strain or morphology. While transmission electron microscopy can yield cross-sectional images as well as selected-area diffraction, sample preparation is time-intensive. In lieu of such techniques, atomic force microscopy can be used to quickly measure surface morphology and assess the influence of PLD deposition conditions on film surface quality. An in-house AFM and PLD system enables quick optimization of deposition conditions to provide smooth and particulate free thin film samples.

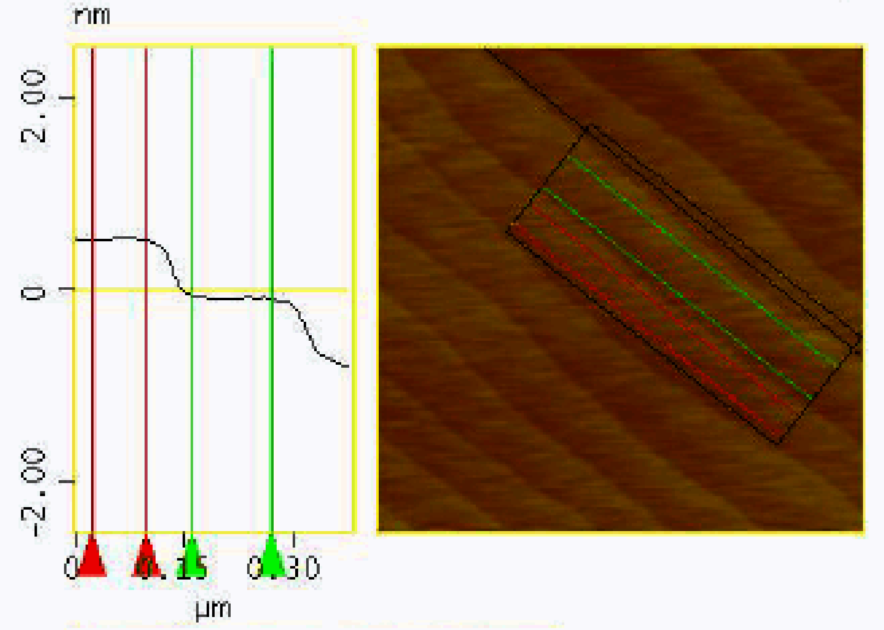

Figure 2.4 – Step height and surface profile of a 1 micron x 1 micron area of a TiO_2*-termninated* $SrTiO_3$ *substrate.*

AFM has typical resolution on the angstrom scale in the vertical direction and tens of nanometers laterally. An example of a typical scan on a TiO_2-terminated $SrTiO_3$ substrate is shown in Figure 2.4, with atomically flat terrace width of approximately 150 nm due to a small miscut of the substrate during wafer cutting and polishing. Each terrace is vertically offset by 1 unit cell or 0.391 nm. Such resolution is obtained through the use of stepper motors and piezoelectric ceramics to finely position a micromachined cantilever near the surface of the sample, and the cantilever is rastered across the sample surface in a similar manner to the rastering of an electron gun to produce a CRT television image.

AFM surface measurements are performed either in ‘contact’ mode or ‘tapping’ mode. In both modes, a diode illuminates the back of the cantilever and the reflection is imaged upon a four-quadrant photodetector. Small deflections of the cantilever such as from van der Waals forces from surface interaction result in a shift of the diode spot on the photodetector, and the diode signal is translated to changes in height as a function of cantilever lateral position. In contact mode, the cantilever tip makes contact with the sample and is dragged across, and any height variations are measured by deflections of the diode spot on the photodiode. In tapping mode, the cantilever tip does not make constant contact with the sample surface, but instead is set to resonant oscillation close to the sample surface, and deviations from this resonant oscillation are translated to changes in surface height information.

Cantilever material for microscopy is usually Si or Si_3N_4 to maintain durability and appropriate stiffness and resonant frequency over the lifetime of the cantilever and tip, as well as a sharply defined tip. Typical radii of curvature for commercial tips are 12.5 nm for uncoated tips and 25 nm for CoPt coated tips, thus features down to tens of nm may be easily imaged. Conductive or magnetic coatings on the tip add either electrostatic or magnetic interaction between the sample surface and the tip, and imaging techniques such as magnetic force microscopy,[41] surface potential microscopy, and piezoelectric force microscopy take advantage of the small additional overhead added to a conventional AFM system. The magnetic or electrostatic interactions can be considered as drag force acting on the sample tip. By modeling the cantilever as a damped driven harmonic oscillator, changes in the resonant frequency or oscillation phase of the cantilever are proportional to the gradient of the force between the surface and the tip.

2.4 X-ray diffraction

X-ray diffraction analysis is a powerful tool for measuring crystallinity and orientation of thin film samples. In this work, the basic geometry is that of a Bragg-Brentano geometry in which incident Cu K X-rays (E~8 keV) diffract off of the out-of-plane oriented layers of both film and substrate, and the difference between incident and diffracted beam angles is proportional to the layer spacing. More complicated geometries may be used to determine in-plane crystallographic registry between film and substrate, and so-called 'reciprocal space maps' may be generated by combining a number of one-dimensional scans into a two-dimensional contour. The so-called four-circle geometry is shown in Figure 2.5.

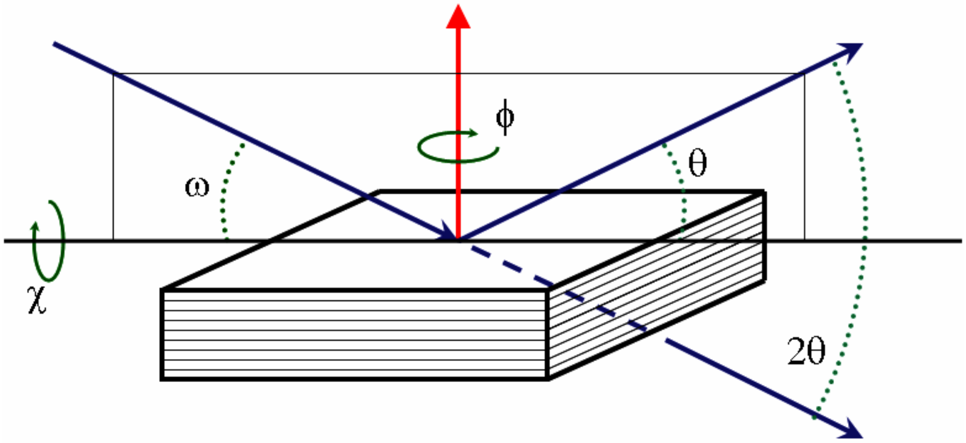

Figure 2.5 – Four-circle X-ray diffraction geometry for a thin film sample on a single crystal substrate.

In the 'coupled' Bragg geometry, the angle between the sample surface and the direction of incident X-rays (ω) is matched to the angle between the sample surface and the center of the detector (θ). When ω is equal to θ, the out of plane lattice spacing may be probed and the angle between incident X-rays and the diffracted beam is called 2θ. The structure factor of elements in the material also modulates the interference, and in some crystal structures there exists diffraction peaks with complete destructive interference when summed over certain orientations.

A derivation of Bragg's law may be found in many introductory solid state texts, and we may relate this angle to the lattice periodicity that produces constructive interference. A geometric argument can be used to derive the Bragg equation $n\lambda = 2d\sin\theta$. By examining Figure 2.6, we see that paths 1, 2, and 3 are parallel and of the same length for sections WX and YZ. We will assume that these path lengths are much longer than the interplane spacing d of the sample of interest, with an X-ray source placed at W and a detector placed at Z. The angle of incidence θ is congruent to all angles marked with arcs in Figure 2.5 Thus by geometry we may find the difference in path length WZ for paths 1 and 2 is $2d\sin\theta$, and the difference is indicated for path 2 by double lines. Similarly, the difference between paths 1 and 3 is $4d\sin\theta$. Assuming 2 photons in phase starting at W, the criterion for constructive interference at Z is that the path length difference XY is an integer number of wavelengths, or $n\lambda = 2d\sin\theta$.

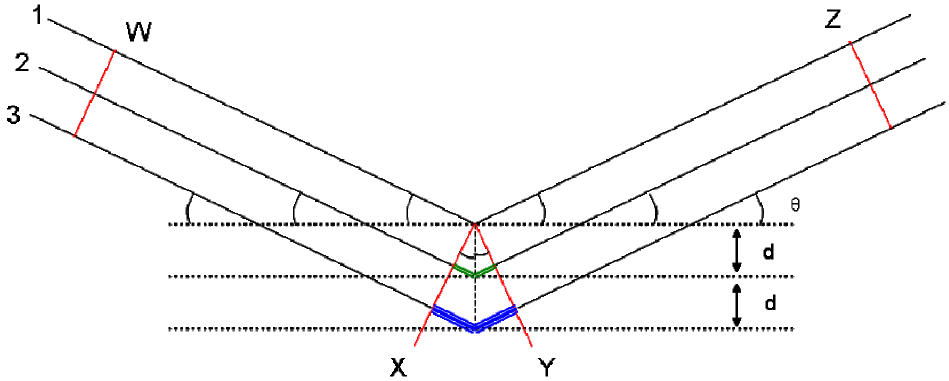

Figure 2.6 – Simple geometric diagram of Bragg diffraction by adjacent planes.

The 'coupled' term refers to the scan varying both θ and ω by the same amount so that the direction of momentum transfer is always the same. Due to miscut of the substrate or sample mounting misorientation, the maximum diffracted intensity may not occur at θ=ω. A small offset may be added to ω and subtracted from θ and the validity of Bragg's law still holds as in the case of a perfectly oriented sample: $(\omega + \delta) + (\theta - \delta) = 2\theta$. To first order, any offset δ can be assumed to be due to sample mounting effects for θ-2θ scans, and more comprehensive four circle scans or reciprocal space mapping is necessary to determine the relative orientation of film with respect to the substrate.

In a randomly-oriented powder, we may ignore such alignment issues as the crystallites should not have a preferred orientation and any illumination of the sample with X-rays will produce some diffraction at certain 2θ values that satisfy Bragg's law. For instance, loose powder from a sintered $CoCr_2O_4$ target is measured, and its diffractogram is compared with that of another sample or a stored list of peaks in the International Centre for Diffraction Data database.[42] A comparison between the database reference for $CoCr_2O_4$ and commercially synthesized powder (Figure 2.7) illustrates the good correspondence between the powder and the reference data.

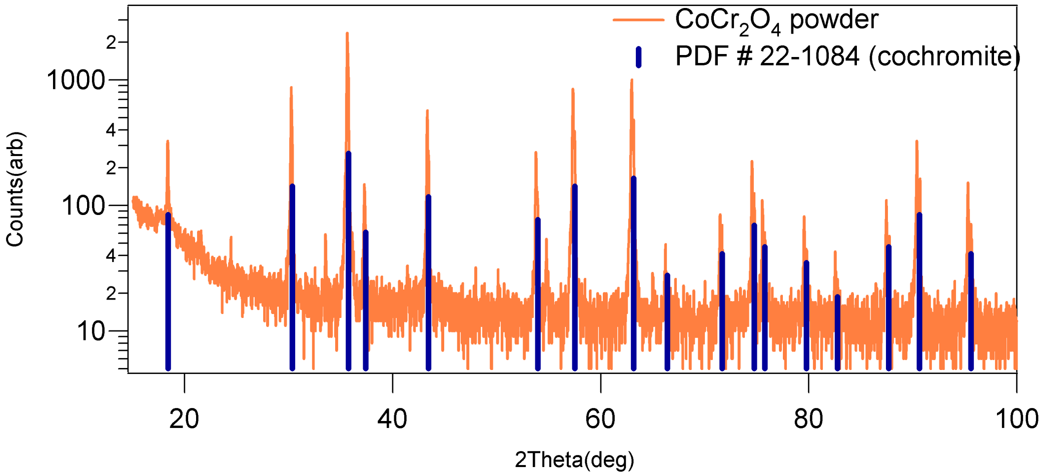

Figure 2.7 – X-ray diffraction of a $CoCr_2O_4$ powder sample with comparison to reference data.

While ω-θ geometry is useful for powder or polycrystalline samples, we may take advantage of the oriented nature of our samples and perform more detailed measurements to confirm registry to the substrate, strain quantification or unit cell distortion measurements. In 'four circle' diffractometry (Figure 2.5), the sample can rotate about its normal (φ) or tilt such that the sample normal is not in the plane determined by the X-ray tube and detector arms (called either χ or ψ). φ scans illustrate the in-plane orientation of a film sample, and reciprocal space mapping can vary all four circles to fully determine the in-plane and out-of-plane lattice parameters.

For a thin film with smooth surface and interface morphology, an interference effect may be observed as a modulation of the film peak intensity as seen in Figure 2.8. These modulations are called Laue oscillations, and may be related to film thickness using the following equation:

$$I \propto (\sin(2\pi N d \sin(\theta)/\lambda))^2 \big/ (\sin(2\pi d \sin(\theta)/\lambda))^2 \qquad \text{(Eqn 2.1)}$$

with N as the number of diffracting thin film planes, and d as the spacing between planes.[43] This technique is best suited to films with very low surface roughness (of order 0.5 nm RMS roughness) when using a conventional lab diffractometer. A monochromatic beam is necessary to observe such oscillations, and synchrotron sources are orders of magnitude brighter than lab sources, thus one may use synchrotron diffraction to resolve Laue oscillations that cannot be seen by a lab diffractometer. LSMO film thickness down to 5 nm show clear oscillations using synchrotron radiation as will be detailed in Chapter 6.

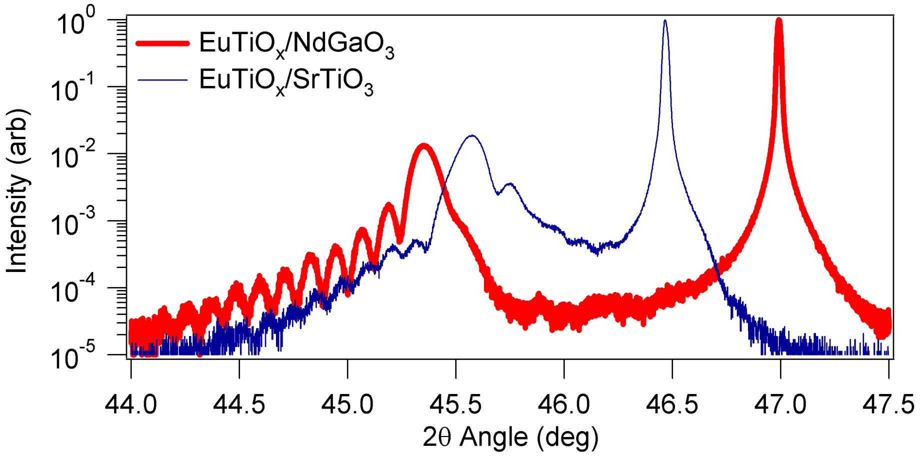

Figure 2.8 – X-ray diffraction of 83 nm (001) $EuTiO_x$ films on various substrates with peak intensity modulated by finite thickness fringes.

2.5 Vibrating Sample Magnetometry

The Vibrating Sample Magnetometer (VSM) uses the oscillation of a magnetic sample to induce an alternating voltage in pickup coils. This voltage is proportional to the sample moment, and thus the sample magnetization may be determined as a function of applied magnetic field, sample orientation, or sample temperature. An electromagnet with 9 kW bipolar power supply is used to generate DC fields of up to 10,000 Oe with approximately 0.05% field stability.

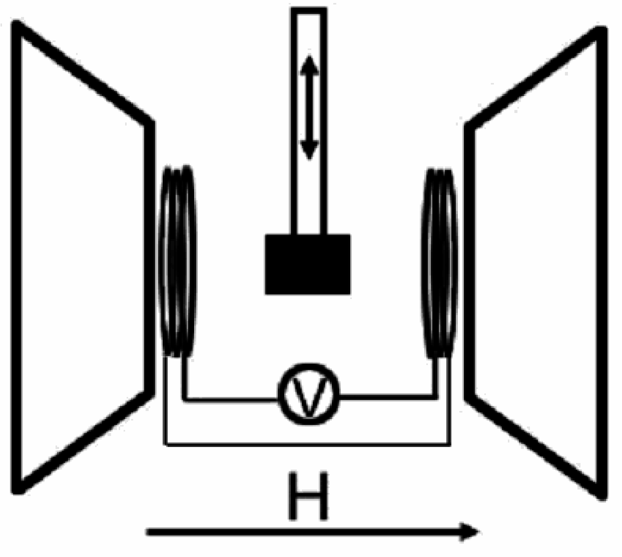

Figure 2.9 – Schematic of VSM coil and electromagnet.

Unlike the SQUID and PPMS cryostats, the VSM has a Hall probe situated next to the sample and thus the DC magnetic field may be directly measured. The applied field is horizontal, and the sample sits in the center of both the pickup coils as well as the electromagnet. The sample is driven in a sinusoidal motion vertically, and thus a small change in magnetic flux is produced by the vertical motion if one considers a fixed area such as the two coils in Figure 2.9. Any change in flux through a set of pickup coils aligned with these areas may be correlated to the frequency of sinusoidal motion, and thus a lock-in amplifier technique can be used to eliminate noise and background drift from the pickup coil output. The absolute sensitivity of the VSM is determined by the sensitivity of the electronics and the strength of the signal induced in the pickup coils, and the LakeShore 7300 VSM used in this work has an absolute sensitivity quoted as 5x10^{-6} emu. In practice, useful measurements down to 10^{-4} emu with error of 1x10^{-5} can routinely be performed at the smallest sensitivity and the largest time constant settings (Figure 2.10).

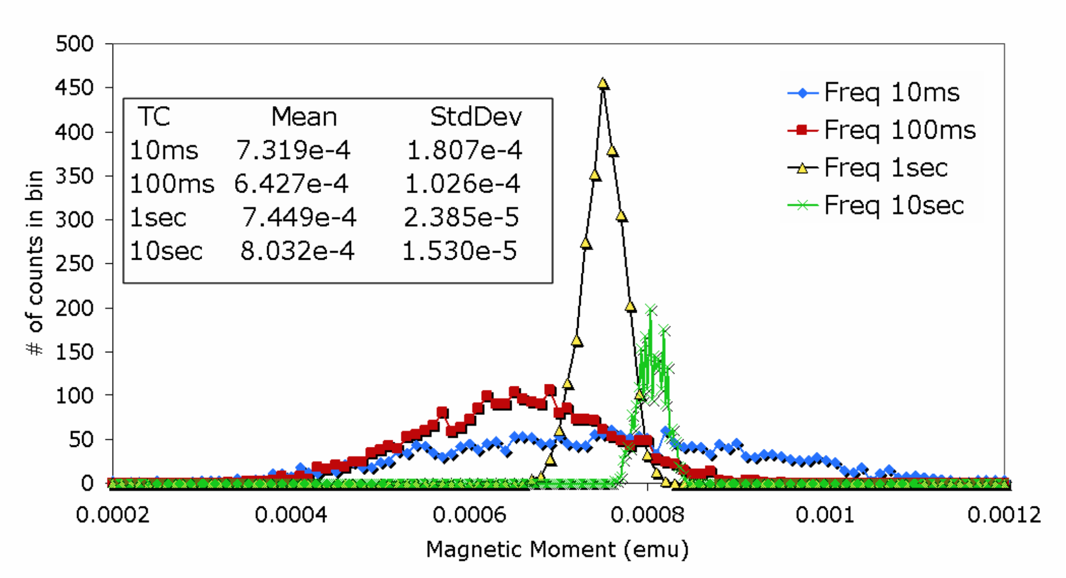

Figure 2.10 – Sensitivity characterization of the Lakeshore 7300 VSM with a typical ferrite thin film.

Only the projection of flux normal to the pickup coil area is measured, thus by rotating the sample along different crystallographic axes in a constant field and one may identify along which axes a given sample has strong or weak magnetic anisotropy. By symmetry one may expect that a sample of a given crystallographic orientation to have n-fold anisotropy. For example, a (001) out of plane oriented sample has four [100] type directions in the plane, and if magnetocrystalline anisotropy dominates other anisotropies then four maxima will be present in an angular scan.

The anisotropy energy of a magnetic material may be expanded in direction cosines:

$$E = K_0 + K_1(\alpha_1^2\alpha_2^2 + \alpha_2^2\alpha_3^2 + \alpha_3^2\alpha_1^2) + K_2\alpha_1^2\alpha_2^2\alpha_3^2 \ldots$$
$$-\frac{3}{2}\lambda_{100}\sigma(\alpha_1^2\gamma_1^2 + \alpha_2^2\gamma_2^2 + \alpha_3^2\gamma_3^2) \qquad \text{(Eqn 2.2)}$$
$$-3\lambda_{111}\sigma(\alpha_1\gamma_1\alpha_2\gamma_2 + \alpha_2\gamma_2\alpha_3\gamma_3 + \alpha_3\gamma_3\alpha_1\gamma_1) + \frac{1}{2}N_d M^2$$

with K_n as the crystal anisotropy material constants, λ_{hkl} as the stress anisotropy material constants, α_i as the direction cosine between the magnetization vector and a crystal axis, and γ_i as the direction cosine between the magnetization vector and applied strain. Shape anisotropy for a thin plate is simple: the demagnetization factor N_d is zero in the plane of the film and 1 for out of the plane of the film.

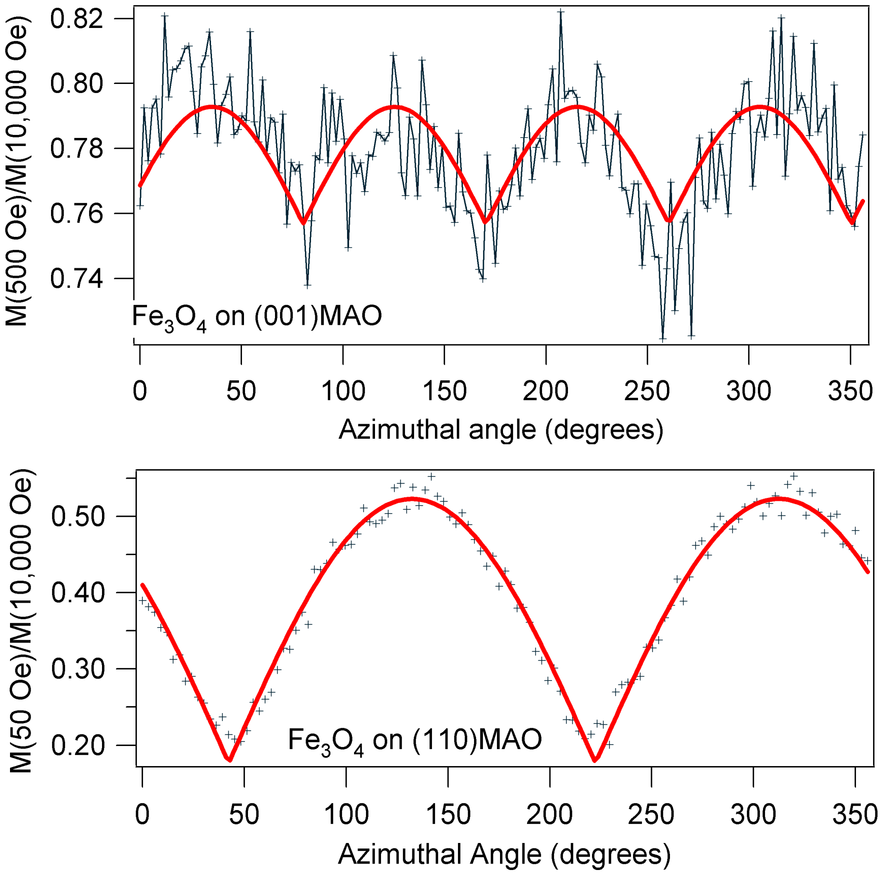

Figure 2.11 – VSM angular scans for a (001) Fe_3O_4 film (top) and a (110)Fe_3O_4 film (bottom). The solid lines are guides for the eye.

The relative strengths of the terms in the above equation dictate the film anisotropy. In the case of Figure 2.11, the film is under small compressive strain, but the K_n constants are such that when energy is minimized, the <100> directions are magnetically easy (i.*e.* retains the highest magnetization when the applied magnetic field is reduced or removed). The magnitude of the film moment at low applied fields when normalized by the value of a nominally saturated state (at H= 10,000 Oe) follows a $\cos^2\theta$ dependence revealing a two-fold symmetry for the (110) oriented film and a four-fold symmetry for the (001) oriented film. While shape anisotropy can be an important contribution to the total anisotropy energy in complex oxide nanostructures,[44] in this work it will be the magnetoelastic and magnetocrystalline anisotropies that will be examined through epitaxial strain and film orientation, respectively.

2.6 Rutherford Backscattering Spectroscopy

Rutherford backscattering spectrometry (RBS) uses a stream of high-energy ionized He particles to probe thin film composition and thickness.[45] He ions are accelerated to MeV energies in a van de Graaf generator for example, and then impinge on a sample with beam area approximately 1x3 mm in area. The effective probe depth for this technique is of order 1-2 microns. While most He particles interact with electrons in the material of interest, some He are elastically scattered backwards by ion cores in the material. A simple point mass model may be used to compute the ion core mass and thus elemental composition from the measured backscattered He yield. Thus a backscattered energy versus He yield graph can be modeled computationally with both thickness and elemental information. In other words, the model contains a quantitative number of scatters from the sample as a function of depth, and this can be converted to a thickness by assuming a material atomic density known from its crystal structure. For heavy ions this simple two-mass model works well, but the accuracy of RBS for quantitative analysis decreases for light elements such as O. There are similar techniques such as oxygen-resonance RBS or nuclear-reaction analysis, but RBS is well-suited to study the 3d transition metal elements in thin film form.

2.7 Soft X-ray Absorption

Soft X-ray absorption spectroscopy allows for unambiguous determination of magnetic species within a multi-element sample as well as elucidating chemical state such as valence or site symmetry.[46-50] Due to strong absorption resonances near the *2p* to *3d*, *1s* to *2p*, and *3d* to *4f* transitions, soft X-rays are ideal chemical probes for *3d* transition metals, biological samples, and rare earth-containing materials. In addition, the nature of the dipole selection rules (preventing a spin flip event in absorption) yields sensitivity to bands in magnetic materials split by Zeeman energy. Thus, by using polarized X-rays of opposing helicity or by reversing the magnetization of the sample, a differential absorption or dichroism may be obtained (Figure 2.12).[51]

While the photoelectrons produced from X-ray absorption are not directly captured as in photoemission experiments, the excited electrons decay through both elastic and inelastic processes, and the total electron yield is proportional to the X-ray absorption cross-section.[52] In thin film samples this assumption may not hold, but a discussion of such effects will be introduced in chapter 6. The sample is grounded through a picoammeter, and with the brightness of modern light sources even a monochromated X-ray beam with high circular polarization from a bending magnet may still produce nanoamperes of current at elemental absorption resonances.

Insertion devices can obtain even higher brightness in the soft X-ray range compared to bending magnet radiation.[53, 54] While a comparison of wiggler and undulators is beyond the scope of this work, undulators such as the Apple-II type elliptically polarizing undulator at beamline 4.0.2 of the Advanced Light Source may produce almost arbitrary X-ray polarization at high photon flux.

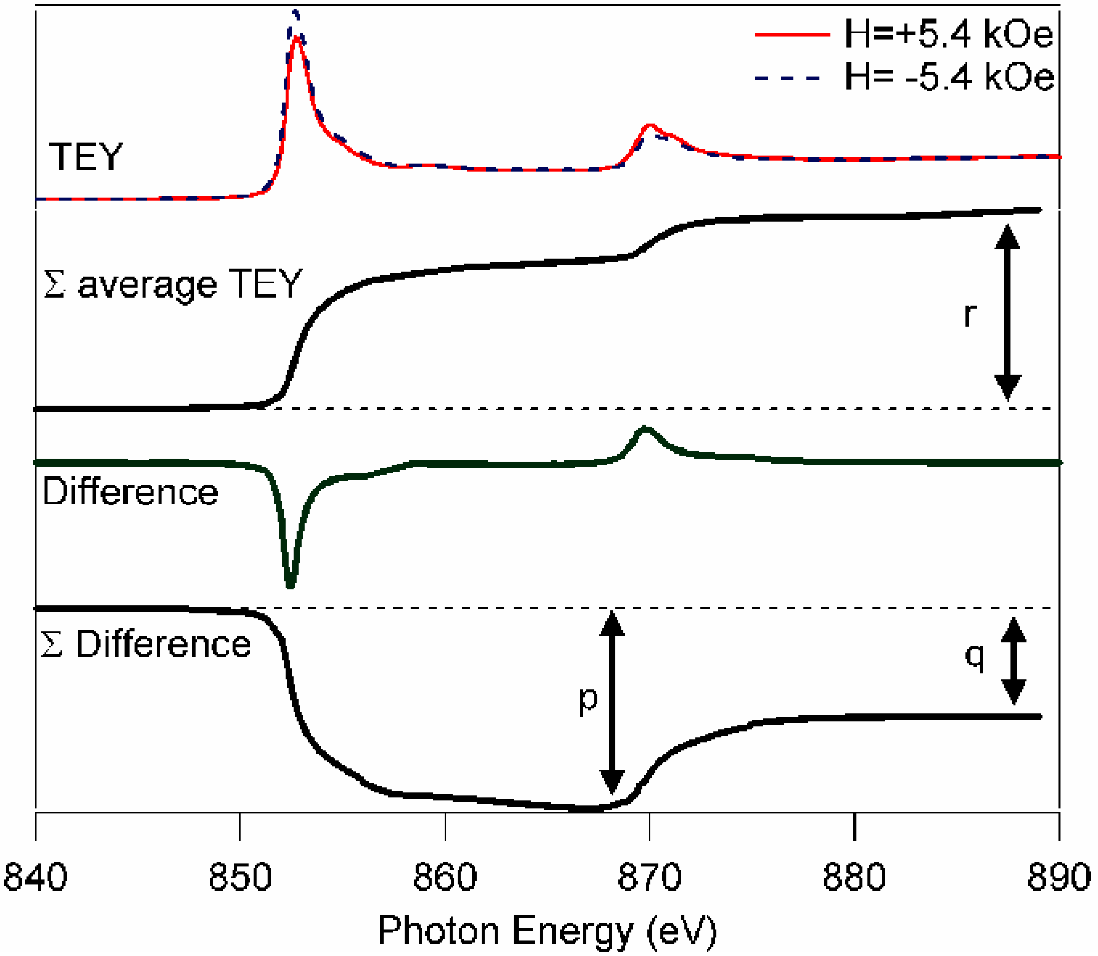

Figure 2.12 – Typical soft X-ray absorption spectra for Ni $L_{3,2}$ edge of a NiCr thin film in the presence of a magnetic field with summed intensity for the average and the difference of the spectra.

In addition to the circular dichroism observed in ferromagnetic materials, a linear dichroism effect may also be observed in materials with orbital or magnetic anisotropy.[55-57] If we assume the *3d* orbitals have low symmetry, then the electric field of the incident X-rays can be oriented along different symmetry directions, and a dichroism may thus be observed. In practice, one could hold the X-ray polarization fixed while rotating the sample in-plane, or by angling the sample normal along versus oblique to the incoming beam direction. In the case of a polycrystalline un-magnetized sample one may see almost no linear dichroism due to the averaging of the absorption anisotropy over the macroscopic sample dimensions, but in a highly strained epitaxial film or saturated ferromagnet one will see a strong dichroism along or orthogonal to the direction of orbital or spin alignment.

Ferromagnetic materials show circular dichroism, but many materials such as ferroelectrics, antiferromagnets, and ferrimagnets can show a linear dichroism effect due to the anisotropic orbital structure in those materials. Integration of the experimental data as shown in Figure 2.12 can be related to physical quantities such as orbital and spin moment per element through theoretical sum rules.[58] Such sum rules have been applicable both for *3d* transition elements both in transmission geometry as well as in electron yield mode.[59]

A spatially resolved technique related to soft X-ray absorption spectroscopy is X-ray photoemission electron microscopy (PEEM).[60] As in XAS, incident X-rays are absorbed and create core holes, which then produces secondary electrons with energies above the work function of the illuminated sample. The sample is biased by at least 10kV and the secondary electrons escape into the vacuum and are accelerated by electrostatic lenses which focus them onto a charge-coupled device. By scanning photon energy, spatially-resolved absorption spectra may be taken. If the XMCD or XMLD spectrum has been previously measured, images may be taken at maxima or minima of the dichroism spectrum, and after division of the images one obtains a domain map of the material. This is applicable both for ferromagnetic materials by using circularly polarized X-rays, and for antiferromagnetic or ferroelectric materials by using linearly polarized light. Since an *in-situ* magnetic field would influence the electrostatic lenses, dichroism spectra may be recorded by changing X-ray polarization angle or helicity in lieu of reversing the magnetization.

2.8 Magnetotransport

In order to measure transport properties of materials, there are a variety of measurement geometries. Perhaps the simplest to visualize is the two-point method: using a bulk three-dimensional sample, electrodes are placed on opposite sides of the sample and either a constant current or a constant voltage is held across the electrodes. For the constant current method, a voltmeter is placed in parallel with the electrodes and assuming the meter internal impedance is much higher than the sample resistance, the resistance is $R_{sample}=V_{measured}/I_{applied}$. For the constant voltage method, an ammeter is placed in series with the sample of interest, and assuming the meter impedance is vanishingly small when compared to the sample resistance, the resistance is $R_{sample} = V_{applied}/I_{measured}$. From either measurement, one may calculate $\rho=Rwt/l$, with ρ as resistivity, and (l w, t) as the respective dimension length, width, and thickness, and current is oriented along the length dimension. Both two-point measurements also assume that the lead resistance, electrode resistance, and the contact resistance are all negligible.

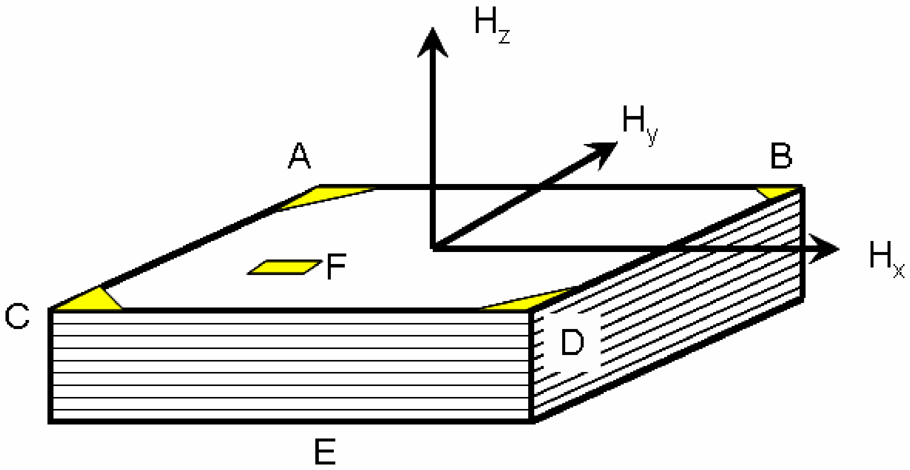

Figure 2.13 – Sample geometry for transport measurement of unpatterned films in the van der Pauw configuration.

For transition metal oxide thin films, such assumptions are poor and thus alternate measurement methods must be taken. For instance, sputtered AuPd contacts shadow-masked onto oxide films can greatly reduce the contact resistance. Another method is to use a remote-sensing configuration with the addition of two extra leads. The four point method allows for determination of thin film resistivity and not only resistance if the geometry between the electrode contact points is known. This obviates the need for detailed knowledge of the sample *geometry*, and only requires sample *thickness* to get a material property (resistivity) from the measured resistance.

A method to measure both the sample resistivity and Hall coefficient is through the van der Pauw (VDP) electrode configuration.[61] Instead of having four identically spaced contacts near the center of the sample as is common for the four point method, the VDP configuration requires contacts at the four corners of a rectangular sample as shown in Figure 2.13 and Table 2.1. In the following discussion we will limit ourselves to thin films such that the thickness is much smaller than the sample length or width. Further modifications to the VDP method can generalize the thin-film measurement to a six point geometry but is beyond the scope of this work.

Table 2.1 – Contact configurations for the transport measurements in this work.

Name	**Type**	**Magnetic Field**	**Current**	**Voltage**
R_{Hall_1}	4 point	H_x, H_z	AD	CB
R_{Hall_2}	4 point	H_x,H_z	CB	DA
R_{vdp_1}	4 point	H_x, H_y, H_z	AB	CD
R_{vdp_2}	4 point	H_x, H_y, H_z	BD	AC
R_{cap}	2 point	H_x, H_z	EF	EF
R_{jcn_2}	2 point	H_x, H_y, H_z	GJ	GJ
R_{jcn_4}	4 point	H_x, H_y, H_z	GI	KJ

The VDP configuration requires two measurements to fully determine sheet resistance assuming an isotropic conductivity tensor, and a further two measurements to determine the Hall coefficient. The sheet resistance may be related to the measured quantities R_{vdp_1} and R_{vdp_2}:

$$\exp(-\pi R_{vdp\_1} / R_s) + \exp(-\pi R_{vdp\_2} / R_s) = 1 \qquad \text{(Eqn 2.3)}$$

Also, the Hall coefficient and mobility may be calculated if we assume a simple one-carrier model:[62]

$$R_{Hall} = t\left(R_{Hall\_1} - R_{Hall\_2}\right)/2H \qquad \text{(Eqn 2.4)}$$

$$\mu_{Hall} = R_{Hall}/\rho \qquad \text{(Eqn 2.5)}$$

The product of sheet resistance and film thickness is the material resistivity ($\rho = R_s\, t$). One assumption for this method is that the sample has a uniform thickness, but sample geometry is unrestricted aside from that. However, practical measurement considerations require that the sample is roughly square, as a large aspect ratio between length and width will necessitate large currents to obtain low-noise resistance measurements. Anisotropy in the conductivity tensor, such as when a magnetic field is applied in the plane of the sample and breaks the cubic symmetry of the sample, may be accounted for using the so-called Montgomery method of resistivity.[63] No additional transport measurements are necessary for this measurement, but instead the real dimensions of the anisotropic material are mapped to elongated dimensions of a correspondingly isotropic material.

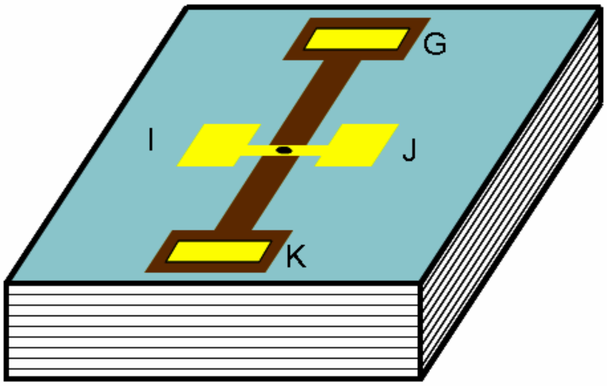

Figure 2.14 – Schematic of a patterned trilayer film for junction measurements.

In this work, as-grown single layer films with small AuPd contacts at the four corners are used in the VDP geometry to measure resistivity. A magnetic field is applied either out of the plane of the sample (H_z) or along either of the in-plane axes.

On the other hand, for pattered junctions, field is scanned azimuthally in-plane only. Junctions are fabricated from thin film trilayers into thin strips to isolate sets of junctions. While previous work fabricated 8 junctions per wafer, in the newer process ten sets of five junctions can be fabricated on a single 6x6 mm wafer. The process flow for such junction fabrication can be found elsewhere.[64] Contact resistance is negligible for the junctions due to Au pads for both the LSMO and Fe_3O_4 electrodes, and for temperatures between 100 K and 300 K, the oxide electrode resistance is much smaller than the resistance through the barrier layer.

2.9 A word about substrates

Table 2.2 lists typical substrates used in this work as well as some structural parameters, and pseudocubic parameters are listed in square brackets.[42, 65, 66] Most substrates have extremely high melting temperatures and thus are quite stable at the growth temperatures of interest (400-700 °C). However, diffusion of light elements such as O or Mg can pose a problem in maintaining proper stoichiometry of the film. For instance, removal of oxygen from the $SrTiO_3$ host lattice increases the conductivity by orders of magnitude and can even sustain a superconductive phase below 1K if the carrier concentration is high enough.

While MgO is a very close lattice match to spinel oxides such as Fe_3O_4 (a=8.39 Å), the combination of perovskite and spinel multilayers has been explored by first growing high-quality single-layer spinel films on perovskite substrates, then by growing initial perovskite layers followed by a spinel capping layer.

Scandate perovskite structure substrates match the large lattice parameters of $SrRuO_3$ or the spinel oxides more closely than LAO or STO, but care must be taken in evaluating the properties of films on such substrates. The rare earths present in the scandates yield large paramagnetic moments which can be comparable or even larger than even a 100 nm thick film's moment. On the other hand, even a miniscule percentage of iron impurity in a $MgAl_2O_4$ substrate can yield a room temperature moment of 10^{-6} emu which can obscure or offset low temperature characterization of ultrathin films. Ideally, one takes high-field magnetization data at high temperatures for every sample under study to measure both the linear background of the substrate as well as to evaluate any room-temperature ferromagnetic impurities embedded in the substrate or introduced from processing or handling.

Table 2.2 – Various single crystal substrate materials used in this work.

Substrate Material	**Structure at 25 °C**	**Melting Temp (°C)**	**Growth method**	**Lattice Parameters (Å) at T=300 K**
$BaTiO_3$	Tetragonal perovskite	1600 °C	Top seeded solution growth	3.994, 3.994, 4.038
$DyScO_3$	Orthorhombic perovskite	2130 °C	Czochralski	5.44, 5.713, 7.887 [3.944]
$GdScO_3$	Orthorhombic perovskite	2130 °C	Czochralski	5.488, 5.746, 7.934 [3.97]
$LaAlO_3$	Rhombohedral perovskite	1810 °C	Czochralski	3.793
LSAT	Pseudocubic perovskite	1840 °C	Czochralski	3.865
$MgAl_2O_4$	Cubic spinel	2130 °C	Czochralski	8.0831
MgO	Cubic rocksalt	2852 °C	Arc melting	4.2112
$SrTiO_3$	Cubic perovskite	2080 °C	Verneuil	3.905

Proper surface treatment is essential to promote layer-by-layer growth of transition metal oxides, and atomically flat TiO_2-terminated STO terraces have been produced using a multi-step etch and anneal process.[67] Soaking STO or LAO substrates in deionized water for 10 minutes followed by a 50:1 buffered hydrofluoric acid etch for 1 minute yields atomically abrupt surfaces, and an anneal step at 1000 °C for 2-6 hours creates sharp terrace features as shown in Figure 2.4 if the step width is less than 250 nm. Such anneal recipes may also be found for MgO substrates, but single-termination of $MgAl_2O_4$ substrates is more elusive. Although as-received substrates can promote the growth of single orientation single phase perovskites and spinels on a variety of substrates, the growth mechanisms and resulting microstructure of thin film samples can have a great impact on the measured film properties.

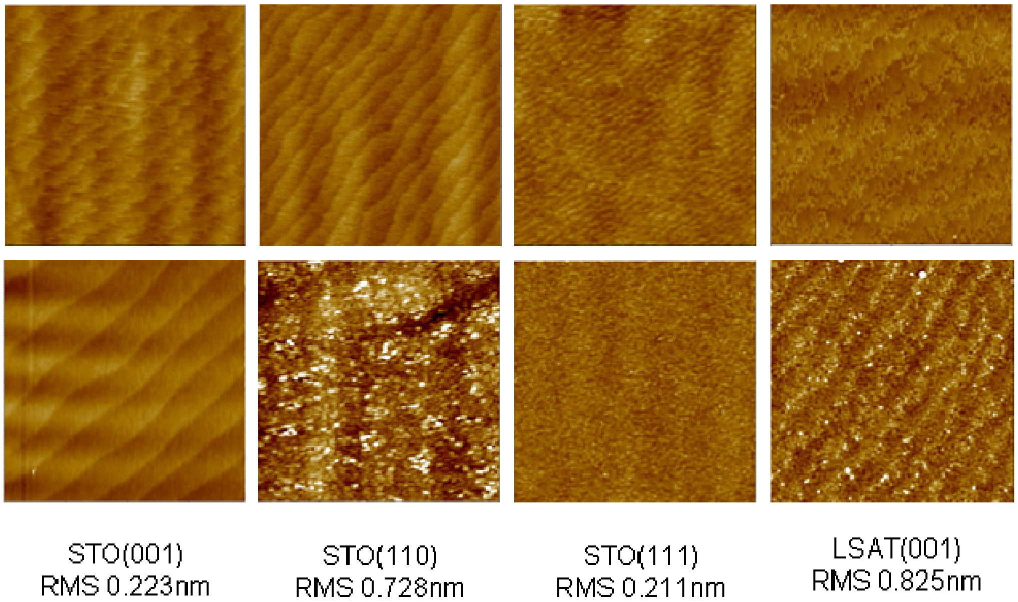
STO(001)
RMS 0.223nm

STO(110)
RMS 0.728nm

STO(111)
RMS 0.211nm

LSAT(001)
RMS 0.825nm

Figure 2.15 – Prepared STO and LSAT substrates (top row) showing sharp terraces, and ~40nm LSMO films grown on the prepared substrates (bottom row). Film RMS surface roughness is indicated at the bottom of each sample.

Note that such an etch and anneal step is beneficial for creation of well defined terrace structures or surface terminations on substrate orientations other than (001) orientations as shown in Figure 2.15,[68, 69] and were used extensively in chapter 6. In addition, substrates such as LSAT or LAO may also have temperature or chemically sensitive surface terminations that may aid in achieving layer-by-layer epitaxial growth modes.[70]

CHAPTER 3:

FERROMAGNETIC METALLIC $SrRuO_3$ THIN FILMS

3.1 Abstract

In this study I explore the influence of disorder on the properties of 3-180 nm thick epitaxial $SrRuO_3$ films. Disorder includes interface effects from misfit strain and bulk effects from cation substitutions and interstitial defects. Isostructural perovskites, including $LaAlO_3$, $SrTiO_3$, $DyScO_3$, $GdScO_3$, and $BaTiO_3$ were used as growth platforms to place films under either biaxial tensile or compressive strain. In addition, films on (001)$SrTiO_3$ were co-deposited with FeO_x, CoO, $SrTiO_3$ and $SrFeO_x$ of concentrations up to 10 % to compare the influence of disorder distributed throughout the film to disorder confined to surfaces and interfaces. Pure $SrRuO_3$ films exhibited metallic behavior with low residual resistivity (<0.1 mΩ-cm), and underwent a ferromagnetic transition at a suppressed Curie temperature (T_c) of 145 K. Films with low substrate lattice mismatch had atomically smooth surfaces, whereas highly mismatched film growth was dominated by island formation. The addition of impurity oxides raised the film residual resistivity and also affected low-temperature magnetotransport. Interface effects did not seem to play a dominant role in carrier localization, but a few percent of oxide impurities increased the low temperature resistivity by an order of magnitude. Higher concentrations pushed the resistivity minimum to temperatures comparable to T_c.

3.2 Introduction

The increased interest in applications of epitaxial thin film oxide multilayers and heterostructures has prompted the use of conductive oxides such as $SrRuO_3$ (SRO) as contact material to other functional oxides. On the other hand, from a basic physics standpoint, SRO is a novel material in its own right – a *4d* correlated ferromagnetic oxide[71] related to materials such as the superconductor Sr_2RuO_4. In recent years, epitaxial complex oxide thin films and heterostructures (e.g. manganites,[72] cuprates,[73] titanates,[74] ferrites,[75] and ruthenates[76]) have been successfully grown by various deposition techniques on a range of single-crystalline substrates to study the impact of strain and microstructure on fundamental properties and device behavior. In this chapter I will use the SRO material system to explore strain and microstructural effects, and in the next chapter a spinel metallic oxide $LiTi_2O_4$ will be explored to compare and contrast such effects in the more complex spinel crystal structure.

One must keep in mind that even thin films that have high structural quality, low residual resistivity and bulk-like magnetism[5, 7, 76-79] can show behavior not seen in single crystals. An example of such behavior is the low-temperature resistivity upturn seen in thin films of SRO grown by sputtering, pulsed laser deposition, and laser molecular beam epitaxy. This upturn is reminiscent of a Kondo minimum and has been attributed to carrier localization induced by cation disorder in the thin film not present in single crystals. In addition, substitution on the Ru site[71, 80, 81] and oxygen stoichiometry at grain boundaries[80] can give semiconducting character to this nominally metallic oxide.

The goal of this chapter is to examine the role of various forms of disorder in ultrathin SRO films to determine their impact on film properties such as transport and magnetization. As a first step I examined film properties as a function of film thickness ranging from a few monolayers to 180 nm on (001) STO substrates. Secondly, to separate the influence of chemical disorder from strain and microstructural effects, I intentionally added impurity oxides of order 10 % to the SRO host matrix. Finally, a number of oxide substrates were used to place SRO films of a given thickness under biaxial tensile or compressive strain. The structure and properties of these SRO films were compared to determine the effects of cation, interface and microstructural disorder.

3.3 Experimental Methods

Epitaxial SRO films of thickness 3-180 nm were grown by pulsed laser deposition on single-crystalline substrates of (001) STO, LAO, LSAT, BTO, $MgAl_2O_4$ and MgO, as well as (110) $DyScO_3$ and $GdScO_3$. SRO has a distorted perovskite structure ($GdFeO_3$-type) and the films under study are all oriented with the pseudocubic (001) direction out of plane. A 248 nm KrF excimer laser at an energy density of 1-2 J/cm^2 and repetition rate of 1-3 Hz ablated stoichiometric pressed powder targets of SRO, CoO, FeO_x, $SrFeO_x$, and STO in an oxygen atmosphere of 100 mTorr. In some cases, after calibrating deposition rates for the various oxides, impurity oxides were ablated after every half-monolayer of SRO to obtain concentrations of up to 10 % in the host SRO film. Substrates were kept at 750 °C during the deposition process, and were annealed in 300 Torr oxygen for 15 minutes before cooling in oxygen ambient in order to ensure good crystallinity and stoichiometric oxygen content.

Surface morphology was studied by atomic force microscopy (AFM) on lateral scales from 1-25 microns. Crystallinity and strain state were assessed by X-ray diffraction (XRD) analysis. Rutherford backscattering spectrometry (RBS) confirmed stoichiometry of the films as well as film thickness. Magnetization of the films was measured by SQUID magnetometry and magnetotransport was measured in the van der Pauw geometry. Ohmic AuPd contacts were shadow-masked on as-deposited films, and Al wires were ultrasonically bonded to the contacts for transport measurements. If not specified otherwise, the direction of applied magnetic field was out of the plane of the film during the measurement.

3.4 Structural Characterization

Films of SRO on STO are under 0.5% compressive strain, and this low lattice mismatch allowed for 2D-like growth. Root-mean-square roughness (R_{RMS}) of a 178 nm film of SRO on STO (Figure 3.1(a)) was of order the pseudocubic unit cell (R_{RMS}=0.324nm), and terraces due to the <0.5° miscut of the STO substrate were clearly seen at the surface of the film. In addition, screw dislocations at the substrate–film interface promoted spiral-island merging of the SRO film terraces as seen in Figure 3.1 (a). Films grown on high-quality substrates (Crystec GmbH) treated with a buffered hydrofluoric acid (BHF) etch before deposition have clearly defined, straight terraces with few spiral islands.

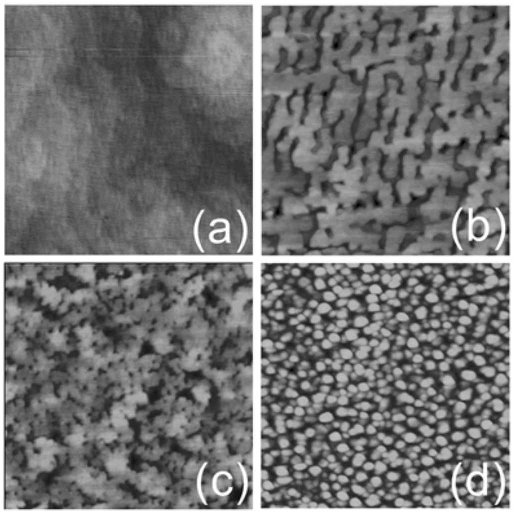

Figure 3.1 – 1x1 micron area AFM scans of SRO films: (a) 178 nm SRO/$SrTiO_3$, R_{RMS} = 0.3 nm; (b) 10 nm SRO/$LaAlO_3$, R_{RMS} = 1.9 nm; (c) 10 nm SRO/$DyScO_3$, R_{RMS} = 1.3 nm; (d) 10 nm SRO/$BaTiO_3$, R_{RMS} = 4.1 nm.

RBS analysis confirms the Sr:Ru ratio was 1:1 to within the 5% accuracy of the measurement (Figure 3.2). Ion channeling data indicated that films were highly crystalline with χ_{min} (the ratio of the backscattered yield of channeled beam to beam at random incidence) of <10% for a 70 nm film on STO. The low percentage of impurity oxide was not measurable by RBS. However, commercial X-ray photoelectron spectroscopy (Evans Analytical Group) with modeling and X-ray absorption spectroscopy at the Lawrence Berkeley National Laboratory Advanced Light Source indicate the presence of impurity oxides in the SRO films. As both techniques are surface-sensitive, I will use the deposition parameters as a basis for the amount of impurity oxide and assume a uniform amount of impurity as a function of thickness.

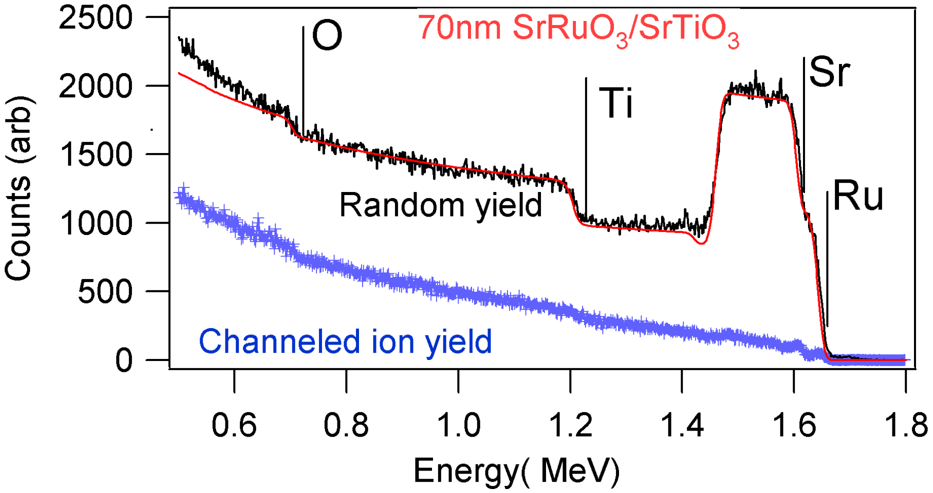

Figure 3.2 – RBS spectra of a 70 nm SRO film on (001)STO. The low density of defects and good crystallinity of the film result in a small channeled yield, with the ratio between the channeled and random yield at the Ru edge of approximately 10 %.

3.5 Magnetic properties

Magnetization measurements on a range of SRO film thicknesses (20-100 nm) indicated that T_c for the films was suppressed from the bulk value of 165 K to 145 K as measured by the Arrott plot method.[82] An example of such a measurement is shown in Figure 3.3 for a film on (001)MgO. The squared magnetization of the film is examined as a function of scaled applied magnetic field around the ferromagnetic transition temperature. If the magnetization is linear in applied magnetic field H as expected from a paramagnet, diamagnet, or antiferromagnet, then there is no net magnetization at H=0 Oe. However, if there is spontaneous magnetization as in a ferromagnet or ferrimagnet, then the intercept will be greater than zero and the magnetization will be nonlinear with applied field. By extracting the intercept as a function of temperature (Figure 3.4) and examining where the intercept becomes zero, one may obtain the Curie temperature. For the film in Figure 3.3 and 3.4 this corresponds to a temperature of 156.5 K.

While Ru or O deficient single crystals[80] have shown reduced T_c, stoichiometric thin films have been reported as having similar suppression in the range of 140-150K.[7, 76, 78, 79] At 5K, hysteresis loops had a saturation magnetization of ~1.6 μ_B per Ru site, comparable to magnetization in other studies of SRO films[5, 79].

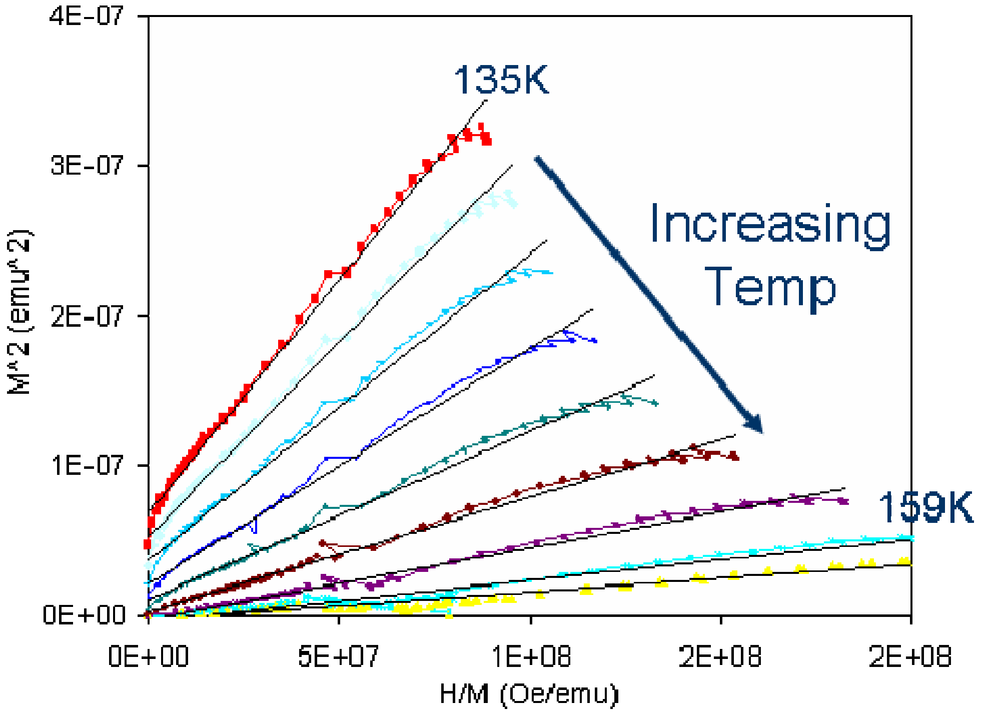

Figure 3.3 – Arrott plot of an SRO film on (001)MgO around the ferromagnetic transition temperature.

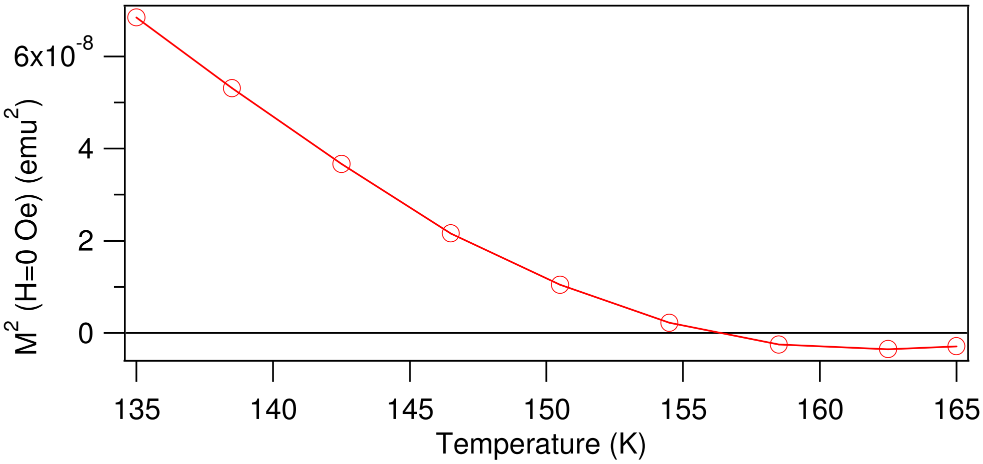

Figure 3.4 – Zero-field intercepts as a function of temperature extracted from an Arrott plot for a SRO/MgO film.

3.6 Transport properties

There is a resistivity anomaly proportional to the magnetization and a corresponding decrease in resistivity below the Curie temperature as shown in Figure 3.5. One may consider the origin of this anomaly as the suppression of spin-dependent scattering in ferromagnetic metals such as Ni or SRO. Above the Curie temperature there is thermally activated random fluctuation of the moments, but below the Curie temperature this fluctuation is suppressed due to the strong exchange between neighboring moments and resulting ferromagnetic order. The reduction of this fluctuation acts to reduce carrier scattering and thus reduces resistivity of the material. The vertical line delineates the Curie temperature measured from Figure 3.4. Thus, the change in slope of the film resistance can be used as another measure of the ferromagnetic transition temperature.

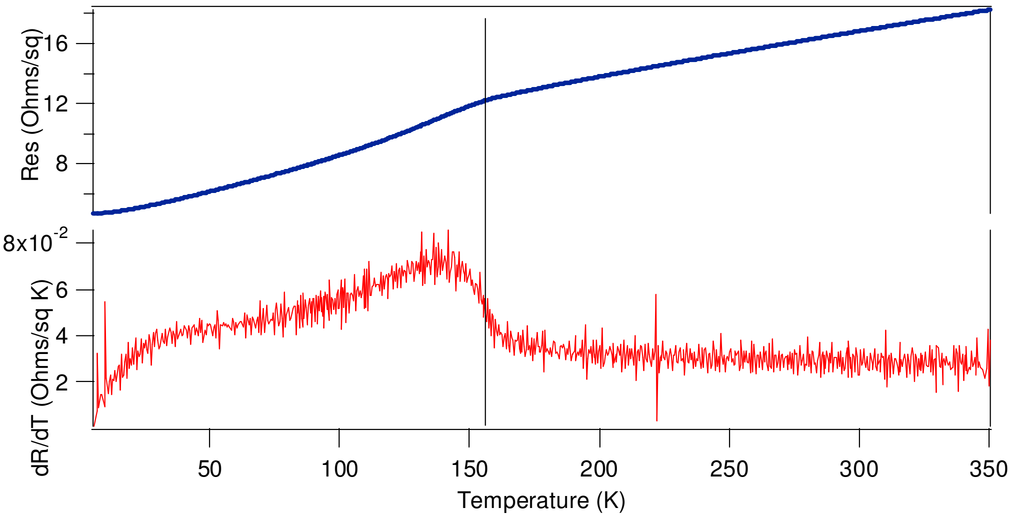

Figure 3.5 – Sheet resistance and derivative of resistance as a function of temperature for a SRO film on (001)MgO.

The ferromagnetic transition temperature also matches the peak in magnetoresistance as calculated from the difference between resistance in zero-field and field applied out of the plane of the film (Figure 3.6). I define the magnetoresistance as:

$$MR(H,T) = (\rho(H,T) - \rho(0,T)) / \rho(0,T) \qquad \text{(Eqn 3.1)}$$

with the difference in resistivity normalized by the zero field resistivity. Note that since sheet resistance $R_s=\rho/t$, the thickness drops out of equation 3.1 if a $\rho= R_s\, t$ substitution is made. Thus, MR can be calculated from the field-dependent van der Pauw sheet resistance directly instead of first calculating the resistivity. Figure 3.6 demonstrates that a small applied field yields a much sharper peak in magnetoresistance at the expense of a much smaller magnitude of the peak. For the case of conductive films, a lock-in amplifier technique was used to ensure a large signal-to-noise ratio in the measured resistance and thus decrease any noise in the calculated quantities such as the MR or the derivative of resistance.

For SRO films of varying thickness grown on STO substrates, zero-field resistivity curves as a function of temperature (Figure 3.7) had similar temperature dependence. High-temperature linear behavior in the paramagnetic regime deviated near the ferromagnetic transition temperature, and at close to 10K the resistivity followed a quadratic dependence. A kink in the curve coincident with the ferromagnetic transition occurred at 145K.

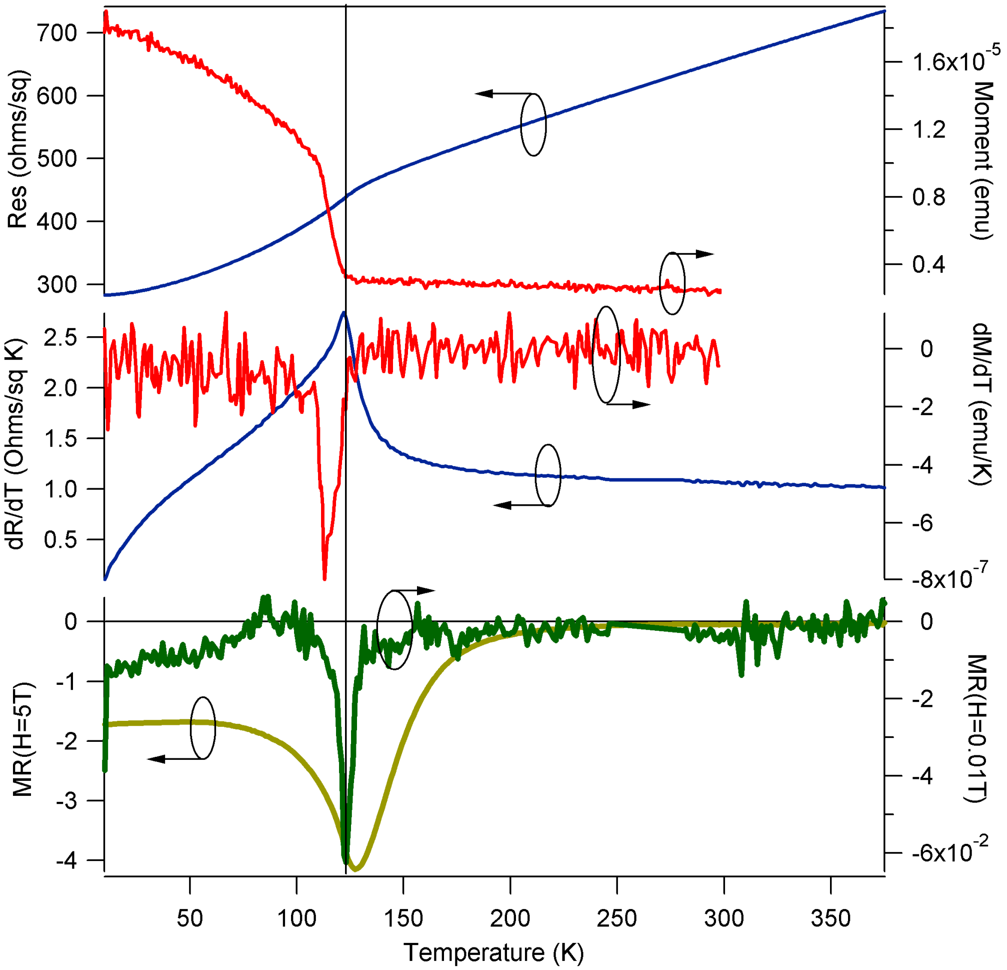

Figure 3.6 – Sheet resistance, magnetic moment, derivatives, and percent MR as a function of temperature for a 7 nm 5 % FeO$_x$:SRO film on (001)STO.

Surface treatment of the STO substrate with BHF etching as mentioned in Chapter 2 reduced interface disorder and thus the residual resistivity. A 3 nm film on a treated substrate had the same residual resistivity as a 6 nm film on an untreated substrate. Misfit dislocations can affect the residual resistivity (vertical shift of the resistivity curve) for ultrathin films, but surface treatment of STO substrates reduced this value for thicker films as well (Figure 3.7, inset). When normalized to resistivity at 380 K, the paramagnetic portions of the curves had similar slopes, but the zero-temperature intercept shifted higher with decreasing thickness. In addition, the slopes of the curves converged to zero in the low temperature regime, and no upturn in resistivity was noted. While ultrathin films remained fully elastically strained to the STO, films thicker than the Matthews-Blakeslee critical thickness of 8.3 nm[83] formed misfit dislocations which acted to reduce the film strain. Such deformation allows distorted Ru-O-Ru bonds to relax to bulk-like angles, and the thickness dependence of the normalized zero-temperature resistivity was consistent with this relaxation.

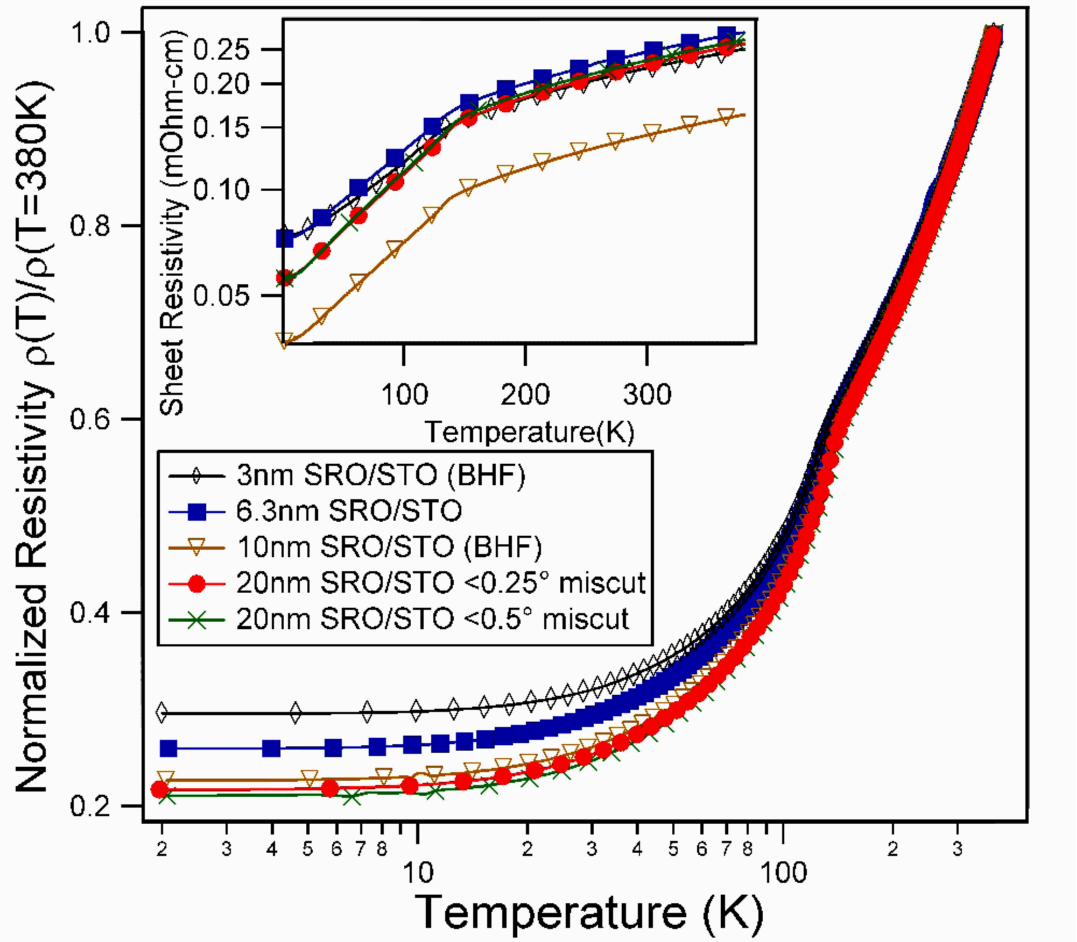

Figure 3.7– Resistivity vs. temperature scans for SRO films (3-20nm thick) deposited on $SrTiO_3$ *substrates, normalized to resistance at 380K. BHF indicates the substrate was etched in dilute buffered hydrofluoric acid solution before deposition. STO#1 and #2 were substrates provided by different manufacturers. Inset: resistivity vs. temperature for above films.*

Studies on single crystals and films[80, 81] indicated that SRO resistivity has a strong dependence on Ru-site substitution. For a fixed thickness of 5 nm, various impurity oxides were co-deposited during film growth (Figure 3.8). Sequential laser pulses ablated from SRO and impurity oxide targets during deposition, and the interspersed material was annealed *in-situ*. The amount of impurity acted to increase the residual resistivity, and the shape of the resistivity curve changed dramatically as well. The slope of the linear paramagnetic regime was reduced upon the addition of CoO, FeO_x, $SrFeO_x$, and $SrTiO_3$ to the SRO host.

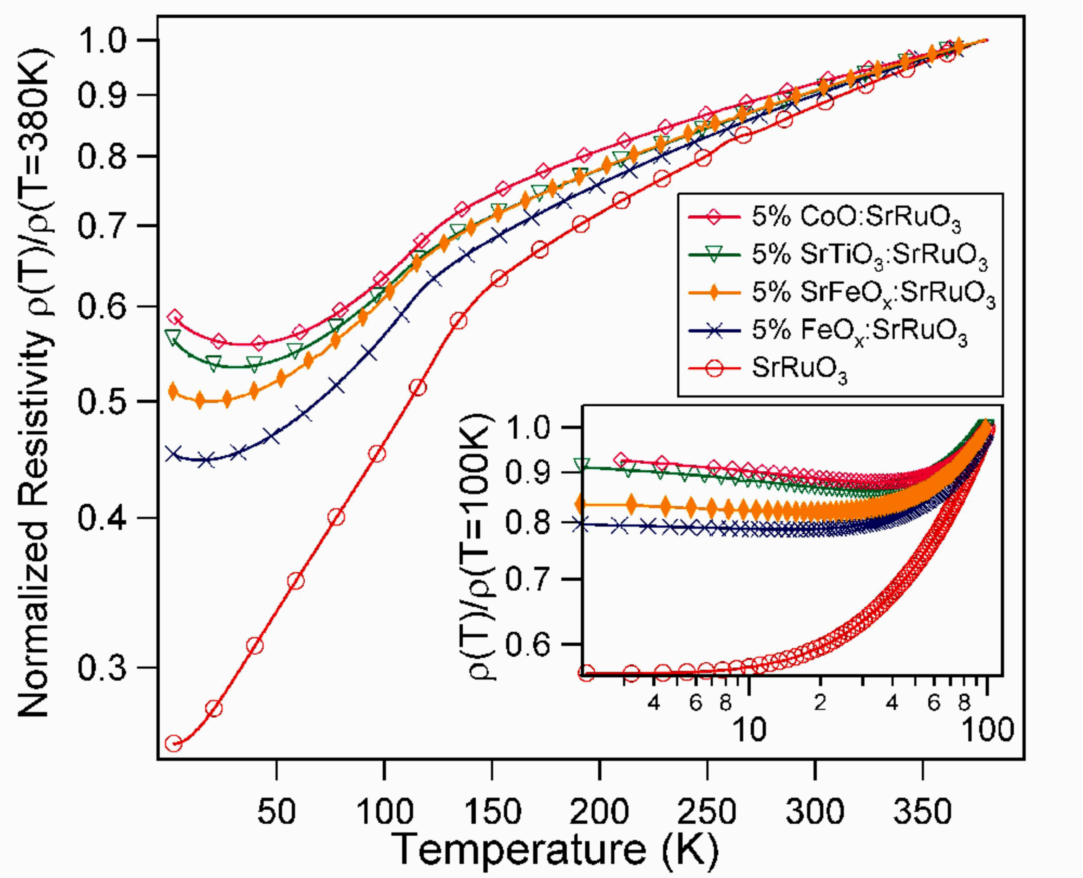

Figure 3.8 - Normalized resistivity vs. temperature scans for 5 nm SRO films on $SrTiO_3$ substrates co-deposited with 5 % impurity oxides. Inset: resistivity normalized to 100 K to emphasize low-temperature behavior.

A minimum in the resistivity was observed for films regardless of impurity type; however, the temperature at which the minimum occurred has a strong dependence on the amount of impurity as well as the thickness of the film. In contrast to the 5 nm films in Figure 3.8, a film with 5 % FeO_x but thickness increased to 10 nm had a $\rho(T=0\ K)/\rho(T=380\ K)$=0.38 with no upturn. On the other hand, a 5 nm film with STO impurity increased to 10 % had a minimum at 130 K and a normalized $\rho(T=0\ K)/\rho(T=380\ K)$=1.84. The disorder induced from strain alone can change the residual resistivity, but the presence of cation disorder distributed throughout the film strongly localized carriers in the SRO host film.

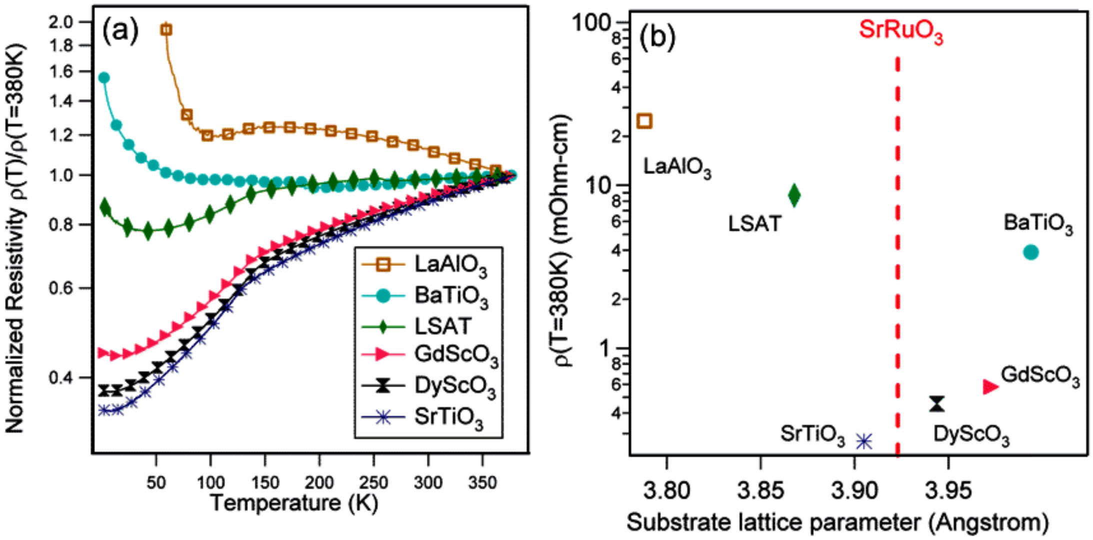

Figure 3.9 –(a) Normalized resistivity vs. temperature for 5 nm SRO films with 5 % FeO_x impurity on various substrates. (b) Resistivity at T=380 K as a function of pseudocubic lattice parameter of the substrate. The SRO pseudocubic lattice parameter is 3.923 Å.

To probe the influence of misfit dislocations on ultrathin films of a given thickness, I grew SRO with 5 % FeO_x impurity on a range of substrates. Relaxation of epitaxial misfit strain in 100 nm thick films was seen for all substrates but STO, $DyScO_3$, and $GdScO_3$. Transport properties were qualitatively similar to thick films on STO substrates. However, thinner films show drastically different morphologies (Figure 3.1b-d) and resistivity behavior (Figure 3.9). Surface roughness was increased for ultrathin films on scandate substrates (Figure 3.1c) as compared to STO films, but films were still metallic with relatively low residual resistivity. On the other hand, morphology of films on LAO and BTO indicated that the large lattice parameter mismatch promoted 3D island growth. The twinned surface of LAO served to form a 2D maze-like network of islands (Figure 3.1b), whereas islands on BTO were circular with 50 nm diameter (Figure 3.1d). While magnetization for these films was similar to films on STO, the differences in resistivity were much more pronounced. Semiconducting behavior from 2-380 K was observed for 5 nm films on LAO, BTO, $MgAl_2O_4$ and MgO, while thicker (10-20 nm) films had metallic behavior with resistivity upturns in the range of 50-100 K. Oxygen content at grain boundaries[80] can change resistivity dramatically in bulk samples, and in ultrathin films grain boundaries had an even larger impact. Resistivity for ultrathin films on LAO and BTO with small grains were orders of magnitude larger than films on STO or scandate substrates (Figure 3.9 (b)).

3.7 Conclusions

I have systematically varied strain and cation-induced disorder as well as microstructure in ultrathin SRO films. While magnetic properties were similar among the films, transport was a sensitive tool to measure the total amount of disorder in the film. Strain and accompanying misfit dislocations have influence on the magnitude of the resistivity, but it is the chemical disorder and microstructure that have the most profound effect on the shape of the temperature-dependent resistivity.

CHAPTER 4

SUPERCONDUCTING SPINEL $LiTi_2O_4$ THIN FILMS

4.1 Abstract

Epitaxial films of $LiTi_2O_4$ on single crystalline substrates of $MgAl_2O_4$, MgO, and $SrTiO_3$ provide model systems to systematically explore the effects of lattice strain and microstructural disorder on the superconducting state. Lattice strain that affects bandwidth gives rise to variations in the superconducting and normal state properties. Microstructural disorder such as antiphase boundaries that give rise to Ti network disorder reduce the critical temperature, and Ti network disorder combined with Mg interdiffusion lead to a much more dramatic effect on the superconducting state. Surface sensitive X-ray absorption spectroscopy has identified Ti to retain site symmetry and average valence of the bulk material regardless of film thickness.

4.2 Introduction

Spinel structure oxides offer a wealth of electronic and magnetic ground states across a broad range of temperatures. Spinel oxides with *3d* transition metals on the octahedral sites exhibit ferromagnetism, antiferromagnetism, charge ordering, and other types of magnetic and electronic ordering depending on the average valence of the cations. However, there is only one known oxide spinel superconductor to date, $LiTi_2O_4$ (LTO), with a superconducting phase that persists up to 13 K. Johnston *et al.* found superconductivity in LTO as the end member of a solid solution of spinel-structure $Li_{1+x}Ti_{2-x}O_4$ ($0 \leq x \leq 0.33$).[84, 85] In the Li spinels half-integral charge exists on each of the octahedral ions due to the monovalent nature of tetrahedrally coordinated

Li ions. Unlike the layered structure of superconducting cuprates, LTO has 3D connectivity of edge-sharing TiO_6 octahedra with average octahedral site valence of $d^{0.5}$ (equal amounts of Ti^{3+} and Ti^{4+}). Oxygen deficient $SrTiO_{3-\delta}$ and LTO both superconduct and both have mixed-valent Ti in octahedral coordination;[86] however, the Ti^{3+}/Ti^{4+} ratio is 1.0 in LTO while significantly more Ti^{4+} exists in $SrTiO_{3-\delta}$.

In bulk studies of primarily polycrystalline samples, there have been widely varying normal state and superconducting properties influenced by vacancies,[87] Li content, and Ti network disorder.[88, 89] Studies probing the effects of lattice strain on the superconductivity in bulk LTO have shown the application of hydrostatic pressure to increase the Debye temperature which in turn increases the critical temperature (T_{crit}) as predicted by Bardeen-Cooper-Schrieffer (BCS) theory. Such enhancement of T_{crit} has been observed in both Li deficient and stoichiometric LTO samples.[90, 91] There have been comparatively fewer bulk single crystal studies on LTO with systematic characterization of physical properties.

Epitaxial thin films of LTO are model systems for the systematic study of the role of lattice strain and microstructural disorder on superconducting properties. Epitaxial lattice strain gives rise to changes in the bandwidth that affect electron-electron correlations in many epitaxial thin film systems.[92-94] In addition, systematic variations in epitaxial film microstructural disorder may be obtained through the choice of substrate with lattice parameters which differ from the film lattice parameter due to changes in film growth mode or nucleation of dislocations and other defects.[95] Such variation in microstructure can shed light on the various scattering processes that may affect its superconducting properties. Finally, the choice of substrate orientation may provide insight into either intrinsic or strain-induced anisotropic film properties.[96, 97] However, to date epitaxial thin film growth has not been reported, although Inukai *et al.* have synthesized polycrystalline thin films.[98, 99]

By comparing the superconducting and normal state transport properties of LTO films on these three different substrates one can identify the role of lattice strain, Ti network disorder and stoichiometry on superconductivity. For example, misregistry and disorder at grain boundaries emerge in films grown on $SrTiO_3$ and MgO due to coalescence of spinel LTO grains that possess twice the unit cell dimension of the underlying substrate, and such defects are referred to as antiphase boundaries. Antiphase boundary disorder has been well-characterized in spinel films grown on MgO substrates via transmission electron microscopy analysis.[100, 101] These defects disrupt Ti-O-Ti octahedral bond ordering in an analogous manner to the disruption of Fe-O-Fe bond ordering in Fe_3O_4,[102, 103] and such Ti network disorder would influence carrier transport in LTO films. On the other hand, Mg interdiffusion combined with antiphase boundary-related Ti disorder has a much larger effect on both normal state and superconducting properties. Surface sensitive X-ray absorption spectroscopy (XAS) has identified Ti to retain site symmetry and average valence of the bulk material.

4.3 Experimental Methods

I have chosen to study epitaxial LTO films on MAO, MgO, and STO substrates. A previous report indicated that diffusion of Mg into LTO could suppress the superconducting phase,[104] and in this case the source of Mg would be interdiffusion from the underlying substrate at the film-substrate interface. STO substrates were used to confirm the trends found in studies on MAO substrates as independent of the presence of Mg. LTO films on MAO and STO show minimal interdiffusion at the film-substrate interface while there is significant Mg diffusion on MgO substrates. Furthermore, each of these substrates placed the film under differing amounts of lattice strain through epitaxy.

Nominally stoichiometric LTO material prepared by solid-state reaction yields a lattice parameter of 0.8405 nm by powder X-ray analysis.[17] Films on MgO (lattice constant a = 0.4211 nm, film-substrate mismatch f = +0.21 %) are under slight tension, while films on MAO (a = 0.8083 nm, f = -3.82 %) are under compressive strain. Since other spinels have been shown to grow epitaxially on perovskite-structure substrates,[105, 106] LTO films were also grown on perovskite STO (a = 0.3905 nm, f =-7.07 %). The perovskite substrate promoted the growth of the spinel superconducting phase in spite of the high compressive strain and anti-phase boundaries due to the unit cell of LTO being twice a perovskite unit cell.

Epitaxial thin films of the normal spinel structure oxide LTO were deposited via pulsed laser deposition on single crystalline (001) MgO, (001), (111) and (110)-oriented MAO, and TiO_2-terminated (001) and (110)-oriented STO with thickness ranging from 5 nm to 1 μm. In contrast to more equilibrium techniques such as evaporation, pulsed laser deposition can enable growth of phases not stable or difficult to grow in bulk form. Stability issues in air and the so-called 'aging effect' were seen in previous samples of stoichiometric LTO,[107, 108] thus the commercial target (Praxair Surface Technologies) was a mixture of the stable phases ramsdellite lithium titanium oxide (Li_2Ti_3O7)[109, 110] and rutile titanium oxide (TiO_2) to achieve a Li:Ti ratio of 1:2. Powder X-ray diffraction confirms the presence of these oxides in the target powder but no spinel-type phase reflections were found.

Substrate temperatures were held at 450-600 °C in a vacuum of better than $5x10^{-6}$ Torr to promote growth of the superconducting phase. Growth of films at elevated temperatures in 100 mTorr of pure oxygen or at 200 °C and below in vacuum yielded insulating films with no superconducting transition. Smooth films with low particulate density (less than 0.05 particles/μm^2) were produced with laser fluence of 1-2 J/cm^2 and a repetition rate of 3 Hz, resulting in a deposition rate of approximately

0.03 nm per pulse.

Rutherford Backscattering Spectrometry (RBS) was used to evaluate both film thickness and composition. However, quantitative analysis of low-Z ions such as Li and O is difficult, so only Ti atom density and uniformity were obtained using this technique. X-ray diffraction both in θ-2θ and 4-circle mode using Siemens D5000 diffractometers assessed film crystallinity and orientation. Cross sectional high-resolution transmission electron microscopy (HRTEM) was performed on a Philips CM300 in order to examine the structure of the film-substrate interface.

Soft X-ray absorption spectroscopy (XAS) on the Ti $L_{2,3}$ and O K edges of LTO films was performed at beamlines 4.0.2 [111] and 6.3.1 [112] of the Lawrence Berkeley National Laboratory Advanced Light Source. X-ray absorption spectra for LTO films of thickness 15-300 nm were taken at room temperature in both normal and grazing incidences (the sample's surface normal direction was collinear with the incoming photon direction and was tilted 60 degrees from the incoming photon direction, respectively). Reference spectra were measured on bare substrates as well as powder from the target material. Spectra were obtained by measuring total electron yield, monitoring the sample drain current as a function of photon energy. Electron yield detection is surface sensitive with a probing depth of 2-5 nm. The sample current was normalized to the incoming photon flux as measured using a gold mesh inserted in the beam path. The degree of linear polarization of the incoming X-ray flux was 99±1 % for both beamlines. The lateral dimensions of the X-ray interaction area are much larger than the electron escape depth vertically, thus the measured signal averages over a large number of intragrain volume as well as grain boundaries.

Normal and superconducting-state magnetic properties were measured in a Quantum Design superconducting quantum interference device (SQUID) magnetometer. Magnetization measurements were performed with DC field applied both in the plane and out of the plane of the sample. To minimize sample flux trapping when cooling through T_{crit}, the trapped flux in the SQUID magnetometer's superconducting magnet was reduced to less than 0.28 Oe as calibrated by a 99.9 % pure Dy_2O_3 sample. Transport was measured in a Quantum Design physical property measurement system (PPMS) modified with a Keithley 236 source-measure unit and HP3488A switching matrix.

Resistivity and Hall measurements were performed both in the normal and superconducting state. DC and low frequency (f = 13.739 Hz) AC resistivity measurements were carried out in varying fields applied out of the plane of the sample from 2-380 K. Measurements in both cryostats were taken from room temperature to 2 K in fields of up to 5 T for SQUID magnetometry measurements and up to 7 T for transport measurements.

4.4 Structure

Structural analysis indicated that films on all substrates were single-phase and single orientation spinel composition. X-ray diffraction in θ-2θ geometry showed spinel phase reflections that were epitaxially matched to the single crystal substrate. No reflections from constituent phases from the target or polymorphs of TiO_2 were observed. Films on MAO and STO under compressive strain exhibited elongation of the out-of-plane lattice parameter. Reciprocal space mapping of the film 444 reflection on (110) STO showed almost full relaxation of the film to bulk lattice parameters for film thickness greater than 100 nm, but only partial relaxation below 100 nm. Careful X-ray diffraction measurements indicated that the lattice parameters of LTO were elongated along the out-of-plane direction with approximately 2 % elongation from bulk for a 22 nm thick film on (001)MAO. This result suggests that biaxial compressive strains for ultrathin films are non-volume preserving and therefore may affect the Debye temperature and in turn the T_{crit}. Films on MgO had reflections which overlay the substrate reflections to within the experimental resolution of the diffractometer, thus the films are under slight tension and show very little contraction of the out-of-plane lattice parameter. Phi scans were performed to measure the in-plane epitaxy of the samples, with clear signs of cube-on-cube epitaxial growth of the spinel on perovskite STO substrates (Figure 4.1, top).

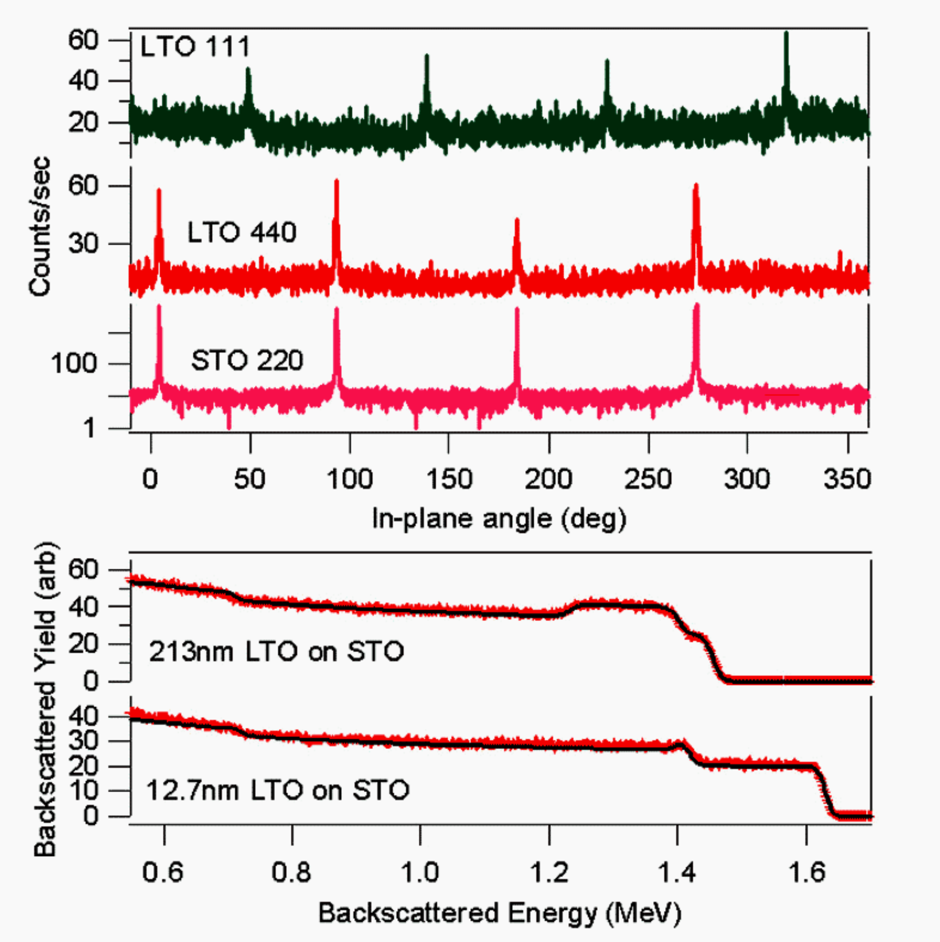

Figure 4. - Top - In-plane (phi) X-ray diffraction scan of various LTO and STO film reflections. Note that the STO reflection is on a logarithmic scale while the LTO reflections are on linear scales. Bottom - RBS spectra for LTO/STO films of 12.7 and 218 nm thickness.

Atomic force microscopy (AFM) indicated the low lattice mismatch between LTO and MgO gave rise to smooth films with an RMS roughness of 0.444 nm (or approximately half of a spinel unit cell) for a 100 nm thick film. However, rougher film morphology was seen on MAO substrates, with 1.6-2.6 nm RMS roughness for films of similar thickness. Films on STO had comparable roughness to those on MAO, and film grain size for both substrates at a deposition temperature of 450 °C or 600 °C was on average 100 nm. The rougher surface morphology was attributed to the larger epitaxial lattice mismatch and the accompanying full lattice relaxation. Since STO and MgO have approximately half the unit cell size of LTO, antiphase boundaries are expected in the LTO films on STO and MgO but not on MAO. Given the similarities of the STO and MAO samples, these antiphase boundaries appear not to affect the surface morphology.

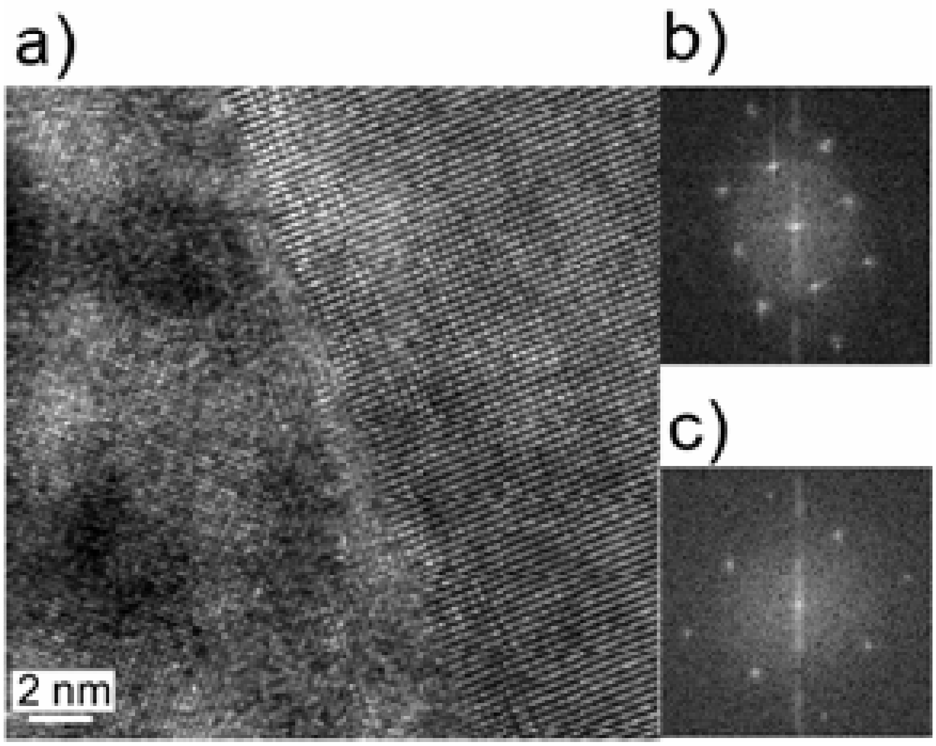

Figure 4.2 - (a) HRTEM image of the film-substrate interface of a LTO/STO(110) sample, with the STO substrate on the right of the micrograph. (b) Fourier transform of the combined image. (c) Fourier transform of an LTO-only area of the sample.

Films on (110) oriented substrates had elongated grains with an aspect ratio of 2:1 favoring the $[1\bar{1}0]$ in-plane axis as the fast-growth direction, as well as increased out of plane roughness compared to (001) oriented films. No measurable anisotropy or roughening compared to (001) films was measured on films grown on (111) oriented MAO, though the average grain size of 30 nm was smaller than grain sizes of (110) films with comparable thickness. RBS analysis enabled us to probe the degree of interdiffusion of species at the film/substrate interface. Because of the difficulty in analyzing low Z ions such as Li and O, I focused on analyzing the uniformity of the atomic density of Ti from the LTO as well as the atomic species from the respective substrates. RBS analysis confirmed the interdiffusion of Mg into the LTO films deposited at 600 °C from MgO substrates with an approximate ratio of Mg to Ti of 0.25:2 assuming a uniform film stoichiometry, but no measurable interdiffusion for films on STO or MAO substrates to within the 5 % accuracy of the measurement (Figure 4.1, bottom) .

HRTEM micrographs of an LTO(110)/STO(110) sample along the [001] zone axis were taken to examine the non-isostructural spinel-perovskite interface (Figure 4.2, (a)). Fourier transforms of the film-substrate interface area (b) as compared to film-only areas (c) confirm epitaxial growth of the film on the STO substrate. The clear presence of well-defined film lattice fringes in multiple areas of the TEM sample corroborates the single phase and single orientation nature of the sample from the X-ray diffraction measurements. However, low angle grain boundaries can be seen on the film side of the interface as areas of differing contrast. Thus such grain boundary defects may influence film properties such as resistivity or magnetization.

4.5 Soft X-ray Absorption

In order to probe the cation environment and its effect on the observation of superconductivity, surface sensitive soft X-ray absorption spectroscopy was performed at the Ti $L_{2,3}$ and O K absorption edges on films of varying thickness below 500 nm to determine the Ti ion environment. Spectra have been aligned to the first sharp peak at each absorption edge: 455 eV for the Ti L_{3a} peak (Figure 4.3) and 530 eV for the first

O K edge peak (Figure 4.4). Unlike heavier *3d* transition metals like Fe with two dominant features at the $L_{2,3}$ edge, each of the Ti L_3 (454-458 eV) and L_2 (460-465 eV) absorption features are split into qualitatively t_{2g} and e_g-like sub-peaks. Crystal fields have a large effect on the relative intensity of each of these peaks for the case of Ti^{4+} in different environments.[47, 50] For the case of Ti^{3+} in compounds such as $LaTiO_3$, the lower energy t_{2g}-like peaks have low intensity compared to the e_g-like peaks. Since bulk LTO has an equal number of Ti^{3+} and Ti^{4+} in octahedral environments, one would expect a spectrum similar to mixed-valence octahedral Ti such as in $La_{1-y}Sr_yTiO_3$.[46] Comparison of the STO Ti^{4+}-only spectrum in Figure 4.3 (a) to spectra (d)-(f) shows that LTO spectra have an increase in spectral weight at a 454 eV pre-peak feature at the expense of L_{3a} intensity, as well as a merging of the L_{2a} and L_{2b} peaks. This trend is also seen in the y=0.4 and y=0.6 spectra from Abbate *et al.*'s study on $La_{1-y}Sr_yTiO_3$.[46]

Ra *et al.*[113] examined powders of stoichiometric and Li-excess $Li_{1+x}Ti_{2-x}O4$ and found qualitatively similar Ti $L_{2,3}$ lineshapes for $0 \leq x \leq 0.33$. Following their analysis, Lorentzian fits were made simultaneously to the pre-edge feature at 454 eV as well as each of the L_{3a}, L_{3b}, L_{2a}, and L_{2b} peaks. The ratio of L_{3a} to L_{3b} peak areas was approximately 0.14 for LTO on MgO and MAO, and showed a trend of increasing L_{3a} contribution for films on STO and 48-hour air-exposed samples. Long-term air-exposed samples will hereafter be referred to as 'aged' samples. This result suggests that the surface of aged samples as well as those of STO have slightly more Ti^{4+} character than similar films on MgO or MAO. Samples on STO capped with 3 nm AuPd deposited in-situ at 400°C showed similar spectra to uncapped samples, suggesting that the more Ti^{4+}-like spectrum is intrinsic to the surface and interface of as-deposited LTO films on STO.

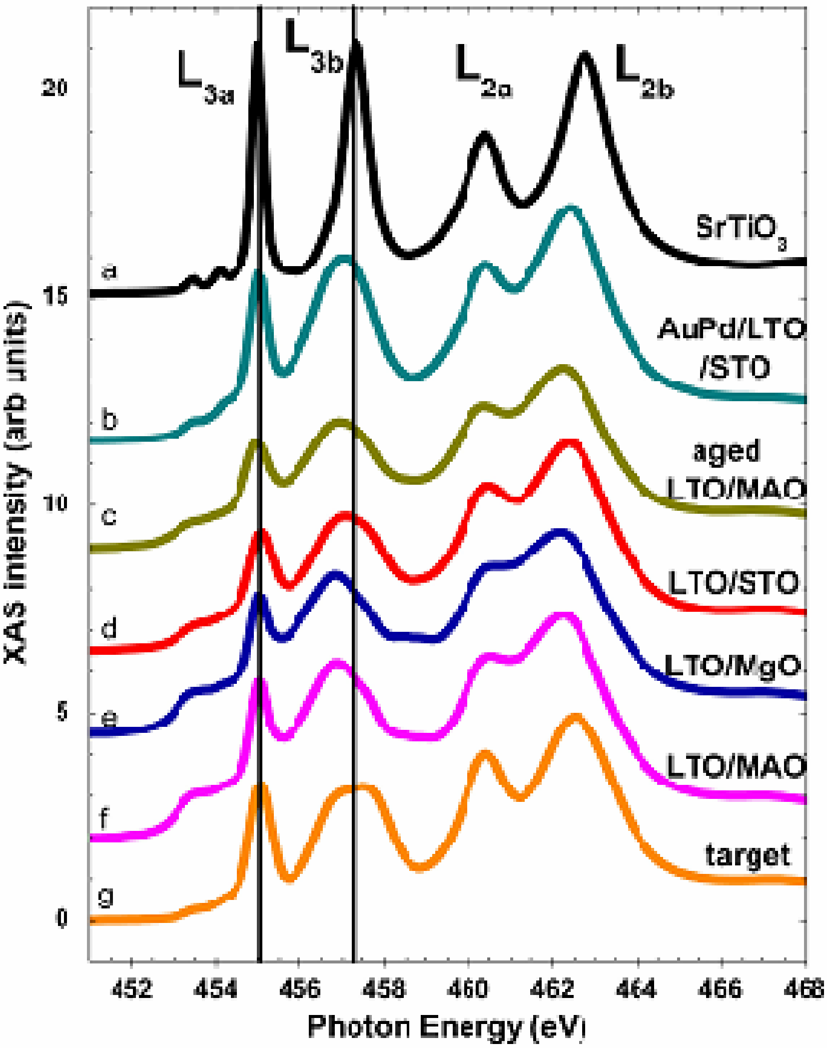

Figure 4.3 - Normal-incidence Ti $L_{2,3}$ absorption edge spectra for LTO films on various substrates: (b) 3 nm AuPd / LTO on (001)STO, (c) prolonged air-exposed LTO on (001)MAO, (d) LTO on (001)STO, (e) LTO on (001)MgO, and (f) LTO on (001)MAO, as well as spectra from (a) a bare STO wafer and (g) the pressed powder target mixture as sources of Ti_{4+}-only compounds.

The O K edge features may be divided into two regions: two low-energy peaks at 530 eV and 532.5 eV that show strong hybridization between O *2p* and Ti *3d* states, and a broader region between 536-548 eV exhibiting mixing of Ti *4sp* and O *2p* states.[50] The lower-energy peaks for the various samples resemble the spectrum from the target material due to similar Ti-O hybridization with the intensity for the two peaks for the fresh samples equal in magnitude and insensitive to film thickness from 15 nm to 87 nm on STO.

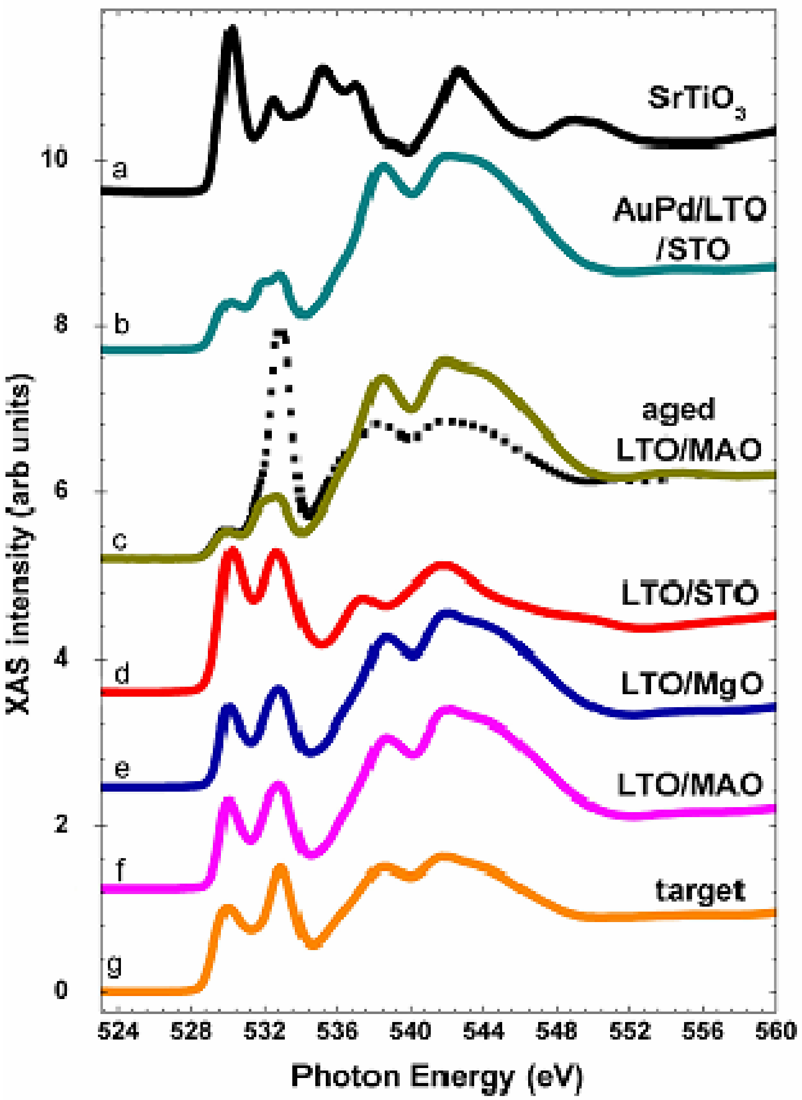

Figure 4.4 - O K absorption edge spectra for LTO films on various substrates as well as reference spectra as described in Figure 4.3. All spectra with solid lines were taken in normal incidence, while the dotted spectra overlaying spectrum (c) was taken in grazing incidence.

Since these lower-energy peaks are sensitive to neighboring Ti ions, one would expect similar spectra between the edge-sharing TiO_6 octahedra in LTO and the distorted edge-sharing octahedra in ramsdellite $Li_2Ti_3O_7$ and rutile TiO_2 in contrast to the corner-sharing octahedra in STO. One would also expect dramatic changes between fresh and aged sample spectra, but the aged LTO/MAO sample (Figure 4.4

(c)) showed large changes only when measured in grazing incidence.

Grazing incidence measurements reduce the effective X-ray penetration depth by cos(θ), thus a very shallow sample volume is probed. A similar but weaker trend of suppression of the 530 eV peak when compared to the 532.5 eV peak can be seen in the AuPd capped LTO/STO sample (Figure 4.4 (b)) as the AuPd cap also serves to reduce the electron yield of the LTO underlayer, but also protects the LTO material from reaction with air. One caveat is that the energy range of the Pd $M_{2,3}$ absorption edge overlaps that of the O K edge, thus I cannot make a quantitative comparison between the O K edge lineshapes for AuPd-capped and uncapped samples. From a qualitative analysis, aging of the sample can affect the surface of LTO samples dramatically as seen by the changes in lineshapes described above. The depth of aged material must be on the order of the photoelectron escape depth (of order 5 nm[114]) due to the difference in normal-incidence and grazing angle measurements. On the other hand, fresh samples show little difference in XAS lineshape between grazing and normal incidence measurements.

Comparison to the spectra from Ra *et al*. confirm that the surface material is close to target stoichiometry as-deposited and such surface material decreases in Li content as the sample ages. Aging affects the surface-sensitive XAS lineshape, but only with aging for longer timescales do significant changes in normal and superconducting state transport properties occur. Therefore the variations in transport properties for different samples described below cannot be attributed to variations in Ti average valence, Ti site symmetry or Li deficiency and hence Ti network disorder.

Although XAS spectra can show strong differences based on site symmetry for isovalent compounds such as rutile and anatase TiO_2,[47] no clear distinction exists as a function of thickness for the LTO films as compared to the lineshapes shown in Figures 4.3 and 4.4. Thus the average valence and site occupation for the surface monolayers of each film should be identical, in spite of the presence of measurable superconductivity in thicker films and no resistive superconducting transition in a 15 nm film on STO. Thick and relaxed films on MAO, MgO and STO substrates also have similar features to the thin films on STO, indicating that the surface monolayers do not change substantially post-deposition as a function of substrate, and the XAS surface measurement is insensitive to the presence of anti-phase boundary disorder.

XAS at the Mg K edge of 100 nm thick as-deposited films on MgO (peak to background of 1.25:1) confirms interface Mg diffusing from the substrate into the film during growth on MgO substrates. Similarity of the aforementioned spectra to normal spinel MAO Mg K edge spectra[115] confirms that the interdiffused Mg substitutes primarily into tetrahedrally coordinated sites. However, a comparable as-deposited 100 nm thick LTO film on MAO shows little Mg at the surface, with a peak to background of approximately 1.01:1 for the Mg K edge.

4.6 Magnetism

The magnetic response of LTO films was measured on all substrates and found to be comparable to LTO bulk single crystals, polycrystalline pellets, and powder samples. Zero-field cooled samples at 1.8 K show diamagnetic shielding with low applied fields. A linear extrapolation at low applied fields for the data presented in Figure 4.5 (a) yielded a typical lower critical field H_{c1} of 46±3 Oe at which point the diamagnetic response deviated from linearity by 1 %. Using the relation $(H_{c1}H_{c2})^{0.5} \sim H_c$, with H_c as the thermodynamic critical field for LTO, an upper critical field H_{c2} of approximately 20 T is extracted from Sun *et al.*'s value for H_c=0.327 T. As discussed below, the upper critical field may be calculated from transport measurements, and such values yield $H_c \sim 0.3$ T.

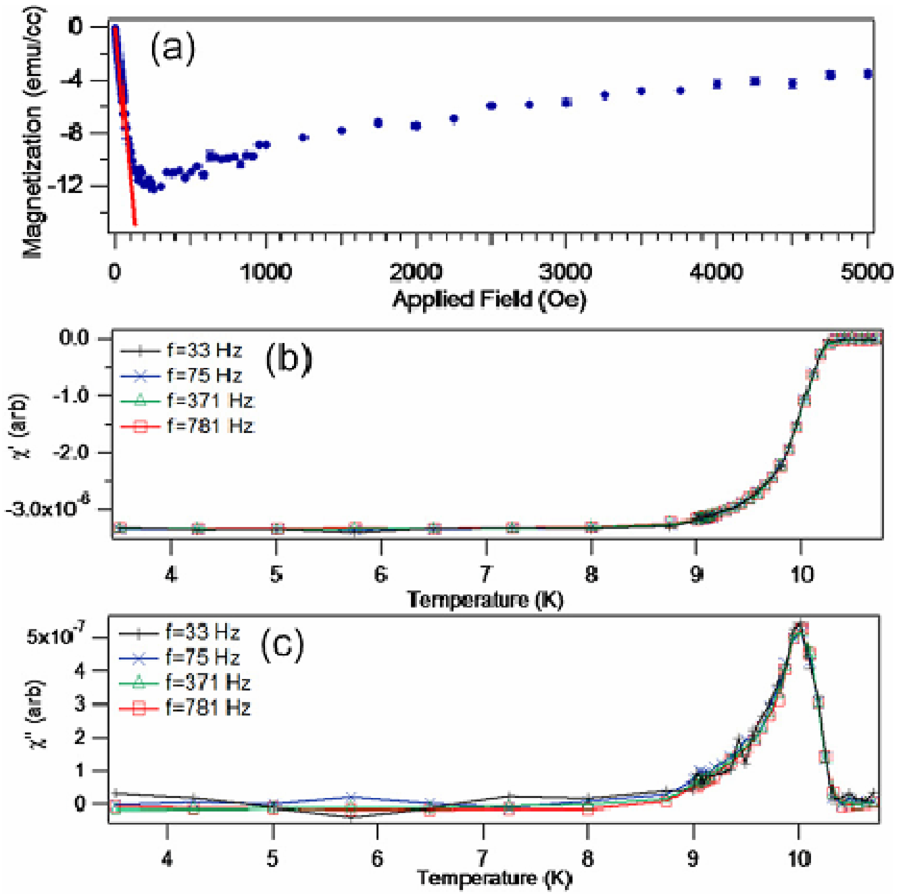

Figure 4.5 - (a) Low-field diamagnetic response at 1.8 K of a zero-field cooled 350 nm LTO film on (001)MAO with magnetic field in the plane of the sample. Deviation from linearity takes place at 46±3 Oe. (b) Zero-DC field in-phase magnetic susceptibility as a function of temperature for a 300 nm LTO film on (110)MAO with excitation field H_{ac} = 14 Oe. (c) Out-of-phase susceptibility of sample in (b).

AC susceptibility has been used to characterize superconducting samples to determine the fraction of superconducting phase as a function of DC magnetic field, AC excitation field and temperature.[116] One can model a polycrystalline sample as a collection of superconducting grains with weak links representing grain boundaries. Thus the intragrain AC response and the intergrain AC response may be separated and individually evaluated. However, as a function of frequency, no secondary peak is observed in the AC response to within the resolution of the measurement as shown in Figure 4.5. Thus the presence of low-angle grain boundaries as determined by TEM does not seem to adversely affect the sample response and that the superconducting material is strongly coupled across such low angle grain boundaries. In spite of the presence of both low-angle grain boundaries and antiphase boundaries in the LTO samples on STO, the measured in and out-of-phase AC response matches the DC temperature-dependent magnetization of the LTO films.

4.7 Transport in thick LTO films

In order to probe the effects of lattice strain and microstructural disorder on the superconducting transition, I performed resistivity and Hall Effect measurements on the LTO films. In particular, this section describes the normal state resistivity values, resistive transition temperatures and widths, the upper critical field, the Ginzburg-Landau coherence length-mean free path product and Hall mobility as a function of substrate.

The normal-state resistivity versus temperature for nominally stoichiometric films on MAO (e.g. Figure 4.6) and STO deposited at 600 °C are comparable to that of polycrystalline thin film samples[98] as well as bulk polycrystalline samples[117] despite the presence of large compressive epitaxial strains. The film on (001) MAO described in Figure 4.6 as well as a film of comparable thickness on (001) STO both have a resistivity of $1.2\text{x}10^{-3}$ Ω·cm at 12K. The similarity in magnitude of normal-state resistivity suggests that the presence of anti-phase boundaries, and hence Ti network disorder, in films on STO does not have a significant effect on the normal state transport in such LTO films. In contrast, films on MgO were found to have an order of magnitude greater normal-state resistivity despite having minimal epitaxial strain and much smoother film morphology compared to films on STO or MAO. The significantly larger normal state resistivity values suggest that partial Mg^{2+} interdiffusion into octahedral sublattice sites[104, 118, 119] at the 600 °C deposition temperature coupled with antiphase boundary-related Ti network disorder[89] give rise to greater scattering in the normal state. A lower deposition temperature of 450 °C yielded films with higher residual resistivity for all substrates, though superconducting transitions for films on MAO and STO remained at approximately 10 K. These results suggest that the higher residual resistivity is associated with the grain boundaries.

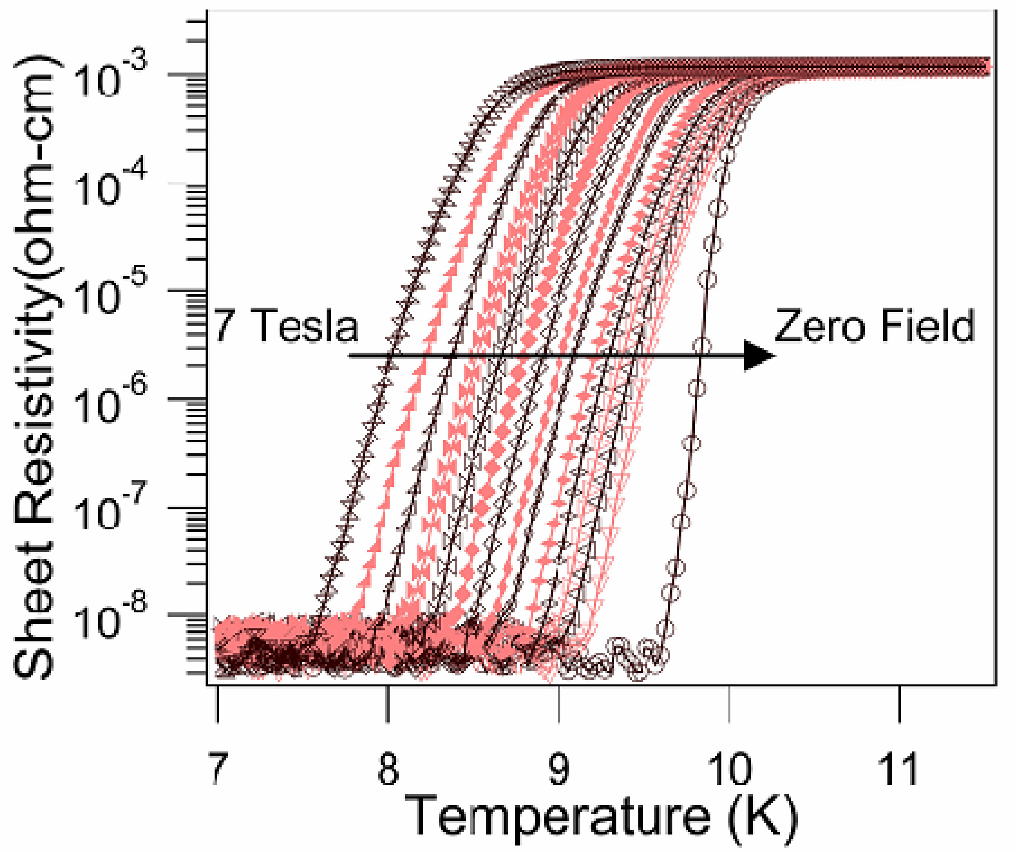

Figure 4.6 - Zero-field cooled field-dependent resistivity taken on warming as a function of temperature of a 60 nm film on (001)MAO in the temperature regime around its superconducting transition. Measurements were taken with field applied out of plane at every 0.5 T from 7 T to zero field, with bold lines indicating data at 1 T intervals.

Figure 4.7 plots a summary of the resistive transition temperatures and widths measured for LTO films of varying thickness grown on different substrates and substrate orientations. Mirroring the trend observed with the normal state resistivity values, the films grown on (001) MAO and STO display similar behavior with a sharp zero field transition width (for 10 % to 90 % of normal state resistivity at 15 K) and transition temperature near 10.8 K. Nominally unstrained films on (001) MgO show a sharper zero field transition width of 0.3 K but with transition temperatures depressed to 6.9-9 K. The lower transition temperatures on MgO substrates, in contrast to those on MAO and STO substrates, can result from more significant Mg interdiffusion into the LTO film.[118] Films on (110) or (111) oriented MAO substrates show broader transition widths of up to 1.5 K which may be linked to smaller grain size seen in the AFM scans.

The increased number of non-superconducting grain boundaries in such samples may dominate the resistivity measurement, or the intragrain volumes themselves may be off-stoichiometry. Similar broadening of transition widths without significant degradation of the transition temperature were seen in powder pellets of LTO[120] as well as artificial $YBa_2Cu_3O_7$ superlattices.[121] The broadening in the aforementioned studies was not due to intrinsic properties of the superconducting regions but instead the boundary regions with the non-superconducting material. Since the LTO film transition temperature remains unchanged as a function of orientation for the 150 nm thick LTO films in Figure 4.7, grain boundaries rather than whole-film non-stoichiometry is the source of the transition broadening. If the grain boundary resistance in LTO films is a significant fraction of the measured normal-state resistance, careful analysis must be performed to measure intrinsic LTO properties from boundary effects. Finally, films on STO have comparable transition temperatures to films on MAO, implying that antiphase boundaries have little effect on the magnitude of the critical temperature.

A closer look at the upper critical field and Ginzburg-Landau coherence length- mean free path product of LTO thin films on different substrates indicates the presence of a disordered phase either at the surface or film-substrate interface in thinner LTO samples. Using the Werthamer, Helfand and Hohemberg[122] (WHH) model for a type II superconductor in the dirty limit, the upper critical field (H_{c2}) is estimated from the low-field slope of the critical temperature as a function of applied magnetic field.

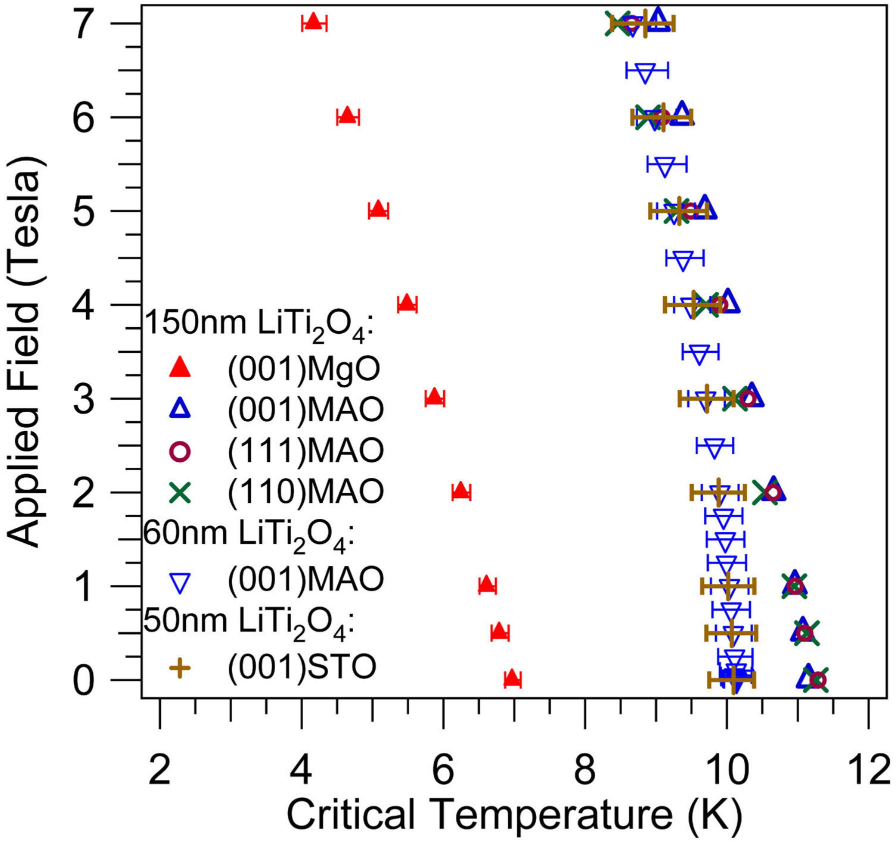

Figure 4.7 - Critical temperature versus applied field for 50 nm, 60 nm and 150 nm LTO films on various substrates with magnetic field applied out of the plane of the sample. The horizontal error bars indicate the superconducting transition temperature width (10%-90% of the resistivity at 15 K).

The extracted H_{c2}(T=0 K) values ranged from 15.5-19.5 T for eighteen samples deposited on MAO and STO, and the coherence length $\xi(T = 0K)$ is calculated from the Ginzburg-Landau formula $H_{c2} = \Phi_0/2\pi\xi^2$ as 4.1-4.6 nm which is consistent with bulk values. Foner and McNiff[123] found that in spite of different starting compositions of $Li_{2.6}Ti_{2-z}O_4$, T_{crit} values were uniformly 12 K for stoichiometry deviations in the range of $-0.7 < z < 0.5$. However, strong variations were observed in the quantities $(dH_{c2}/dT)_{T=Tcrit}$, the zero-field slope of the H_{c2} vs. T_{crit} curve, and λ_{so}, the spin-orbit scattering parameter. In analogy, the T_{crit} of films on MAO and STO for a given thickness is suppressed in thinner films to a value of on average 10.8±0.5 K compared to 900 nm thick films with an average critical temperature of 11.3 K. Thinner films such as the 60 nm film on (001)MAO or 50 nm film on (001)STO in Figure 4.7 show a field dependence with suppressed critical temperatures in zero field, though in high field their behavior approaches those of thicker films.

The films on MgO had a suppressed critical temperature but fit very well to the universal WHH curve if the reduced field $h_{c2} = H_{c2}(T)/[T_{crit}(H=0)\cdot(dH_{c2}/dT)_{T=Tcrit}]$ is plotted as a function of reduced critical temperature $t=T_{crit}(H)/T_{crit}(H=0)$. The increase in the reduced h_{c2} for low applied fields over that estimated from the WHH model can result from increased localization due to a disordered or inhomogeneous phase[124, 125] in thinner LTO samples, whereas the significant interdiffusion of Mg in films on MgO yields a more uniform $Li_uMg_vTi_2O_4$ phase.

The Ginzburg-Landau coherence length-mean free path product $\xi_0 l$ may also be obtained from the transport data using the dirty-limit formula

$$\xi(T) = 0.855\left(\xi_0 \ell \middle/ 1 - T/T_{crit} \right)^{1/2} \qquad \text{(Eqn 4.1)}$$

For the resistive transitions plotted in Figure 4.7, $\xi_0 l$ for the 150 nm thick films is close to 1400 Å^2 and is consistent with crystals at 5 % or closer in composition to the stoichiometric $LiTi_2O_4$ phase.[117, 126] However, the 50 nm and 60 nm films on both MAO and STO have $\xi_0 l$ values close to 800 Å^2, suggesting that deviations from bulk-like behavior at either the surface or the film-substrate interface dominate at these thicknesses. Examination of the film-substrate interface in the HRTEM micrographs does not reveal an interface layer, and there is no clear thickness dependence of the surface layer as measured by XAS. Thus epitaxial strain may cause thin film properties to deviate from bulk, while thick and relaxed film properties are closer to those of bulk LTO.

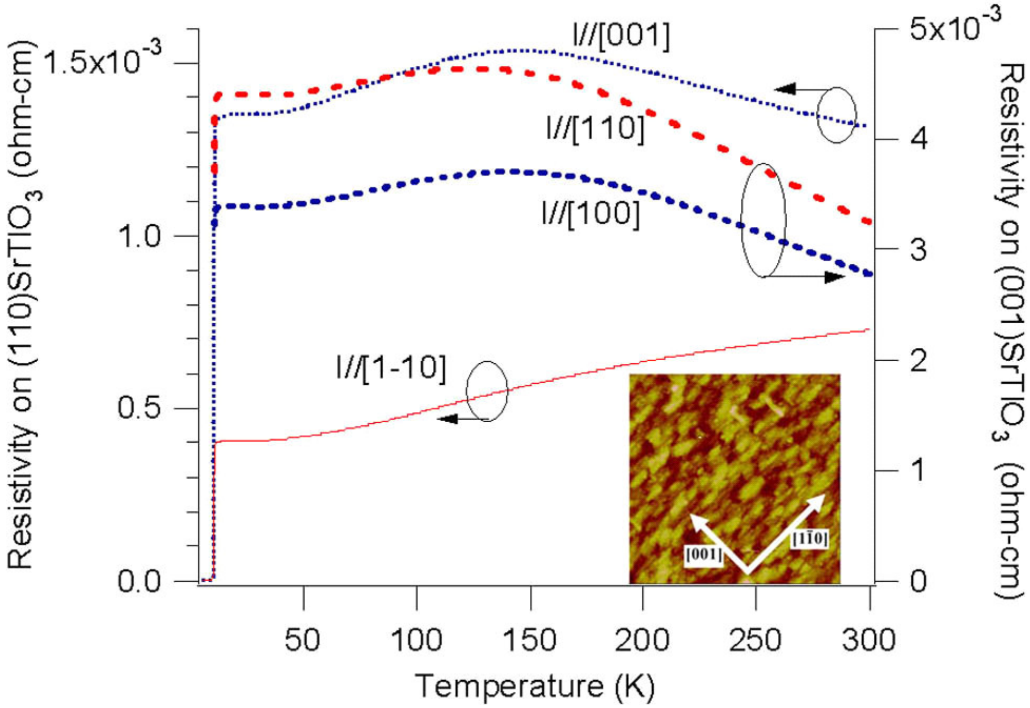

Figure 4.8 - Resistivity of thin rectangular LTO film sections along different crystallographic directions with every 15th point plotted for (001)STO (squares) and (110)STO (circles). Each data set indicates along which crystallographic direction current was directed during measurement. Solid lines indicate fits to equation 4.2 as detailed in the text. Inset: AFM scan of 2.5 x 2.5 micron area on an LTO film on (110)STO showing elongation of grain structure along the [1-10] *substrate direction.*

The Hall mobility of films on MAO and STO substrates was measured by computing the ratio between the Hall resistance and the sheet resistance in the van der Pauw configuration from the critical temperature up to room temperature. Assuming a simple one-carrier type model, films are n-type with carrier concentration of 1.3x10^{22} cm^{-3} for most films; this carrier concentration is equivalent to a single carrier per LTO formula unit as one would expect from the mixed-valent Ti ions. Carrier concentration and mobility were extracted by simultaneous van der Pauw and Hall measurements as a function of applied field out of the plane of the sample up to 7 T between 11 K and 305 K.[61]

Films deposited on STO and MAO at higher temperatures (600 °C) showed better crystallinity as confirmed by XRD rocking curves as well as mobility as high as 0.7 $cm^2/V \cdot s$ at room temperature as measured by the Hall effect. Similar values for LTO mobility were found for polycrystalline LTO films annealed at 850 °C.[99] A suppression of mobility by a factor of two was seen in films on STO at 450 °C, but the carrier concentration remained at approximately one electron per LTO formula unit for films on STO at both 450 °C and 600 °C.

A detailed look at the normal state resistivity of LTO shows non-monotonic behavior with both positive and negative slope. Such features have been attributed to non-stoichiometry or substitution in LTO bulk samples.[119, 127] As discussed above, grain boundary resistance may play a role in the measured sample resistance and thus must be taken into consideration when performing quantitative analysis on transport data. Thus, a two component model of resistivity consisting of metallic and semiconducting components was used to account for disorder and inhomogenieties in thinner superconducting LTO films as well as films deposited at 450 °C. Similar modeling was successfully applied to $(Ba,K)BiO_3$ films.[128]

$$\rho(T) = \left\{ (1-A)\left[\frac{1}{\rho_s e^{E_s/k_B T}}\right] + \frac{A}{\rho_m(T)} \right\}^{-1} \qquad \text{(Eqn 4.2)}$$

The first bracketed term models the semiconducting component of the resistivity which freezes out at low temperatures, and is parameterized by the semiconducting channel resistivity asymptote ρ_s and hopping activation energy E_s. The second term models a metallic resistivity, and the weighting parameter A details the relative contributions between the metallic and semiconducting channels. The normal-state resistivity has been fit in vanadium-silicon alloy films[129] using the electron-phonon scattering form of the Bloch-Gruneisen equation with a series residual resistivity ρ_0 as well as a phenomenological parallel saturation resistivity ρ_{sat} (Equation 4.3). The Bloch-Gruneisen equation (Equation 4.4) parameters include the high temperature resistivity coefficient α_{BG} and the Debye temperature θ_D. We may use this model for the metallic resistivity term in Equation 4.2 for samples with non-monotonic resistivity, as well as only using Equation 4.3 for samples with monotonic metallic resistivity such as 60 nm and thicker films on both MAO and STO substrates deposited at 600 °C.

$$\frac{1}{\rho_m(T)} = \left[\frac{1}{\rho_{sat}} + \{\rho_0 + \rho_{BG}\}^{-1}\right] \qquad \text{(Eqn 4.3)}$$

$$\rho_{BG} = \frac{4\alpha_{BG}T^5}{\theta_D^4}\int_0^{\theta_D/T} dz \frac{z^5}{(e^z - 1)(1 - e^{-z})} \qquad \text{(Eqn 4.4)}$$

For samples that have monotonic resistivity with a positive temperature coefficient of resistivity, such as the LTO/(110)STO I//[1-10]data in Figure 4.8, equation 4.3 may be used to obtain α_{BG} and θ_D. For a range of different sample thicknesses with non-monotonic resistivity, equation 4.2 is better suited to fit the data by leaving A, ρ_s, E_s, ρ_{sat}, and ρ_0 floating during data fitting while constraining α_{BG} and θ_D to match values obtained from samples with monotonic resistivity.

Values for the LTO/(110)STO I//[1-10] data in Figure 4.8 when fit to equation 4.3 are $\alpha_{BG} = 4.6\text{x}10^{-6}\cdot\Omega$ cm/K and $\theta_D = 420$ K. The resulting Debye temperature of 420 K is suppressed compared to measured Debye temperature of 537-700 K via heat capacity experiments.[126] Tang *et al.*[127] assumed a closed-form solution of the Bloch-Gruneisen equation by assuming an Einstein phonon distribution, and their best fit

Einstein temperature of 367 K is consistent with our best fit temperature of approximately 280 K with the same closed-form equation applied to the data in Figure 4.8.

Table 4.1 – Fitting parameters using Equations 4.2-4.4 for data from Figure 4.8 and MAO twin samples.

Sample	ρ_s (Ω cm)	E_s/k_B (K)	A	ρ_0 (Ω cm)
(110)STO I//[1-10]	1.25E-04	1061.08	1.00	6.18E-04
(110)STO I//[001]	5.22E-04	436.18	0.37	8.48E-04
(001)STO I//[110]	6.10E-04	732.51	0.16	1.73E-03
(001)STO I//[100]	9.14E-04	580.15	0.17	1.15E-03
(001)MAO I//[110]	5.87E-04	675.87	0.28	7.98E-04
(001)MAO I//[100]	4.56E-04	721.71	0.30	8.07E-04

If one compares the films on STO from Figure 4.8 and their twins on (001) and (110)MAO using the dimensionless weighting parameter *A*, one may evaluate the relative contribution of the metallic and semiconducting components in the fit. Elongation of the grain structure for films on (110)STO (e.g. Figure 4.8 inset) and MAO allows for the measurement of differing ratios of intragrain and intergrain volumes along different crystallographic directions in the same sample. Thus by using Equation 4.2 one may separate the intrinsic LTO resistivity from contributions to the resistivity by non-intrinsic sources such as grain boundaries and other microstructural disorder. As the grains on (110)STO are elongated along the [1-10] direction, current confined along the [1-10] direction probes a large fraction of intragrain volumes with fewer intergrain areas contributing to the resistivity. On the other hand, when current is confined along the [001] in-plane direction for the same sample, the relative amount of intergrain resistivity contributions are increased, and accordingly the measured sheet resistivity increases as well as a decrease in resistivity with increasing temperature above 150K. This suggests that while intragrain volumes are well-connected along the [1-10] direction, grain boundary resistance can have substantial influence along the [001] crystallographic direction. The similarity in shape for the (001)STO resistivity data along both the [100] and [110] in-plane directions point to a more isotropic contribution of grain boundary resistance on the measured sheet resistivity.

For the above samples, A falls between 1.0 (LTO on (110)STO with current along [1-10]) and 0.16 (LTO on (001)STO with current along [110]) suggesting that even in thick films the semiconducting channel is not negligible. Additionally, $A_{110} \sim A_{100}$ for films on STO and MAO confirms that there is little anisotropy in the ratio of the two resistivity channels along different crystallographic directions for (001) oriented films. Finally, $A_{MAO} > A_{STO}$ and the reduced ρ_0 for MAO samples indicate that antiphase boundaries in films on STO can increase the apparent contribution from a high resistivity channel in the temperature region of 20-100 K for thick LTO films without substantially affecting the T_{crit}.

4.8 Conclusions

Epitaxial films of the spinel superconductor LTO were grown on a variety of substrates to explore the effects of strain and microstructure on measured normal state and superconducting properties. Initial transport and magnetic measurements were consistent with bulk samples with an average critical temperature of 10.8 K and sharp transition width for films deposited on (001)MAO and STO. The surface properties of freshly-deposited films on a variety of substrates were identical as measured by soft X-ray absorption spectroscopy on the Ti $L_{2,3}$ edges, though substantial aging of the LTO samples can show a spectroscopic signature in the O K edge spectrum low energy 530 eV and 532.5 eV peaks. Anti-phase boundaries have a strong anomalous effect on the magnetization of spinels oxides such as Fe_3O_4, but little if any contribution of this type of defect alone was seen when comparing the normal and superconducting transport and magnetic properties of films thicker than 100 nm deposited on perovskite STO and isostructural spinel MAO-type substrates. By contrast, the interface Mg interdiffusion combined with antiphase boundaries in LTO films on MgO substrates gives rise to suppressed critical temperature accompanied by higher than bulk normal-state resistivity values. Together these results indicate the robustness of the superconducting state of LTO to lattice strain and microstructural disorder.

CHAPTER 5

MAGNETOSTRICTIVE-PIEZOELECTRIC $CoFe_2O_4$/$BaTiO_3$ COUPLING

5.1 Abstract

I have synthesized epitaxial $CoFe_2O_4$ films on piezoelectric $BaTiO_3$ single crystal substrates as a model magnetoelectric system. The $BaTiO_3$ substrate provides a surface lattice that can be dynamically changed in an attempt to alter the strain state and hence the magnetization of the $CoFe_2O_4$ film. Magnetization measurements indicate that the magnetic anisotropy of $CoFe_2O_4$ is dominated by compressive epitaxial strain effects and can be understood in terms of the symmetry of the substrate surface unit cell.

5.2 Introduction

Recently there has been an enormous surge in the study of multifunctional materials, especially multiferroic materials that exhibit two or more switchable states of magnetization, polarization or strain.[130] Of the family of multifunctional oxides, those that exhibit a significant magnetoelectric effect are of fundamental and technological interest. In magnetoelectric materials, ferroelectricity coexists with either ferromagnetism or anti-ferromagnetism. Such materials may become the basis of a new class of devices that include modulators, switches, generators and sensors. A number of single-phase magnetoelectric materials have been studied recently in both bulk and thin film form.[131-135] In order to generate a significant magnetoelectric effect, many studies have focused on bulk composites or tape cast multilayers.[136-138] There has been much less effort in developing magnetoelectric thin film materials that could be integrated into planar technology, largely due to the issues associated with generating large enough strains in epitaxial films constrained by a macroscopically thick substrate. Epitaxial thin film analogs of bulk magnetostrictive-piezoelectric composites are of interest in order to understand the role of interfaces on the magnetoelectric effect, to enhance these properties in films, and to integrate these functional materials into planar technology.

In order to integrate magnetoelectric material into planar technology, there have been a few studies of note. Nanopillars of magnetostrictive $CoFe_2O_4$ have been synthesized in ferroelectric $BiFeO_3$ and $BaTiO_3$ epitaxial thin film matrices.[105, 139] By observing changes in the magnetization loops when 10 % of the sample is covered with 30μm diameter test capacitors and electrically poled, they infer magnetoelectric coupling. Others have grown piezoelectric $Pb(Zr,Ti)O_3$ films on $(La,Sr)_3Mn_2O_7$ (327) single crystals and have probed the magnetoelectric coupling between the two materials by measuring the change in ferroelectric polarization due to the magnetostrictive change that occurs at the Curie temperature of the 327.[140]

In this chapter, I present the synthesis and characterization of a model magnetoelectric system composed of a magnetostrictive film of $CoFe_2O_4$ (CFO) deposited on top of a ferroelectric $BaTiO_3$ (BTO) single crystal. We probe the magnetoelectric coupling by studying the changes in magnetization in the CFO induced by structural phase transitions in the BTO. BTO is cubic above 410 K, tetragonal above 290 K, orthorhombic (monoclinic in a pseudocubic setting) above 190 K and rhombohedral at lower temperatures.[141] The BTO substrate provides a surface lattice that can be dynamically changed in an attempt to significantly alter the strain state and its symmetry and hence the magnetization and magnetic anisotropy of the CFO film. The magnetic anisotropy of the CFO can be understood in terms of the symmetry of the substrate unit cell.

5.3 Magnetization

CFO has an inverse spinel structure where the O anions make up a face-centered cubic lattice, an eighth of the tetrahedral (A or T_d) sites are occupied by Fe^{3+} ions and half of the octahedral (B or O_h) sites are occupied by Co^{2+} and Fe^{3+} ions. CFO is unique among the spinel structure ferrites in that it has a large magnetic anisotropy accompanied by large anisotropic magnetostriction. The large magnetostriction coefficients (*e.g.* $\lambda_{100} \sim -590 \times 10^{-6}$ and $\lambda_{111} = 120 \times 10^{-6}$ for $Co_{0.8}Fe_{2.2}O_4$)[142] make CFO an excellent candidate in composite magnetoelectric materials. In this study, we have grown epitaxial (001) CFO thin films with thicknesses of 500 Å and 1500 Å at 450 °C in a vacuum of 10^{-6} Torr on (001) BTO substrates by pulsed laser deposition with a KrF excimer laser operating at 3 Hz and a fluence of 2-2.5 J/cm^2. X-ray diffraction indicates that (001) CFO grows epitaxially on (001) BTO; in normal incidence θ-2θ scans, there is no evidence of the presence of film orientations other than those of the (001) family. CFO has a cubic unit cell with room-temperature lattice parameter of 8.38 Å while the various phases of BTO have lattice parameters within 1% of 4 Å.[141] The large -5% lattice mismatch between the film and BTO results in partial lattice relaxation of the CFO films.

Since BTO's unit cell is approximately half that of the CFO unit cell, it is inevitable that there are antiphase boundaries in the CFO film. Antiphase boundaries (APB) in single crystalline spinel structure ferrite films grown on MgO substrates have exhibited anomalous magnetic properties due to an enhanced intrasublattice superexchange coupling[102, 103, 143]. Anomalous magnetic properties include the difficulty in saturating the material in high magnetic fields. A previous study on epitaxial CFO films have shown that even in the absence of APBs, the lattice strain and cation disorder can dramatically change the magnetic properties of CFO from bulk.[144] In fact, as discussed in Chapter 2, the magnetic anisotropy is a balance between shape anisotropy, strain anisotropy due to internal lattice strain or equivalent external strain effects, and magnetocrystalline anisotropy due to cation distribution. By annealing the CFO films in that study, the symmetry and the magnitude of the magnetic anisotropy were both altered as both the cobalt cation distribution among the T_d and O_h sites as well as the strain state of the films were changed.

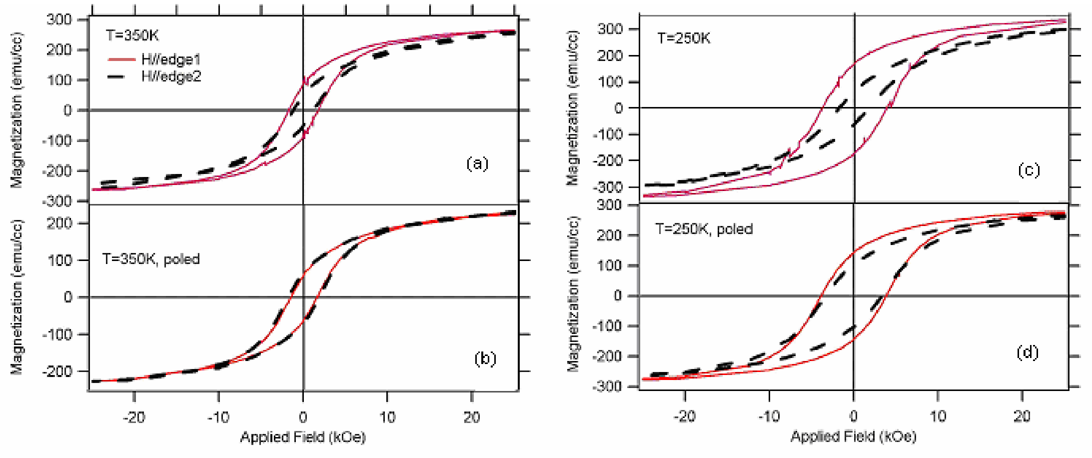

Figure 5.1 – Magnetization of a 145 nm CFO film on a (001)BTO substrate as a function of field at 350 K ((a) as-deposited and (b) poled along the film surface normal) and 250 K ((c) as-deposited and (d) poled along the film surface normal).

In this present study, I have measured in-plane magnetization loops of CFO along the edge directions of the substrate at the following temperatures (and substrate phases): 350 K (tetragonal), 250 K (orthorhombic) and 150 K (rhombohedral). These edge directions are nominally the [100] and [010] directions of the BTO. After initial cooling of the sample from deposition temperature and repeated thermal cycling, X-ray diffraction reveals that the BTO substrate is multidomain. However, when the BTO substrate is poled by the application of a 10 kV/cm electric field along the substrate normal in its cubic phase (T=450K) and subsequent cooling to room temperature in the applied electric field, the tetragonal BTO substrate can be nominally oriented with its a and b axes along the sample edges while the longer c axis is perpendicular to the substrate plane. The edges will be identified as edge #1 (nominally [100]) and edge #2 (nominally [010]).

In order to gain insight into the relationship between the magnetic properties of CFO film and underlying BTO structure, magnetization loops along both edge directions were measured after electrical field application at 450 K. After cooling down to 350 K, one can observe the magnetization loops at 350 K along the two edges to be identical to one another, thus suggesting that cubic CFO is under a biaxial compressive strain from the square surface unit cell of tetragonal BTO (Figure 5.1 (a, b)). In fact, magnetoelastic theory predicts that CFO grown under compressive strain has a hard out-of-plane direction and has been verified in CFO films grown on $CoCr_2O_4$ buffered $SrTiO_3$ and $MgAl_2O_4$ substrates.[144] Our CFO films on BTO also exhibit a hard out-of-plane direction and are consistent with previous work. At 250 K, there develops a small anisotropy in the magnetization loops along the two edge directions (Figure 5.1(c, d)).

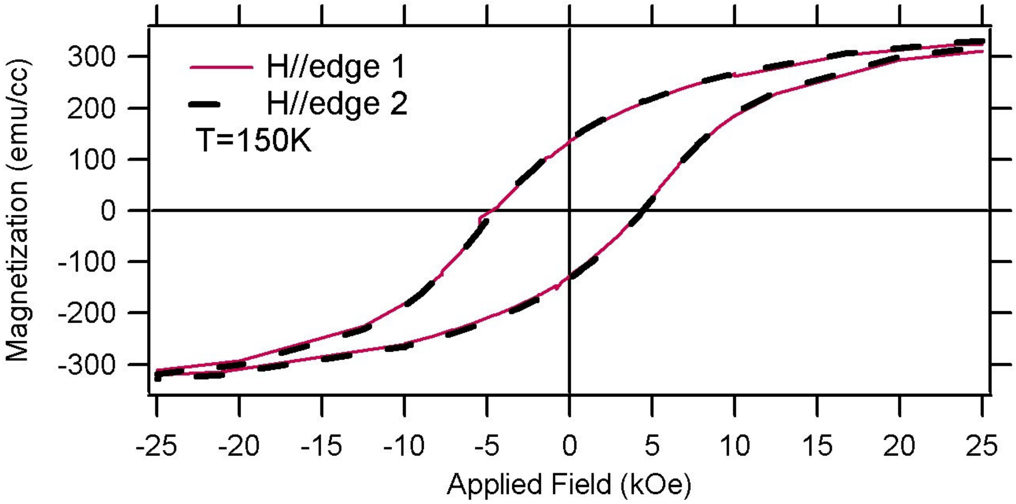

Figure 5.2 – Magnetization of a 145nm CFO film on a (001)BTO substrate as a function of field at 150K.

This anisotropy suggests that there is a preferential formation of one of two in-plane orientations of (001) BTO orthorhombic domains as the sample is cooled from the tetragonal to orthorhombic phase. At an even lower temperature of 150 K (Figure 5.2), the surface unit cell of BTO is a rhombus such that there is no difference in the magnetization loops measured along the two edge directions.

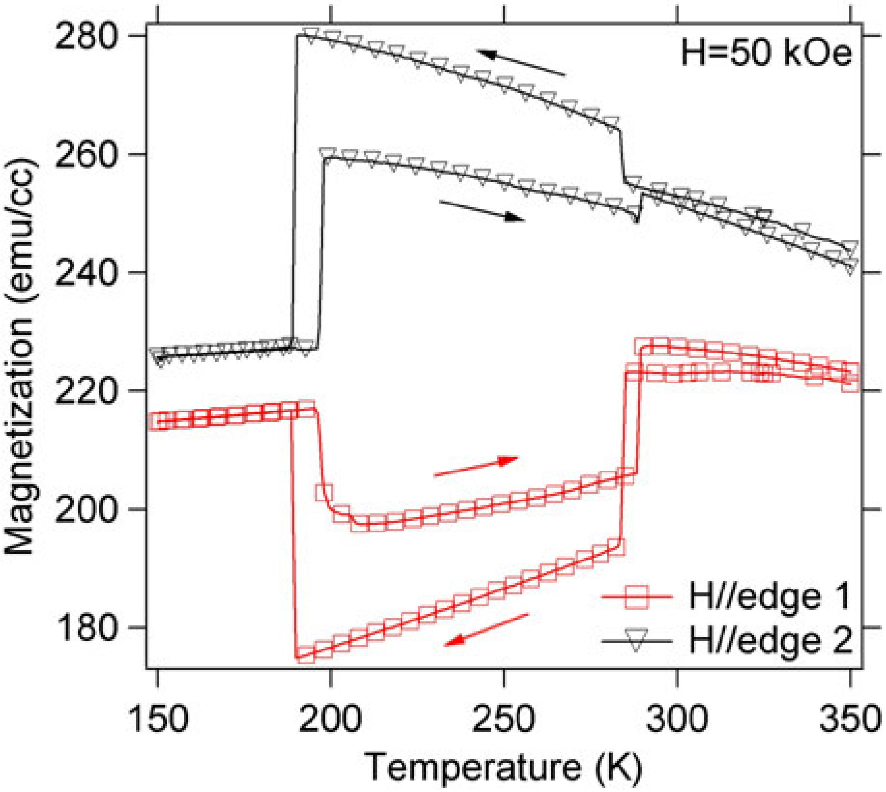

Figure 5.3 –Magnetization of a 56 nm CFO film on (001)BTO as a function of temperature in a field of 50 kOe, with every tenth data point shown. Arrows indicate the direction of temperature sweep. Irreversible domain formation between the cubic and rhombohedra phases of the substrate leads to magnetization hysteresis in the CFO film.

To probe the magnetoelectric coupling in the CFO/BTO system, I measured the magnetization as a function of temperature while warming and cooling in fields of 2.5 kOe and 50 kOe through the structural phase transitions of BTO. As temperature is decreased, the BTO crystal lattice changes from cubic to tetragonal at 410 K, tetragonal to orthorhombic at 290 K and orthorhombic to rhombohedral at 190 K. In all temperature regimes, the CFO is under compression so that the out-of-plane direction is the magnetically hardest direction. Figure 5.3 shows the magnetization along both edge directions as a function of temperature. The abrupt jumps in the magnetization at the structural transitions correlate well with the changes in lattice parameters observed in BTO.[141] More specifically, the magnetization decreases as the lattice parameter increases. This trend is also observed in magnetization measured out-of-the-plane of the substrate where two abrupt decreases in the c-axis lattice parameter of BTO correlate with two abrupt increases in magnetization. A decrease in the in-plane lattice parameter results in an increase in compressive strain and thus strain anisotropy. The increase in strain anisotropy translates into an increase in magnetization along the magnetically easy in-plane directions. While the difference in linear coefficient of thermal expansion for $CoFe_2O_4$ (9 ppm/K at room temperature)[145] and $BaTiO_3$ (approximately 35 ppm/K at 350 K)[141] could account for part of the change in epitaxial film strain state as a function of temperature, the equivalent coefficient of thermal expansion at the structural phase transitions approaches 5000 ppm/K and thus any strain effects from thermal expansion mismatch may be neglected.

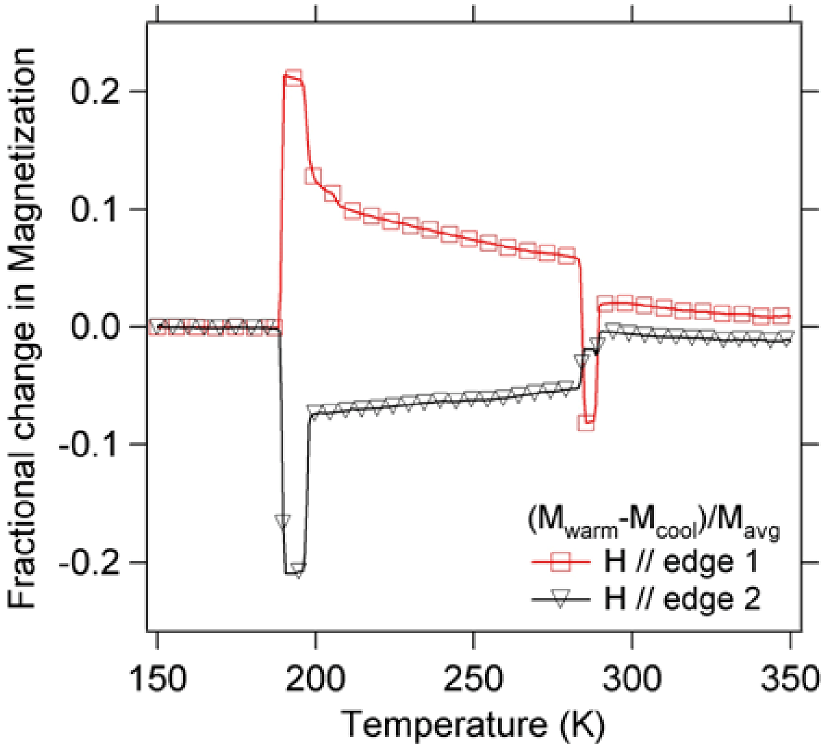

Figure 5.4 – Normalized change of magnetization of a 56 nm CFO film on (001)BTO as a function of temperature in an applied field of 50 kOe, with every tenth data point shown. Changes in magnetization are coincident with the structural phase transitions in the substrate.

A plot of the fractional change in magnetization shows that the structural change induces dramatic changes in the symmetry of the anisotropy (Figure 5.4). For example, the large peak at the orthorhombic-rhombohedral transition along one edge is accompanied by a corresponding decrease along the other edge. This change corroborates the in-plane magnetization results where magnetization versus magnetic field loops along the two edges are different in the orthorhombic phase and identical in the rhombohedral phase. Moreover, the magnitude of the fractional change in magnetization is larger for thinner films although the temperature dependences of the fractional change in magnetization are similar for different film thicknesses. Since the misfit dislocation critical thickness of CFO on BTO is ~30 Å, our films with thicknesses 500-1500 Å are partially relaxed.[146] Therefore, the fraction of CFO that is affected by the changing surface unit cell of BTO should decrease as a function of increasing film thickness.

A careful look at the magnetization versus temperature plots reveal that that hysteresis exists throughout the orthorhombic phase. Our previous studies of epitaxial films grown on BTO substrates have shown that the film lattice parameters themselves show hysteretic behavior throughout the orthorhombic phase.[147] This hysteresis is attributed to the irreversible formation of domains in the orthorhombic phase of BTO. In other words, when the sample is cooled from the tetragonal phase to the orthorhombic phase after electric field poling perpendicular to the substrate, the surface unit cell of (001) orthorhombic domains (**a** x **b**) can have two in-plane orientations. Upon warming from the rhombohedral phase to the orthorhombic phase, there are three different surface unit cells possible, i.e., **a** x **b**, **b** x **c** and **c** x **a** (each with two different in-plane orientations). Therefore the CFO unit cell and thus its magnetization measured upon cooling and warming in the orthorhombic phase is hysteretic. Subsequent warming of the sample from the orthorhombic to tetragonal (room temperature) phase gives rise to a mixture of (001) and (100) BTO as detected in X-ray diffraction at room temperature.

5.4 Soft X-ray absorption and PEEM

It is clear from Figures 5.3 and 5.4 that the magnetization of CFO films is significantly changed upon structural phase transitions in BTO. However, it is unclear as to what length scale the change in anisotropy of Figures 5.1 and 5.2 occur. As the ferroelectric/piezoelectric domain structure of the BTO can be modified with temperature or electric field, it is also likely that the magnetic anisotropy would follow such changes. In other words, through the application of an electric field, one may change the magnitude or direction of magnetization due to the strong elastic coupling between the epitaxial film and single crystal substrate. We may use soft X-ray techniques to probe this coupling and vary the piezoelectric domains while monitoring the ferromagnetic properties of the film.

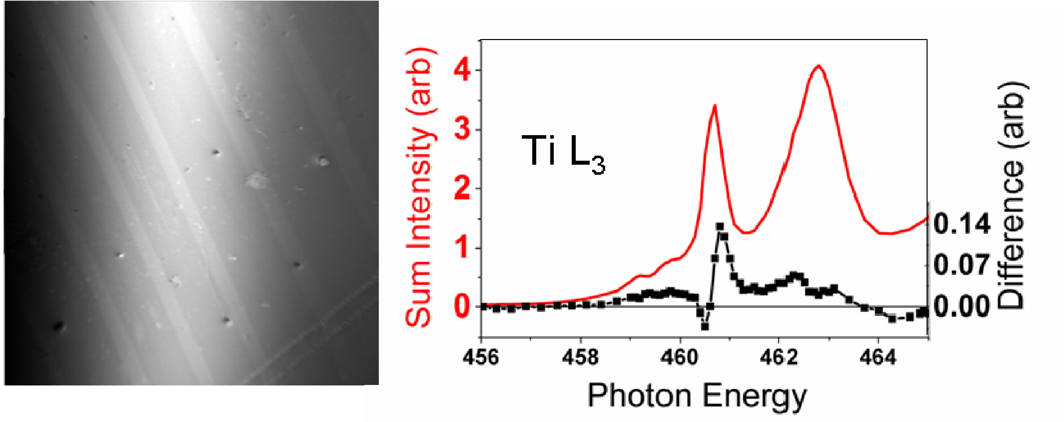

Figure 5.5 – Room temperature 55 micron field of view PEEM image (left) at the Ti L_3 *peak of energy E=460.5 eV, and sum and difference X-ray absorption spectra (right) of light and dark areas in the PEEM image as a function of energy.*

To that end, we have examined (100) BTO substrates with a thin AuPd cap (to reduce charging) to evaluate the piezoelectric domain structure. Although the as-received crystals are oriented, thermal cycling will tend to randomize the domains and thus the state of the BTO substrates after CFO deposition will not be identical to the as-received domain state. Figure 5.5 illustrates light and dark contrast when the BTO surface is imaged, and such stripes are arranged either along [001] or [011] directions for BTO crystals.[148] In this case, the contrast is due to the tetragonal axis of the BTO unit cell being either along the polarization axis of the incident linearly-polarized X-rays or oblique to it. Linear dichroism is only sensitive to the axis of anisotropy and not the direction, so while we can resolve the difference between domains pointing left versus up, we cannot resolve the difference between up and down domains. Integration of either light or dark domains yields energy-dependent spectra that reveal a strong linear dichroism doublet at the first Ti L_3 peak at E=460.5 eV.

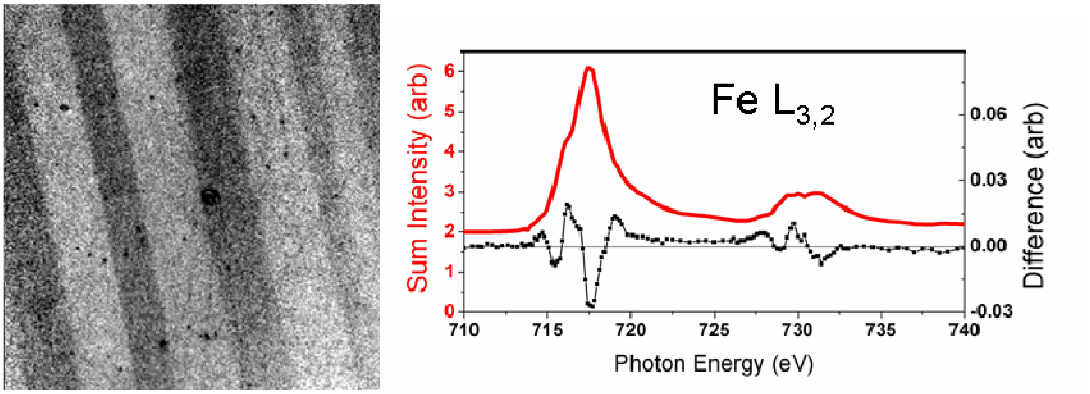

Figure 5.6 – Room temperature 55 micron field of view divided PEEM image (left) at the Fe L_2 edge at energies E=729.5 and 731 eV, and sum and difference X-ray absorption spectra (right) of light and dark areas in the PEEM image as a function of energy.

A twin sample with a thin CFO layer on BTO was measured using the same field of view, and linear dichroism stripes were observed in the CFO material by dividing the images taken at the two sub-peaks of the Fe L_2 edge at approximately 730 eV. Similar evaluation of antiferromagnetic domains were taken for $LaFeO_3$.[57] For CFO, this represents the anisotropy axis of the Fe sublattice. Again, we cannot resolve the magnetization direction of the ferromagnetic domains using linearly polarized X-rays, but we can resolve the strong shift in anisotropy between neighboring elastic domains, and these Fe linear anisotropy domains have the same length scale (~5-10 microns in width) as the piezoelectric domains in BTO.

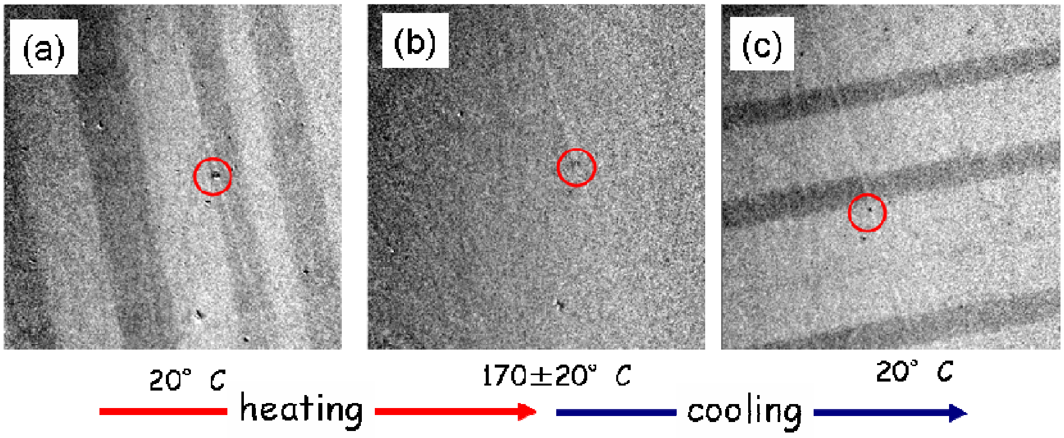

Figure 5.7 - 55 micron field of view divided PEEM images at the Fe L_2 *edge at energies E=729.5 and 731 eV. The circled defect is the same in each image, and the heating of the sample in (b) takes the sample above the BTO substrate ferroelectric Tc~135 °C. The ferroelectric BTO and thus the elastically coupled CFO linear domains randomize between (a) and (c).*

We may also examine these Fe linear anisotropy domains as a function of temperature. In Figure 5.7, the same field of view is monitored as a function of heating from room temperature to 170 °C and then cooling to room temperature again. As mentioned before, the BTO becomes cubic and paraelectric above 410 K, thus we would expect to see a change in anisotropy between room temperature and 170 °C. Indeed, there is a uniformity in the divided image in Figure 5.7 (b) that indicates no preferred anisotropy axis on the 5-10 micron length scale as was seen at room temperature. Due to the large magnetostriction constants of CFO, a small distortion in unit cell from cubic to tetragonal can result in a large change in the magnetic anisotropy energy due to the contribution of the magnetoelastic anisotropy energy term.

However, the film magnetization is still present above 410 K as seen in Figure

5.8, so the disappearance of the Fe stripe anisotropy is not a loss of ferromagnetism but only a change of anisotropy. While we would expect the ferrimagnetic domain structure of the CFO to have its own anisotropy, since the Fe net ferrimagnetic direction per domain could have a projection in any one of four easy in-plane directions or out of the plane of the sample, the length scale of the CFO ferrimagnetic domains is much smaller than the BTO piezoelectric stripe length scale.

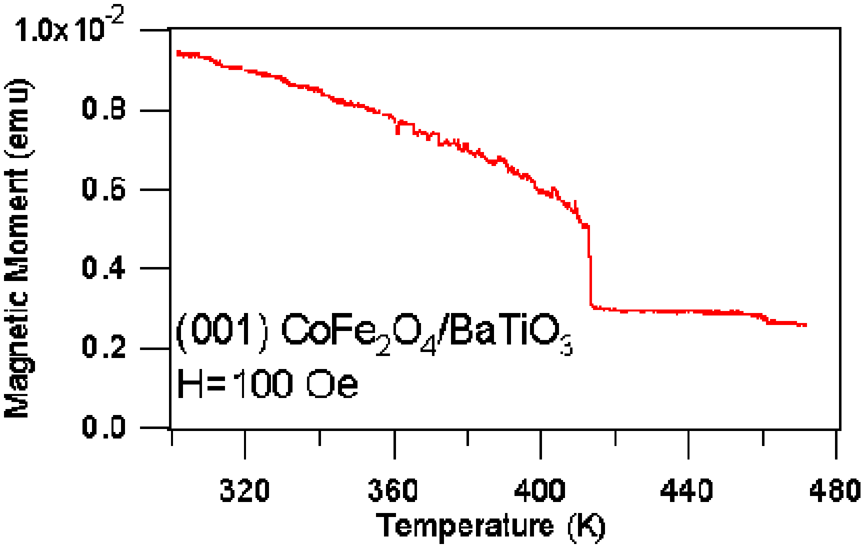

Figure 5.8 – Temperature dependence of moment for a thick CFO on (001)BTO substrate. While the magnitude of the moment changes at the BTO structural transition, the film is still ferromagnetic above the transition.

For comparison, we may examine a (001) CFO film grown on a MAO substrate using magnetic force microscopy to examine the ferromagnetic domain structure without perturbation by the underlying BTO domain structure. In Figure 5.9, the size of the CFO domains is on the order of 250 nm and thus is below the instrumental resolution of the images taken in Figures 5.5-5.7. Note that although the MAO substrate is cubic, the FFT of the domain structure image produces an azimuthally symmetric pattern and the domain wall alignment is not strongly affected by the substrate crystal axes even if the easy in-plane axis is along a (100) direction.

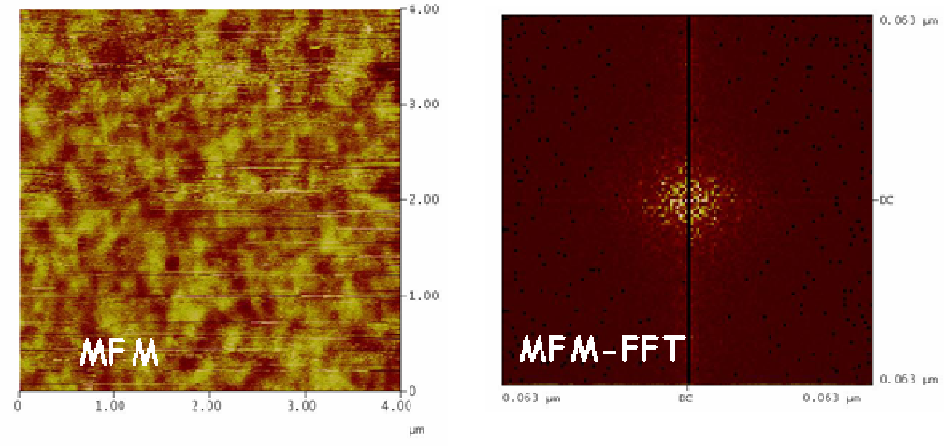

Figure 5.9 – Magnetic force microscope image (left) and fast Fourier-transformed image (right) of a (001)CFO/MAO sample. Note that the FFT is almost azimuthally symmetric.

On the other hand, an examination of a similar CFO sample deposited on (001) BTO shows a much different domain structure as shown in Figure 5.10. Near a BTO domain defect, the CFO magnetic domain structure has an extremely strong fourfold FFT pattern (Figure 5.10 center) which reveals the strong anisotropy coupling between substrate and film. It is not only the Fe anisotropy axis that is pinned to the BTO as shown in Figure 5.7, but the domain walls are affected as well and arrange themselves along the <100> in-plane directions. Away from the defect, the FFT has a weaker fourfold pattern (Figure 5.10, right) but can still be resolved.

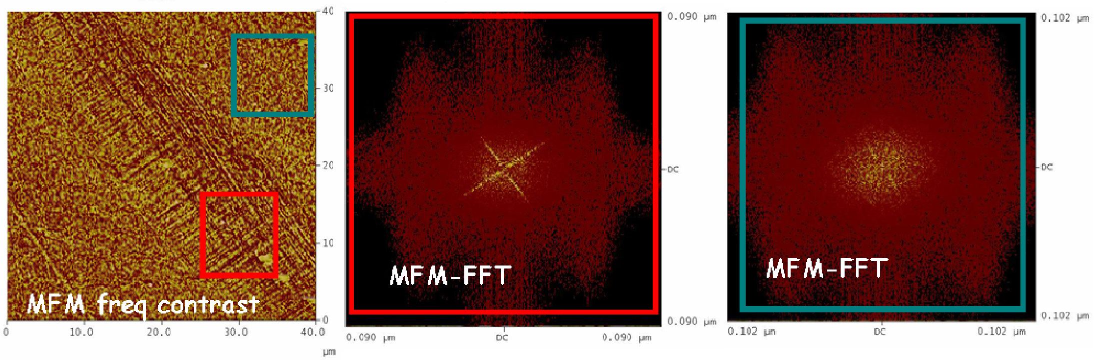

Figure 5.10 – Magnetic force microscope image (left) and fast Fourier-transformed images (right and center) of a (001)CFO/BTO sample. Note that the FFT and thus the domain structure has a strong fourfold anisotropy which matches the <100> in-plane directions.

5.5 Conclusions

In summary, I have synthesized epitaxial $CoFe_2O_4$ films on piezoelectric $BaTiO_3$ single crystal substrates as a model magnetoelectric system. Magnetization versus applied field loops at different temperatures reflect the symmetries of the surface unit cell of the underlying BTO substrate. Magnetization versus temperature plots show abrupt jumps in the magnetization that inversely correlate with the changes in lattice parameters at the structural phase transitions of BTO, thus demonstrating the symmetry of the coupling between CFO and BTO.

The nature of the elastic coupling between the CFO and the BTO strongly affects both the anisotropy of the film as a whole as measured by SQUID magnetometry, but on a microscopic scale the BTO constrains the anisotropy of the CFO on a domain-by-domain basis, and even acts to align CFO domain walls along crystallographic directions.

CHAPTER 6

MAGNETIZATION OF $La_{0.7}Sr_{0.3}MnO_3$ SURFACES AND INTERFACES

6.1 Abstract

The spin polarization of $La_{0.7}Sr_{0.3}MnO_3$ thin films is not intrinsically suppressed at all surfaces and interfaces but is highly sensitive to both the epitaxial strain state as well as the substrate orientation. Through the use of soft X-ray spectroscopy, the magnetic properties of (001), (110) and (111)-oriented $La_{0.7}Sr_{0.3}MnO_3/SrTiO_3$ interfaces have been investigated and compared to bulk magnetometry and resistivity measurements. The magnetization of (110) and (111) -oriented $La_{0.7}Sr_{0.3}MnO_3/SrTiO_3$ interfaces are robust as a function of thickness whereas the magnetization at the (001)-oriented $La_{0.7}Sr_{0.3}MnO_3/SrTiO_3$ interface is suppressed significantly below a thickness of 20 nm. Such findings are correlated with the biaxial strain state of the $La_{0.7}Sr_{0.3}MnO_3$ films; for a given film thickness it is the tetragonal distortion of (001) $La_{0.7}Sr_{0.3}MnO_3$ that severely impacts the magnetization, whereas the trigonal distortion for (111)-oriented films and monoclinic distortion for (110)-oriented films have less of an impact. These observations provide evidence that surface magnetization and thus spin polarization depends strongly on the crystal surface orientation as well as epitaxial strain.

6.2 Introduction

Given the potential of high spin polarization at manganite surfaces,[149] many researchers have used LSMO thin films in magnetic tunnel junctions with mixed results. The figure of merit of magnetic tunnel junctions is junction magnetoresistance (JMR) which should be 100 % for completely spin polarized electrodes. To date, nearly half metallic behavior has been observed in LSMO based junctions at low temperatures by a number of groups but JMR falls quickly with increasing temperature.[150-152] JMR values in (001)-oriented Fe_3O_4 based junctions with $SrTiO_3$ or MgO barrier layers have exhibited JMR only at low temperatures.[31] More recently, the observation of large temperature dependent tunneling in Fe/MgO/Fe junctions and of significant JMR values in LSMO and Fe_3O_4 based magnetic tunnel junctions has prompted a reinvestigation of the nature of magnetism at the surfaces and interfaces of spin polarized materials.[153, 154]

Correlating the structure and the origin of the magnetism from multiple magnetic species at the oxide interfaces is crucial in understanding the nature of magnetism at the surface and interfaces of highly spin polarized materials such as LSMO. Optimally doped LSMO has a rhombohedral perovskite structure where the magnetism is found in octahedrally coordinated Mn^{3+} and Mn^{4+} sites.[155] In order to determine the details of the interface magnetism, element specific and interface sensitive probes such as X-ray absorption spectroscopy (XAS) and X-ray magnetic circular dichroism (XMCD) must be used. XAS and XMCD allows for the determination of interface cation magnetization, valence, and site symmetry.

In this chapter, I present a study of the magnetism at the surfaces and interfaces of (001), (110) and (111)-oriented $La_{0.7}Sr_{0.3}MnO_3$. Detailed spectroscopy experiments indicate that magnetism at the (110) and (111)-oriented LSMO surface is not substantially suppressed while at the (001)-oriented LSMO surface magnetism is significantly suppressed in agreement with previous spin-polarized photoemission experiments.[18] Our results on LSMO surfaces and interfaces, combined with previous results of suppression of magnetization observed in (001) LSMO samples,[18, 21] indicate that spin polarization is not intrinsically suppressed at a surface or interface but that spin polarization at a surface or interface depends on the crystal surface orientation and reconstruction as well as epitaxial film strain.

6.3 Experimental Methods

In order to probe the magnetization at $La_{0.7}Sr_{0.3}MnO_3$ surfaces and interfaces, I have synthesized epitaxial LSMO thin films by pulsed laser deposition on (001), (110) and (111)-oriented $SrTiO_3$ (STO) substrates supplied by Crystec GmbH. Two types of samples with uniform thickness were prepared: 5 nm single layers of LSMO and 50 nm LSMO layers with STO cap layers of 1-2 nm thickness In addition, 10 mm x 5 mm 'wedge' samples were fabricated with a uniform STO cap layer and a LSMO film thickness ranging from 5-40 nm along the sample long axis to study thickness-dependent effects. Commercial sintered powder targets of stoichiometric single-phase oxides were used for ablation at an energy density of 1-1.5 J/cm^2. Deposition parameters for single layers are as follows: LSMO in 320 mTorr of O_2 at 700 °C and $SrTiO_{3-\delta}$ in a 15 mTorr of O_2 at 600 °C. Samples were cooled to room temperature at 10K/min in a 300 Torr O_2 ambient.

Structural characterization of the thin films and bilayers included atomic force microscopy in a Digital Instruments Dimension 3100 microscope to characterize the surface morphology of the deposited films. X-ray diffraction and reciprocal space mapping was performed on a Philips Analytical X'pert MRD diffractometer to study the crystallinity and strain state of the epitaxial layers. Film thickness for both uniform and wedge samples was determined by fitting intensity oscillations around the Bragg peak to the Laue equation. As the beam size in the MRD can be of order 1 mm, the thickness variation across the wedge was confirmed from a 0.2 mm wide collimated beam at beamline 7.2 of the Stanford Synchrotron Radiation Laboratory.

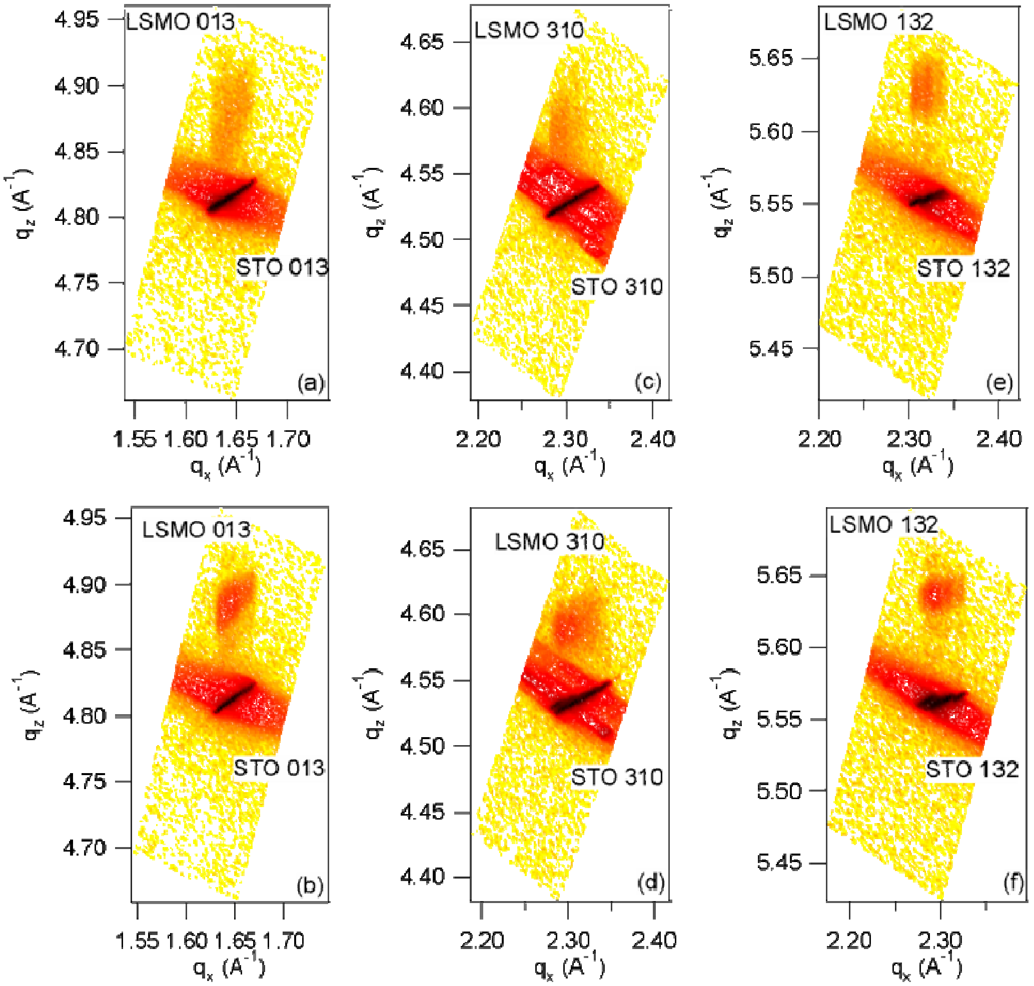

Figure 6.1 – Reciprocal space maps at two ends of the LSMO/STO wedges as a function of orientation: (a) 5 nm LSMO(001), (b) 40 nm LSMO(001), (c) 5 nm LSMO(110), (d) 40 nm LSMO(110), (e) 5 nm LSMO(111), (f) 40 nm LSMO(111).

Field and temperature-dependent magnetization measurements for both single layers and bilayers were performed in a Lake Shore Cryotronics series 7300 Vibrating Sample Magnetometer as well as a Quantum Design MPMS 5XL magnetometer, and resistivity measurements were performed in a modified Quantum Design Physical Property Measurement System. The resistivity of films with uniform thickness were measured using the van der Pauw technique, while the wedge samples were sectioned into ten parts and resistivity was measured by a 4-point-in-line technique.

Soft X-ray absorption spectroscopy experiments in total electron yield (TEY) mode were performed at beamlines 4.0.2[111] and 6.3.1[112] of the Advanced Light

Source (ALS) at Lawrence Berkeley National Laboratory. Spectroscopy experiments were performed with the sample surface normal 60° inclined from the X-ray beam from 25 K–325 K in fields of up to 0.8T. The X-ray beam height was approximately 0.2 mm; thus the quoted thickness for measurements on the wedge samples have an uncertainty in film thickness of 0.6nm.

6.4 Structure

Surface morphology for LSMO single films and bilayers on (001), (110) and (111)-oriented STO was smooth, with maximum RMS surface roughness for 50 nm thick films of 0.223 nm, 0.778 nm and 0.211 nm, respectively. In general, LSMO thin films and bilayers had rougher morphology on (110) STO substrates as compared to (001) and (111)-oriented STO substrates. X-ray diffraction analysis reveals that LSMO films undergo different distortions from the rhombohedral unit cell depending on substrate orientation. In addition, reciprocal space maps of asymmetric reflections for the three orientations at the two extreme ends (5 nm and 40 nm film thickness) of the wedge samples are shown in Figure 6.1. Regardless of film thickness across the wedge, the film is pseudomorphically matched to the in-plane substrate lattice parameter as shown by the same q_x values for film and substrate reflections.

The type and extent of the distortion of the unit cell varies with substrate orientation. The rhombohedral unit cell undergoes a biaxial tensile stress on (001)-oriented STO that imposes a tetragonal distortion on the unit cell. On the other hand, (110) and (111)-oriented STO impose a monoclinic and trigonal distortion of the unit cell, respectively. Thus even with the pseudomorphic nature of the films on all three orientations, the out of plane distortion should differ as a function of orientation due to the anisotropic Young's moduli of LSMO films.[156]

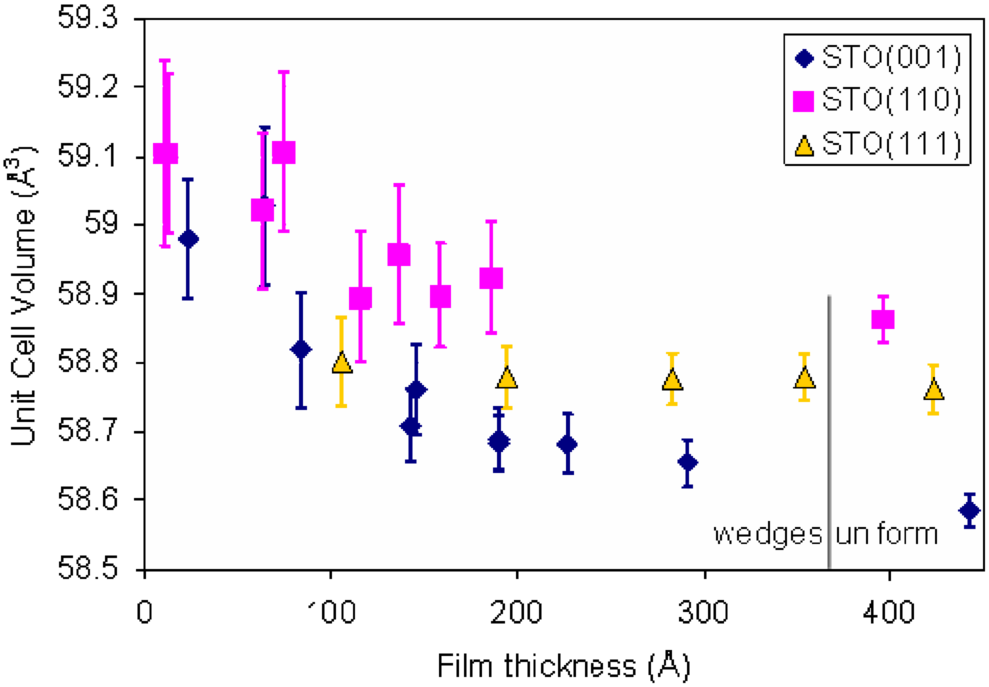

Figure 6.2 – Unit cell volume determined from X-ray diffraction as a function of film orientation for both wedge-type samples as well as LSMO films of uniform thickness. Error bars indicate the full-width of the film reflection at half-maximum intensity.

Calculation of the biaxial moduli[157] for LSMO films based on Darling *et al.*'s tabulated elastic constants on an $La_{0.83}Sr_{0.17}$MnO3 single crystal[158] yields M_{001}=164 GPa, M_{111}=268 GPa, M_{110}^{001}=211 GPa, and $M_{110}^{1\text{-}10}$=279 GPa at T=300K. While the biaxial modulus is isotropic in the plane for (001) and (111)-oriented films, a large difference in modulus exists along the orthogonal in-plane directions for a (110) LSMO film. In spite of the variation in the magnitude of the biaxial modulus, none of the 40nm films relax to the bulk pseudocubic lattice parameter of 3.873 Å,[159] and instead converge towards an out of plane value of 3.84-3.86 Å (Figure 6.2). The relaxed pseudocubic cell volume is approximately 58.1 Å^3 and the distorted cell volume for a 40nm thick film is 1% larger. At small film thicknesses the unit cell volume is not preserved, and thus substantial changes in the magnetic behavior of the films for all three orientations are expected due to out of plane or in-plane changes in the Mn-O-Mn bond angle and bond length.

6.5 Transport

In colossal magnetoresistive manganites, the metal insulator transition is coincident with the magnetic transition as described by the double exchange mechanism.[160] Thus, resistivity measurements may be performed to determine the onset and evolution of both ferromagnetism and metallicity in the LSMO films.

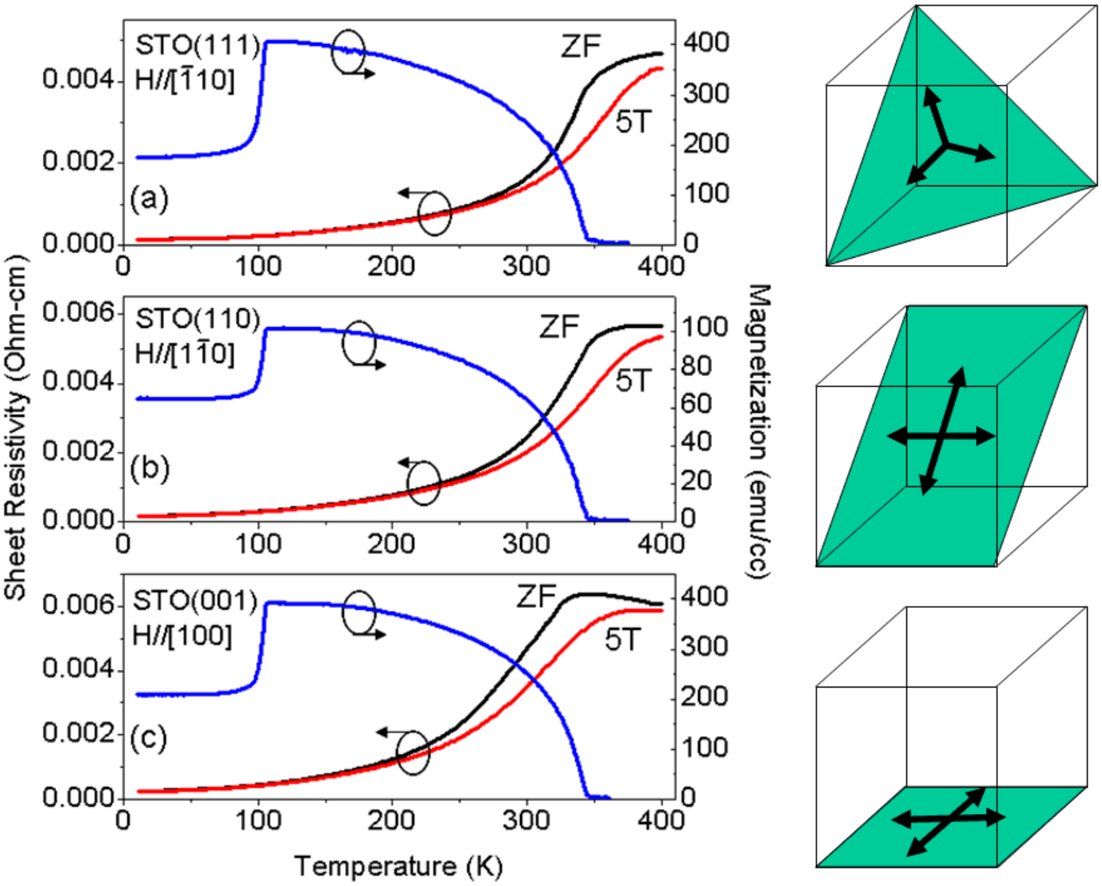

Figure 6.3 – Sheet resistivity and magnetization of 2 nm STO/50nm LSMO bilayers on various orientations of STO. ZF and 5 T refer to resistivity measurements taken in H=0 T and H=5 T with decreasing temperature. Magnetization was measured upon sample cooling in a field of 0.001 T. The corresponding crystallographic planes under strain are indicated on the right.

Figures 6.3(a)-(c) compare the field-dependent sheet resistivity of STO-capped 50 nm LSMO films, and the normalized ratio between resistivity in zero field and in an applied field out of the plane of the sample $MR(H,T)=(\rho(H,T)-\rho(0,T))/\rho(0,T)$

approaches -35% for all three samples at H= 5 T. The peak value in magnetoresistance (MR) is used as a measure of the Curie temperature T_c, and is plotted as a function of sample thickness in Figure 6.4.

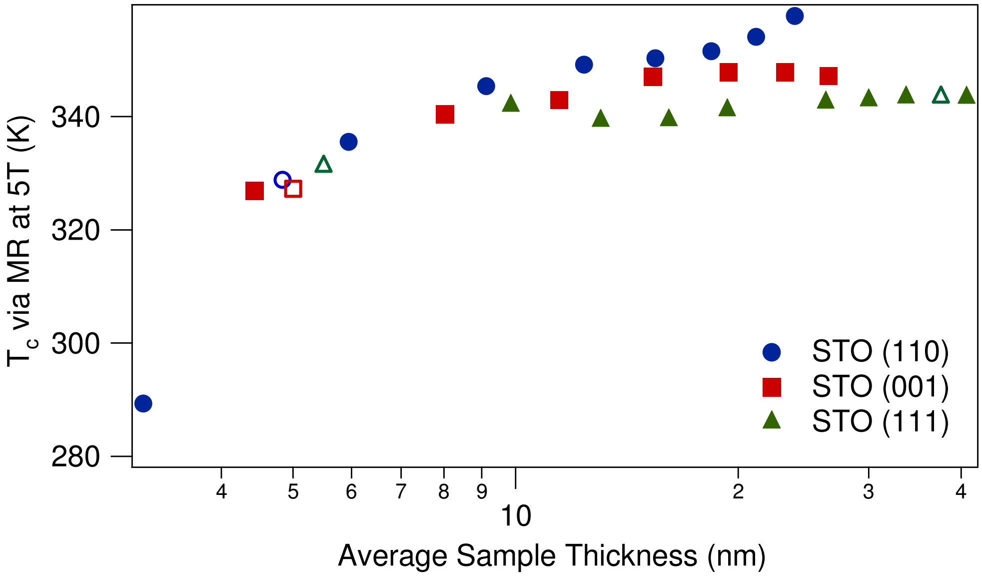

Figure 6.4 –Curie temperature of LSMO thin films determined from the peak in magnetoresistance between zero field and H=5 T as a function of LSMO film thickness. Open shapes are uniform films measured in the van der Pauw configuration, and solid shapes are measured in a 4-in-line contact configuration from 1mm sections of the wedge samples.

Below 8 nm the LSMO transition temperature drops substantially from the bulk value of 360 K for all samples. Above 8 nm, the (111)-oriented LSMO films have a constant transition temperature with thickness which is consistent with the unit cell volume data in Figure 6.2. On the other hand, the (110)-oriented LSMO film transition temperature increases with increasing film thickness without saturating at the largest film thickness on the wedge. Finally, the (001)LSMO films have the largest difference in out of plane lattice parameter compared to bulk, yet the transition temperature above a thickness of 8 nm is consistently larger than its (111)LSMO counterpart. While finite size effects and gradual loss of the ferromagnetic metallic state below 8 nm dominate the transport behavior,[161] above a film thickness of 8 nm crystal orientation plays a large role in determining the transport properties.

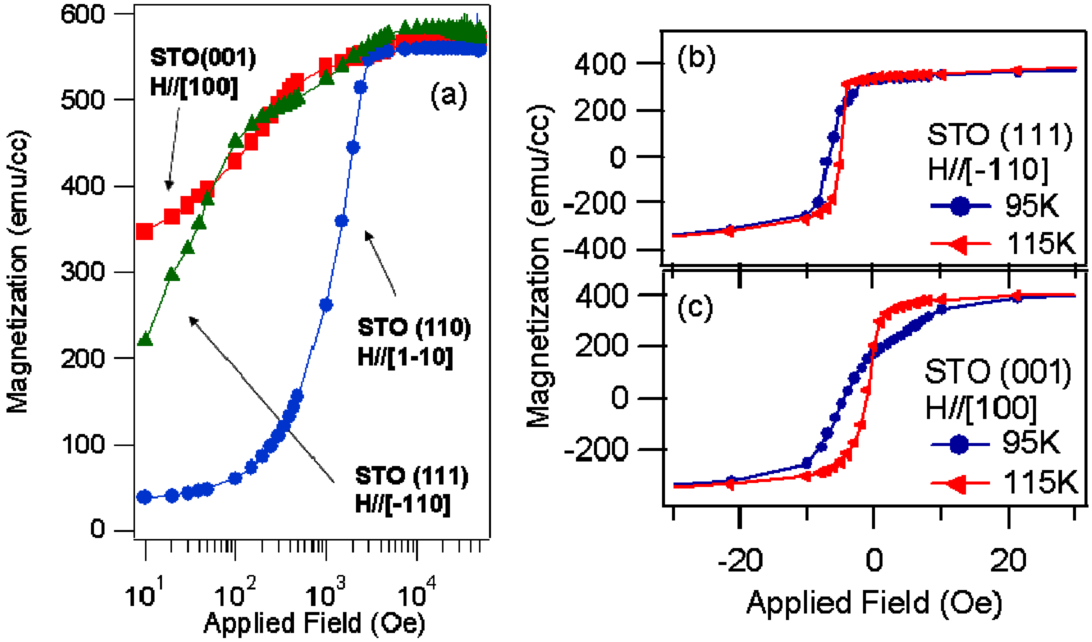

Figure 6.5 – (a) Magnetization at T=10K with decreasing field for (001) (red squares), (110) (blue circles) and (111) (green triangles) -oriented LSMO films. All 3 samples saturate at approximately 580 emu/cc. Low-field magnetization for (b) (111)-oriented and (c) (001)-oriented films show marked differences above and below the structural transition of the STO substrate.

6.6 Magnetism

As the transport properties differ between samples of the same thickness but different orientations, the magnetic properties of such films should also vary due to the double-exchange mechanism. The magnitude of the bulk saturation moment at low temperature for the LSMO x=0.3 stoichiometry is 3.7 μ_B per Mn or 600 emu/cm^3. For comparison, the magnetization as a function of temperature is plotted for 50 nm thick films on STO (111), STO (110), and STO (001) at H=0.001 T in Figure 6.3(a), (b) and (c), respectively. The T_c obtained from the temperature-dependent magnetization data in 0.001 T matches well with the peak in MR. Saturation magnetization of 570-590 emu/cm^3, equivalent to 3.5-3.63 μ_B per Mn, is achieved at fields greater than 5000 Oe at 10 K as shown in Figure 6.5(a). The large two-fold in-plane anisotropy of (110)-oriented LSMO is inferred by the reduced low-field magnetization, but the saturation magnetization is consistent with the other film orientations.

The abrupt decrease in magnetization for all three types of samples in Figure 6.3 at 105 K is coincident with the STO cubic-tetragonal antiferrodistortive transition. While the change in lattice parameter is on the order of 0.1 %, the coherent strain state of the LSMO films is extremely sensitive to such breaking of symmetry as seen by the low-field magnetization data in Figures 6.5(b) and (c). In thick manganite films on STO, strain relief occurs via creation of microtwin domains.[162, 163] While the low field film anisotropy below the transition changes substantially as shown in Figure 6.5, this change is reversible and disappears for temperature-dependent magnetization scans taken at 3000 Oe. No coincident feature is observed in the zero-field resistivity, which suggests that there is no irreversible structural change in the films that would increase boundary scattering or other mechanism to alter transport properties. As near-bulk saturation magnetization can be obtained below this transition, this structural perturbation can be considered as a change in film anisotropy rather than a change in total film magnetization.

A quantitative analysis of the sample magnetization, composed of spin moment m_{spin} and orbital moment m_{orb}, may be extracted from the experimental XMCD spectra through sum rule analysis for the 3d transition metals.[55, 59] However, certain criteria must be met for sum rules to be applicable. For example, samples measured in grazing incidence invalidate the assumption that the total electron yield is proportional to the X-ray absorption coefficient due to electronic saturation effects.[164, 165] In addition, for the lighter *3d* transition metals, the comparatively small energy difference between the L_3 and L_2 absorption edges can lead to *jj* mixing and the transfer of spectral weight between the L_3 and L_2 absorption peaks.[166] Finally, a correction to the spin moment m_{spin} due to magnetic anisotropy from spin-orbit interactions and low-symmetry crystal field effects may not be negligible when calculating the spin moment for magnetic ions in non-cubic symmetry such as at surfaces and interfaces.[167] The correction may be represented by the expectation value of the magnetic dipole operator term $<T_z>$. With this in mind, the relative change in extracted spin moment is calculated as a function of position across the wedge samples, and thus as a function of probe depth into the LSMO layer.

One can evaluate the spin moment ($m_{spin} + 7<T_z>$) and orbital moment m_{orb} using only the integrated intensity of the XAS and XMCD experimental spectra as well as the number of 3d electrons per transition metal cation. However, $7<T_z>$ must be known to calculate m_{spin}. The evaluation of the spin moment may be performed as:

$$m_s^* = \left(m_{spin} + 7\langle T_z \rangle\right) = (10 - N_{3d}) * -{(6p-4q)}\big/{r} \qquad \text{(Eqn. 6.1)}$$

where p is the XMCD integral over the L_3 edge, q is the XMCD integral over both L_3 and L_2 edges, r is the XAS integral over L_3 and L_2 edges with the continuum background subtracted, and N_{3d} is the number of 3d electrons per cation. Without correction for magnetic anisotropy induced from spin orbit interactions or surface effects as represented by $<T_z>$, m_s^* at the thickest portion of all three orientations of wedge layers is approximately 2.75 μ_B per Mn at room temperature at 1500 Oe.

Figure 6.6 shows the room temperature uncorrected spin moment m_s^* for LSMO/STO wedge samples as a function of film thickness. While the spin moment of all three orientations converge towards a maximum value of approximately 2.75 μ_B, it is the (110) LSMO film orientation that approaches the maximum value at the smallest film thicknesses. In contrast to the (110) LSMO interface, Park *et al.* had observed significant suppression of the magnetization at the surface of (001)-oriented 190 nm thick LSMO thin films.[18] Infante *et al.'s* more recent results,[19] indicating a difference in temperature dependence and Curie temperature of (001) and (110) LCMO thin films, are consistent with the more robust magnetization that is observed at the (110)

LSMO surface as compared to the (001) LSMO surface studied by Park *et al.*

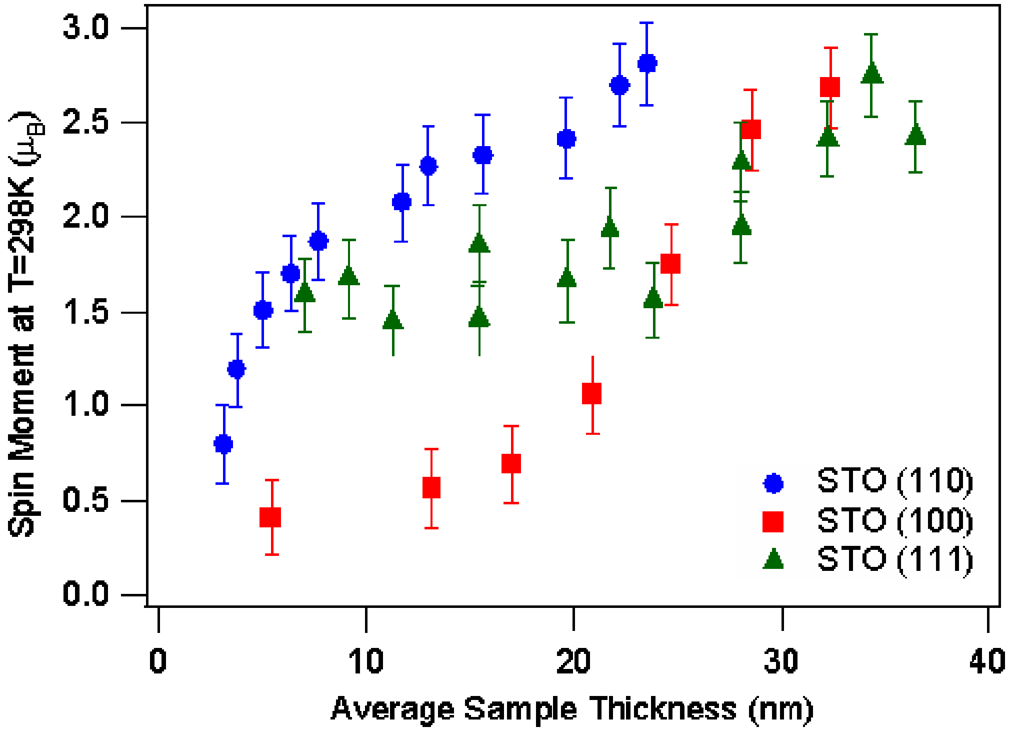

Figure 6.6 – Room temperature uncorrected spin moment m_s^* derived from XMCD spectra using sum rule analysis for LSMO films of various orientations as a function of thickness. Above 8 nm, all films had similar transport properties yet the surface magnetization differs substantially.

The dependence of spin polarization on the crystallographic orientation of LSMO suggests that the mere presence of a surface or interface does not necessarily suppress the spin polarization in these materials. Experimentally, the (110) $[ABO]^{4+}$ surface of the perovskite appears to be more robust magnetically compared to the AO or BO_2 planes of the (001) surface. This robustness stems in part due to the strong driving force to relieve strain that in turn affects the B-O-B exchange interaction.[168] Lebedev *et al.* found that microtwinning of the $La_{0.84}Sr_{0.16}MnO_3$ film on a (110)STO substrate occurred due to corrugation of the nominal (110) surface into (001) planes, thus allowing for strain relaxation without the need for the formation of interfacial misfit disloations.[169] It should be noted that the (001) ABO_3 cubic perovskite stacks with alternating [AO] and [BO_2] layers while the (110) orientation stacks with alternating $[ABO]^{4+}$ or $[O_2]^{4-}$ planes of atoms,[68, 170] and the (111) orientation stacks with alternating $[AO_3]^{3-}$ and B^{3+} planes.[171] The polar (110) and (111) surfaces may be more susceptible to reconstruction and hence strain relaxation.

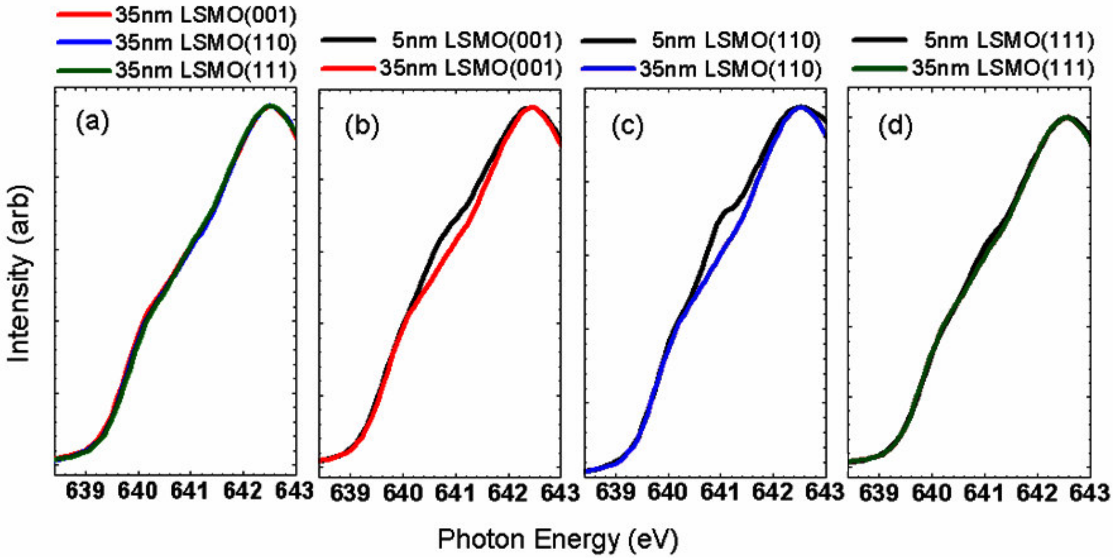

Figure 6.7 – Mn L_3 X-ray absorption spectra as a function of film orientation. While the lineshapes for the 35 nm thick films (a) lie on top of each other, there is substantial difference in the lineshape for the (b) (001) and (c) (110)-oriented 5 nm LSMO films. In comparison, the (111)-oriented sample (d) shows little change in lineshape as a function of thickness.

A further examination of the room-temperature Mn L_3 XAS in Figure 6.7 illustrates that 35 nm films of all orientations exhibit identical lineshapes which implies the same chemical environment exists at those LSMO/STO interfaces. As film thickness is decreased below 35 nm, the Mn L_3 lineshape changes substantially for both (001) and (110) film orientations. de Jong *et al.* attribute a feature on the low photon energy side of the Mn L_3 absorption edge as originating from Mn^{2+},[172] but the suppression of magnetization for (001) films and retention of magnetization for (110) films point to the changing symmetry of the Mn environment under epitaxial strain as the cause of this change in Mn L_3 spectral weight.

The difference in the unit cell volume for thin films of different orientations combined with the above change in spectral weight for the Mn L_3 lineshapes suggest that the Mn environment varies both as a function of strain and film orientation. Examination of strained (La,Ca)MnO_3 films illustrated that Mn-Mn cation distances and thus Mn-O bond angles varied under epitaxial strain.[173] A change in Mn-O bond angle results in variation of the double exchange transfer integral and thus directly affects both transport and magnetization properties. Clearly, the changes in structural symmetry due to epitaxial strain give rise to significant variations in surface spin polarization in LSMO, with the larger strain in thinner films resulting in substantial differences in spin moment at the surface. This variation can, in turn, be exploited by choosing (110) and (111)-oriented films that achieve near-bulk magnetization for devices such as magnetic tunnel junctions in which the interface spin polarization plays a dominant role in determining device properties.

6.7 Conclusions

In summary, magnetism at the (110) and (111)-oriented LSMO/STO interfaces is robust and bulk-like while (001)-oriented LSMO interfaces have suppressed magnetization. Both magnetization and spin polarization depends on the crystal surface plane and is not equally suppressed for all surfaces or interfaces. In particular, devices with (110)LSMO electrodes should provide larger figures of merit such as junction magnetoresistance combined with strong uniaxial magnetic anisotropy compared to (001) and (111) LSMO electrodes.

CHAPTER 7

MAGNETISM AT ISOSTRUCTRUAL Fe_3O_4/CHROMITE INTERFACES

7.1 Abstract

Magnetism and coupling at the interface of highly spin polarized Fe_3O_4 heterostructures has been evaluated by surface sensitive and element specific soft X-ray spectroscopy and spectro-microscopy techniques. At the interface between paramagnetic $CoCr_2O_4$ or $MnCr_2O_4$ and ferrimagnetic Fe_3O_4 isostructural bilayers, long range induced magnetic order of Co, Mn and Cr cations is induced by the adjacent Fe_3O_4 layer. Magnetism at the interface region exceeds the chromite bulk Curie temperature of 55-95 K and is observable at room temperature. Structural characterization via scanning transmission electron microscopy indicates that this magnetism cannot be explained in terms of interdiffusion at the interface. Temperature-dependent analysis of spectroscopy data reveals that the interaction at the nominal ferrimagnet-paramagnet interface is robust and an induced polarization of the paramagnet cations persists up to 500 K.

7.2 Introduction

Studies of ferromagnetic interfaces have resulted in the discovery of new coupling phenomena and associated technological device since Meiklejohn and Bean discovered exchange coupling between ferromagnetic Co and antiferromagnetic CoO in 1956.[174] Short-range exchange interactions tend to keep magnetic moments in the two materials oriented with respect to one another. Since the original discovery of exchange coupling, exchange phenomena have been extensively studied at ferromagnetic interfaces. Examples include Rudderman-Kittel-Kasuya-Yoshida coupling in metallic multilayers that exhibit giant magnetoresistance (GMR),[175] positive exchange bias in FeF_2-Fe bilayers,[176] and perpendicular exchange coupling in Co/Pt multilayers.[177]

Beyond metallic elements and alloy materials, the complex oxide family of spinel structure ferrites has provided model systems for the study of phenomena such as modified superexchange interactions,[102] perpendicular exchange coupling[178] and nearly ideal exchange interactions.[14] Margulies *et al.* showed that modified superexchange interactions across antiphase boundaries give rise to anomalously large saturation fields and quasi-random zero-field magnetic moment distribution. Ijiri *et al.* demonstrated perpendicular coupling of antiferromagnetic CoO spins with the net Fe_3O_4 moment in Fe_3O_4/CoO superlattices via neutron diffraction experiments. Nearly ideal exchange coupling has been observed in bilayers of hard and soft spinel ferrite layers, suggesting that in some materials systems simple theoretical models may be applied. In $(Mn,Zn)Fe_2O_4/CoFe_2O_4$ bilayers, the exchange interaction between the two materials is as strong as the exchange interaction within each material.[14] This isostructural interface between a soft and hard ferrimagnet is particularly robust to extrinsic factors such as random surface roughness that would otherwise suppress interface exchange coupling between a ferromagnet and an antiferromagnet. However, by the same token, it is difficult to probe the nature of magnetism in the two isostructural ferrite materials at the interface due to the presence of Fe in both layers.

Recently, isostructural spinel bilayers have been used in magnetic tunnel junctions, resulting in significant improvements in junction magnetoresistance.[28-30] In these bilayers, magnetite (Fe_3O_4) electrodes were combined with a variety of lattice-matched spinel barrier layers, such as $CoCr_2O_4$ and $NiMn_2O_4$. The magnetically harder $CoCr_2O_4$ and $NiMn_2O_4$ strongly coupled to the softer Fe_3O_4 above and below their respective Curie temperatures (T_c), thus creating a hybrid magnetic tunnel junction/spin filter device. This new device's multifunctional behavior is possible due to the strong magnetic coupling at the isostructural spinel-spinel interface and no magnetic coupling at the non-isostructural perovskite-spinel interfaces. An explanation of the lack of magnetic coupling on one side of the barrier and strong coupling on the other requires a fundamental understanding of the interface exchange coupling.

In such complex oxides, correlating the structure and the origin of the magnetism from multiple magnetic species at the oxide interfaces is crucial in explaining the large JMR and strong exchange coupling observed in Fe_3O_4 based heterostructures. In order to determine the details of the interface magnetism, element specific and interface sensitive probes such as X-ray absorption spectroscopy (XAS) and X-ray magnetic circular dichroism (XMCD) must be used. Such probes can determine interface cation magnetization, valence, and site symmetry, while field-dependent and element-specific hysteresis loops along different in-plane crystallographic directions highlight the anisotropy of the interface moments. Local structural probes such as scanning transmission electron microscopy (STEM) complement the soft x-ray techniques and shed light on the high figures of merit for these epitaxial complex oxide heterostructures.

In this chapter, I will discuss the magnetism at the isostructural spinel interfaces of ferromagnetic insulator Fe_3O_4 and paramagnetic insulators CCO and MCO. There is induced magnetization of a PM insulator by an adjacent FM insulator up to 500 K in these systems. Both structural analysis via STEM and chemical and magnetic analysis via XAS/XMCD provide a local probe to obtain a comprehensive picture of the complex magnetic interactions at the isostructural spinel interface. Small structural and chemical roughness at the interface does not explain the robust and high-temperature magnetic behavior at the ferrimagnet-paramagnet interface, and thus magnetization is induced in the paramagnetic layer via a proximity effect to the isostructural ferrimagnet.

7.3 Experimental methods

In order to probe both isostructural interfaces, I have synthesized epitaxial thin films and multilayers of metallic Fe_3O_4 as well as insulating $CoCr_2O_4$ and $MnCr_2O_4$ (MCO) grown by pulsed laser deposition on (110) oriented $SrTiO_3$ (STO) and Nb-doped STO substrates. Four sets of samples with uniform thickness were prepared: 20 nm single layers of magnetite, 40 nm single layers of chromite spinel, 20 nm magnetite with various thickness of chromite cap layer (3-18 nm), and 40 nm chromite layers with a 5 nm magnetite cap layer. Commercial sintered powder targets of stoichiometric single-phase oxides were used for ablation at an energy density of 1-1.5 J/cm^2. Deposition parameters for single layers are as follows: Fe_3O_4 in a vacuum of better than $4x10^{-6}$ Torr at 450 °C, and MCO and CCO in 25 mTorr of O_2 at 600 °C. In order to prevent magnetite from oxidizing during growth of subsequent layers grown in an oxygen ambient, the deposition of the Fe_3O_4 layer was followed by a 1 monolayer of chromite deposition in vacuum and then the remainder of the chromite layer grown in 25 mTorr of a 1% O_2 / 99% N_2 mixture. Reference spectra were taken on a single crystal sample of $CoFe_2O_4$ (CFO) as well as an Fe_3O_4 film deposited on (110)$MgAl_2O_4$ under similar deposition conditions to the Fe_3O_4/STO samples.

Structural characterization of the thin films included atomic force microscopy to characterize the surface morphology of the deposited films, 2 and 4-circle X-ray diffraction to study the crystallinity of the epitaxial spinel layers deposited on perovskite substrates, and Rutherford Backscattering Spectrometry (RBS) to assess film thickness and composition. Further characterization of the oxide interfaces were performed via transmission electron microscopy (TEM) as well as STEM with electron energy loss spectroscopy (EELS).

Temperature and field-dependent magnetization measurements for both single layers and bilayers were performed in a Quantum Design MPMS 5XL magnetometer with field oriented along the [001] in-plane direction for (110) oriented films. Soft X-ray absorption spectroscopy experiments in total electron yield mode were performed at beamlines 4.0.2[111] and 6.3.1[112] of the Advanced Light Source (ALS) at Lawrence Berkeley National Laboratory, and spectro-microscopy measurements took place at the PEEM2 microscope (beamline 7.3.1.1)[179] of the ALS. Spectroscopy experiments were performed from 10 K–300 K in fields of up to 0.8 T, while microscopy was performed at 300 K-550 K in zero magnetic field. The incident X-ray propagation vector was projected onto the [001] or [1-10] in-plane crystallographic direction of the sample.

7.4 Structural characterization of interfaces

Surface morphology for spinel single films and bilayers on (110)STO substrates was smooth, with maximum RMS surface roughness of 0.9 nm (on the order of the spinel lattice parameter). Four circle X-ray diffraction analysis indicated that each component layer was single phase and epitaxially matched to the underlying (110) substrates. While RBS analysis confirmed the stoichiometry of the 40nm single layers, the composition of 10nm and thinner layers and any interdiffusion in such layers could not be quantified via RBS alone.

TEM analysis in our previous study has indicated that the interfaces were chemically distinct to within the 2 nm probe size,[106] but interface roughness could induce magnetic coupling between electrodes across a thin insulating barrier layer due to so-called orange-peel coupling.[180] In order to assess the possible role of structural roughness at these oxide interfaces, cross-section samples of multilayers were prepared for TEM and STEM analysis. Figure 7.1 (a)-(d) focus on micrographs and

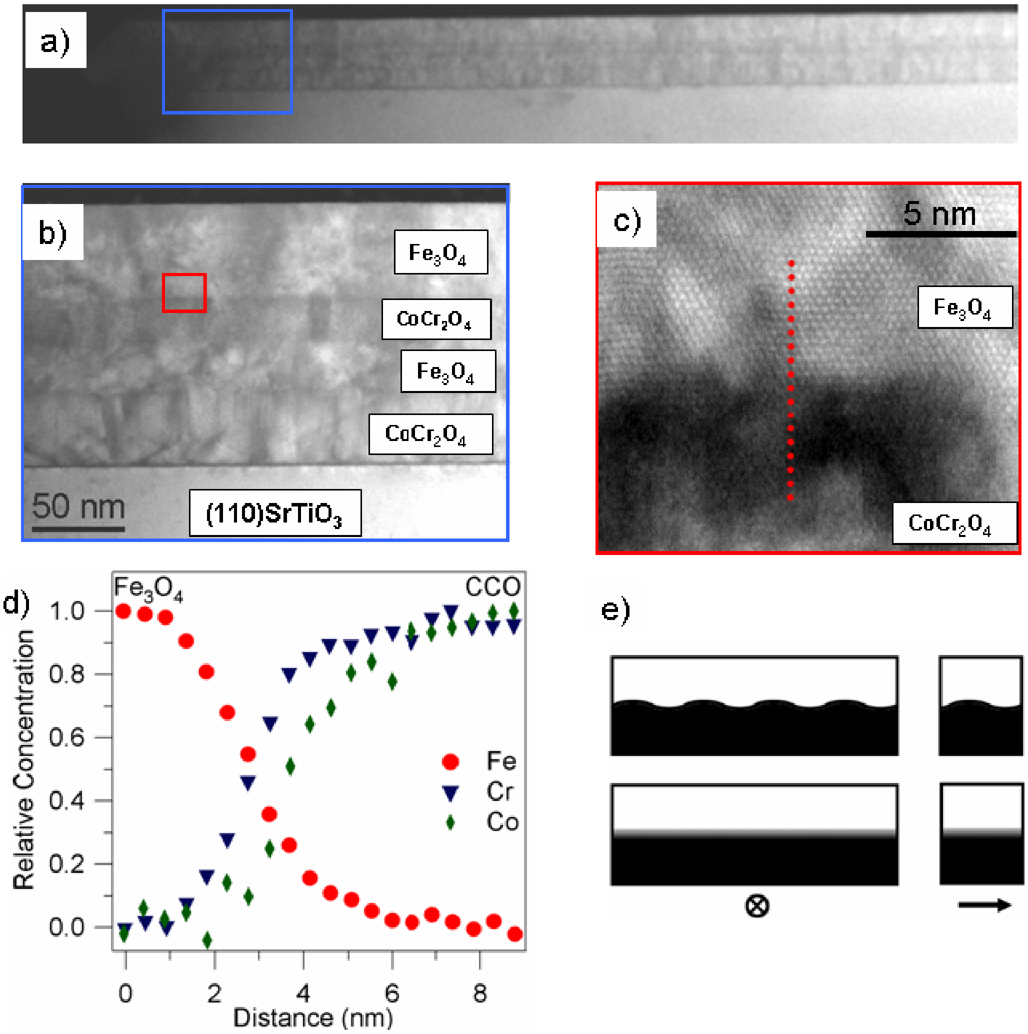

Figure 7.1 –High-angle annular dark field STEM images of a Fe_3O_4/CCO multilayer: (a) low magnification, (b) mid magnification, (c) high magnification, and (d) integrated EELS intensity for Fe, Cr, and Co edges across the dotted line indicated in (c). Two possible cases of interface roughening are illustrated in (e), with the top schematic indicating a chemically distinct but structurally rough interface and the bottom indicating a chemically interdiffused interface. The arrow indicates the direction of the incident electron beam.

EELS linescans at the upper isostructural spinel-spinel interface for a STO(110) // 41 nm CCO // 26 nm Fe_3O_4 // 24 nm CCO // 43 nm Fe_3O_4 sample. While defects such as low-angle grain boundaries occur in the spinel layers due to the large (-7%) lattice mismatch between the spinel unit cell and the STO substrate, the film are crystalline with all grains matched to the (110) out of plane orientation of the substrate. Examination of the Fe_3O_4-CCO interface shows distinct layers in the low magnification high-angle annular dark field STEM images, but chemical mapping of the interface (Figure 7.1 (d)) shows a lack of sharp chemical transition between the spinel layers, and the transition width is of order 2 nm from the nominal interface.

If there is little divergence of the electron beam as it passes through the sample, two limiting cases could be responsible for the 4 nm wide elemental transition at the spinel interface. Figure 7.1 (e) illustrates these cases: the initial layer may have roughness due to three-dimensional film growth followed by conform growth of the second layer (top schematic), or the initial layer may have had a smooth surface but the energetics of the second layer's growth have induced an interdiffusion at the interface (bottom schematic). It is likely that the sample has contributions from both cases as the large epitaxial misfit strain can induce defects such as the low angle grain boundaries seen in the STEM micrographs, and the highly energetic PLD plume may accelerate diffusion of the layers. Keller *et al.* had seen similar interdiffusion in multilayers of antiferromagnetic NiO and α–Fe_2O_3 and the formation of a ferrimagnetic $NiFe_2O_4$ layer at each NiO/α–Fe_2O_3 interface.[181] The temperature dependence of the $NiFe_2O_4$ formation revealed that interface diffusion was facilitated both by the elevated growth temperature and the high kinetic energies of the plume species during the pulsed laser ablation process. Since similar growth parameters were used for the samples in this study, it is not surprising that this nanometer-scale interdiffusion between cations in the adjacent spinel layers occurred. As the deposition rate of the 43 nm top Fe_3O_4 layer was slower than that of the CCO or MCO layers under study, the STEM sample was held at 450 °C for a longer duration than the bilayers examined with XAS and XMCD. Thus, 4 nm represents an upper bound for the size of the intermixed region if one assumes that the EELS elemental concentration transition width is wholly due to interdiffusion during PLD process.

From the relative concentrations of the cations as measured by EELS linescans, the stoichiometry of the spinel material on both tetrahedral (A or T_d) and octahedral (B or O_h) sublattices can be estimated from equilibrium site preferences of Mn, Cr, and Co in the Fe_3O_4 host. As the interface material is primarily a mixture of Cr and Fe, magnetic behavior should be dominated by material with composition $Fe^{2+}Cr_{2-x}Fe^{3+}{}_xO_4$ and modified by the presence of Co or Mn. Robbins *et al.* examined the magnetite-chromite solid solution and found that while the Curie temperature monotonically decreased with increasing Cr, the shift from normal spinel $FeCr_2O_4$ to inverse spinel Fe_3O_4 produced non-monotonic dependence of lattice parameter on x which was correlated with substitution of tetrahedral Fe^{2+} for x~0 (the 'normal' spinel $FeCr_2O_4$) with tetrahedral Fe^{3+} for x~2 (the inverse spinel Fe_3O_4).[182]

Using XAS and XMCD we may examine the valence and site symmetry of Co, Cr, Mn and Fe and determine whether or not such equilibrium cation distributions are also valid for the case of the interdiffused interface material at the isostructural spinel interfaces. As these techniques are sensitive to the surface 5 nm of the sample due to the small size of the photoelectron escape depth, I have grown bilayers with either Fe_3O_4 or chromite as the top layer to examine the dominant magnetic species on either side of the Fe_3O_4-chromite interface. If the depth of intermixing is on the order of the 5 nm probe depth, similar cation valence and site symmetries are expected regardless of the placement of Fe_3O_4 as the top or bottom layer. However, if the intermixing is smaller than the probe depth then one would expect to see a difference in cation valence and site symmetry with the chromite layer adjacent to the substrate as contrasted with the chromite layer as the surface layer.

7.5 Magnetic characterization of interfaces

Figure 7.2(a)-(c) shows the temperature dependence of the maximum dichroism at the Fe, Co and Cr edges as well as the bulk magnetization as measured by

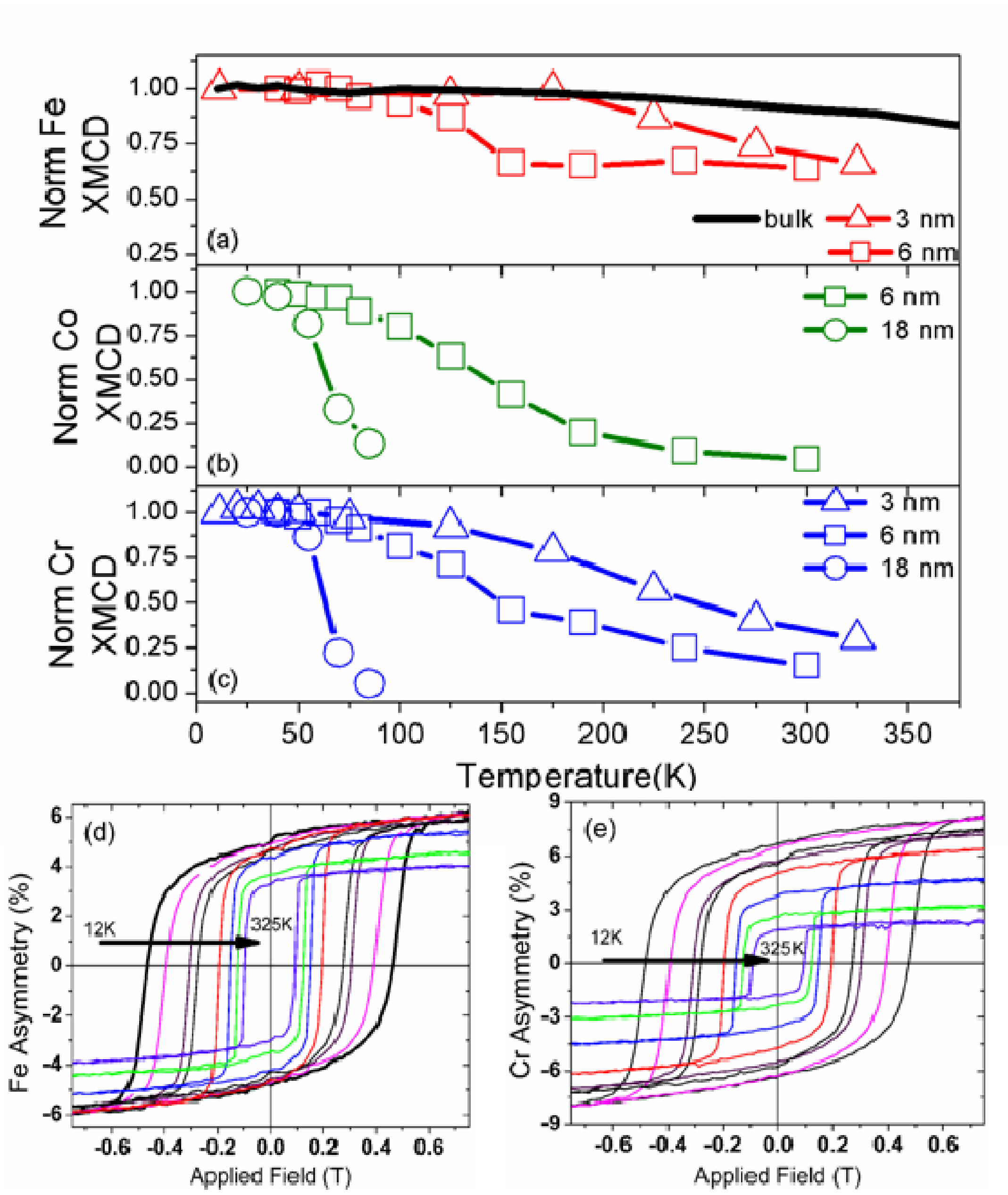

Figure 7.2 – Temperature dependence of the saturation magnetization for a CCO cap layers on Fe_3O_4 as measured by a SQUID magnetometer (solid line, 3 nm CCO cap sample) and saturation asymmetry of XMCD signal measured on (a) Fe, (b) Co, and (c) Cr $L_{3,2}$ edges normalized to 12 K values. Element specific hysteresis loops were taken on (d) Fe L_3 and (e) Cr L_3 edges for the 3nm CCO cap sample to verify magnetic saturation at all temperatures.

SQUID magnetometry of a 3 nm CCO / 20 nm Fe_3O_4 bilayer. All values are normalized to data taken at 15 K. For comparison, single layer chromite films had bulk-like magnetic properties: T_c=95 K for CCO with a coercive field of 2 T and a saturation magnetization of 0.23 μ_B/formula unit at 5 K, and T_c=55 K for MCO with a coercive field of 1000 Oe and saturation magnetization of 0.97 μ_B/formula unit at 5 K. The entire CCO layer of the 3 nm CCO/Fe_3O_4 bilayer is probed but only a few nm of the Fe_3O_4 close to the interface is measured. Element-specific coercive fields were also extracted from XMCD hysteresis measurements. Both the Cr and Fe edge coercive fields match as a function of temperature, although the magnitude of the Cr dichroism falls more quickly than the Fe edge dichroism (Figure 7.2 (d) and (e)). The normalized Fe and Cr XMCD signals for the 3nm CCO cap layer decreased more quickly as a function of increasing temperature above 175 K than as measured by SQUID magnetometry (Figure 7.2 (a), solid line). The persistence of magnetization in the Cr signal above room temperature, and hence above the T_c of bulk CCO, is surprising if one assumes a chemically sharp interface between the two spinel oxides and no influence of the Fe_3O_4 on CCO above T_c=95 K. Similar XMCD measurements of 18nm CCO/Fe_3O_4 bilayers probed CCO away from the Fe_3O_4 interface and showed only bulk-like magnetism that disappears by approximately 80 K (Figure 7.2 (b) and (c)) due to the thickness of the CCO exceeding the mean XMCD probing depth.

Magnetic domain images were taken of uncapped and chromite capped Fe_3O_4 layers at the PEEM2 photoemission electron microscope of the ALS. Both MCO and CCO capped Fe_3O_4 layers confirmed two-fold in-plane anisotropy of the samples, with easy axis along the in-plane [001] for the 3 nm CCO/Fe_3O_4 sample as measured by vibrating sample magnetometry. Fe_3O_4 domains ferromagnetically coupled to Cr in CCO capping layers of thickness 3nm (Figure 7.3(a) and (b)) and 6 nm with identical domain structure between the Cr and Fe edges. The domain structure in CCO persisted up to 500 K on the Cr L_3 edge, well above the T_c of bulk CCO, but cannot be

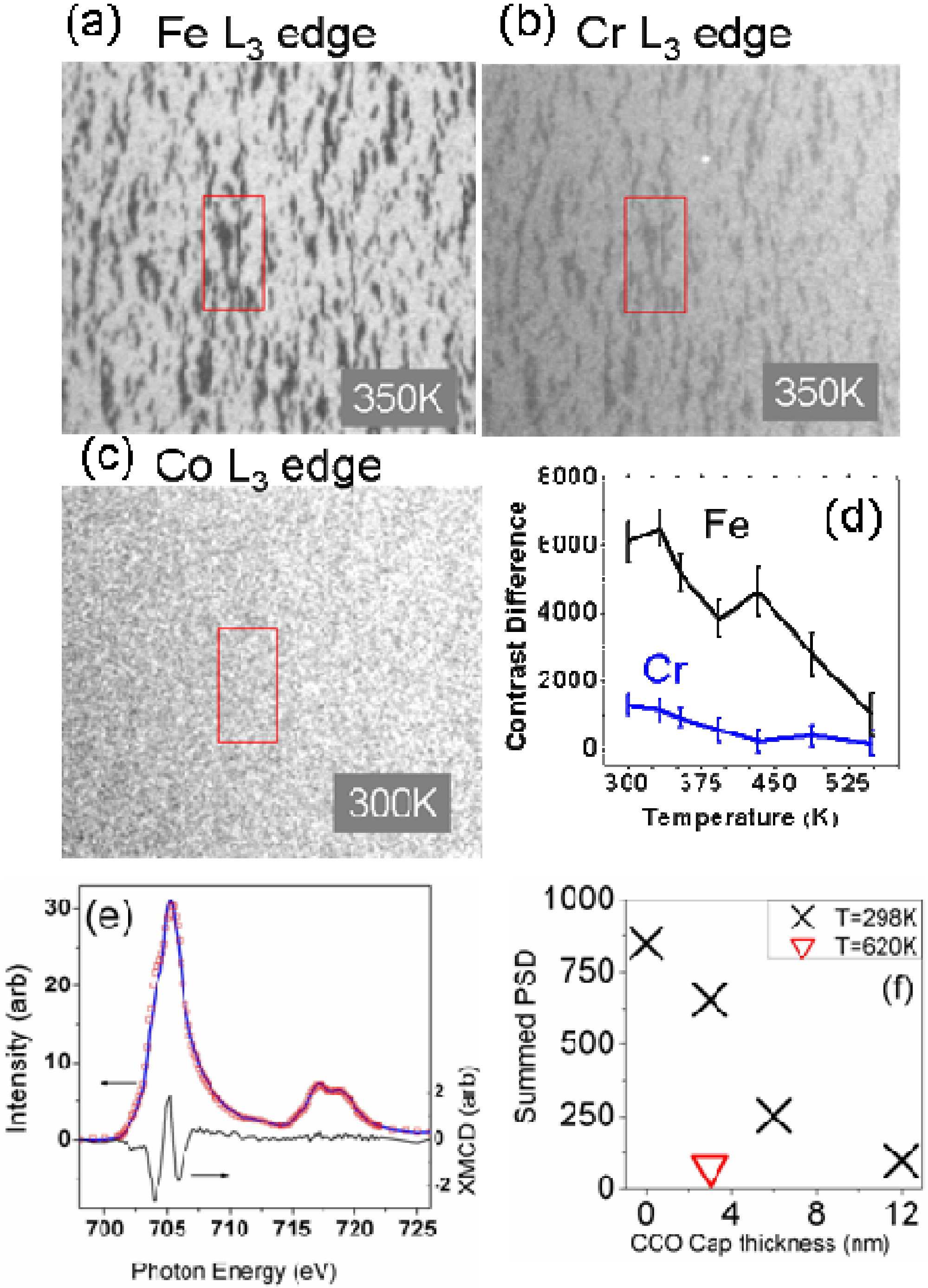

Figure 7.3 – PEEM domain images from a 3nm CCO/Fe_3O_4/(110)STO sample at T=298 K. The boxed region shows identical domain structure with same polarity on the Fe (a) and Cr (b) edges, but no detectable polarization of Co (c). Contrast difference as a function of temperature (d) shows magnetization up to 550 K. Room temperature Fe spectroscopy (e) on dark domains (solid line) compared to light domains (open squares) with resulting XMCD difference. (f) Summed power spectrum density of PEEM domain images as a function of CCO cap thickness.

seen on the Co L_3 edge even at 300K to within the experimental resolution of the microscope. The difference in contrast for light and dark areas in Figures 7.3 (a) and (b) as a function of temperature is plotted in Figure 7.3(d). While the domain structure at elevated temperatures remained identical to the room temperature domain structure for both Cr and Fe L_3 edges, the contrast between light and dark areas, equivalent to the magnitude of difference for an XMCD spectrum, fell to below the noise floor of the measurement by 540K.

Integration of domain areas as a function of photon energy produced spatially localized spectra as shown in Figure 7.3(e), with the solid line corresponding to X-ray absorption of the dark areas of the boxed region in Figure 7.3(a), and the difference in absorption of light areas compared to dark areas producing a spectrum similar to the single layers of Fe_3O_4.[183] Thus the area-averaged results from the spectroscopy measurements are identical to the micron-scale spectro-microscopy measurements, and in addition uniform domain structure and dichroism appears across the 20 micron field of view used in Figures 7.3(a)-(c). Samples of different CCO cap thickness had varying average domain structures, so the contrast between light and dark regions was not used to directly compare interface magnetism as was done in the temperature series of the 3 nm CCO sample. Instead, the domain images were Fourier transformed, and the power spectrum density for the radially averaged transforms was summed for low wavenumbers to filter out noise below the 100nm instrumental resolution of the microscope. The summed power spectrum density (PSD), equivalent to the contrast difference in Figure 7.3(d), is shown in Figure 7.3(f) for room temperature measurements of an uncapped Fe_3O_4 sample as well as samples with CCO caps of 3 nm, 6 nm, and 12 nm. Interfacial Fe moments are magnetic at room temperature and have similar domain structure to a single layer Fe_3O_4 sample. The magnetism of a buried Fe_3O_4 layer may be resolved through a 6nm CCO cap layer, but beyond that thickness the photoelectron escape depth is too small to measure substantial chemical or magnetic information. The magnetism in these interface moments falls to below the detection limit of the microscope by 620 K which is far above room temperature but below the bulk Fe_3O_4 T_c of 860 K.

In order to understand the origin of the enhanced long range order observed in chromite caps on Fe_3O_4, I examined in detail the XAS and XMCD spectra of the Fe, Cr, Co, and Mn $L_{2,3}$ edges. Figure 7.4 compares the Fe $L_{2,3}$ XMCD spectra for Fe_3O_4 with various spinel capping or buffer layers with a single layer Fe_3O_4 sample as reference. Multiplet calculations have been compared to experimental dichroism spectra from Fe in various spinels,[49] and the dominant contribution of each peak as seen in Figure 7.4 can be assigned as follows: 708.9 eV as octahedral Fe^{2+}, 709.9 eV as tetrahedral Fe^{3+}, and 710.8 eV as octahedral Fe^{3+}. Air exposure is known to oxidize the surface of Fe_3O_4 and reduce the relative amount of octahedral Fe^{2+} with respect to the amount of Fe^{3+}.[56] This oxidation results in a reduction in spectral weight at the first XMCD peak at 708.9 eV for the uncapped Fe_3O_4 (Figure 7.4(a)) as well as the Fe_3O_4 layers on CCO and MCO (Figure 7.4(c)) compared to the Fe_3O_4/STO bilayer (Figure 7.4(a)). In addition, the presence of Mn reduces the tetrahedral Fe^{3+} 709.9 eV peak in Figure 7.4 (b) and (c) when compared to similar CCO samples, which indicates that Mn is displacing the interfacial tetrahedral Fe^{3+} in a similar manner to more bulk-like manganese ferrites and ferrichromites.

XAS and XMCD on Cr, Mn and Co $L_{3,2}$ edges indicated that octahedrally coordinated Cr atoms were strongly polarized by the adjacent ferromagnetic oxide layers, while the tetrahedrally coordinated Co and Mn atoms were less polarized. The Co and Mn XAS lineshapes for as-deposited and annealed single chromite layers, when compared to chromite cap layers, showed almost identical structure (Figures 7.5

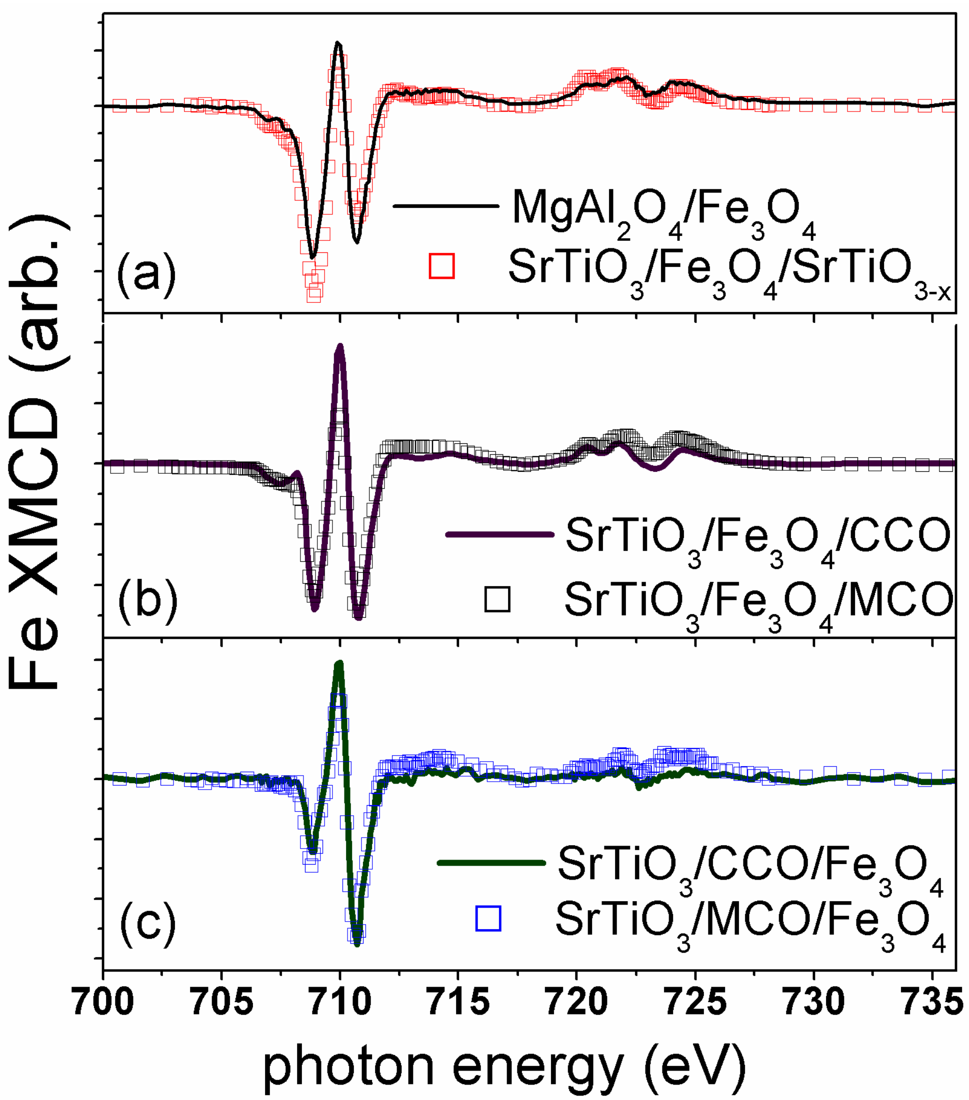

Figure 7.4 – Room temperature Fe $L_{2,3}$ XMCD spectra for Fe_3O_4 bilayers on (110)$SrTiO_3$: (a) Fe_3O_4 with an $SrTiO_{3-x}$ cap compared to single layer Fe_3O_4 on (110) $MgAl_2O_4$, (b) Fe_3O_4 with a $CoCr_2O_4$ or $MnCr_2O_4$ cap, and (c) $CoCr_2O_4$ or $MnCr_2O_4$ with an Fe_3O_4 cap layer.

(a) and 7.6 (a)), indicating that the chemical environment of the cap layer is similar to that of a single chromite layer. However, both Mn, Co and Cr in the capping layer showed marked increase in XMCD signal as compared to single layer films. This behavior persisted up to room temperature for both CCO and MCO cap layers (Figures 7.5 (b) and 7.6, (b)). While Cr-rich spinels have low T_cs compared to ferrites, the proximity of the Cr-rich interface to Fe_3O_4 yields room temperature magnetization for Cr, Co, and Mn.

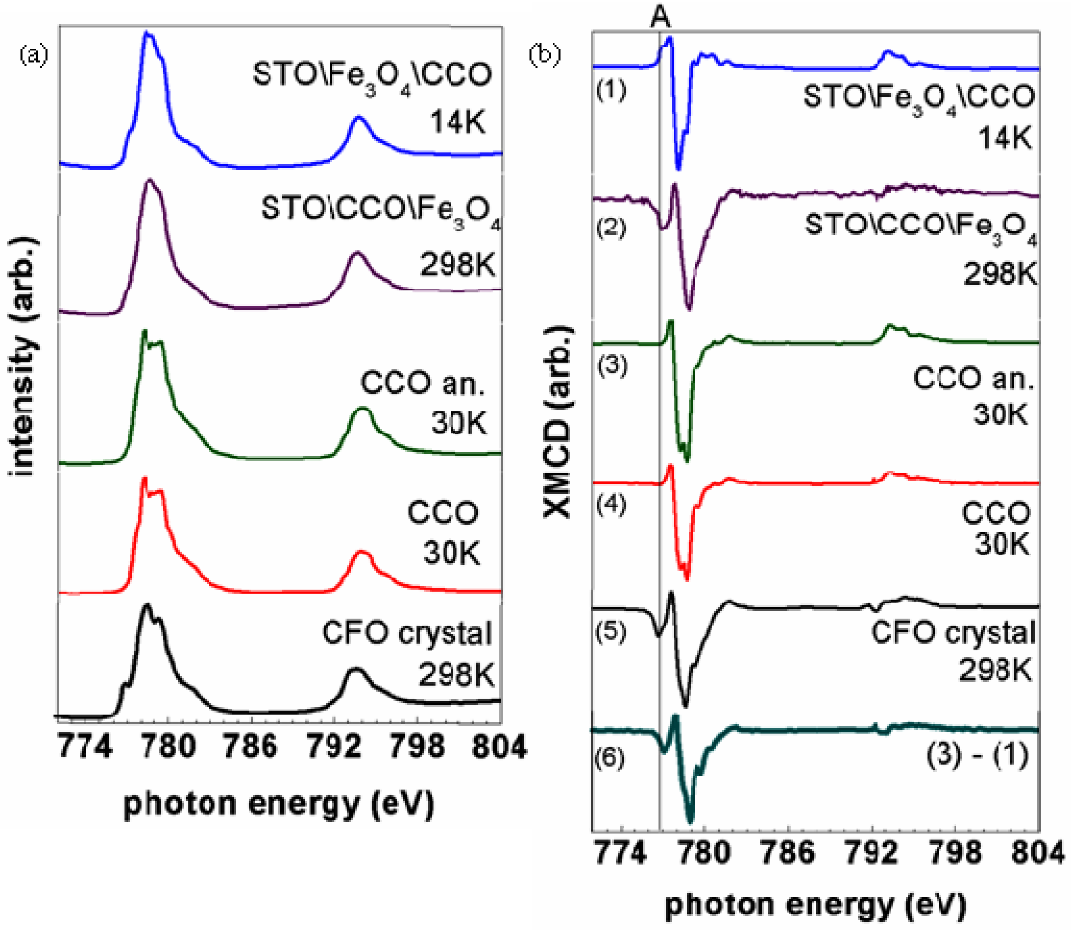

Figure 7.5 – Co $L_{3,2}$ (a) XAS and (b) XMCD spectra for CCO/Fe_3O_4 interfaces compared to reference $Co^{2+}{}_{Td}$ (CCO) and $Co^{2+}{}_{Oh}$ (CFO) sample spectra. Spectrum (6) is the difference between the CCO/Fe_3O_4/STO spectrum and the annealed CCO spectrum.

Comparison of XMCD lineshapes for the Co edge shows a similarity in lineshape between the room-temperature magnetic Co for an Fe_3O_4/CCO bilayer (Figure 7.5(b) spectrum 2) and the octahedral Co^{2+} in a CFO crystal (Figure 7.5, right, spectrum (3)). Alignment of the XMCD pre-peak feature to the line indicated as ‘A’ in Figure 7.5 and subsequent subtraction of the low-temperature tetrahedral Co^{2+} lineshape of a CCO single layer from the low-temperature bilayer dichroism (Figure 7.5 (b) spectrum 6) results in a lineshape that reproduces the CFO crystal dichroism (spectrum 5). The subtraction was obtained by taking the T_d-only Co^{2+} lineshape for a single layer of CCO and the predominantly O_h Co^{2+} lineshape of a CFO crystal and using these spectra in a least-squares fitting of the bilayer spectrum. The integrals of the base T_d and O_h spectra were normalized to unity, and the ratio between the T_d and O_h contributions to spectrum 2 of Figure 7.5 is -0.2 ±0.02. For comparison, the ratio for Figure 7.5 (b) spectrum 1 is -1.0±0.02, with the negative sign indicating that the two contributions are antiparallel and thus are in opposing sublattices in the isostructural spinel multilayer.

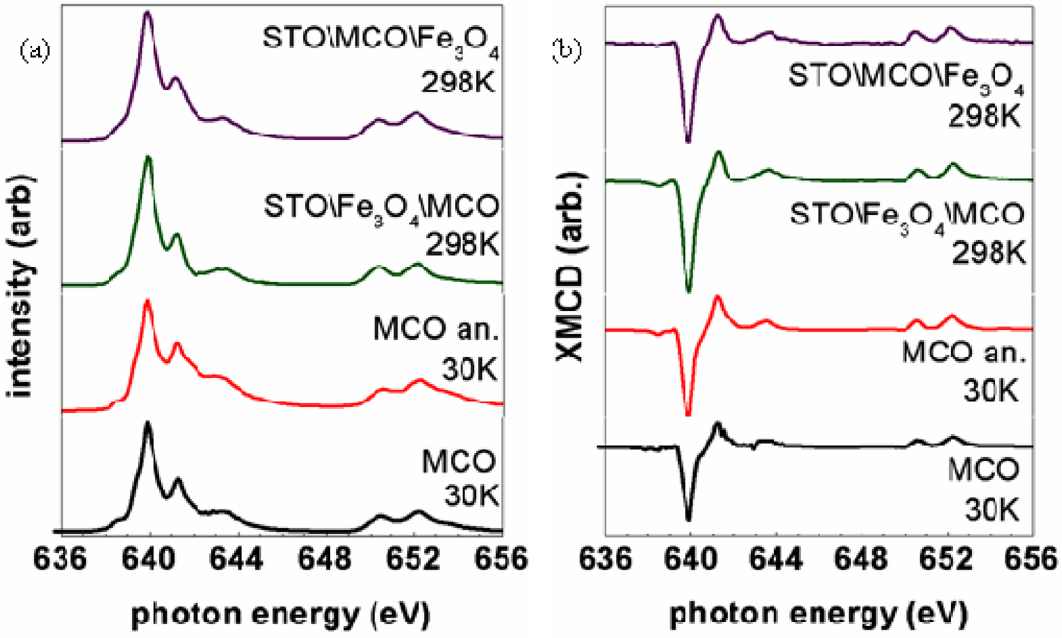

Figure 7.6 – Mn $L_{3,2}$ (a) XAS and (b) XMCD spectra for MCO/Fe_3O_4 interfaces compared to reference $Mn^{2+}{}_{Td}$ (MCO) sample spectra.

The low-temperature XMCD for the CCO bilayer is composed of a tetrahedral Co^{2+} signal from the CCO and an octahedral Co^{2+} from the interface region. Since the A and B sublattices in spinels are antiparallel, the CCO and Fe_3O_4 are coupled ferromagnetically via this interface. The ferromagnetic coupling is also confirmed by the same sign of the domain contrast of the Cr and Fe domains measured via PEEM. Co^{2+} is predominantly octahedral in CFO, but due to the strong Cr^{3+} preference for octahedral sites, Co^{2+} in CCO is only found in tetrahedral sites. For intermediate concentrations of Cr in cobalt ferrichromite, Mohan *et al.* found that Co is both in tetrahedral and octahedral sites and assigned cation distribution as $(\mathrm{Fe}^{+3}_{0.3}\mathrm{Co}^{2+}_{0.7})^{A}[\mathrm{Co}^{2+}_{0.3}\mathrm{Cr}^{3+}_{0.6+y}\mathrm{Fe}^{3+}_{1.1-y}]^{B}\mathrm{O}_4$ for $0<y<1$.[184]

A similar analysis on the MCO-Fe_3O_4 system may also be performed. The XMCD lineshapes for the Mn in MCO and the MCO/Fe_3O_4 bilayer are identical, suggesting that there is only tetrahedral Mn^{2+} at the interface. Mn^{2+} is expected to be in tetrahedral sites in both MCO and in $(Mn,Cr,Fe)_3O_4$. Saksonov and Somenkov assigned Mn to be primarily divalent and tetrahedral in manganese ferrichromite $(\mathrm{Mn}^{2+}_{\varepsilon}\,\mathrm{Fe}^{3+}_{1-\varepsilon})^{A}[\mathrm{Mn}^{3+}_{1-\varepsilon}\mathrm{Fe}^{2+}_{1-\varepsilon}\mathrm{Fe}^{3+}_{2\varepsilon-t}\,\mathrm{Cr}^{3+}_{t}]^{B}\mathrm{O}_4$ with $0.84<\varepsilon<0.98$ and $0.5<t<1.5$.[185] Thus, any presence of O_h Mn^{3+} would be antiparallel to the tetrahedral Mn^{2+}, and would act to reduce the large peak in dichroism at 640 eV in Figure 7.6(b). While $MnFe_2O_4$ tends to have a small amount of O_h Mn^{3+}, this contribution to the dichroism is overwhelmed by the T_d Mn^{2+} dichroism. A bilayer of perovskite ferromagnetic LSMO with a 4 nm MCO cap layer was used to simulate a small contribution of predominantly O_h Mn^{3+} to the MCO spectrum. At room temperature, this sample has a similar XAS spectrum to a single-layer MCO sample, but the XMCD is identical to a single layer LSMO sample. This XMCD spectrum in linear combination with the low-temperature MCO spectrum can reproduce the spectra plotted in Figure 7.6 (b).

Thus the strong low temperature T_d Co^{2+} signal for a 3 nm CCO/Fe_3O_4 bilayer and the lack of O_h Mn^{3+} contribution for the MCO/Fe_3O_4 bilayer suggest that the spinel layers are distinct up to a few nanometers away from the nominal interface but that the interface monolayers do have significant cation mixing due to the energetics of the growth process.

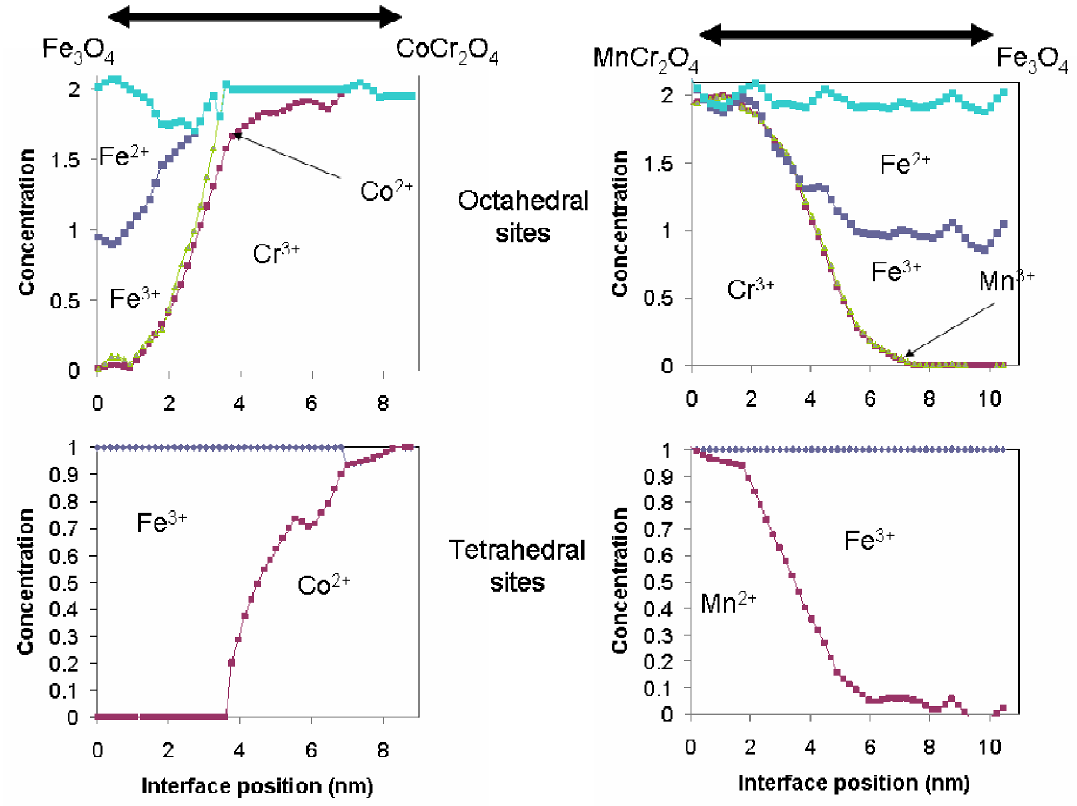

Figure 7.7 – Computed equilibrium compositions as a function of interface position extracted from EELS linescans of chromite-Fe$_3$O$_4$ multilayers.

The XAS and XMCD spectra of Figures 7.5 and 7.6 can elucidate the site preferences of Co and Mn into the Fe$_3$O$_4$ host at the chromite-Fe$_3$O$_4$ interface, but we may also revisit the EELS linescan composition data as shown in Figure 7.1(d). Using the equilibrium compositions as quoted in the above paragraphs for chromite-ferrite mixtures, we determine from the concentration as a function of linescan position that the interface Co occupies a mixture of T_d and O_h sites, and the Mn resides in predominantly T_d sites. These compositions match the XMCD results, and imply that the interface mixture is similar to a heavily Cr-doped CoFe$_2$O$_4$ or MnFe$_2$O$_4$ composition. Thus the magnetic anisotropy properties of the CCO and MCO interfaces should differ drastically.

7.6 Conclusions

At the interfaces of paramagnetic $CoCr_2O_4$ and $MnCr_2O_4$ and ferromagnetic Fe_3O_4, an induced ferromagnetic polarization of the Co, Mn and Cr lattices persists to room temperature. In fact, induced magnetism at the $Fe_3O_4/CoCr_2O_4$ interface region can persist up to 500 K, which is over five times CCO's bulk Curie temperature. Structural characterization via STEM indicated that the strong coupling in the isostructural spinel system is due to a nanometer-scale intermixed region formed during growth. Microscopy and detailed spectroscopy indicate that the cations are ferromagnetically coupled across the spinel interface. Thus the isostructural chromite/Fe_3O_4 bilayer acts as a single ferromagnet at the interface region rather than a distinct ferromagnetic metal/paramagnetic insulator composite. These spinel chromite layers may serve as effective spin filters layers in devices with Fe_3O_4 spin-polarized electrodes.

CHAPTER 8

ISOTSTRUCTRUAL CHROMITE-Fe_3O_4 JUNCTIONS

8.1 Abstract

Epitaxial magnetite (Fe_3O_4)-based all-spinel heterostructures have been grown by pulsed laser deposition to examine the nature of the isostructural interface. Trilayers of magnetite, separated by a paramagnetic insulating $CoCr_2O_4$ layer, exhibit two distinct coercive fields corresponding to the two magnetite layers, which at first implies that the layers can switch independently. However, detailed magnetic measurements indicate that the two magnetite layers are exchange coupled across $CoCr_2O_4$ layers as thick as 10nm. Current-voltage characteristics in a range of temperatures show nonlinear behavior. However, magnetoresistance and its temperature dependence is characteristic of a single magnetic layer.

8.2 Introduction

Magnetite has received renewed interest in light of the search for highly spin-polarized materials for implementation in spin based electronic devices. Fe_3O_4 has been theoretically predicted to be half metallic or completely spin polarized. In other words, all of the electrons at the Fermi level are of one spin polarization. The high spin polarization of Fe_3O_4 has been verified by a number of spin resolved photoemission studies.[20-22] Fe_3O_4 is also negatively spin polarized which means that the electrons at the Fermi level are polarized in a direction anti-parallel to the overall magnetization of the sample. From a technological point of view, its high Curie temperature (858 K) is very appealing but the mixed valence of the iron places severe restrictions on the oxygen growth conditions.

Many groups have incorporated Fe_3O_4 as ferromagnetic electrodes in spin polarized tunnel junctions. Epitaxial tunnel junctions based on Fe_3O_4 have not been as successful as many have hoped. Until recently, a few groups have observed junction magnetoresistance on the order of one percent or less across magnetic tunnel junctions with magnetite electrodes.[26, 27] These studies have incorporated MgO as the tunneling barrier. MgO has a rock salt structure with a lattice parameter approximately half that of the spinel structure Fe_3O_4. Previous studies of ferrite films grown on MgO substrates have shown that antiphase boundaries in the ferrite thin films give rise to anomalous magnetic behavior.[103, 186] Therefore it is not too surprising Fe_3O_4/MgO/Fe_3O_4 junctions may not exhibit ideal magnetic switching behavior. Others have fabricated junctions with a polycrystalline iron oxide electrode with higher junction magnetoresistance values.[187, 188] In a previous study, epitaxial junctions fabricated with magnetite and manganite ($La_{0.7}Sr_{0.3}MnO_3$) electrodes with a spinel structure tunnel barrier, $CoCr_2O_4$ (CCO), can exhibit junction magnetoresistance of up to 25 %.[28] The achievement of these higher junction magnetoresistance values appears to be closely related to the quality of the Fe_3O_4/CCO interface. CCO is a paramagnetic insulator at room temperature with a T_c of 95 K in the bulk. Despite its paramagnetism, the junctions exhibited substantial junction magnetoresistance. One may be led to believe that two Fe_3O_4/CCO interfaces may then make a junction with even higher values of junction magnetoresistance. In this chapter, I examine the magnetism and magnetotransport in detail of Fe_3O_4/CCO/Fe_3O_4 trilayers.

8.3 Experimental

Epitaxial trilayers composed of two Fe_3O_4 layers sandwiching CCO were synthesized on (110) $SrTiO_3$ and $MgAl_2O_4$ substrates by pulsed laser deposition. Trilayers with electrodes 90-140 nm thick and CCO layers 6 nm thick were deposited.

During deposition, the substrates were kept at a temperature of 400 °C. In order to prevent oxidation of Fe_3O_4, the electrode layers were grown in vacuum. On the other hand, CCO was grown in 7 mTorr of a 1% O_2 balance N_2 mixture to prevent oxygen-deficiency. Pulse energies and fluences at the target were kept near 100 mJ and 2 J/cm^2 respectively.

Magnetite has an inverse spinel structure where the O anions make up a face-centered cubic lattice, with an eighth of the tetrahedral sites occupied by Fe^{3+} ions and half of the octahedral sites occupied by equal numbers of Fe^{2+} and Fe^{3+} ions. The large fraction of empty interstitial sites makes the spinel structure a very open structure that lends itself to cation migration. On the other hand, CCO has a normal spinel structure in which the tetrahedral sites contain only Co^{2+} ions while the octahedral sites are occupied only by Cr^{3+} ions due to the strong Cr octahedral site preference.

Structural characterization was performed on these trilayers in the form of X-ray diffraction, Rutherford backscattering spectroscopy, atomic force microscopy, transmission electron microscopy and electron energy loss spectroscopy. Magnetic characterization of the trilayers was performed on a Quantum Design SQUID magnetometer (MPMS 5) and a vibrating sample magnetometer (LakeShore 7300).

The as-deposited films were coated with 1000 Å Au and lithographically defined using a UV contact aligner. A subsequent ion mill step defined vertical junctions ranging from 40 μm x 40 μm to 4 μm x 4 μm in area, and the milling was halted just below the CCO layer. Low temperature sputtered SiO_2 electrically isolated the junctions, and a final plasma-etch step opened windows in the oxide to make contact with the bottom electrode. Four-point transport measurements through the barrier layer were taken in a cryostat at temperatures down to 70 K and fields of up to 1 T. These measurements included current voltage characteristics as well as resistance as a function of magnetic field.

8.4 Results

X-ray diffraction measurements indicate good epitaxy of as-deposited films on the (110) $SrTiO_3$ and $MgAl_2O_4$ substrates; θ-2θ scan reveal (hh0) peaks only. A φ-scan using a Bruker General Area Diffraction Detection System showed four clear (311) peaks, indicating good in-plane crystallographic alignment.

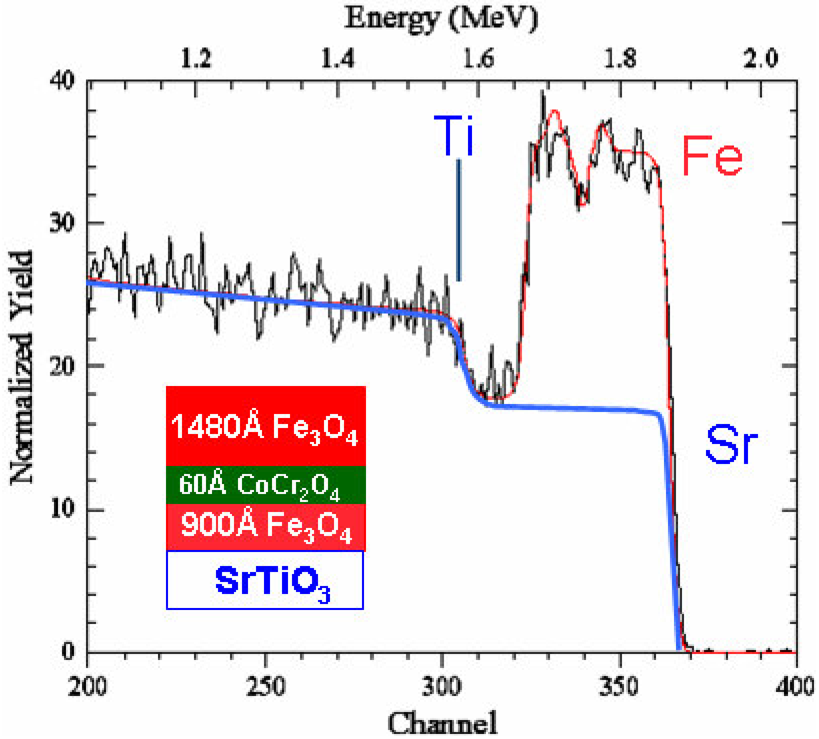

Figure 8.1 – RBS spectrum and fit for a 148 nm Fe_3O_4*/6 nm* $CoCr_2O_4$*/90 nm* Fe_3O_4*/(110)*$SrTiO_3$ *sample. The dip in the Fe peak indicates the presence of a Fe-deficient barrier layer of order 6nm thick.*

Rutherford backscattering spectroscopy (RBS) reveals both thickness and composition of our Fe_3O_4/CCO/Fe_3O_4 heterostructures. Although no strong cobalt or chromium signal was seen, a clear separation between the iron peaks of the top and bottom electrodes imply the presence of the 60 Å barrier layer (Figure 8.1). The figure shows typical RBS data and accompanying simulation corresponding to a 148 nm Fe_3O_4/ 6 nmCCO/ 90 nm Fe_3O_4 heterostructure on a STO substrate.

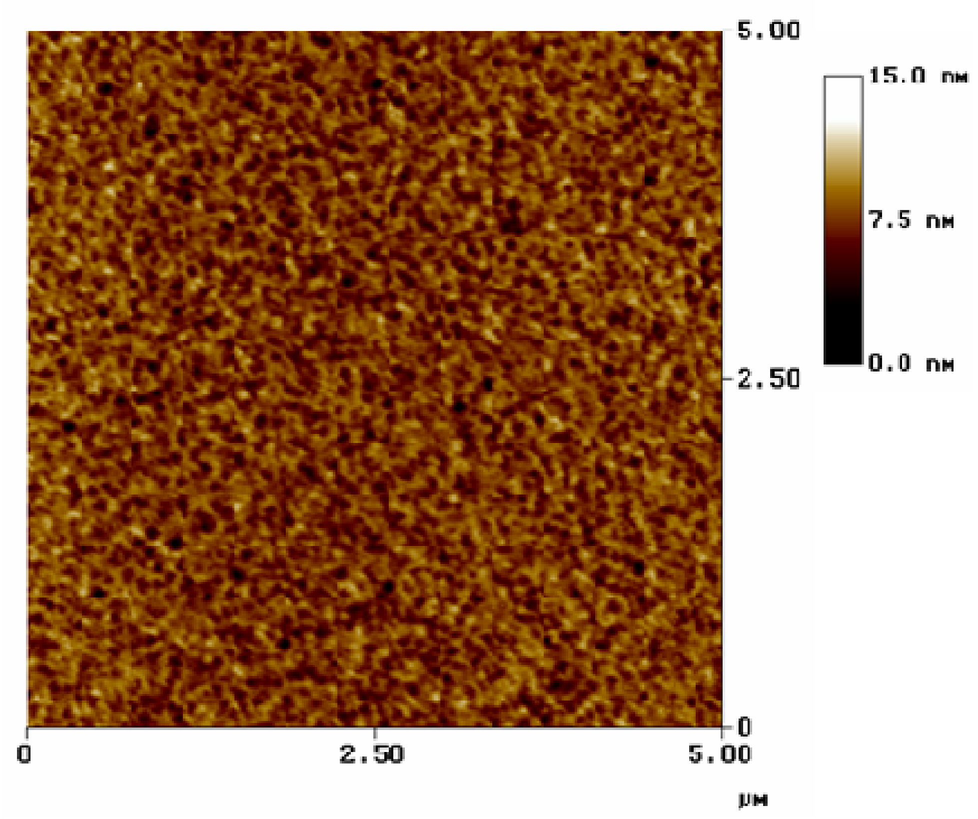

Figure 8.2 – AFM scan for an unpatterned Fe_3O_4/$CoCr_2O_4$/Fe_3O_4/(110)$SrTiO_3$ sample. The RMS surface roughness is 1.22 nm, or 1.5 spinel unit cells.

A typical atomic force microscopy scan (Figure 8.2) of a 5 µm x 5 µm area shows an RMS roughness of about 1.2 nm which is about 1.5 times the cubic spinel unit cell (0.83-0.84 nm). The CCO barrier layer is about 5 times the RMS roughness. Therefore, direct contact of the Fe_3O_4 electrode layers is not present. This was confirmed by multiple cross sectional transmission electron microscopy (TEM) specimens. The TEM images indicated not only good coverage of the bottom electrode with no evidence of pinholes, but also good crystallinity in the CCO layer. Figure 8.3 shows a cross sectional view of the Fe_3O_4/CCO/Fe_3O_4 stack. The slight variations in the grayscale correspond to the thickness variation of the specimen itself. These micrographs also confirm that the roughness of the top and bottom electrodes are similar indicating that there is very little roughening that occurs with increased film thickness.

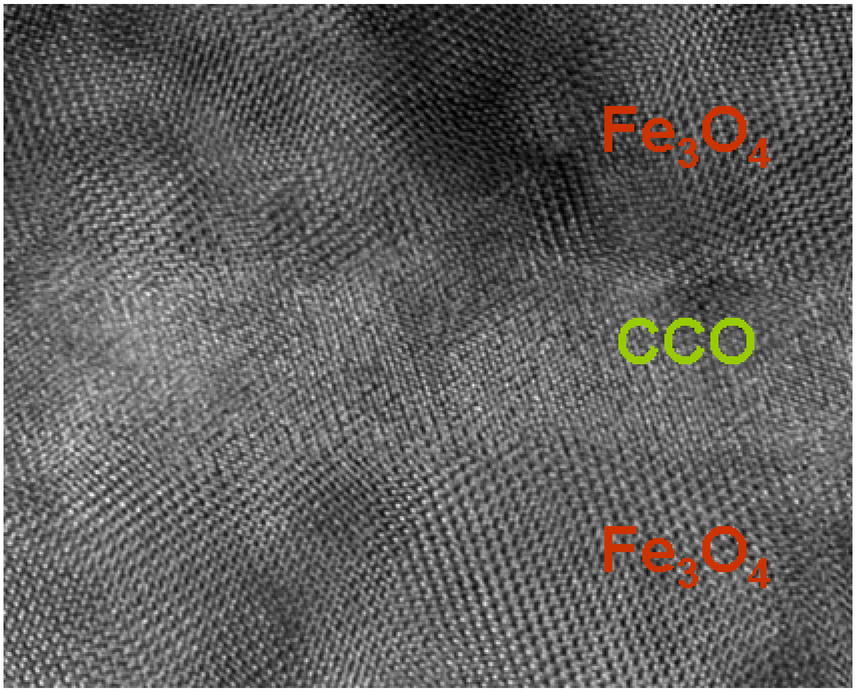

Figure 8.3 – High-resolution TEM cross section including the CCO barrier area. Interface roughness is consistent with surface roughness values taken from AFM scans.

As shown in Figure 8.4, the compositional variations across these cross sectional specimens have been examined. The figure shows a specimen with a buffer layer of LSMO which shows significant contrast with the spinel structure Fe_3O_4 and CCO as well as the $SrTiO_3$. The presence or absence of the buffer layer does not change the crystalline quality of the heterostructure. However, Fe_3O_4 and CCO layers are difficult to distinguish. X-ray energy dispersive spectrometry (XEDS) line mappings of the Co content across electrode-barrier interfaces show a sharp increase in Co content as one scans into the barrier from the electrode. Figure 8.4(b) shows a decrease in the Fe content and an accompanying increase in the Co and Cr content as the line scan reaches the barrier. Given the 2 nm resolution of this probe, the results suggest that a distinct barrier exists between the electrodes.

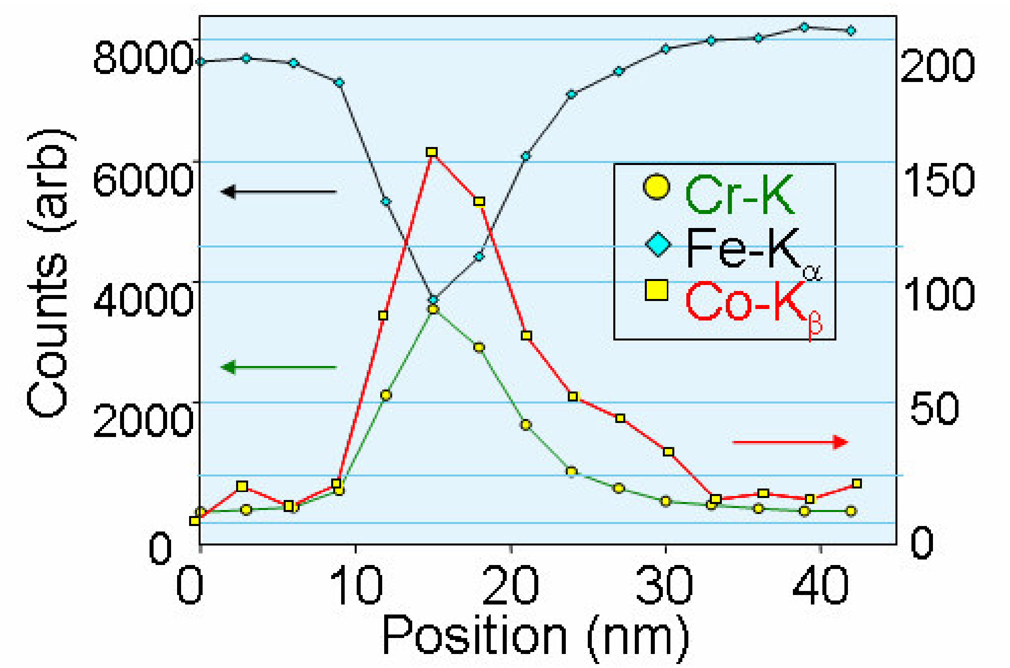

Figure 8.4- X-ray energy dispersive spectrometry analysis of the CCO barrier. A linescan across the CCO region shows peaks in Co and Cr signal and a drop in Fe signal, with all three having a FWHM of 8nm.

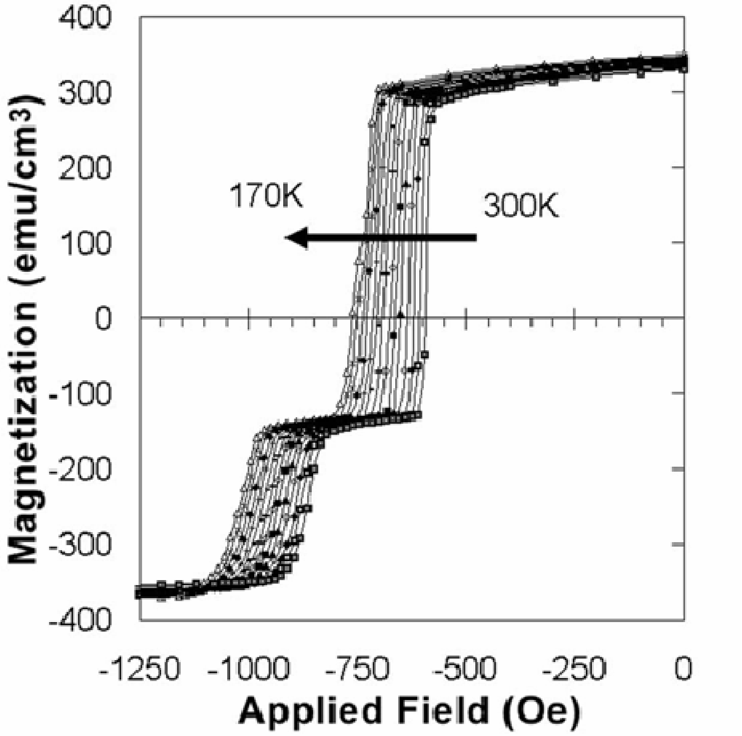

Figure 8.5 – Magnetic switching behavior of a $Fe_3O_4/CoCr_2O_4/Fe_3O_4/(110)$*STO unpatterned sample at various temperatures. After saturation at 5T, the coercive field increases linearly with decreasing temperature for both magnetite layers in the stack.*

Magnetic hysteresis curves for trilayers on (110) STO and (110) MAO substrates were taken at temperatures between 10 K and 300 K. From such curves, a saturation magnetization of 420±10 emu/cm^3 at 10 K was extracted for the magnetite thin films. The coercivity of each of the layers increases monotonically with decreasing temperature (Figure 8.5). Coercivity can be a function of microstructure, anisotropy or thin film strain. For our samples, the epitaxial misfit strain between the trilayer and the substrate changes approximately linearly as a function of temperature due to the differences in coefficients of thermal expansion. The coefficient of thermal expansion of magnetite below T_c is 8.417×10^{-6} K^{-1} to first order in temperature,[189] whereas $SrTiO_3$ has a coefficient of 3.2×10^{-5} K^{-1}.[190] Thus the already compressive strain imposed on the trilayer at room temperature increases in magnitude at decreasing temperatures. This increased strain anisotropy contributes significantly to the increasing coercivity with decreasing temperature.

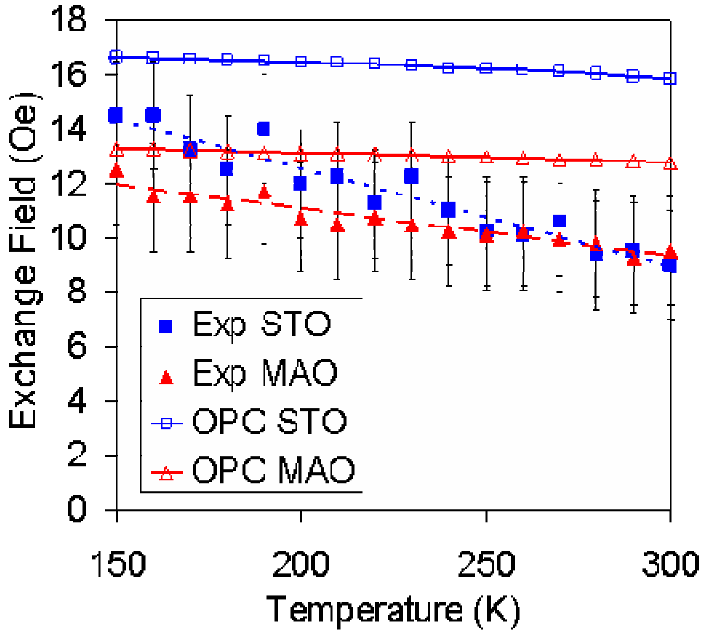

Figure 8.6 – Exchange coupling field as a function of temperature for trilayers on (110)$SrTiO_3$ (squares) and (110)$MgAl_2O_4$ substrates (triangles). The solid points represent experimental data taken from minor loops, whereas the open points are calculated values for the orange peel coupling field (Eqn. 8.1).

When examining the magnetic properties of the trilayers in more detail, evidence of exchange coupling across the CCO barrier up to room temperature was found. This behavior was not seen in similar trilayers with an LSMO electrode, but was found in multiple samples with the isostructural Fe_3O_4/CCO/Fe_3O_4 stack. Quantitatively, the exchange field between the two magnetite layers is of order 10 Oe, and increases substantially with decreasing temperature (Figure 8.6) in films on (110) STO and (110) MAO.

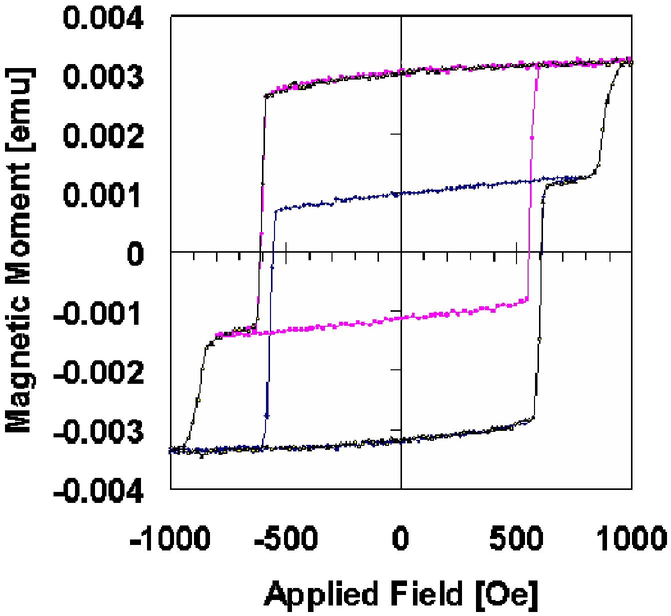

Figure 8.7 – Room temperature major and minor loops for an Fe_3O_4/CCO/Fe_3O_4 trilayer along the [001] in-plane direction.

The exchange field was calculated by measuring the shift of the minor hysteresis loop of the thicker and magnetically easier Fe_3O_4 layer from the origin when the magnetization of the magnetically harder layer is unchanged. In a multilayer with no exchange coupling, the minor loop should be centered around the origin. A shift indicates ferromagnetic or antiferromagnetic coupling among the layers. In other words, the harder magnetite layer acts as a source of extra local magnetic field for the softer magnetite layer (Figure 8.7). In this case, the harder layer is ferromagnetically coupled to the softer layer, as the field required to switch the layers to a parallel configuration is less than the field required to switch the layers to an antiparallel configuration.

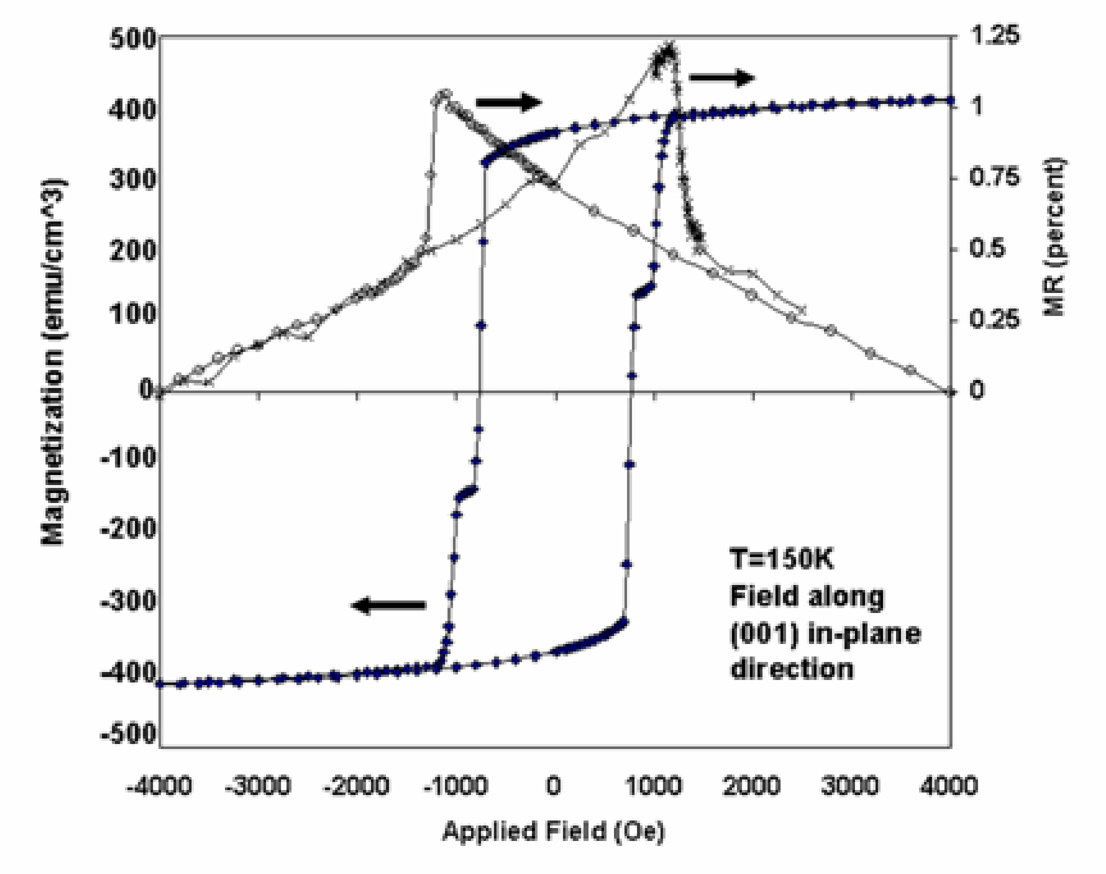

Figure 8.8 –Junction magnetoresistance as a function of applied field at 150 K for patterned junctions as well as magnetization for the film before patterning. Circles indicate MR for a 100 μm^2 junction in a decreasing field, and the x-points are from a 1600 μm^2 junction in an increasing field. Note that the peaks in MR correspond to the coercive field of the harder magnetite layer.

Transport measurements of patterned samples were performed over a range of temperatures and fields. Current-voltage curves were nonlinear and similar to transport characteristics of magnetic tunnel junctions previously studied.[28] The MR changes monotonically as the field is decreased from saturation, and peaks at the coercive field of the magnetically harder layer (Figure 8.8). However, there is no feature in the magnetoresistance that directly corresponds to the coercive field of the magnetically softer electrode. Measurements were limited to above 70K due to the Verwey transition in magnetite. No large changes or features in magnetoresistance as a function of temperature were observed between 70K and 300K.

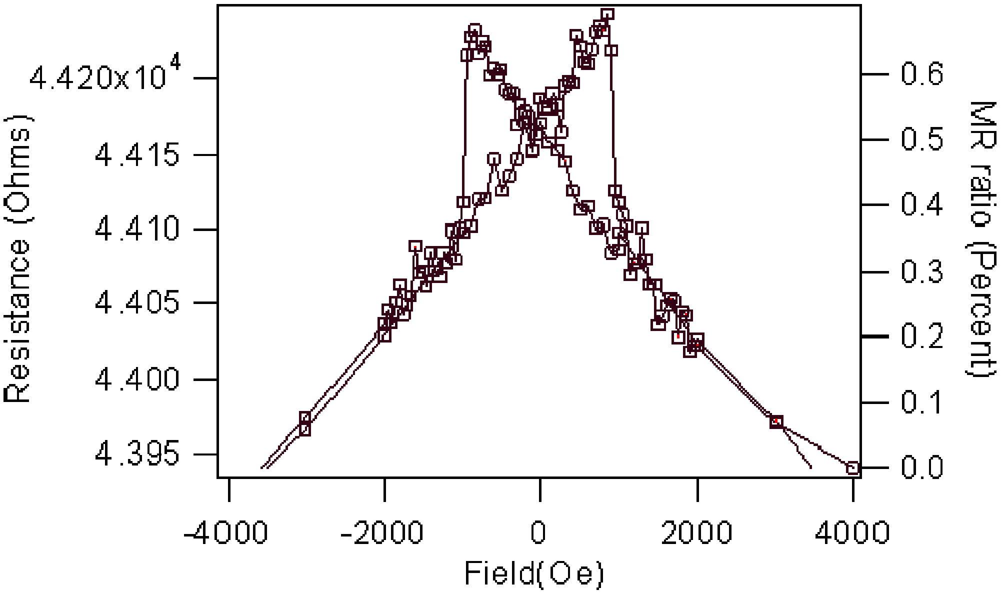

Figure 8.9 –Magnetoresistance of a single (110)Fe_3O_4 layer at T=80K with field applied in-plane along the magnetically easy [001] direction.

While single layer thin films of Fe_3O_4 had linear IV characteristics, the field-dependent MR behavior is remarkably similar to the trilayer junctions as seen when comparing Figures 8.8 and 8.9. The approximately 1% magnetoresistance seen in Fe_3O_4 films is attributed to anti-phase boundary magnetoresistance as well as magnetic frustration at other structural defects.[191] For the (001) orientation, the MR peaks at the coercive field of the film, but the (110) orientation shows a peak asymmetry and a very sharp switching of resistance. When comparing Figures 8.8 and 8.9, the asymmetry of the peak is intrinsic to the Fe_3O_4 film and not due to additional spin-dependent tunneling across the CCO barrier layer. However, there is an increase of the magnitude of the JMR in Figure 8.8 when compared to the MR in Figure 8.9, in spite of the lower temperature for the single film measurement.

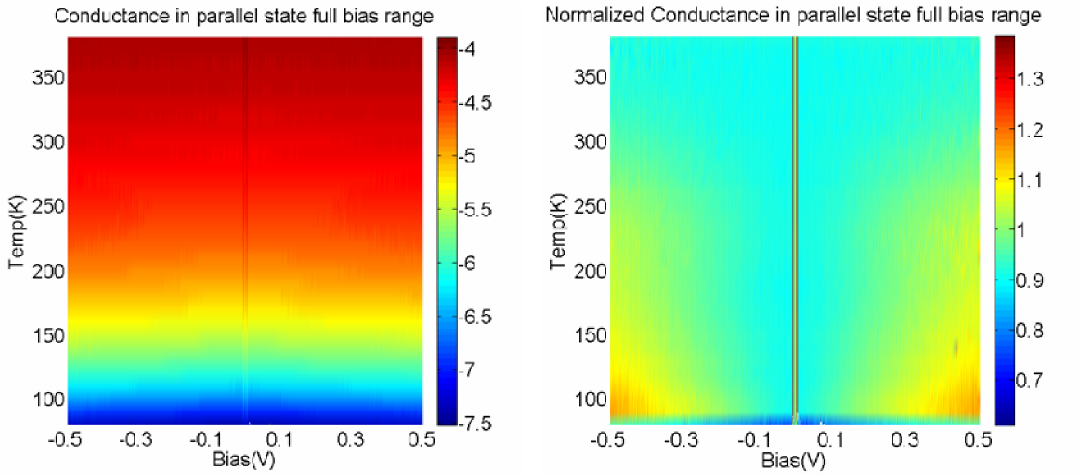

Figure 8.10 –Bias and temperature dependence maps of log conductance (left) and conductance normalized to zero bias (right) for a 100 μm^2 junction on a (110)MAO substrate. The color scale for the left figure is in log_{10}(conductance) in log_{10}(siemens), and the right figure color scale is conductance normalized to zero bias conductance (unitless).

Figure 8.10 illustrates the conductance and normalized conductance as a function of both temperature and applied bias. In this case, the sign convention of positive bias for junction measurements is with the bottom Fe_3O_4 electrode positively biased. Figure 8.10 (right) clearly shows that the transport through the junction is nonlinear and becomes more nonlinear with decreasing field in spite of the temperature range being higher than the bulk Verwey temperature of ~110K.

8.5 Discussion

There is a paramagnetic to ferrimagnetic transition in bulk CCO at 95 K, and the thin film transition is suppressed due to anti-phase boundary defects. However, in magnetization versus temperature curves for the trilayer stack, there is no sign of a clear transition near 95 K from the 6 nm barrier layer using bulk magnetometry measurements. The exchange between magnetite layers cannot be mediated by a ferrimagnetic CCO layer in the temperature regions plotted in Figures 8.5 and 8.6. It is surprising to find this exchange coupling in magnetite layers separated by a paramagnetic layer 6nm thick.

Due to inherent roughness of the film, I postulated that a possible source of the exchange coupling was Neel orange peel coupling as seen in other magnetic tunnel junction devices.[180] For two semi-infinite magnetic electrodes separated by an undulating barrier layer, the waviness of the barrier allows magnetic moments from one electrode to induce free poles in the other electrode, thus allowing the electrode layers to be coupled ferromagnetically. An analytic form of the exchange field involves geometrical factors such as the amplitude and frequency of the barrier roughness as well as the barrier thickness:

$$H_{OPC}(T) = \frac{\pi^2}{\sqrt{2}}\left(\frac{h^2}{\lambda t_f}\right)\exp\left\{-2\pi\sqrt{2}t_{barr}/\lambda\right\}M_s(T) \qquad \text{(Eqn. 8.1)}$$

with h and λ as the amplitude and wavelength of the periodic interface roughness, t_f is the thickness of the layer with lower coercive field, t_{barr} is the thickness of the barrier layer, and $M_s(T)$ is the magnetization of the layer with lower coercive field. Parameters were extracted from structural analysis techniques such as RBS, AFM, and HRTEM. However, the only temperature-dependent factor in this form is in the temperature dependence of the saturation magnetization, or $H_{OPC}(T) \sim M_s(T)$. Since magnetite has a T_c of 858K, the saturation magnetization is almost constant in the temperature region studied in this work. Thus in Figure 8.6 the linear temperature dependence of our data cannot be explained by orange peel coupling alone.

Regardless of the source of the exchange coupling, it has a dramatic effect on the magnetoresistance. Instead of transport through a trilayer with distinct parallel and anti-parallel states, the magnetoresistance resembles transport through a single ferromagnetic layer as seen in Figure 8.9. If there is strong ferromagnetic exchange coupling across the CCO layer, then an applied field will not be able to bring interfacial moments from one side of the CCO to be perfectly antiparallel to interfacial moments on the other side of the barrier. The application of a magnetic field merely inserts a domain wall into the trilayer. Only when the harder magnetite layer switches does the magnetoresistance change abruptly. Thus the isostructural chromite-Fe_3O_4 interface is expected to have fewer structural defects than a rocksalt-Fe_3O_4 interface, but possesses strong magnetic coupling through the chromite layer . The increase in MR over that of a single Fe_3O_4 layer points to a small amount of spin-dependent transport in an analogue to spin-dependent transport across an antiphase boundary in a single-layer Fe_3O_4 film, but the strong exchange coupling between electrodes precludes the large JMR that was expected from the isostructural defect-limited spinel-spinel interface.

8.6 Conclusions

Epitaxial trilayer junctions of spinel structure magnetite and cobalt chromite have been fabricated and characterized. Various structural characterization techniques have shown the trilayers to have a well-ordered crystal structure and low interface and surface roughness. Magnetic measurements indicated that there is exchange coupling mediated by the cobalt chromite insulating barrier. Instead of the large magnetoresistance expected from junctions with well-ordered interfaces, the exchange coupling served to suppress the JMR significantly. Transport across the exchange-coupled layers was similar to that of a single composite ferromagnetic layer instead of a tunnel junction or spin-valve device.

CHAPTER 9

LSMO-Fe_3O_4 BASED HETEROSTRUCTURES

9.1 Abstract

Hybrid magnetic tunnel junction-spin filter devices based on $La_{0.7}Sr_{0.3}MnO_3$ (LSMO) and Fe_3O_4 electrodes with spinel chromite barrier layers were fabricated. The choice of barrier layers ($CoCr_2O_4$ and $MnCr_2O_4$) that are isostructural with the Fe_3O_4 electrode is responsible for significant junction magnetoresistance (JMR), but also leads to unexpected magnetic coupling at the isostructural barrier-electrode interface over a range of temperatures. Non-monotonic bias dependence of the conductance and JMR above the bulk Curie temperature of the barrier layer suggests that junction transport cannot be explained in terms of a simple magnetic tunnel junction model alone. Low-field JMR values of -10% are observed with sharp switching at the softer LSMO electrode coercive field down to 30 K. The Fe_3O_4 electrode coercive transition exhibits both a gradual broadening and an increase to higher fields with decreasing temperature. In the trilayer junction, the isostructural spinel interface can effectively filter spins with the Fe_3O_4 electrode coupled strongly to a ferromagnetic chromite insulator. However, the structural frustration at the perovskite-spinel chromite interface precludes strong coupling, and the LSMO electrode may cleanly switch magnetization directions in spite of the proximity of the strong coupling between the spinel layers.

9.2 Introduction

In the previous chapters, it was found that the isostructural interface between Fe_3O_4 and chromite spinel layers showed an unexpected ferromagnetism due to a nanoscale interdiffusion between the spinel layers. Such interdiffusion was facilitated by the open structure of the spinel unit cell.[34] In other words, the large fraction of empty tetrahedral and octahedral sites in the spinel structure allowed for cation migration at the nominally abrupt interface. The interface ferromagnetism as probed by X-ray magnetic circular dichroism was strongly coupled to the Fe_3O_4 electrode. Thus the chromite-Fe_3O_4 bilayer structure served as a single composite ferromagnet. In devices, such a strong proximity magnetic coupling between an insulator and a metallic ferromagnet could serve to preserve the interface spin polarization and thus yield a large spin-polarized current injected into adjacent layers.

In this chapter, the structural and magnetic characteristics of trilayer junctions comprised of a perovskite LSMO electrode and an isostructural chromite Fe_3O_4 bilayer are explored. While we expect strong magnetic coupling in the spinel bilayer, the non-isostructural interface must also be evaluated to ensure the independent switching of the LSMO layer with respect to the spinel bilayer switching. Indeed, the structural dissimilarity at the perovskite-spinel interface shows that there is little interaction between LSMO and paramagnetic chromite layers, but below the bulk chromite T_c there can be magnetic coupling between the two layers. Therefore, at high temperatures, the LSMO/chromite/Fe_3O_4 device is a hybrid structure – the dissimilar interface between LSMO and chromite acts as a conventional ferromagnetic metal to paramagnetic insulator interface, but the isostructural interface is more akin to that of a ferromagnetic metal-ferromagnetic insulator exchange-coupled bilayer.

9.3 Experimental Methods

As in previous chapters, films were deposited by pulsed laser deposition, with deposition conditions similar to those reported in chapters 6 and 7. Following thin film growth, one half of twin samples were characterized for coercive fields and morphology while the other half were fabricated into junctions between 16-1600 square microns in area. The fabrication process flow details are reported elsewhere.[64]

9.4 Structural and magnetic characterization

Examination of a phase-contrast TEM micrograph from a STO(110) // 32 nm LSMO // [6nm MCO/5nm CCO]$_{n=5}$ // 8nm Fe_3O_4 multilayer along the 001 zone axis (Figure 9.1) shows that while the spinel layers are not without defects, good registry between perovskite and chromite film layers can be obtained with little disorder at the non-isostructural interface. Fourier transforms of the lower and upper sections show that the LSMO and chromite layers are both oriented with the (110) direction out of plane. Thus one would expect similar structural quality of spinel layers grown directly on STO as those templated on an LSMO layer grown on STO.

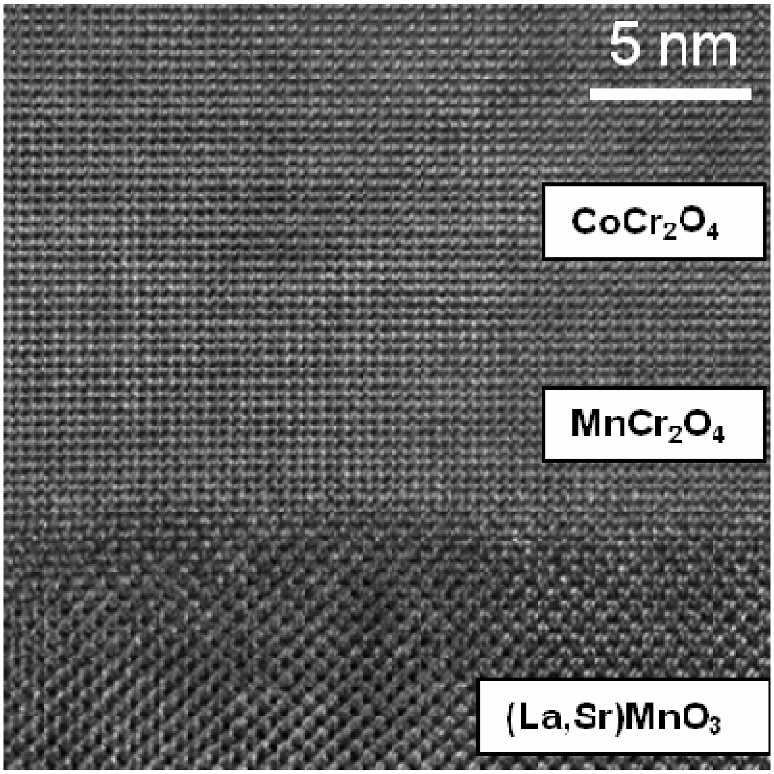

Figure 9.1 – TEM micrograph of the interface between perovskite structure (110) LSMO and a spinel chromite multilayer.

While the XMCD spectra were evaluated at large applied magnetic fields of either 1500 Oe or 5000 Oe, the field dependence and anisotropy of the interdiffused regions may also be characterized via element specific hysteresis loops along orthogonal in-plane directions. At low temperatures one may expect that the ferrimagnetic chromite layers strongly exchange couple to the Fe_3O_4, but it is less clear as to the nature of the coupling above the chromite T_c. Room temperature element-specific hysteresis loops on the Fe L_3 edge along the [001] and [1-10] directions as shown in the solid lines of Figure 9.2 reveal that the presence of Co and Mn have marked effect on the anisotropy and coercivity of the Fe_3O_4 cap layer, even though it is the Cr that interdiffuses more strongly into the Fe_3O_4 from the EELS data.

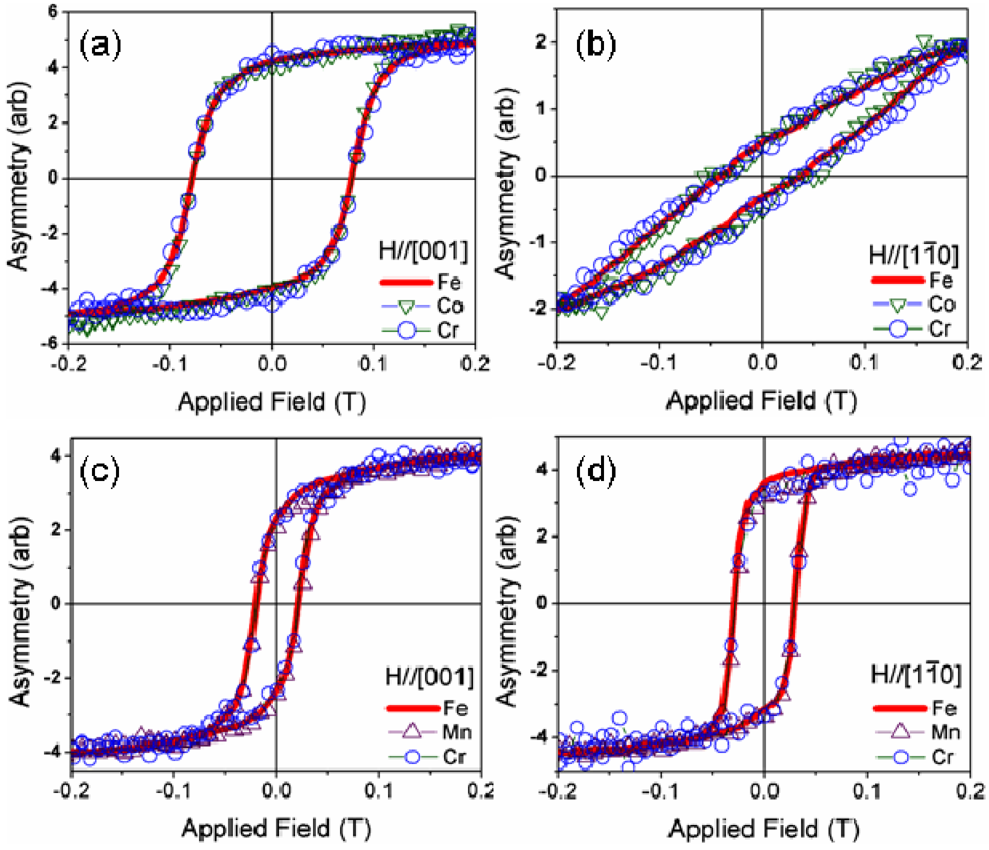

Figure 9.2 – Element-specific hysteresis loops for an Fe_3O_4/CCO/STO sample measured with magnetic field along the (a) [001] or (b) [1-10] *in-plane direction, and an Fe_3O_4/MCO/STO sample along the (c) [001] or (d)* [1-10] *in-plane direction*

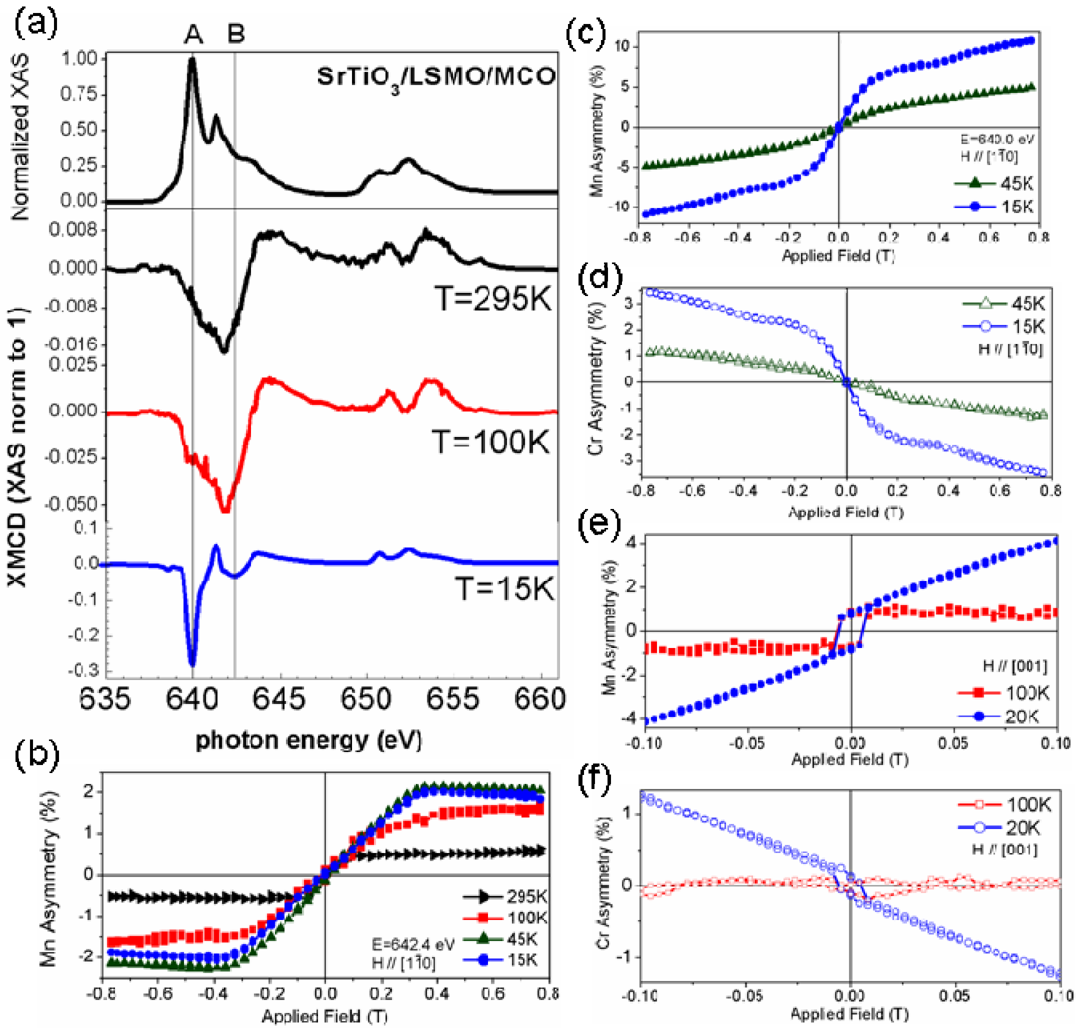

Figure 9.3 – (a) Mn $L_{2,3}$ XAS and XMCD lineshapes of an LSMO/MCO capped sample as a function of temperature, with (b)-(f) as element-specific hysteresis loops of Mn or Cr taken either along the [001] or [1-10] *in-plane direction as indicated. Line A denotes E=640.0 eV, and line B denotes E=642.4 eV.*

The CCO bilayer shows an increase of the Fe_3O_4 coercive field to approximately 1000 Oe along the [001] direction, and the sample could not be saturated even in 2000 Oe along the [1-10] direction. On the other hand, the MCO sample coercive field was approximately 500 Oe but the anisotropy of the Fe_3O_4 cap layer reversed to lie along the [1-10] in-plane direction. Comparison to cobalt and manganese ferrites show that the coercivity and anisotropy behavior matches the behavior in these samples, and thus the Cr at the interface does not have a large influence on the room-temperature interface magnetism. Similar loops on Cr, Co, and Mn lie on top of the Fe loops, confirming that the interface material is coupled strongly to the Fe_3O_4 layer even at room temperature.

From the discussion in chapter 7, it is clear that the isostructural nature of the chromite/Fe_3O_4 interface allows for a nano-scale cation migration that results in room-temperature ferromagnetism at the interface. However, it is less clear as to what occurs at a non-isostructural (110) complex oxide interface. Defects such as anti-phase boundaries and misfit dislocations at a perovskite-spinel LSMO/chromite interface would frustrate any exchange coupling to the magnetic ions in the paramagnetic capping layer. In order to probe the magnetism of such an interface in more detail, the (110) LSMO/MCO interface was explored in an analogous manner to the Fe_3O_4/MCO interface. At room temperature and at 100 K, the XMCD lineshape on the Mn $L_{2,3}$ edge was identical to the XMCD lineshape of the octahedral Mn^{3+} and Mn^{4+} in a LSMO/STO sample even though the XAS lineshape was dominated by the tetrahedral Mn^{2+} in the MCO cap layer (Figure 9.3 (a)).

Thus, there is little if any increase in magnetization of the MCO layer as a function of temperature. It is only below the bulk Curie temperature that the XMCD lineshape becomes dominated by the magnetism in the MCO cap layer. Element-specific hysteresis loops on the Mn edge sample Mn in both layers, but Cr edge loops sample only the magnetism in the MCO cap layer. By tuning the photon energy to match the maximum dichroism for the MCO layer (line A = 640.0 eV) or near the maximum dichroism for LSMO but close to zero dichroism for a single MCO layer (line B = 642.4 eV), hysteresis loops can show the field dependence of Mn in either of the MCO or LSMO layers. Figure 9.3 (b) indicates that the (110)LSMO retains its uniaxial anisotropy with the magnetically hard direction along the in-plane [1-10] direction. The reduction in magnitude between 15 K and 45 K is an artifact due to a small positive contribution of the MCO dichroism lineshape reducing the LSMO dichroism at 642.4 eV.

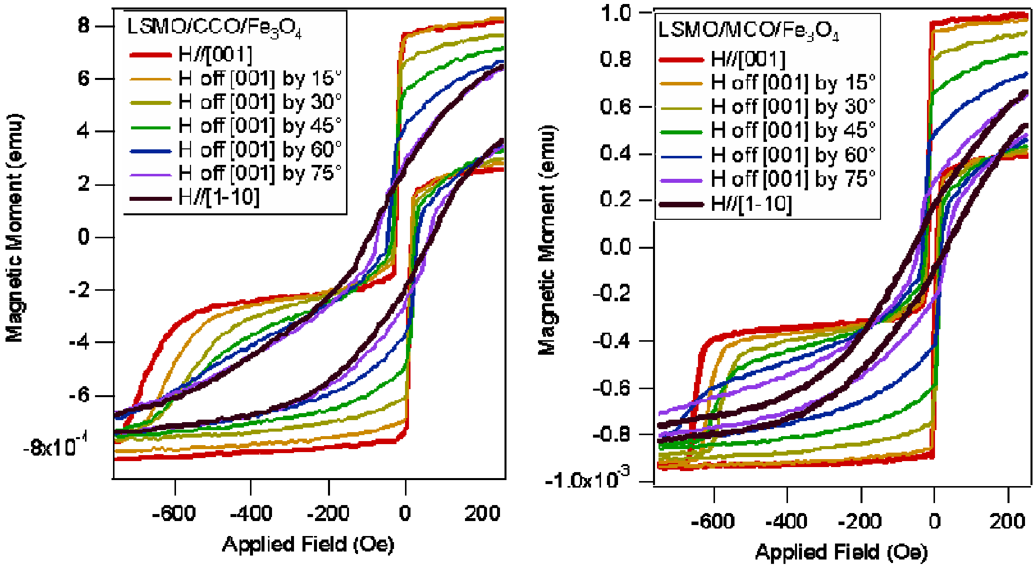

Figure 9.4 – Major magnetic hysteresis loops for unpatterned trilayers with CCO barrier (left) or MCO barrier (right).

For the 15 K and 45 K cases, above the anisotropy field of approximately 3500 Oe the LSMO signal seems to decrease in magnitude. Comparison to Mn hysteresis loops taken at 640.0 eV as well as Cr hysteresis loops (Figure 9.3 (c) and (d)) show that the MCO layer is frustrated by the LSMO underlayer and does not saturate even out to 8000 Oe, despite the [1-10] direction being the easy axis for (110)MCO single layers. Thus the orthogonal easy axes for (110) LSMO and (110)MCO frustrate each other resulting in a lack of saturation for the bilayer as a whole. Similar results may be obtained from the equivalent Mn and Cr loops measured along the [001] direction (Figure 9.3 (e) and (f)). At 100K the Mn in the LSMO layer saturates in a field of less than 200 Oe and there is no magnetic signal from the Cr in the MCO. When the temperature is reduced to below the T_c of the MCO in bulk, the MCO magnetization prevents saturation of the LSMO up to fields of 1000 Oe, with identical non-saturating behavior seen in the Cr and Mn edge hysteresis loops.

If the LSMO/chromite/Fe_3O_4 junctions are measured well above the bulk chromite T_c, then the LSMO will be effectively decoupled from the spinel bilayer and independent switching of the electrodes should be possible. As an example, hysteresis loops of trilayers with 2 nm chromite barrier layers were measured at room temperature as a function of in-plane angle (Figure 9.4) to see if the interface anisotropy reversal shown in Figure 9.2 can be resolved using a bulk-sensitive probe. The LSMO has a coercive field of approximately -50 Oe and has an easy axis along the [001] in plane direction. The Fe_3O_4 layer has a coercive field of -600 Oe for both samples and the region between -100 and -400 Oe appears to be constant in magnetization. Both MCO and CCO-based trilayers have a hard axis along the [1-10] direction, though the width of the CCO-based trilayer hysteresis along the hard axis is wider than the MCO sample hysteresis in agreement with the data in Figure 9.2. However, the data in Figure 9.2 was only taken to 1500 Oe so a direct comparison of the magnitudes of the hard axis coercive fields may not be performed.

To first order, the magnetization of these samples looks similar, and we may examine the magnetotransport in junctions fabricated from these samples to evaluate how the transport is affected by interface anisotropy as compared to the whole-film magnetization.

9.5 Magnetotransport with chromite barriers

Previous studies by Hu *et al.* indicated that high-field JMR values of up to -30 % were achievable with a CCO barrier layer when using LSMO and Fe_3O_4 electrodes,[28, 29] and further studies have confirmed that similar barrier layers such as $FeGa_2O_4$, Mg_2TiO_4, and $NiMn_2O_4$ can produce similarly large JMR values.[30, 192] This is due in part to the use of (110) oriented LSMO in which the surface magnetization is more robust than the (001) orientation as discussed in Chapter 6. However, the JMR in these junctions has a strong dependence both on temperature and bias. To explore the JMR in more detail, I have recorded junction resistance as a function of applied field, temperature, and bias. A typical two-dimensional representation of the JMR is shown in Figure 9.5, with the difference in resistance between H=0 Oe (parallel magnetization state of the trilayer) and H=-300 Oe (antiparallel magnetization state of the trilayer) normalized by the zero field resistance. Note that the junction was saturated at 30,000 Oe to ensure a parallel magnetization state for each temperature step, and the field was applied along the [001] in-plane direction

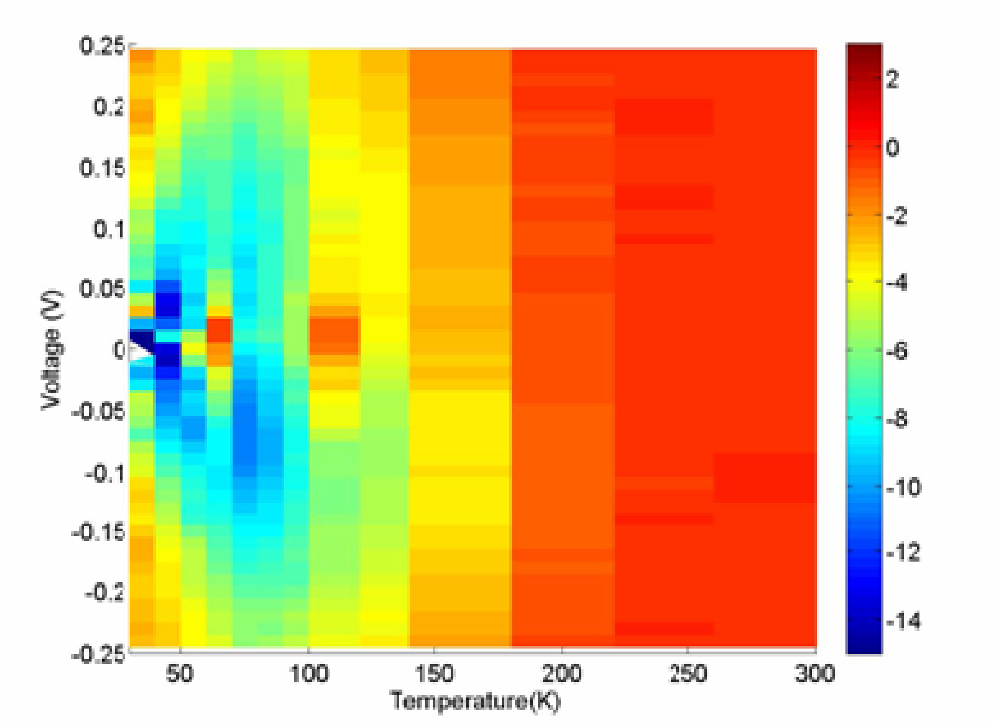

Figure 9.5 – Junction magnetoresistance map as a function of bias and temperature for a device with a 2 nm CCO barrier layer, with color scale indicating JMR in percent.

There are three temperature regimes of interest for Figure 9.5: T=0-70 K, T=70-175 K, and T=175-300 K. In the lowest temperature region, the JMR decreases with decreasing temperature in contrast to the expected increase of LSMO spin polarization with decreasing temperature. In this temperature regime, the Fe_3O_4 electrode resistance is large due to the Verwey metal-insulator transition, and the junction resistance is obscured by the Fe_3O_4 resistance. In the intermediate temperature region, the bias dependence of the JMR is asymmetric and the JMR increases with decreasing temperature. An isothermal cutline (Figure 9.6, right panel) illustrates this asymmetry quite clearly for a 4 nm CCO barrier. In this temperature region, the spin polarization of the electrodes is large at low temperatures, but the asymmetric structure of the barrier layer interfaces produces an asymmetric conduction barrier. The LSMO-chromite interface is non-isostructural and may have barrier lowering defects, and the intermixing at the chromite-Fe_3O_4 will create a graded structure that also deforms the idealized insulating barrier shape.

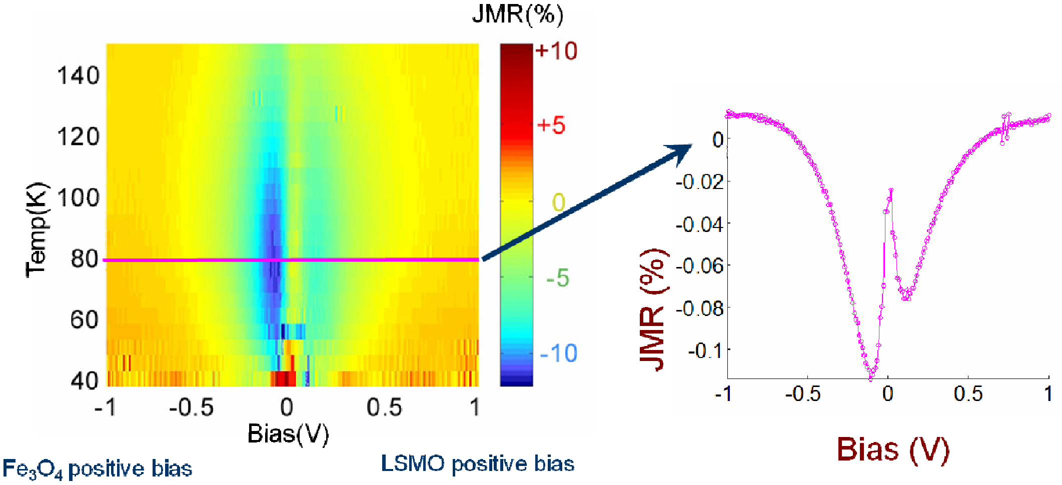

Figure 9.6 – Junction magnetoresistance map as a function of bias and temperature for a device with a 4 nm CCO barrier layer, and isothermal cutline across map (right) to show non-monotonic bias dependence.

At the highest temperature region, the magnitude of JMR is negligible and has little bias dependence, thus most likely stems from the electrode MR rather than spin-polarized transport at the chromite barrier. One might wonder why the spin polarization seems to decrease so much above 175 K if the Fe_3O_4 T_c is 858K and the LSMO T_c is 360 K . By examining the temperature dependence of the magnetic coupling at the spinel interface (Figure 7.2 (a)), the magnetization of the Fe, Cr and Co sublattices decreases substantially between T=150-200 K. Thus it is expected that the spin-filtering efficiency for the exchange-coupled chromite-Fe_3O_4 bilayer also decreases substantially in this temperature region. Additionally, temperature-dependent measurements with LSMO electrodes and nonmagnetic barrier layers have shown that the interface spin polarization is suppressed almost as much as the surface spin polarization.[193] Suppression at both interfaces leads to a vanishingly small JMR at room temperature.

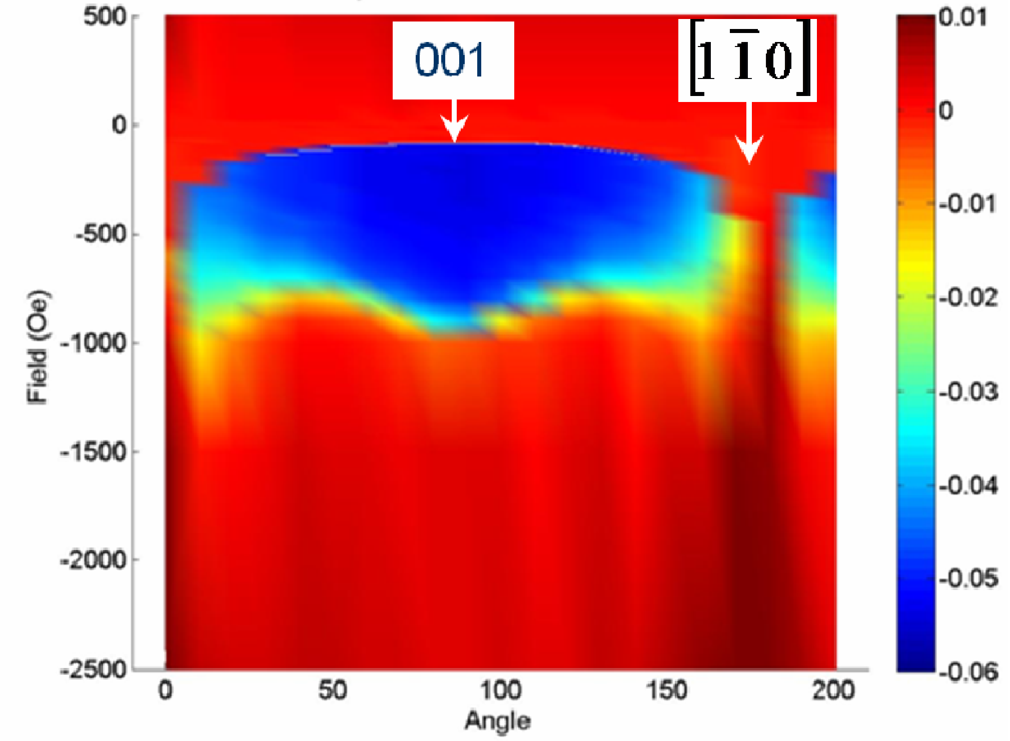

Figure 9.7 – Junction magnetoresistance map as a function of magnetic field and azimuthal angle for a 2 nm CCO based junction.

The angular dependence of the JMR for these junctions should be similar if the whole film magnetization as in Figure 9.4 is the dominant contribution to the JMR, but if the interface anisotropy shift of Figure 9.2 is the dominant quantity, then we would expect a difference in the angular JMR dependence for MCO and CCO barriers. In the angular dependence experiment, the temperature is held fixed, and the sample is saturated at H=30,000 Oe for each in-plane angle measured. Again, the JMR values are normalized to the zero-field resistance value.

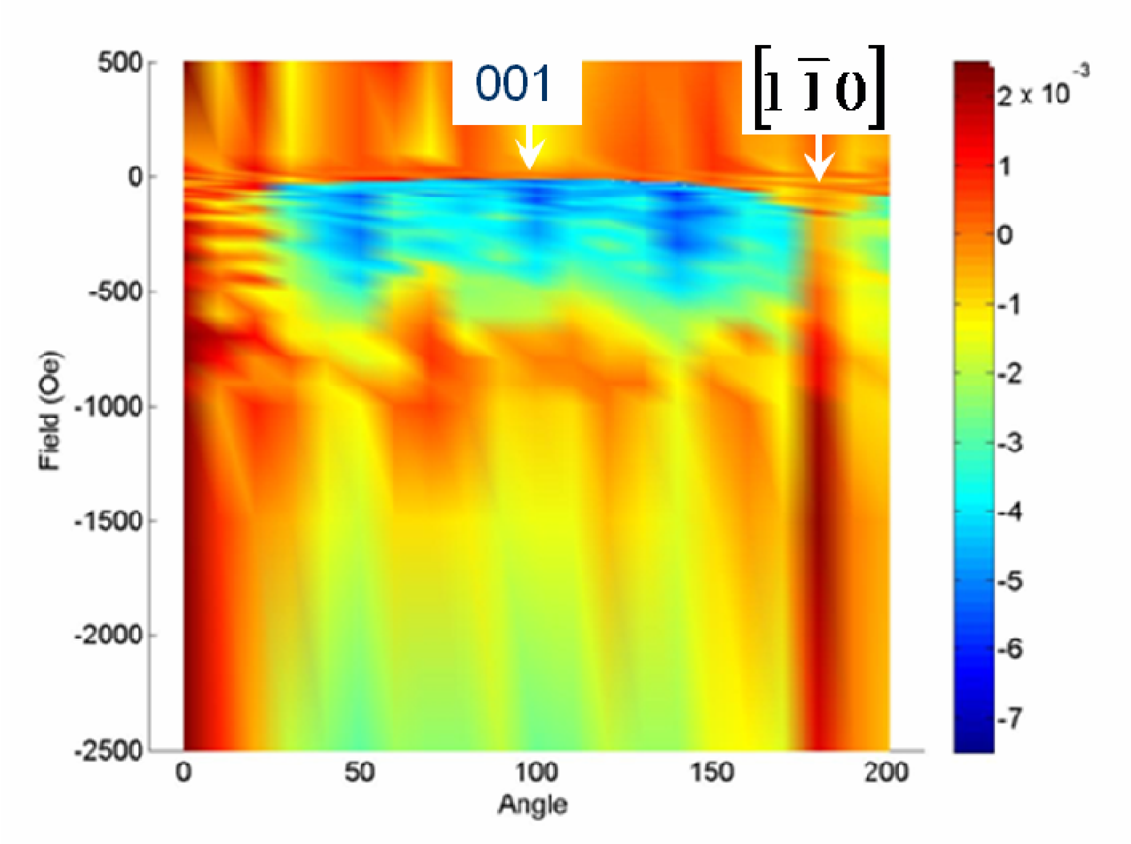

Figure 9.8 – Junction magnetoresistance map as a function of magnetic field and azimuthal angle for a 2 nm MCO based junction.

The CCO barrier yields a large low-field JMR of -6 % even at 130 K (Figure 9.7), but the MCO–based junction has a maximum JMR value of -0.7 % that is an order of magnitude less at the same temperature (Figure 9.8). The CCO junction's maximum MR is centered along the [001] in plane direction and vanishes along the [1-10] direction. Though the MCO junction has a similar suppression of JMR along the [1-10]direction and a JMR maximum along the [001] direction, there are additional maxima near the [1-11] directions. The suppression of JMR even along the [001] direction confirms that it is the interface anisotropy that dominates the JMR behavior, and the stabilization of relatively high JMR along the near-[1-11] directions is most likely a modification of the crystal anisotropy constants (K_n) at the interface due to the addition of Mn into Fe_3O_4.[13] Thus, even though the LSMO and Fe_3O_4 are decoupled at 130 K, only the CCO barrier can stabilize moments at both interfaces along or antiparallel to the [001] direction, and the MCO barrier has a smaller projection of the Fe_3O_4 magnetization along the [001] direction. This results in a high JMR for the CCO device, and a reduced JMR for the MCO device due to the smaller difference between parallel and antiparallel configurations at the barrier interface and thus lowered effective spin injection efficiency.

9.6 Conclusions

In this chapter I have described the magnetic properties of LSMO-Fe_3O_4 multilayers using both whole-film and interface-sensitive probes. The nanoscale interdiffusion at the chromite-Fe_3O_4 interface as found in previous chapters is responsible for a strong modification of the magnetic anisotropy of the Fe moments at the interface, and the adjacent chromite moments couple strongly to those Fe moments. On the other hand, the non-isostructural LSMO/chromite interface has no coupling at room temperature or even at 100 K, though below the bulk chromite T_c there is some magnetic coupling between the layers. This strong coupling at one interface but almost no coupling at the other interface results in a hybrid spin-filter type structure: the isostructural interface acts as a ferromagnetically coupled spin-filter bilayer, whereas the non-isostructural interface enables independent magnetic switching between the LSMO and spinel. However, the anisotropy of the spinel-spinel interface is affected by the presence of Mn or Co, and in the MCO device the interface magnetization cannot be switched into clear parallel or antiparallel states as in the CCO device.

CHAPTER 10

CONCLUSIONS AND FUTURE WORK

A variety of magnetic and electronic ground states are available in the *3d* transition metal oxide family, and by tuning their properties with epitaxial strain or insertion of materials into heterostructures, one may obtain a variety of functionalities. In this dissertation, I have discussed how single layer thin film properties can be extremely sensitive to thin film strain magnitude and symmetry, such as the resistivity of $SrRuO_3$ films, the magnetization and anisotropy of $CoFe_2O_4$ films, or the surface magnetization of (001)LSMO films. On the other hand, many thin film properties are quite robust to thin film microstructure or the presence of defects like antiphase boundaries, as is the case with superconducting spinel $LiTi_2O_4$ thin films.

Incorporation of these highly tunable yet also robust materials into heterostructures can also create functionalities not expected from the constituent materials. The isostructural spinel-spinel interface leads to a strong exchange coupling mediated by a nanometric interdiffusion at the interface. This coupling may stabilize ferromagnetic properties not seen in the component materials as seen with the above room temperature magnetization of Co and Mn ions at the chromite-Fe_3O_4 interface. On the other hand, this stabilization of additional ferromagnetic moments can influence the interface magnetic anisotropy, and in turn can either increase spin-dependent transport figures of merit or suppress those same figures of merit.

Results of spin filtering using a $NiFe_2O_4$ barrier by Luders *et al.*[33], a $BiMnO_3$ barrier by Gajek *et al.*,[194] and a $CoFe_2O_4/MgAl_2O_4$ barrier by Chapline *et al.*[195] show that the use of complex oxides for spin filtering is a promising avenue of injecting spin polarized current into non-magnetic electrodes such as Au. In addition, the robust surface magnetization of (110) and (111) LSMO found in this work as well as the (110) LCMO interface found by Infante *et al.*[19] illustrate that manganite oxides may retain their bulk properties depending on the crystal orientation of the surface and thus may show large spin polarization when such crystal orientations are used in heterostructures. The variety of reported surface and interface spin polarizations for Fe_3O_4 make it clear that one must not only consider bulk properties, but also microstructural and interface properties when using such a material in spin-dependent devices. Emergent properties at interfaces may influence and even dominate the measured properties of these heterostructures.

The usage of these oxides is quite promising, but much work still needs to be done in terms of optimization of interface properties. As LSMO shows a large magnetoresistance but shows a decrease in conductivity in ultrathin films and a so-called 'dead' layer below 10 monolayers, careful construction of LSMO based heterostructures must be performed so that the LSMO electrode properties do not degrade device properties. For example, the use of a thick SRO layer capped with a thin LSMO layer would reduce electrode resistance while still preserving an LSMO interface for spin injection. In a similar vein, LTO layers can be used as an isostructural low-resistance contact material to most spinel oxide layers, though cation diffusion of Li must be carefully controlled to preserve the LTO conductivity.

Optimization of deposition conditions for CCO and MCO were performed to ensure robust magnetic as well as insulating properties, but other spinel oxide compositions could result in higher effective barrier heights in junction devices which would lead to an increase in the contribution of spin-polarized tunneling over that of spin-randomized hopping conductivity. Additional understanding of the conduction mechanisms through spinel chromite barriers and at the interdiffused chromite Fe_3O_4

interface is necessary to extract the Fe_3O_4 spin polarization at such interfaces. And the role of antiphase boundary defects has been well studied in Fe_3O_4, but it is less clear as to how such defects affect the properties of the less commonly used spinels such as CCO or MCO. Finally, LTO or another superconductor such as $YBa_3Cu_3O_7$ may be used to directly probe the Fe_3O_4 spin polarization or chromite spin filtering efficiency through a Meservey-Tedrow type epitaxial structure, and thus evaluate how the surface spin polarization as measured by photoemission experiments can compare to interface polarization in a test structure.

APPENDIX A

DATA CONVERSION FOR RECIPROCAL LATTICE MAPPING

Modern high resolution X-ray diffractometry is often automated, and a series of one-dimensional scans can produce what is commonly known as a reciprocal space map (RSM). Depending on the geometry of the x-ray tube and detector as well as the size of acceptance slits, this can produce broad features or very sharp peaks. This appendix will detail how to convert multiple one-dimensional scans from a text file to a presentation-quality contour of a reciprocal space map.

Note that an RSM is different than a pole figure scan, in which the ω and 2θ are held fixed while φ and χ are varied in order to measure the multiplicity and orientation of specific reflections. For instance, holding 2θ and χ fixed while scanning φ can show the in-plane orientation of a film and can confirm cube-on-cube epitaxy, but a RSM can be used to determine the lattice parameters of the film unit cell and thus determine and distortion from the bulk lattice parameters.

The most common two-dimensional scan to explore both in-plane and out-of-plane lattice parameters is to hold φ and χ fixed while varying ω and 2θ independently. This can measure diffracted planes that are aligned along the same φ and χ directions, but does not resolve planes with large mismatches that would most likely change the χ value that would maximize diffracted intensity. For instance, in a (001) cubic system one would set $\chi=45°$ to probe a 011 plane, but in a tetragonally distorted film on that cubic system χ could vary from 45° by a degree or more. In any case, we will sacrifice maximum intensity for the film by maximizing intensity of the substrate in φ and χ.

The MRD has an applet that will allow visualization of the ideal reciprocal space map as calculated from the bulk lattice parameters, and this can be used as a guideline to show all possible ω and 2θ values that the goniometer can reach as well as the possible diffraction peaks that can be resolved. Note that the user should choose a film reflection from the material PDF card with a high intensity and multiplicity, thus a fine gridding of ω and 2θ may be performed without sacrificing measurement time to obtain a large amount of counts per second. Typical scans for perovskite-spinel heteroepitaxy are centered around the substrate peak and measure 2 degrees in ω and 4 degrees in 2θ, though this is a strong function of the difference in lattice parameter of the film and substrate. If the film and substrate have a low mismatch, the user is encouraged to use the MRD low-intensity by high-resolution mode called ‘triple-axis mode’ with an extra monochromator on the detector arm, whereas more common scans use the ‘rocking curve mode’ without the extra monochromator.

Once the data is taken, the MRD calculates ‘reciprocal lattice units’ from the ω and 2θ values to plot the logarithmic counts as a function of both in-plane and out-of-plane momentum transfer (q_{para} and q_{perp}). I have derived the following equations to match the calculations that the MRD performs:

$$Q = (4\pi/\lambda)\sin(\theta) \qquad \text{(Eqn A.1)}$$

$$\gamma = \omega + (180 - 2\theta)/2 \qquad \text{(Eqn A.2)}$$

with the magnitude of the momentum transfer as Q and the tilt of the momentum transfer vector from the sample surface as γ. Thus a two dimensional array of the components of Q may be used to plot the logarithmic intensity as shown in Figure 6.1. The in-plane and out-of-plane components are

$$q_{para} = Q\cos(\gamma) \qquad \text{(Eqn A.3)}$$

$$q_{perp} = Q\sin(\gamma) \qquad \text{(Eqn A.4)}$$

A quick check is that q_{perp} -> Q if the tilt γ is 90°, and γ =90° if $\omega = \theta$ as in a conventional out of plane θ-2θ scan. The RSM can be done either close to an out-of-plane reflection to measure mosaic spread projected along an in-plane direction, or can be used at a partially in-plane reflection such as the 103 for a (001)-oriented film to test whether or not the film is pseudomorphic to the substrate or if there is partial relaxation of the film towards the bulk lattice parameter.

Igor code:

After importing the data from the comma-separated variable text output of the MRD XRDML file, run the following code in Igor 5.0 or later with the input waves as (2Theta_position, Omega_position, and Intensity)

```
•Rename X2Theta_position,twotheta; Rename Omega_position,omega;
;DelayUpdate
•Rename Intensity,cts;
•Make /n=10746 logcts, qperp, qpara, Qmag, tilt
•AppendToTable logcts, qperp, qpara, Qmag, tilt
•logcts=log(cts)
•tilt=(180-twotheta)/2 + omega
•Qmag=sin(3.14159*twotheta/360)
•qpara = 4*3.14159*qmag*cos(3.14159*tilt/180)/1.5405
•qperp = 4*3.14159*qmag*sin(3.14159*tilt/180)/1.5405
```

The output waves (qpara, qperp, and logcts) are three Igor data columns that describe the reciprocal space map. The qpara and qperp columns are in inverse Å, and may further be converted to *hkl* values. However, in the case of this dissertation many heteroepitaxial perovskite-spinel systems are studied and thus the hkl values are less instructive than the momentum transfer components in absolute units. Note that it is assumed that the X-ray tube side 4-bounce Ge monochromator in the MRD is set to maximize the λ=1.5405Å wavelength, and the code uses this number to convert from the MRD ‘reciprocal lattice units’ to absolute units. Igor will interpolate the logcts into color levels, and I typically use 100 levels across a color scale from yellow to orange to red to black for maximum contrast and detail of small features.

Similar code may be implemented in worksheet form in Origin 7.5 or the graphing program of your choice.

APPENDIX B

TRANSPORT MEASUREMENTS USING MODIFIED PPMS CRYOSTATS

B.1 Introduction

While the Physical Property Measurement System (PPMS) from Quantum Design is a versatile tool for measuring transport as well as AC magnetization, the need for both sensitive low-resistance measurements as well as low-noise high-resistance measurements on epitaxial thin films has led to my development of a modular system in which to accommodate a wide range of sample types. High throughput was also a leading factor in developing this system – while careful measurements on individual samples can show interesting behavior, a systematic study of careful measurements allows for trends in deposition parameters or film thickness to be seen much more quickly.

The PPMS electrical contacts include 12 unshielded wires helically wrapped around the sample chamber leading to the so-called ‘grey LEMO’ connector at the back of the PPMS storage dewar. Normally this connector would accommodate a cable from the PPMS console to allow for simple resistivity measurements as well as additional thermometry and resistivity capabilities such as the horizontal rotator. In the replacement setup, four wires normally dedicated to the horizontal rotator thermometer are connected to the PPMS console via a splitter, and the remaining eight wires are connected to shielded cables that lead to an HP3488A matrix controller. This matrix controller takes the eight wires and multiplexes them to four outputs so that the following wiring setups can be configured via software:

A) 6x2 point measurements (junction initial characterization)

B) 2x van der Pauw/van der Pauw-Hall or 2x 4-point junction measurement

Four output terminals from the matrix controller (labeled I+, I-, V+, and V-) can connect to a variety of hardware. Current setups include:

a) Keithley 237 or 238 source-measure unit for direct-current IV characterization

b) SRS 830 lock-in amplifier and Keithley 2001 multimeter for low-frequency and high-sensitivity alternating current resistivity characterization

c) HP 4262A LCR meter for low-frequency inductance-capacitance-resistance measurement

d) Keithley 6482 high-resistance meter with internal 1000V voltage source

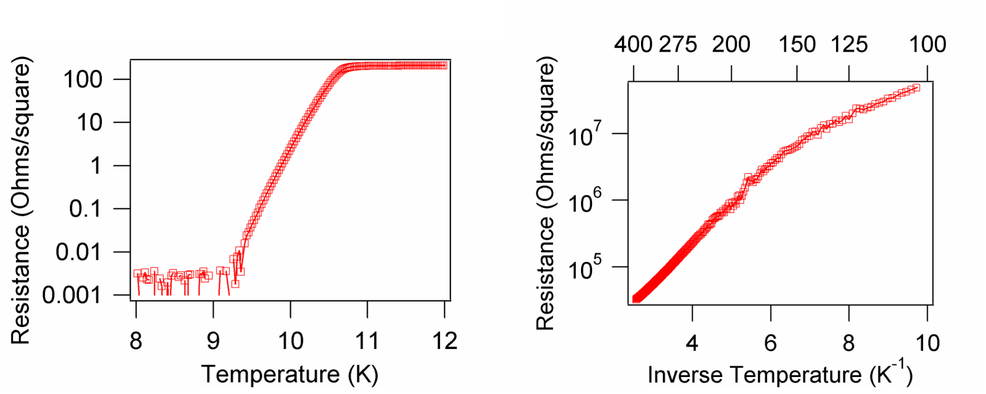

Figure B.1 – (left) Low resistance measurement data of a $LiTi_2O_4$ film using the SR830 lock-in amplifier setup and (right) high-resistance measurement data of a $La_{0.5}Sr_{0.5}MnO_3$ film using the conventional Keithley 237 setup.

An example of a data obtained from various configurations are shown in Figure B.1. While there are many optional daughterboard cards for the HP3488A matrix controller, availability of parts is limited due to the age of the controller. While both matrix controllers for PPMS1 and PPMS2 perform similar operations, the hardware is not the same and thus the wiring between the PPMS sample chamber and the HP3488A is not the same. Such differences are transparent to the user as the LabVIEW code automatically configures the HP3488A, but care must be taken in not running PPMS2 software on PPMS1 and vice versa. Calibration measurements on thin Co and Cu films were taken to show reproducibility between the two PPMS cryostats as well as the accuracy of the measurements compared to those found in the literature.

The most common measurements are performed are unpatterned thin films, and the van der Pauw configuration is used in order to calculate resistivity while only knowing the general properties of the contact configuration as shown in Figure 2.13. In other words, four contacts are placed at the four corners of a rectangular sample, and sheet resistance is obtained from two resistance measurements with current along the principal axes of the rectangle.

B.2 Fitting to the van der Pauw equation

The van der Pauw equation described in Chapter 2 is a transcendental equation, and can be solved iteratively using the Newton-Rhapson method. Differentiation of equation 2.3 and substitution leads to equation B.1:

$$R_{n+1} = R_n - \frac{\exp\left(-\pi R_{vdp\_1}/R_n\right) + \exp\left(-\pi R_{vdp\_2}/R_n\right) - 1}{\frac{\pi}{R_n^2}\left(R_{vdp\_1}\exp\left(-\pi R_{vdp\_1}/R_n\right) + R_{vdp\_2}\exp\left(-\pi R_{vdp\_2}/R_n\right)\right)} \qquad \text{(Eqn B.1)}$$

with $R_{n=0}$ taken as the average of R_{vdp_1} and R_{vdp_2}. I have found that ten iterations are adequate to get a converging solution to the precision of the experimental data, and the R_n may be substituted into equation 2.3 along with the experimental data to verify the accuracy of the numerical solution.

As the resistances R_n, R_{vdp_1} and R_{vdp_2} are assumed to be real and positive, each of the exponential terms in equation 2.3 is monotonic in R_s ($R_s \sim R_{n>>1}$) and bounded by (0,1). Thus there is only one nontrivial solution that satisfies the relation that the sum of both terms is equal to 1. The initial guess that R_0 is the average of the experimental values ensures that the guess is near the correct order of magnitude and requires few iterations to converge. Most thin films have a resistivity tensor that has either fourfold or twofold symmetry in the plane, and thus R_{vdp_1} and R_{vdp_2} have similar orders of magnitude for square samples. Elongated samples can still be measured but it is often the case that $R_{vdp\_1} << R_{vdp\_2}$ and thus one of the terms in equation 2.3 is susceptible to noise.

The LabVIEW code outputs a delimited file that can easily be imported into Microsoft Excel or a graphing program. Therefore, equation B.1 may be applied to each data pair either as a function of temperature or applied field, and the resistivity is obtained from the numerical solution of B.1 by $\rho=R_st$ with t as the film thickness.

B.3 Methodology of Program Construction

The LabVIEW code to measure resistivity as a function of temperature, voltage, or sample orientation (by using the horizontal rotator) takes advantage of the GPIB instrument communications protocol to both set the status of attached instruments as well as to read the result of any instrument measurements. For instance, a 'virtual instrument' may be constructed in software and the user may initiate measurements and read-back results as if they were physically controlling a current source or voltage meter. This allows for automation of repeated measurements as a function of applied magnetic field or temperature.

In lieu of making a monolithic program to control multiple instruments, smaller virtual instruments (called subVIs) are used for simple tasks such as setting the temperature or magnetic field of the PPMS cryostat or for controlling the Keithley 237 source-measure unit. One can assemble a virtual instrument to perform temperature or field sweeps and simply call the subVI while monitoring the temperature or field.

The graphical nature of LabVIEW code precludes a detailed explanation of each portion of the virtual instruments. For example, the total size of the code base for a single PPMS cryostat is approximately 45 megabytes. The naming convention of the files includes both prefixes and suffixes to differentiate between measurement operations. Note that the program prefix includes:

- information such as which cryostat the program was built for (PPMS1=P1 and PPMS2=P2)
- whether or not the horizontal rotator is inserted into the cryostat for the program to operate correctly (Puck=standard copper puck sample mount, HR=horizontal rotator probe with green PCB sample mount).
- the instruments to be connected to the matrix card setup (K237= standard Keithley 237 source-measure unit, SR830=lock-in amplifier, K6517= Keithley Electrometer, HP4262 = LCR meter)
- the scan to be performed (RvsTsweep = repeated resistance measurements taken while sweeping the temperature at a fixed rate (~1K/min) between two target temperatures, RvsH= measure resistance at fixed temperature but arbitrary array of field points)
- the number of samples to be measured (1 channel, 2 channels, or 6 junctions)

I will describe the function of the most commonly used subVIs and main programs below by referencing to the program suffix.

MagCtrl.vi – controls magnetic field and charging rate for the PPMS magnet. Note that the specified field for each PPMS probe is different (9 T max for PPMS1 vs 7 T for PPMS2), and it is the user's responsibility to use fields that will not quench the magnet. I recommend using a maximum of 7 T under normal operations.

TempControl.vi – controls temperature set rate as well as target temperature, and the program will loop until the target temperature is set. There are modified versions of this program to work with the Horizontal Rotator thermocouple as well as to use Sweep mode.

TempStat.vi – used to read the current temperature and magnetic field of the system without disturbing either field or temperature set points.

2VDPSheetCheck.vi – a manual program to measure the two-point resistances between contacts when the samples of interest are wired in the van der Pauw configuration. IV curves for each contact pair are shown in succession. This is used to verify the measurements performed after wire bonding to the sample using a handheld multimeter and the breakout box supplied by Quantum Design. At a cryostat temperature of 300K, the resistances output by this program should be within a few percent of the handheld multimeter values. Either sample channel may be disabled at the request of the user.

6JunctionCheck.vi – a manual program to measure the two-point resistance in a junction configuration (6xtwo-point). IV curves are measured for each sample, and even at room temperature it is expected that non-shorted MTJ samples should have nonlinear IV curves. Any junction channel may be disabled at the request of the user.

Averaging-4typeIV-PPMS2.vi – a subVI used to measure both four-point van der Pauw measurements as well as two van der Pauw-Hall measurements. Note that any of the four measurements may be disabled when using the program manually, or when called by other programs. Thus this subVI may be used to measure a standard four-in-line measurement by using the first VDP configuration. Or a measurement of all four VDP-type measurements for both sample channels may be performed.

LinearRegression.vi – as the name implies, this implements a linear regression algorithm to output the fit slope and standard deviation of that slope from an input IV curve. The results of this fitting are usually listed in the "-LinResFit.txt" output data files of the below programs.

RvsHFMultipleT-ConstantVoltage6junctions.vi – IV curves with evenly-spaced voltage points (apply voltage, measure current) are taken at a fixed temperature but different applied magnetic fields. An arbitrary array of comma-separated field values are allowed as input, so a single positive to negative field sweep, a sweep from zero field, or scan with coarse points at high field but fine points around zero field are all possible.

RvsHFMultipleT-VDPandHALL-2channels.vi – similar to the above program, but uses a constant current mode (apply current, measure voltage) to measure resistances for 2 channels of van der Pauw type samples. Again, arbitrary fields are allowed at every temperature.

RvsTSWEEP-VariableFieldLinearPredictionBothVDP – since the IV curve measurement takes from 1-30 seconds depending on integration time and number of points, an efficient use of cryogens may be performed by sweeping the temperature of a sample at a slow rate (~1 K/min) and taking up to 1000 IV curves between room temperature and 5K in a six hour period. Other measurements such as with the lock-in amplifier are slower and require a slower sweep rate. A field-cooling subVI is also available to measure temperature hysteresis in those materials with first-order phase transitions.

B.4 – Wiring table for PPMS1 connection to HP 3488 matrix card

Board	Channel	sheath	cond1	cond2	I+	I-
1	00	red	red	black	3	4
1	01	red	white	black	3	5
1	02	green	green	black	3	6
1	03	blue	orange	black	4	5
1	04	blue	yellow	black	4	6
1	05	blue	red	white	5	6
1	06	blue	red	green	7	8
1	07	blue	brown	black	7	9
1	08	blue	blue	black	7	10
1	09	red	red	black	8	9
2	00	red	white	black	8	10
2	01	green	green	black	9	10
2	02	blue	orange	black	11	12
2	03	blue	yellow	black	11	13
2	04	blue	red	white	11	14
2	05	blue	red	green	12	13
2	06	blue	brown	black	12	14
2	07	blue	blue	black	13	14
3	00	red	red	black	3	4
3	01	red	white	black	3	5
3	02	green	green	black	3	6
3	03	blue	orange	black	4	5
3	04	blue	yellow	black	4	6
3	05	blue	red	white	5	6
3	06	blue	red	green	7	8
3	07	blue	brown	black	7	9
3	08	blue	blue	black	7	10
3	09	red	red	black	8	9
4	00	red	white	black	8	10
4	01	green	green	black	9	10
4	02	blue	orange	black	11	12
4	03	blue	yellow	black	11	13
4	04	blue	red	white	11	14
4	05	blue	red	green	12	13
4	06	blue	brown	black	12	14
4	07	blue	blue	black	13	14

APPENDIX C

MATLAB CODE FOR $LiTi_2O_4$ DATA

C.1 – Description of MATLAB code

In chapter 4, a study of $LiTi_2O_4$ thin films was performed in which the upper critical field H_{c2} was extracted from field and temperature dependent resistivity measurements. The largest field applied was 7 T, yet most studies of LTO show that the upper critical field is close to 20 T. Thus, fitting of the data to extrapolate the upper critical field was necessary. From the resistivity vs. temperature data measured in different fields, one can obtain pairs of data points that relate the applied field to the superconducting-normal transition of the film. The temperature at which the film becomes non-superconducting as measured by resistivity as a function of applied field ($T_{transition}$, $H_{applied}$) is equivalent to evaluating ($T_{crit}(H)$, $H_{c2}(T)$) if one assumes that the film is a homogeneous phase. $T_{transition}$ was defined as the temperature at which R(T)/R(T=15 K)=0.5. As the path of least resistance is what is probed in resistivity measurements, one must be careful to consider inhomogeneities that would lead to a non-simple shape for the R vs. T curve near the transition temperature.

From the ($T_{crit}(H)$, $H_{c2}(T)$) pairs, one can take the slope near H=0 Oe and extrapolate the H_{c2}(T=0 K) from that slope. A more robust method is to use the WHH equation to obtain the Maki parameter α and the spin-orbit coupling parameter λ_{so}.

$$\ln\frac{1}{t} = \sum_{n=-\infty}^{\infty}\left\{\frac{1}{|2n+1|} - \left[|2n+1| + \frac{\bar{h}}{t} + \frac{(\alpha\bar{h}/t)^2}{|2n+1| + (\bar{h}+\lambda_{so})/t}\right]^{-1}\right\} \quad \text{(Eqn C.1)}$$

with temperature (T) and upper critical field (H_{c2}) scaled as

$$t = T/T_{crit} \quad \text{(Eqn C.2)}$$

$$\bar{h} = (4/\pi^2)H_{c2}/(-dH_{c2}/\ dt)_{t=1} \quad \text{(Eqn C.3)}$$

Instead of implementing the digamma functions and using the closed form, the integral form was numerically computed using |n|=20,000 steps. Fitting to the WHH equation by nonlinear least squares fitting in MATLAB yielded fitting parameters α, λ_{so}, T_{crit}(H=0), and H_{c2}(T=0) but also indicated if the (T_{crit}(H), H_{c2}(T)) datasets deviated substantially from the WHH equation lineshape. Again, film inhomogneities could cause such a deviation, but the fit parameters from this fitting technique can be compared to the more conventional high-temperature and low-field slope fitting to estimate H_{c2}.

For each dataset (T_{crit}(H), H_{c2}(T)) measured from the R vs. T data for various H, two vectors *t* and *h* are used as the inputs as well as the number of steps *n* in the numerical integration step. The two input vectors are the non-reduced (NR) temperature and field from the raw data, and we can obtain the scaling factors T_{crit}(H=0) and $dH_{c2}/dt|_{t=1}$ from fitting the experimental data to the WHH equation. The fit parameters for a given dataset are obtained using WHHcompNR.m as the main program. In particular, WHH2vectorNR.m is called to minimize the difference between the numerical WHH equation and the fit data. Furthermore, WHHsolve.m takes the fit parameters and generates the WHH curve for arbitrary evenly spaced fields, so the WHH equation can be graphed with the experimental data and compared for accuracy as well as examining the sum of the minimized residual differences between the fit and the data.

C.2 - WHHcompNR.m

```
% generate fit of Tc vs Hc2 data using WHH equation
% use non reduced field and temp as input, n=# of segments in
numerical integration
% output Tc(H=0), Hc2(T=0) from fit
function WHHcompNR(t, h, n)
tstart=clock;

[M, b]=fminsearch(@(coeff) WHH2vectorNR(t,h,coeff, n), [3 0.5 3]);

M(1)=abs(M(1));
M(2)=abs(M(2));
```

```
M(3)=abs(M(3));

for i=1:600
    redfield1(i) = (i-1)*0.0005;
    redtemp1(i)=WHHSolve(M(1),M(2), n, redfield1(i));
    if redtemp1(i)<0
        break
    else
    end
end

hstar1=redfield1*(pi^2)/4;
Fields=hstar1*(M(3)*M(1)/.52758);
Temps=redtemp1*M(3);

min=floor(0.75*(i-1));
P=polyfit(Temps(min:i-1), Fields(min:i-1),3);
Hc2zeroT=polyval(P,0);

H1=figure;
hold on
plot(Temps(1:i-1), Fields(1:i-1), 'b-.')
plot(t,h,'k^')
xlabel('Temp (K)')
ylabel('Field (T)')
legend(['free params (alpha,lambda)=(' num2str(M(1)) ','
num2str(M(2)) '), sum variance = ' num2str(b, '%10.3e') ', T_c(H=0)='
num2str(M(3)) 'K, Hc2(T=0)=' num2str(Hc2zeroT) 'T'], 'data')
title(['Field vs Temp for sample ' inputname(1) ', nu for eq 28 WHH
is ' num2str(n) ])
saveas(H1, [inputname(1) 'NR_'  num2str(n) 'nu.jpg'], 'jpg')
saveas(H1, [inputname(1) 'NR_'  num2str(n) 'nu.fig'], 'fig')
hold off

done=[ inputname(1) ' ' num2str(b, '%10.3e') '  ' num2str(M(3)) '  '
num2str(Hc2zeroT) '  ' num2str(etime(clock,tstart)) ' seconds
elapsed']
save(inputname(1))
```

C.3 - WHH2vectorNR.m

```
% generate eq 28 of WHH paper; output difference of LHS and RHS
% form is WHH(t,h,alpha,lambda,n)
function residuals=WHH2vectorNR(Temps,Fields,coeff, n);
format long

Tc0=abs(coeff(3));
t=Temps/Tc0;
alpha=abs(coeff(1));
lambda=abs(coeff(2));
hstar=Fields/(Tc0*alpha/.52758);
h=hstar*4/(pi^2);


sum=-1.*log(1./t);
```

```
for i=-n:n
    sum=sum + 1./abs(2*i+1) - 1./(abs(2*i+1) + h./t +
((alpha*h./t).^2)./( abs(2*i+1)+ (h+lambda)./t));
end

residuals=norm(sum,1)^2;
```

C.4 - WHH.m

```
% generate eq 28 of WHH paper;
% form is WHH(t,h,alpha,lambda,n)
function sum=WHH(t,h,alpha,lambda,n);

format long

sum=-1*log(1/t);
%sum=0;
for i=-n:n
    sum=sum + 1/abs(2*i+1) - 1/(abs(2*i+1) + h/t + ((alpha*h/t)^2)/(
abs(2*i+1)+ (h+lambda)/t));
end
```

C.5 - WHHsolve.m

```
% use secant method to generate universal WHH curve for given alpha
and
% lambda
function tfin=WHHSolve(alpha, lambda, n, H)

format long
iter=20;
epsilon=1e-6;
tguess1= (1 - 2*(H+2*epsilon))^0.334;
tguessN= (1 - 2*(H+epsilon))^0.334;

    for i=1:iter
        W1=WHH(tguess1,H,alpha,lambda,n);
        W2=WHH(tguessN,H,alpha,lambda,n);
        delta = W2*(tguessN-tguess1)/( W2 - W1);
        test1=not(isequal(imag(delta),0)) ;
        test2=real(delta)>epsilon ;
        if test1==1
            break
        elseif test2==0
            break
        else
            tguess1=tguessN;
            tguessN=tguessN-delta;
        end
    end

    tfin=tguessN;
```

REFERENCES

1 A. Ohtomo and H. Y. Hwang, "A high-mobility electron gas at the LaAlO3/SrTiO3 heterointerface," Nature **427**, 423 (2004).

2 J. H. Haeni, P. Irvin, W. Chang, R. Uecker, P. Reiche, Y. L. Li, S. Choudhury, W. Tian, M. E. Hawley, B. Craigo, A. K. Tagantsev, X. Q. Pan, S. K. Streiffer, L. Q. Chen, S. W. Kirchoefer, J. Levy, and D. G. Schlom, "Room-temperature ferroelectricity in strained SrTiO3," Nature **430**, 758 (2004).

3 P. G. de Gennes, "Effects of Double Exchange in Magnetic Crystals," Physical Review **118**, 141 (1960).

4 H. Y. Hwang, T. T. M. Palstra, S. W. Cheong, and B. Batlogg, "Pressure effects on the magnetoresistance in doped manganese perovskites," Physical Review B **52**, 15046 (1995).

5 L. Klein, J. S. Dodge, C. H. Ahn, J. W. Reiner, L. Mieville, T. H. Geballe, M. R. Beasley, and A. Kapitulnik, "Transport and magnetization in the badly metallic itinerant ferromagnet SrRuO3," Journal of Physics-Condensed Matter **8**, 10111 (1996).

6 Q. Gan, R. A. Rao, C. B. Eom, J. L. Garrett, and L. Mark, "Direct measurement of strain effects on magnetic and electrical properties of epitaxial SrRuO3 thin films," Applied Physics Letters **72**, 978 (1998).

7 P. Orgiani, C. Aruta, G. Balestrino, S. Lavanga, P. G. Medaglia, and A. Tebano, "Strain effect on transport properties of SrRuO3 films grown by laser MBE," European Physical Journal B **26**, 23 (2002).

8 C. U. Jung, Y. Hiroyuki, M. Kawasaki, and Y. Tokura, "Magnetic anisotropy control of SrRuO3 films by tunable epitaxial strain," Applied Physics Letters **84**, 2590 (2004).

9 M. Isobe and Y. Ueda, "Observation of phase transition from metal to spin-singlet insulator in MgTi2O4 with S=1/2 pyrochlore lattice," Journal of the Physical Society of Japan **71**, 1848 (2002).

10 M. Lauer, R. Valenti, H. C. Kandpal, and R. Seshadri, "First-principles electronic structure of spinel LiCr2O4: A possible half-metal," Physical Review B **69** (2004).

11 K. Tomiyasu, J. Fukunaga, and H. Suzuki, "Magnetic short-range order and reentrant-spin-glass-like behavior in Co Cr2 O4 and Mn Cr2 O4 by means of neutron scattering and magnetization measurements," Physical Review B **70**, 214434 (2004).

12 Y. Yamasaki, S. Miyasaka, Y. Kaneko, J. P. He, T. Arima, and Y. Tokura,

"Magnetic Reversal of the Ferroelectric Polarization in a Multiferroic Spinel Oxide," Physical Review Letters **96**, 207204 (2006).

[13] R. M. Bozorth, E. F. Tilden, and A. J. Williams, "Anisotropy and Magnetostriction of Some Ferrites," Physical Review **99**, 1788 (1955).

[14] Y. Suzuki, R. B. van Dover, E. M. Gyorgy, J. M. Phillips, and R. J. Felder, "Exchange coupling in single-crystalline spinel-structure (Mn,Zn)Fe2O4/CoFe2O4 bilayers," Physical Review B **53**, 14016 (1996).

[15] G. Hu, J. H. Choi, C. B. Eom, V. G. Harris, and Y. Suzuki, "Structural tuning of the magnetic behavior in spinel-structure ferrite thin films," Physical Review B **62**, R779 (2000).

[16] E. G. Moshopoulou, "Superconductivity in the spinel compound LiTi2O4," Journal of the American Ceramic Society **82**, 3317 (1999).

[17] P. M. Lambert, P. P. Edwards, and M. R. Harrison, "Magnetism, Superconductivity, and the Metal Nonmetal Transition in the Spinel LiAl(x)Ti(2-x)O4 and LiCr(x)Ti(2-x)O4,," Journal of Solid State Chemistry **89**, 345 (1990).

[18] J. H. Park, E. Vescovo, H. J. Kim, C. Kwon, R. Ramesh, and T. Venkatesan, "Magnetic properties at surface boundary of a half-metallic ferromagnet La0.7Sr0.3MnO3," Physical Review Letters **81**, 1953 (1998).

[19] I. C. Infante, F. Sanchez, J. Fontcuberta, S. Fusil, K. Bouzehouane, G. Herranz, A. Barthelemy, S. Estrade, J. Arbiol, F. Peiro, R. J. O. Mossanek, M. Abbate, and M. Wojcik, "Structural and functional characterization of (110)-oriented epitaxial La2/3Ca1/3MnO3 electrodes and SrTiO3 tunnel barriers," Journal of Applied Physics **101**, 093902 (2007).

[20] Y. S. Dedkov, U. Rüdiger, and G. Güntherodt, "Evidence for the half-metallic ferromagnetic state of Fe3O4 by spin-resolved photoelectron spectroscopy," Physical Review B **65**, 064417 (2002).

[21] D. J. Huang, C. F. Chang, J. Chen, L. H. Tjeng, A. D. Rata, W. P. Wu, S. C. Chung, H. J. Lin, T. Hibma, and C. T. Chen, "Spin-resolved photoemission studies of epitaxial Fe3O4(100) thin films," Journal of Magnetism and Magnetic Materials **239**, 261 (2002).

[22] S. A. Morton, G. D. Waddill, S. Kim, I. K. Schuller, S. A. Chambers, and J. G. Tobin, "Spin-resolved photoelectron spectroscopy of Fe3O4," Surface Science **513**, L451 (2002).

[23] J. G. Tobin, S. A. Morton, S. W. Yu, G. D. Waddill, I. K. Schuller, and S. A. Chambers, "Spin resolved photoelectron spectroscopy of Fe3O4: the case against half-metallicity," Journal of Physics: Condensed Matter, 315218

(2007).

[24] M. Fonin, Y. S. Dedkov, R. Pentcheva, U. Rudiger, and G. Guntherodt, "Magnetite: a search for the half-metallic state," Journal of Physics: Condensed Matter, 315217 (2007).

[25] Z. Zhang and S. Satpathy, "Electron states, magnetism, and the Verwey transition in magnetite," Physical Review B **44**, 13319 (1991).

[26] P. J. van der Zaag, P. J. H. Bloemen, J. M. Gaines, R. M. Wolf, P. A. A. van der Heijden, R. J. M. van de Veerdonk, and W. J. M. de Jonge, "On the construction of an Fe3O4-based all-oxide spin valve," Journal of Magnetism and Magnetic Materials **211**, 301 (2000).

[27] X. W. Li, A. Gupta, G. Xiao, W. Qian, and V. P. Dravid, "Fabrication and properties of heteroepitaxial magnetite, (Fe3O4) tunnel junctions," Applied Physics Letters **73**, 3282 (1998).

[28] G. Hu and Y. Suzuki, "Negative spin polarization of Fe3O4 in magnetite/manganite-based junctions," Physical Review Letters **89** (2002).

[29] G. H. Hu, R. Chopdekar, and Y. Suzuki, "Observation of inverse magnetoresistance in epitaxial magnetite/manganite junctions," Journal of Applied Physics **93**, 7516 (2003).

[30] B. B. Nelson-Cheeseman, R. V. Chopdekar, L. M. B. Alldredge, J. S. Bettinger, E. Arenholz, and Y. Suzuki, "Probing the role of the barrier layer in magnetic tunnel junction transport," Physical Review B **76**, 220410 (2007).

[31] S. B. Ogale, K. Ghosh, S. P. Pai, M. Robson, E. Li, I. Jin, R. L. Greene, R. Ramesh, T. Venkatesan, and M. Johnson, "Fe3O4/SrTiO3/La0.7Sr0.3MnO3 heterostructure: growth and properties," Materials Science and Engineering: B **56**, 134 (1998).

[32] M. P. Singh, B. Carvello, and L. Ranno, "Giant magnetoresistance in an all-oxide spacerless junction," Applied Physics Letters **89**, 022504 (2006).

[33] U. Luders, M. Bibes, S. Fusil, K. Bouzehouane, E. Jacquet, C. B. Sommers, J. P. Contour, J. F. Bobo, A. Barthelemy, A. Fert, and P. M. Levy, "Bias dependence of tunnel magnetoresistance in spin filtering tunnel junctions: Experiment and theory," Physical Review B **76**, 134412 (2007).

[34] J. S. Armijo, "The kinetics and mechanism of solid-state spinel formation — A review and critique," Oxidation of Metals **1**, 171 (1969).

[35] H. M. Christen and G. Eres, "Recent advances in pulsed-laser deposition of complex oxides," Journal of Physics: Condensed Matter, 264005 (2008).

[36] S. Amoruso, R. Bruzzese, N. Spinelli, and R. Velotta, "Characterization of laser-ablation plasmas," Journal of Physics B: Atomic, Molecular and Optical Physics, R131 (1999).

[37] Y. Yamagata, A. Sharma, J. Narayan, R. M. Mayo, J. W. Newman, and K. Ebihara, "Optical emission study of ablation plasma plume in the preparation of diamond-like carbon films by KrF excimer laser," Journal of Applied Physics **86**, 4154 (1999).

[38] D. Dale, *In-Situ X-Ray Diffraction Studies Of Pulsed Laser Deposition: Growth Of Epitaxial Manganite Thin Films*, Ph.D. dissertation, (Cornell University, Ithaca, NY, 2005).

[39] A. Fleet, *Time Resolved X-Ray Scattering During Strontium Titanate Homoepitaxy By Pulsed Laser Deposition*, Ph.D. dissertation, (Cornell University, Ithaca, NY, 2005).

[40] A. Ohtomo, D. A. Muller, J. L. Grazul, and H. Y. Hwang, "Epitaxial growth and electronic structure of LaTiO(x) films," Applied Physics Letters **80**, 3922 (2002).

[41] U. Hartmann, "Magnetic Force Microscopy," Annual Review of Materials Science **29**, 53 (1999).

[42] ICDD, *Powder Diffraction File database*

[43] B. E. Warren, *X-ray Diffraction* (Addison Wesley, Reading, MA., 1969).

[44] Y. Takamura, R. V. Chopdekar, A. Scholl, A. Doran, J. A. Liddle, B. Harteneck, and Y. Suzuki, "Tuning Magnetic Domain Structure in Nanoscale La0.7Sr0.3MnO3 Islands," Nano Lett. **6**, 1287 (2006).

[45] L. G. Earwaker, "Rutherford backscattering and nuclear reaction analysis," Vacuum **45**, 783 (1994).

[46] M. Abbate, F. M. F. de Groot, J. C. Fuggle, A. Fujimori, Y. Tokura, Y. Fujishima, O. Strebel, M. Domke, G. Kaindl, J. van Elp, B. T. Thole, G. A. Sawatzky, M. Sacchi, and N. Tsuda, "Soft-x-ray-absorption studies of the location of extra charges induced by substitution in controlled-valence materials," Physical Review B **44**, 5419 (1991).

[47] F. M. F. de Groot, M. O. Figueiredo, M. J. Basto, M. Abbate, H. Petersen, and J. C. Fuggle, "2p X-ray absorption of titanium in minerals," Physics and Chemistry of Minerals **19**, 140 (1992).

[48] G. van der Laan and I. W. Kirkman, "The 2p absorption spectra of 3d transition metal compounds in tetrahedral and octahedral symmetry," Journal of Physics: Condensed Matter, 4189 (1992).

[49] R. A. D. Pattrick, G. Van der Laan, C. M. B. Henderson, P. Kuiper, E. Dudzik, and D. J. Vaughan, "Cation site occupancy in spinel ferrites studied by X-ray magnetic circular dichroism: developing a method for mineralogists," European Journal of Mineralogy **14**, 1095 (2002).

[50] F. M. F. de Groot, J. Faber, J. J. M. Michiels, M. T. Czyzyk, M. Abbate, and J. C. Fuggle, "Oxygen 1s X-ray absorption of tetravalent titanium oxides: a comparison with single-particle calculations," Physical Review B **48**, 2074 (1993).

[51] J. Stöhr, "X-ray magnetic circular dichroism spectroscopy of transition metal thin films," Journal of Electron Spectroscopy and Related Phenomena **75**, 253 (1995).

[52] W. Gudat and C. Kunz, "Close Similarity between Photoelectric Yield and Photoabsorption Spectra in the Soft-X-Ray Range," Physical Review Letters **29**, 169 (1972).

[53] J. Stöhr and H. C. Siegmann, *Magnetism: From Fundamentals to Nanoscale Dynamics* (Springer, Berlin, 2006).

[54] J. Als-Nielsen and D. McMorrow, *Elements of Modern X-ray Physics* (Wiley, 2001).

[55] B. T. Thole, P. Carra, F. Sette, and G. van der Laan, "X-ray circular dichroism as a probe of orbital magnetization," Physical Review Letters **68**, 1943 (1992).

[56] E. Arenholz, G. van der Laan, R. V. Chopdekar, and Y. Suzuki, "Anisotropic x-ray magnetic linear dichroism at the Fe L2,3 edges in Fe3O4," Physical Review B **74**, 094407 (2006).

[57] J. Lüning, F. Nolting, A. Scholl, H. Ohldag, J. W. Seo, J. Fompeyrine, J. P. Locquet, and J. Stöhr, "Determination of the antiferromagnetic spin axis in epitaxial LaFeO3 films by x-ray magnetic linear dichroism spectroscopy," Physical Review B **67**, 214433 (2003).

[58] G. van der Laan and B. T. Thole, "Strong magnetic x-ray dichroism in 2p absorption spectra of 3d transition-metal ions," Physical Review B **43**, 13401 (1991).

[59] C. T. Chen, Y. U. Idzerda, H. J. Lin, N. V. Smith, G. Meigs, E. Chaban, G. H. Ho, E. Pellegrin, and F. Sette, "Experimental Confirmation of the X-Ray Magnetic Circular Dichroism Sum Rules for Iron and Cobalt," Physical Review Letters **75**, 152 (1995).

[60] A. Scholl, "Applications of photoemission electron microscopy (PEEM) in magnetism research," Current Opinion in Solid State and Materials Science **7**, 59 (2003).

[61] L. J. van der Pauw, "A method of measuring the resistivity and hall coefficient on Lamellae of arbitrary shape," Philips Technical Review **20**, 220 (1958).

[62] Z. Ndlela and Clayton W. Bates, Jr., "Sampling procedure for measuring Hall coefficients using the van der Pauw method," Review of Scientific Instruments **60**, 3482 (1989).

[63] H. C. Montgomery, "Method for Measuring Electrical Resistivity of Anisotropic Materials," Journal of Applied Physics **42**, 2971 (1971).

[64] L. M. B. Alldredge, *Studies Of Epitaxial Complex-Oxide Thin Films And Magnetic Tunnel Junctions*, Ph.D. dissertation, (Cornell University, Ithaca, NY, 2006).

[65] http://www.crystec.de/oxides-e.html

[66] http://www.mtixtl.com/

[67] M. Kawasaki, K. Takahashi, T. Maeda, R. Tsuchiya, M. Shinohara, O. Ishiyama, T. Yonezawa, M. Yoshimoto, and H. Koinuma, "Atomic Control of the SrTiO3 Crystal Surface," Science **266**, 1540 (1994).

[68] Y. Mukunoki, N. Nakagawa, T. Susaki, and H. Y. Hwang, "Atomically flat (110) SrTiO3 and heteroepitaxy," Applied Physics Letters **86**, 171908 (2005).

[69] C. Jaewan, P. Yoon-Seok, and K. Sang-Koog, "Atomically flat single-terminated SrTiO3 (111) surface," Applied Physics Letters **92**, 152910 (2008).

[70] J. Yao, P. B. Merrill, S. S. Perry, D. Marton, and J. W. Rabalais, "Thermal stimulation of the surface termination of LaAlO3(100)," The Journal of Chemical Physics **108**, 1645 (1998).

[71] G. Cao, S. Chikara, X. N. Lin, E. Elhami, V. Durairaj, and P. Schlottmann, "Itinerant ferromagnetism to insulating antiferromagnetism: A magnetic and transport study of single crystal SrRu1-xMnxO3 (0 <= x < 0.60)," Physical Review B **71** (2005).

[72] W. Prellier, P. Lecoeur, and B. Mercey, "Colossal-magnetoresistive manganite thin films," Journal of Physics-Condensed Matter **13**, R915 (2001).

[73] S. Miyazawa, Y. Tazoh, H. Asano, Y. Nagai, O. Michikami, and M. Suzuki, "High-T(C) Superconducting Thin-Films," Advanced Materials **5**, 179 (1993).

[74] R. W. Schwartz, "Chemical solution deposition of perovskite thin films," Chemistry of Materials **9**, 2325 (1997).

[75] Y. Suzuki, "Epitaxial spinel ferrite thin films," Annual Review of Materials Research **31**, 265 (2001).

[76] C. B. Eom, R. J. Cava, R. M. Fleming, J. M. Phillips, R. B. Vandover, J. H. Marshall, J. W. P. Hsu, J. J. Krajewski, and W. F. Peck, "Single-Crystal Epitaxial Thin-Films of the Isotropic Metallic Oxides Sr(1-x)Ca(x)RuO3 (0<x<1)," Science **258**, 1766 (1992).

[77] Q. X. Jia, F. Chu, C. D. Adams, X. D. Wu, M. Hawley, J. H. Cho, A. T. Findikoglu, S. R. Foltyn, J. L. Smith, and T. E. Mitchell, "Characteristics of conductive SrRuO3 thin films with different microstructures," Journal of Materials Research **11**, 2263 (1996).

[78] L. M. Wang, H. E. Horng, and H. C. Yang, "Anomalous magnetotransport in SrRuO3 films: A crossover from Fermi-liquid to non-Fermi-liquid behavior," Physical Review B **70** (2004).

[79] S. C. Gausepohl, M. Lee, K. Char, R. A. Rao, and C. B. Eom, "Magnetoresistance Properties of Thin-Films of the Metallic Oxide Ferromagnet SrRuO3," Physical Review B **52**, 3459 (1995).

[80] L. Pi, A. Maignan, R. Retoux, and B. Raveau, "Substitution at the Ru site in the itinerant ferromagnet SrRuO3," Journal of Physics-Condensed Matter **14**, 7391 (2002).

[81] K. W. Kim, J. S. Lee, T. W. Noh, S. R. Lee, and K. Char, "Metal-insulator transition in a disordered and correlated SrTi(1-x)Ru(x)O3 system: Changes in transport properties, optical spectra, and electronic structure," Physical Review B **71** (2005).

[82] A. Arrott, "Criterion for Ferromagnetism from Observations of Magnetic Isotherms," Physical Review **108**, 1394 (1957).

[83] S. H. Oh and C. G. Park, "Misfit strain relaxation by dislocations in SrRuO3/SrTiO3 (001) heteroepitaxy," Journal of Applied Physics **95**, 4691 (2004).

[84] D. C. Johnston, "Superconducting and normal state properties of Li(1+x)Ti(2)O(4) spinel compounds. I. Preparation, crystallography, superconducting properties, electrical resistivity, dielectric behavior, and magnetic susceptibility," Journal of Low Temperature Physics **25**, 145 (1976).

[85] D. C. Johnston, H. Prakash, W. H. Zachariasen, and R. Viswanathan, "High temperature superconductivity in the Li-Ti-O ternary system," Materials Research Bulletin **8**, 777 (1973).

[86] L. J. Dejongh, "A Comparative-Study of (Bi)Polaronic (Super)Conductivity in High-Tc Superconducting and Low-Tc Superconducting Oxides," Physica C **152**, 171 (1988).

[87] M. R. Harrison, P. P. Edwards, and J. B. Goodenough, "Localized Moments in

the Superconducting Li(1+x)Ti(2-x)O4 Spinel System," Journal of Solid State Chemistry **54**, 136 (1984).

88 E. Moshopoulou, P. Bordet, J. J. Capponi, C. Chaillout, B. Souletie, and A. Sulpice, "Evolution of Structure and Superconductivity with Lithium Content in Li-1-Xti2O4," Journal of Alloys and Compounds **195**, 81 (1993).

89 E. Moshopoulou, P. Bordet, A. Sulpice, and J. J. Capponi, "Evolution of Structure and Superconductivity of Li-1-Xti2O4 Single-Crystals without Ti Cation Disorder," Physica C **235**, 747 (1994).

90 J. H. Lin, T. H. Lin, and C. W. Chu, "High-Pressure Study on Li(1+x)Ti(2-x)O4," Journal of Low Temperature Physics **58**, 363 (1985).

91 R. N. Shelton, D. C. Johnston, and H. Adrian, "Measurement of Pressure-Dependence of Tc for Superconducting Spinel Compounds," Solid State Communications **20**, 1077 (1976).

92 W. Prellier, A. M. Haghiri-Gosnet, B. Mercey, P. Lecoeur, M. Hervieu, C. Simon, and B. Raveau, "Spectacular decrease of the melting magnetic field in the charge-ordered state of Pr0.5Ca0.5MnO3 films under tensile strain," Applied Physics Letters **77**, 1023 (2000).

93 G. G. N. Angilella, G. Balestrino, P. Cermelli, P. Podio-Guidugli, and A. A. Varlamov, "Effect of strain-induced electronic topological transitions on the superconducting properties of La(2-x)Sr(x)CuO4 thin films," The European Physical Journal B - Condensed Matter and Complex Systems **26**, 67 (2002).

94 S. Autier-Laurent, B. Mercey, D. Chippaux, P. Limelette, and C. Simon, "Strain-induced pressure effect in pulsed laser deposited thin films of the strongly correlated oxide V2O3," Physical Review B **74**, 195109 (2006).

95 M. Henzler, "Growth of epitaxial monolayers," Surface Science **358**, 809 (1996).

96 J. Z. Wu, P. Y. Hsieh, A. V. McGuire, D. L. Schmidt, L. T. Wood, Y. Shen, and W. K. Chu, "Anisotropic properties of the high-quality epitaxial YBa2Cu3O(7-x) (110) thin film," Phys. Rev. B **44**, 12643 (1991).

97 H. U. Habermeier, "Controlled Modifications of HTSC Thin-Film Properties by Tailoring Substrate Surfaces," Journal of Superconductivity **13**, 871 (2000).

98 T. Inukai, T. Murakami, and T. Inamura, "Preparation of Superconducting LiTi2O4 Thin-Films," Thin Solid Films **94**, 47 (1982).

99 T. Inukai and T. Murakami, "Influence of Film Thickness and Annealing Temperature on Superconducting Li(1+X)Ti(2-x)O4 Thin-Films," Thin Solid Films **128**, 275 (1985).

[100] G. Hu, V. G. Harris, and Y. Suzuki, "Microstructure and magnetic properties of cobalt ferrite thin films," IEEE Transactions on Magnetics **37**, 2347 (2001).

[101] W. Eerenstein, T. T. M. Palstra, T. Hibma, and S. Celotto, "Origin of the increased resistivity in epitaxial Fe3O4 films," Phys. Rev. B **66**, 201101 (2002).

[102] D. T. Margulies, F. T. Parker, M. L. Rudee, F. E. Spada, J. N. Chapman, P. R. Aitchison, and A. E. Berkowitz, "Origin of the anomalous magnetic behaviour in single crystal Fe3O4 films," Physical Review Letters **79**, 5162 (1997).

[103] F. C. Voogt, T. T. M. Palstra, L. Niesen, O. C. Rogojanu, M. A. James, and T. Hibma, "Superparamagnetic behavior of structural domains in epitaxial ultrathin magnetite films," Physical Review B **57**, R8107 (1998).

[104] M. Dalton and M. Kurmoo, "Structural, Electronic and Magnetic-Properties as a Function of Bandfilling in the Superconducting System Li(1-x)Mg(x)Ti2O4," Synthetic Metals **71**, 1623 (1995).

[105] H. Zheng, J. Wang, S. E. Lofland, Z. Ma, L. Mohaddes-Ardabili, T. Zhao, L. Salamanca-Riba, S. R. Shinde, S. B. Ogale, F. Bai, D. Viehland, Y. Jia, D. G. Schlom, M. Wuttig, A. Roytburd, and R. Ramesh, "Multiferroic BaTiO3-CoFe2O4 nanostructures," Science **303**, 661 (2004).

[106] R. V. Chopdekar, G. Hu, A. C. Ford, and Y. Suzuki, "Magnetics and magnetoresistance in epitaxial magnetite heterostructures," Journal of Electronic Materials **33**, 1254 (2004).

[107] T. Inukai, T. Murakami, and T. Inamura, "Aging Effects of Li-Ti-O Superconducting Compounds," Japanese Journal of Applied Physics **20**, L681 (1981).

[108] F. C. Xu, Y. C. Liao, M. J. Wang, C. T. Wu, K. F. Chiu, and M. K. Wu, "The preparation effect of Li(1+x)Ti2O4 and its aging effect," Journal of Low Temperature Physics **131**, 569 (2003).

[109] R. G. Buckley, B. P. Clayman, and J. C. Mikkelsen, "Infrared Study of the Fast-Ion Conductor Li2Ti3O7," Physical Review B **26**, 6509 (1982).

[110] I. Abrahams, P. G. Bruce, W. I. F. David, and A. R. West, "Refinement of the lithium distribution in Li2Ti3O7 using high-resolution powder neutron diffraction," Journal of Solid State Chemistry **78**, 170 (1989).

[111] A. T. Young, J. Feng, E. Arenholz, H. A. Padmore, T. Henderson, S. Marks, E. Hoyer, R. Schlueter, J. B. Kortright, V. Martynov, C. Steier, and G. Portmann, "First commissioning results for the elliptically polarizing undulator beamline at the Advanced Light Source," Nuclear Instruments & Methods in Physics Research Section a-Accelerators Spectrometers Detectors and Associated

Equipment **467**, 549 (2001).

[112] P. Nachimuthu, J. H. Underwood, C. D. Kemp, E. M. Gullikson, D. W. Lindle, D. K. Shuh, and R. C. C. Perera, "Performance Characteristics of Beamline 6.3.1 from 200 eV to 2000 eV at the Advanced Light Source," AIP Conference Proceedings: Eighth International Conference on Synchrotron Radiation Instrumentation **705**, 454 (2004).

[113] W. Ra, M. Nakayama, H. Ikuta, Y. Uchimoto, and M. Wakihara, "X-ray absorption study of the electronic structure of Li-excess spinel Li(1+x)Ti(2-x)O4 (0 <= x <= 0.33)," Applied Physics Letters **84**, 4364 (2004).

[114] B. H. Frazer, B. Gilbert, B. R. Sonderegger, and G. De Stasio, "The probing depth of total electron yield in the sub-keV range: TEY-XAS and X-PEEM," Surface Science **537**, 161 (2003).

[115] L. A. Bugaev, A. P. Sokolenko, H. V. Dmitrienko, and A. M. Flank, "Fourier filtration of XANES as a source of quantitative information of interatomic distances and coordination numbers in crystalline minerals and amorphous compounds," Phys. Rev. B **65**, 024105 (2001).

[116] F. Gomory, "Characterization of high-temperature superconductors by AC susceptibility measurements," Supercond. Sci. Technol. **10**, 523 (1997).

[117] Y. Ueda, T. Tanaka, K. Kosuge, M. Ishikawa, and H. Yasuoka, "Superconducting Properties in the Li(1+x)Ti(2-x)O4 System with the Spinel Structure," Journal of Solid State Chemistry **77**, 401 (1988).

[118] P. M. Lambert, M. R. Harrison, and P. P. Edwards, "Magnetism and Superconductivity in the Spinel System Li(1-x)Mn(x)Ti2O4 and Li(1-x)Mg(x)Ti2O4," Journal of Solid State Chemistry **75**, 332 (1988).

[119] M. Steinbruck and A. Feltz, "Investigations on Electronically Conducting Oxide Systems .19. Substitution of Magnesium for Lithium in the Superconducting Spinel LiTi2O4," Journal of Materials Science Letters **11**, 216 (1992).

[120] M. R. Harrison, P. P. Edwards, and J. B. Goodenough, "The superconductor-semiconductor transition in the Li(1+x)Ti(2-x)O4 spinel system," Philosophical Magazine Part B **52**, 679 (1985).

[121] D. P. Norton, D. H. Lowndes, S. J. Pennycook, and J. D. Budai, "Depression and broadening of the superconducting transition in superlattices based on YBa2Cu3O7-x: influence of the barrier layers," Physical Review Letters **67**, 1358 (1991).

[122] N. R. Werthamer, E. Helfand, and P. C. Hohenberg, "Temperature and Purity Dependence of Superconducting Critical Field Hc2 .3. Electron Spin and Spin-

Orbit Effects," Physical Review **147**, 295 (1966).

123 S. Foner and E. J. McNiff, Jr., "Paramagnetic limiting in superconducting Li-Ti-O ternary system," Solid State Communications **20**, 995 (1976).

124 L. Coffey, K. A. Muttalib, and K. Levin, "Theory of upper critical fields in highly disordered superconductors: localization effects," Physical Review Letters **52**, 783 (1984).

125 M. Tenhover, W. L. Johnson, and C. C. Tsuei, "Upper critical fields of amorphous transition metal based alloys," Solid State Communications **38**, 53 (1981).

126 C. P. Sun, J. Y. Lin, S. Mollah, P. L. Ho, H. D. Yang, F. C. Hsu, Y. C. Liao, and M. K. Wu, "Magnetic field dependence of low-temperature specific heat of the spinel oxide superconductor LiTi2O4," Physical Review B **70** (2004).

127 L. Tang, P. Y. Zou, L. Shan, A. F. Dong, G. C. Che, and H. H. Wen, "Electrical resistivity and Andreev reflection spectroscopy of the superconducting oxide spinel LiTi2O4," Physical Review B **73**, 184521 (2006).

128 E. S. Hellman and E. H. Hartford, "Normal-state resistivity and Hall effect in Ba(1-x)K(x)BiO3 epitaxial films," Phys. Rev. B **47**, 11346 (1993).

129 F. Nava, O. Bisi, and K. N. Tu, "Electrical transport properties of V3Si, V5S3, and VSi2 thin films," Phys. Rev. B **34**, 6143 (1986).

130 N. A. Hill, "Density functional studies of multiferroic magnetoelectrics," Annual Review of Materials Research **32**, 1 (2002).

131 N. Hur, S. Park, P. A. Sharma, J. S. Ahn, S. Guha, and S. W. Cheong, "Electric polarization reversal and memory in a multiferroic material induced by magnetic fields," Nature **429**, 392 (2004).

132 T. Kimura, T. Goto, H. Shintani, K. Ishizaka, T. Arima, and Y. Tokura, "Magnetic control of ferroelectric polarization," Nature **426**, 55 (2003).

133 A. Sharan, J. Lettieri, Y. F. Jia, W. Tian, X. Q. Pan, D. G. Schlom, and V. Gopalan, "Bismuth manganite: A multiferroic with a large nonlinear optical response," Physical Review B **69** (2004).

134 J. Dho, C. W. Leung, J. L. MacManus-Driscoll, and M. G. Blamire, "Epitaxial and oriented YMnO3 film growth by pulsed laser deposition," Journal of Crystal Growth **267**, 548 (2004).

135 J. Wang, J. B. Neaton, H. Zheng, V. Nagarajan, S. B. Ogale, B. Liu, D. Viehland, V. Vaithyanathan, D. G. Schlom, U. V. Waghmare, N. A. Spaldin,

K. M. Rabe, M. Wuttig, and R. Ramesh, "Epitaxial BiFeO3 multiferroic thin film heterostructures," Science **299**, 1719 (2003).

136 J. Ryu, A. V. Carazo, K. Uchino, and H. E. Kim, "Magnetoelectric properties in piezoelectric and magnetostrictive laminate composites," Japanese Journal of Applied Physics Part 1-Regular Papers Short Notes & Review Papers **40**, 4948 (2001).

137 S. Shastry, G. Srinivasan, M. I. Bichurin, V. M. Petrov, and A. S. Tatarenko, "Microwave magnetoelectric effects in single crystal bilayers of yttrium iron garnet and lead magnesium niobate-lead titanate," Physical Review B **70** (2004).

138 G. Srinivasan, E. T. Rasmussen, B. J. Levin, and R. Hayes, "Magnetoelectric effects in bilayers and multilayers of magnetostrictive and piezoelectric perovskite oxides," Physical Review B **65** (2002).

139 F. Zavaliche, H. Zheng, L. Mohaddes-Ardabili, S. Y. Yang, Q. Zhan, P. Shafer, E. Reilly, R. Chopdekar, Y. Jia, P. Wright, D. G. Schlom, Y. Suzuki, and R. Ramesh, "Electric field-induced magnetization switching in epitaxial columnar nanostructures," Nano Letters **5**, 1793 (2005).

140 M. A. Zurbuchen, T. Wu, S. Saha, J. Mitchell, and S. K. Streiffer, "Multiferroic composite ferroelectric-ferromagnetic films," Applied Physics Letters **87** (2005).

141 R. Clarke, "Phase-Transition Studies of Pure and Flux-Grown Barium-Titanate Crystals," Journal of Applied Crystallography **9**, 335 (1976).

142 B. D. Cullity, *Introduction to Magnetic Materials* (Addison-Wesley, Reading, MA, 1972).

143 G. Q. Gong, A. Gupta, G. Xiao, W. Qian, and V. P. Dravid, "Magnetoresistance and magnetic properties of epitaxial magnetite thin films," Physical Review B **56**, 5096 (1997).

144 Y. Suzuki, G. Hu, R. B. van Dover, and R. J. Cava, "Magnetic anisotropy of epitaxial cobalt ferrite thin films," Journal of Magnetism and Magnetic Materials **191**, 1 (1999).

145 Y. Iwasaki, M. Kaneko, K. Hayashi, Y. Ochiai, M. Hayakawa, and K. Aso, "A new apparatus for measuring thermal expansion of thin films," Journal of Physics E: Scientific Instruments **22**, 498 (1989).

146 A. Fischer, H. Kuhne, and H. Richter, "New Approach in Equilibrium-Theory for Strained-Layer Relaxation," Physical Review Letters **73**, 2712 (1994).

147 D. Dale, A. Fleet, J. D. Brock, and Y. Suzuki, "Dynamically tuning properties

of epitaxial colossal magnetoresistance thin films," Applied Physics Letters **82**, 3725 (2003).

148 A. von Hippel, "Ferroelectricity, Domain Structure, and Phase Transitions of Barium Titanate," Reviews of Modern Physics **22**, 221 (1950).

149 W. E. Pickett and D. J. Singh, "Electronic structure and half-metallic transport in the La(1-x)Ca(x)MnO3 system," Physical Review B **53**, 1146 (1996).

150 Y. Lu, X. W. Li, G. Q. Gong, G. Xiao, A. Gupta, P. Lecoeur, J. Z. Sun, Y. Y. Wang, and V. P. Dravid, "Large magnetotunneling effect at low magnetic fields in micrometer-scale epitaxial La0.67Sr0.33MnO3 tunnel junctions," Physical Review B **54**, R8357 (1996).

151 M. Viret, M. Drouet, J. Nassar, J. P. Contour, C. Fermon, and A. Fert, "Low-field colossal magnetoresistance in manganite tunnel spin valves," EPL (Europhysics Letters) **39**, 545 (1997).

152 M. Bowen, M. Bibes, A. Barthelemy, J. P. Contour, A. Anane, Y. Lemaitre, and A. Fert, "Nearly total spin polarization in La(2/3)Sr(1/3)MnO3 from tunneling experiments," Applied Physics Letters **82**, 233 (2003).

153 W. H. Butler, X. G. Zhang, T. C. Schulthess, and J. M. MacLaren, "Spin-dependent tunneling conductance of Fe vertical bar MgO vertical bar Fe sandwiches," Physical Review B **6305** (2001).

154 S. S. P. Parkin, C. Kaiser, A. Panchula, P. M. Rice, B. Hughes, M. Samant, and S.-H. Yang, "Giant tunnelling magnetoresistance at room temperature with MgO (100) tunnel barriers," Nat Mater **3**, 862 (2004).

155 P. G. Radaelli, M. Marezio, H. Y. Hwang, S. W. Cheong, and B. Batlogg, "Charge localization by static and dynamic distortions of the MnO6 octahedra in perovskite manganites," Physical Review B **54**, 8992 (1996).

156 L. M. Berndt, V. Balbarin, and Y. Suzuki, "Magnetic anisotropy and strain states of (001) and (110) colossal magnetoresistance thin films," Applied Physics Letters **77**, 2903 (2000).

157 W. Nix, "Mechanical properties of thin films," Metallurgical and Materials Transactions A **20**, 2217 (1989).

158 T. W. Darling, A. Migliori, E. G. Moshopoulou, S. A. Trugman, J. J. Neumeier, J. L. Sarrao, A. R. Bishop, and J. D. Thompson, "Measurement of the elastic tensor of a single crystal of La0.83Sr0.17MnO3 and its response to magnetic fields," Physical Review B **57**, 5093 (1998).

159 J. L. Maurice, F. Pailloux, A. Barthelemy, O. Durand, D. Imhoff, R. Lyonnet, A. Rocher, and J. P. Contour, "Strain relaxation in the epitaxy of

La(2/3)Sr(1/3)MnO3 grown by pulsed-laser deposition on SrTiO3(001)," Philosophical Magazine **83**, 3201 (2003).

160 J. M. D. Coey, M. Viret, L. Ranno, and K. Ounadjela, "Electron Localization in Mixed-Valence Manganites," Physical Review Letters **75**, 3910 (1995).

161 J. Z. Sun, D. W. Abraham, R. A. Rao, and C. B. Eom, "Thickness-dependent magnetotransport in ultrathin manganite films," Applied Physics Letters **74**, 3017 (1999).

162 F. Pailloux, R. Lyonnet, J.-L. Maurice, and J.-P. Contour, "Twinning and lattice distortions in the epitaxy of La0.67Sr0.33MnO3 thin films on (0 0 1) SrTiO3," Applied Surface Science **177**, 263 (2001).

163 M. Zhang, X. L. Ma, D. X. Li, H. B. Lu, Z. H. Chen, and G. Z. Yang, "Microdomains in thin films of rhombohedral La0.7Sr0.3MnO3," physica status solidi (a) **196**, 365 (2003).

164 R. Nakajima, J. Stöhr, and Y. U. Idzerda, "Electron-yield saturation effects in L-edge x-ray magnetic circular dichroism spectra of Fe, Co, and Ni," Physical Review B **59**, 6421 (1999).

165 S. Gota, M. Gautier-Soyer, and M. Sacchi, "Fe 2p absorption in magnetic oxides: Quantifying angular-dependent saturation effects," Physical Review B **62**, 4187 (2000).

166 E. Goering, "X-ray magnetic circular dichroism sum rule correction for the light transition metals," Philosophical Magazine **85**, 2895 (2005).

167 R. Wu and A. J. Freeman, "Limitation of the Magnetic-Circular-Dichroism Spin Sum Rule for Transition Metals and Importance of the Magnetic Dipole Term," Physical Review Letters **73**, 1994 (1994).

168 J. Fontcuberta, I. C. Infante, V. Laukhin, F. Sanchez, M. Wojcik, and E. Jedryka, (AIP, 2006), Vol. 99, p. 08A701.

169 O. I. Lebedev, J. Verbeeck, G. Van Tendeloo, S. Amelinckx, F. S. Razavi, and H. U. Habermeier, "Structure and microstructure of La(1-x)Sr(x)MnO3 (x=0.16) films grown on a SrTiO3 (110) substrate," Philosophical Magazine A **81**, 2865 (2001).

170 E. Heifets, I. W. A. Goddard, E. A. Kotomin, R. I. Eglitis, and G. Borstel, "Ab initio calculations of the SrTiO3 (110) polar surface," Physical Review B **69**, 035408 (2004).

171 A. Pojani, F. Finocchi, and C. Noguera, "Polarity on the SrTiO3 (111) and (110) surfaces," Surface Science **442**, 179 (1999).

172 M. P. de Jong, I. Bergenti, V. A. Dediu, M. Fahlman, M. Marsi, and C. Taliani, "Evidence for Mn2+ ions at surfaces of La0.7Sr0.3MnO3 thin films," Physical Review B **71**, 014434 (2005).

173 A. Miniotas, A. Vailionis, E. B. Svedberg, and U. O. Karlsson, "Misfit strain induced lattice distortions in heteroepitaxially grown La(x)Ca(1-x)MnO3 thin films studied by extended x-ray absorption fine structure and high-resolution x-ray diffraction," Journal of Applied Physics **89**, 2134 (2001).

174 W. H. Meiklejohn and C. P. Bean, "New Magnetic Anisotropy," Physical Review **102**, 1413 (1956).

175 S. S. P. Parkin, N. More, and K. P. Roche, "Oscillations in exchange coupling and magnetoresistance in metallic superlattice structures: Co/Ru, Co/Cr, and Fe/Cr," Physical Review Letters **64**, 2304 (1990).

176 J. Nogués, C. Leighton, and I. K. Schuller, "Correlation between antiferromagnetic interface coupling and positive exchange bias," Physical Review B **61**, 1315 (2000).

177 S. Maat, K. Takano, S. S. P. Parkin, and E. E. Fullerton, "Perpendicular Exchange Bias of Co/Pt Multilayers," Physical Review Letters **87**, 087202 (2001).

178 Y. Ijiri, J. A. Borchers, R. W. Erwin, S. H. Lee, P. J. van der Zaag, and R. M. Wolf, "Perpendicular Coupling in Exchange-Biased Fe3O4/CoO Superlattices," Physical Review Letters **80**, 608 (1998).

179 S. Anders, H. A. Padmore, R. M. Duarte, T. Renner, T. Stammler, A. Scholl, M. R. Scheinfein, J. Stohr, L. Seve, and B. Sinkovic, "Photoemission electron microscope for the study of magnetic materials," Review of Scientific Instruments **70**, 3973 (1999).

180 B. D. Schrag, A. Anguelouch, S. Ingvarsson, X. Gang, L. Yu, P. L. Trouilloud, A. Gupta, R. A. Wanner, W. J. Gallagher, P. M. Rice, and S. S. P. Parkin, "Neel "orange-peel" coupling in magnetic tunneling junction devices," Applied Physics Letters **77**, 2373 (2000).

181 N. Keller, A. Das, M. Guyot, M. Porte, and R. Krishnan, "Study of the interdiffusion at the interfaces of NiO/alphaFe2O3 multilayers prepared by pulsed laser deposition," Solid State Communications **105**, 333 (1998).

182 M. Robbins, G. K. Wertheim, R. C. Sherwood, and D. N. E. Buchanan, "Magnetic properties and site distributions in the system FeCr2O4-Fe3O4 FeCr(2-x)Fe(x)O4," Journal of Physics and Chemistry of Solids **32**, 717 (1971).

183 V. N. Antonov, B. N. Harmon, and A. N. Yaresko, "Electronic structure and x-

ray magnetic circular dichroism in Fe3O4 and Mn-, Co-, or Ni-substituted Fe3O4," Physical Review B **67** (2003).

184 H. Mohan, I. A. Shaikh, and R. G. Kulkarni, "Magnetic properties of the mixed spinel CoFe(2-x)Cr(x)O4," Physica B: Condensed Matter **217**, 292 (1996).

185 Y. G. Saksonov and V. A. Somenkov, "The relationship between the spinel crystal lattice constant, cationic distribution and oxygen parameter," Fizika Metallov i Metallovedenie **18**, 853 (1964).

186 D. T. Margulies, F. T. Parker, F. E. Spada, R. S. Goldman, J. Li, R. Sinclair, and A. E. Berkowitz, "Anomalous moment and anisotropy behavior in Fe3O4 films," Physical Review B **53**, 9175 (1996).

187 P. Seneor, A. Fert, J. L. Maurice, F. Montaigne, F. Petroff, and A. Vaures, "Large magnetoresistance in tunnel junctions with an iron oxide electrode," Appl. Phys. Lett. **74**, 4017 (1999).

188 A. F. Panchula, *Magnetotransport in Magnetic Nanostructures*, Ph.D. dissertation, (Stanford University, 2003).

189 V. L. Mazzocchi and C. B. R. Parente, J. Appl. Cryst. **31**, 718 (1998).

190 D. de Ligny and P. Richet, "High-temperature heat capacity and thermal expansion of SrTiO3 and SrZrO3 perovskites," Physical Review B **53**, 3013 (1996).

191 S. K. Arora, R. G. S. Sofin, and I. V. Shvets, "Magnetoresistance enhancement in epitaxial magnetite films grown on vicinal substrates," Physical Review B **72**, 134404 (2005).

192 L. M. B. Alldredge, R. V. Chopdekar, B. B. Nelson-Cheeseman, and Y. Suzuki, "Spin-polarized conduction in oxide magnetic tunnel junctions with magnetic and nonmagnetic insulating barrier layers," Applied Physics Letters **89**, 182504 (2006).

193 V. Garcia, M. Bibes, A. Barthélémy, M. Bowen, E. Jacquet, J. P. Contour, and A. Fert, "Temperature dependence of the interfacial spin polarization of La2/3Sr1/3MnO3," Physical Review B **69**, 052403 (2004).

194 M. Gajek, M. Bibes, A. Barthelemy, K. Bouzehouane, S. Fusil, M. Varela, J. Fontcuberta, and A. Fert, "Spin filtering through ferromagnetic BiMnO3 tunnel barriers," Physical Review B **72**, 020406 (2005).

195 M. G. Chapline and S. X. Wang, "Room-temperature spin filtering in a CoFe2O4/MgAl2O4/Fe3O4 magnetic tunnel barrier," Physical Review B **74**, 014418 (2006).